UC Santa Barbara

UC Santa Barbara Electronic Theses and Dissertations

Title

Structural Ordering of Semiconducting Polymers and Small-molecules for Organic Electronics

Permalink

https://escholarship.org/uc/item/7rw1m682

Author

OHara, Kathryn Allison

Publication Date

2017

Peer reviewed|Thesis/dissertation

UNIVERSITY OF CALIFORNIA

Santa Barbara

Structural Ordering of Semiconducting Polymers and Small-molecules for Organic

Electronics

A dissertation submitted in partial satisfaction of the

requirements for the degree Doctor of Philosophy

in Materials

by

Kathryn Allison O'Hara

Committee in charge:

Professor Michael L. Chabinyc, Chair

Professor Omar A. Saleh

Professor Craig J. Hawker

Professor Glenn H. Fredrickson

September 2017

The dissertation of Kathryn Allison O'Hara is approved.

_____

Omar A. Saleh

_____

Craig J. Hawker

_____

Glenn H. Fredrickson

_____

Michael L. Chabinyc, Committee Chair

September 2017

Structural Ordering of Semiconducting Polymers and Small-molecules for Organic

Electronics

iii

ACKNOWLEDGEMENTS

The completion of this work would not have been possible without help from a long list of people. I want to first thank my advisor Michael Chabinyc and the rest of my committee. Michael was an amazing mentor that led the group with a strong enthusiasm for science and always encouraged creative thinking. I also appreciated the constant encouragement to expand my horizons through collaborations with other universities, visits to national labs, and travel to conferences. My graduate school experience has been extremely positive and I attribute that to not only being in a great department, but being in Michael's group.

I have also been incredibly lucky to have so many wonderful group members over the years. A big shout out to the X-ray crew for the educational yet also entertaining trips to the beamlines. Thank you to Jes Sherman, Justin Cochran, Greg Su, and Mike Brady for teaching me how to do X-ray scattering experiments. I am especially thankful for Chris Takacs for being such a great mentor, teaching me to use the TEM, and always having endless good ideas.

I am also very appreciative of the wonderful staff scientists at the UCSB shared facilities, especially Mark Cornish, Stephan Kraemer, and Aidan Hopkins. Additionally, the scientists and postdocs at SSRL and ALS provided invaluable assistance during the many beamline trips including Mike Toney, Tim Dunn, Chris Tassone, Chris Takacs, Hans Steinrueck, Cheng Wang, and David Kilcoyne.

Finally, thank you to my fiancé, Blake, my parents, Jan and Tom, and all of my amazing friends who have been so supportive during this journey.

VITA OF KATHRYN ALLISON O'HARA
September 2017

EDUCATION

Bachelor of Science in Biological Engineering, University of Florida, May 2012

Doctor of Philosophy in Materials, University of California, Santa Barbara, September 2017 (Expected)

PROFESSIONAL EMPLOYMENT

2008-2010: Undergraduate Research Assistant, Materials Science & Engineering Department, University of Florida, Gainesville, FL

Summer 2011: Product Engineering Intern, Applied Materials, Varian Semiconductor Equipment, Gloucester, MA

2010-2012: Research Consulting Assistant, Materials Science & Engineering Department, University of Florida, Gainesville, FL

2012-2017: Graduate Student Researcher, Materials Department, University of California, Santa Barbara, Santa Barbara, CA

PUBLICATIONS

O'Hara, K. A., Pokuri, B. S. S., Chabinyc, M. L., and Ganapathysubramanian, B. Automated Framework to Analyze High Resolution TEM Images Grain Boundaries in Semiconducting Polymer Thin Films. *In preparation.*

O'Hara, K. A., Pokuri, B. S. S., Takacs, C. J., Beaujuge, P. M., Ganapathysubramanian, B., and Chabinyc, M. L. The Effect of the Alkyl Side-chains on Intercrystallite Order in Semiconducting Polymers. *In preparation.*

Pokuri, B. S. S., Stimes, J., **O'Hara, K. A.**, Chabinyc, M. L., and Ganapathysubramanian, B. GRATE: A framework and software for GRaph based Analysis of Transmission Electron Microscopy (TEM) images of polymer films. *In preparation.*

Larson, B. W., Koldemir, U., Ostrowski, D. P., **O'Hara, K. A.**, Shaheen, S. E., Sellinger, A., Chabinyc, M. L., Ferguson, A. J., and Kopidakis, N. Probing Nanoscale Carrier Dynamics in P3HT Blended with a Non-Fullerene Acceptor: Impact of Mixing on Device-Relevant Carrier Generation. *In preparation.*

Perry, E., Chiu, C., Schlitz, R., Moudgil, K., Takacs, C. J., Labram, J., **O'Hara, K. A**., Glaudell, A., Sherman, J., Barlow, S., Hawker, C. J., Marder, S., and Chabinyc, M. L. High Conductivity in a Non-Planar n-Doped Ambipolar Semiconducting Polymer. *Chem. Mater.* *Submitted.*

O'Hara, K. A., Ostrowski, D. P., Koldemir, U., Takacs, C. J., Shaheen, S. E., Sellinger, A., and Chabinyc, M. L. Role of Crystallization in the Morphology of Polymer:Non-fullerene Acceptor Bulk Heterojunctions. *ACS Appl. Mater. Interfaces* **9,** 19021–19029 (2017).

Patel, S., Glaudell, A., Peterson, K., Thomas, E., **O'Hara, K. A**, Lim, E., and Chabinyc, M. L. Morphology controls the thermoelectric power factor of a doped semiconducting polymer. *Sci. Adv.* **3,** e1700434 (2017).

Gujral, A., Gómez, J., Jiang, J., Huang, C., **O'Hara, K. A.,** Toney, M. F., Chabinyc, M. L., Yu, L., and Ediger, M. D. Highly Organized Smectic-like Packing in Vapor-Deposited Glasses of a Liquid Crystal. *Chem. Mater.* **29,** 849–858 (2017).

Di Pietro, R., Nasrallah, I., Carpenter, J., Gann, E., Kölln, L. S., Thomsen, L., Venkateshvaran, D., **O'Hara, K.,** Sadhanala, A., Chabinyc, M., McNeill, C. R., Facchetti, A., Ade, H., Sirringhaus, H., and Neher, D. Coulomb Enhanced Charge Transport in Semicrystalline Polymer Semiconductors. *Adv. Funct. Mater.* (2016). doi:10.1002/adfm.201602080

Tremolet De Villers, B. J., **O'Hara, K. A.,** Ostrowski, D. P., Biddle, P. H., Shaheen, S. E., Chabinyc, M. L., Olson, D. C., and Kopidakis, N. Removal of Residual Diiodooctane Improves Photostability of High-Performance Organic Solar Cell Polymers. *Chem. Mater.* 28, 876–884 (2016). doi:10.1021/acs.chemmater.5b04346

Gujral, A., **O'Hara, K. A.** Toney, M. F., Chabinyc, M. L., and Ediger, M.D. Structural Characterization of Vapor-Deposited Glasses of an Organic Hole Transport Material with X-ray Scattering. *Chem. Mater.* 27, 3341–3348 (2015). doi: 10.1021/acs.chemmater.5b00583

Gostovic, D., Vito, N. J., **O'Hara, K. A.,** Jones, K. S., and Wachsman, E. D. Microstructure and connectivity quantification of complex composite solid oxide fuel cell electrode 3D networks. *J. Am. Ceram. Soc.* 94, 620–627 (2011). doi: 10.1111/j.1551-2916.2010.04111.x

FIELDS OF STUDY

Major Field: Organic Electronics

Studies in Morphological Characterization of Semiconducting Polymers and Small-Molecules Using X-ray Scattering and Transmission Electron Microscopy (Professor Michael L. Chabinyc)

ABSTRACT

Structural Ordering of Semiconducting Polymers and Small-molecules for Organic

Electronics

by

Kathryn Allison O'Hara

Semiconducting polymers and small-molecules can be readily incorporated into electronic devices such as organic photovoltaics (OPVs), thermoelectrics (OTEs), organic light emitting diodes (OLEDs), and organic thin film transistors (OTFTs). Organic materials offer the advantage of being processable from solution to form flexible and lightweight thin films. The molecular design, processing, and resulting thin film morphology of semiconducting polymers drastically affect the optical and electronic properties. Charge transport within films of semiconducting polymers relies on the nanoscale organization to ensure electronic coupling through overlap of molecular orbitals and to provide continuous transport pathways. While the angstrom-scale packing details can be studied using X-ray scattering methods, an understanding of the mesoscale, or the length scale over which smaller ordered regions connect, is much harder to achieve.

Grain boundaries play an important role in semiconducting polymer thin films where the average grain size is much smaller than the total distance which charges must traverse in order to reach the electrodes in a device. The majority of semiconducting polymers adopt a lamellar

packing structure in which the conjugated backbones align in parallel π-stacks separated by the alkyl side-chains. Only two directions of transport are possible – along the conjugated backbone and in the π-stacking direction. Currently, the discussion of transport between crystallites is centered around the idea of tie-chains, or "bridging" polymer chains connecting two ordered regions. However, as molecular structures become increasingly complex with the development of new donor-acceptor copolymers, additional forms of connectivity between ordered domains should be considered.

High resolution transmission electron microscopy (HRTEM) is a powerful tool for directly imaging the crystalline grain boundaries in polymer and small-molecule thin films. Recently, structures comparable to quadrites were discovered in the semiconducting polymer, PSBTBT, where the angle of chain overlap could be predicted by the geometry of the backbone and alkyl side-chains. Such structures are hypothesized to improve the electronic connectivity and enable 3D transport. Now, it has been determined that another semiconducting polymer, PBDTTPD, forms cross-chain structures in thin films. PBDTTPD is a low band-gap donor-acceptor copolymer used in high efficiency OPVs. The effect of the alkyl side-chains on intercrystallite order is determined by examining three different derivatives of the PBDTTPD polymer with HRTEM. Additionally, the expansion and contraction of films during thermal annealing and slow cooling is monitored through *in-situ* grazing incidence wide-angle X-ray scattering (GIWAXS) measurements. Results show that minor variations in side-chain structure drive both crystallite orientation and the formation of crossed structures. Overall, these studies suggest design principles to continue to advance the field of organic electronics.

TABLE OF CONTENTS

Chapter 1

Introduction

Semiconducting polymers and small-molecules can be readily incorporated into electronic devices such as organic photovoltaics (OPVs)[1], thermoelectrics (OTEs)[2], light emitting diodes (OLEDs)[3], and thin film transistors (OTFTs)[4]. Organic materials offer the advantage of being processable from solution into flexible thin films, and therefore devices may have a lower production cost than inorganic materials[5]. The synthetic design of conjugated backbone of semiconducting polymers provides for easy dissolution in common solvents to form (semi-)conductive inks[6]. Therefore, high-throughput methods of printing and deposition are possible [7].

There is tremendous synthetic flexibility in the design of polymers and small-molecules. Their molecular design drastically affects the mechanical, optical, and electronic properties.[8] The semiconductive properties of polymers are afforded by the delocalized electrons within the π-orbitals of double bonds along the backbone. Early work on doped polyacetylene resulted the Nobel Prize in Chemistry being awarded to Alan J. Heeger, Alan MacDiarmid, and Hideki Shirakawa in 2000 [9]. Since the breakthrough work on polyacetylene, the chemical structures of semiconducting polymers have been gradually increasing in complexity [10], [11]. Semi-flexible polymers such as poly(3-hexylthiophene) (P3HT) have been extensively investigated for bulk heterojunction (BHJ) solar cells and transistors. Currently, there is a focus on the development of donor-acceptor (D-A) copolymers[12], [13] which tend to have more rigid and extended backbones. Combined with optimized processing methods, the use of D-A polymers has further increased the charge

carrier mobilities and power conversion efficiencies (PCEs) that can be achieved in OTFTs and OPVs, respectively.

1.1 Understanding the Morphology of Charge Transport Pathways

Charge transport in semiconducting organic materials relies on effective morphological control from the macro to molecular scale for efficient charge transport processes [14]. Organic materials are prone to structural disorder due to the weak van der Waals forces holding together chains in ordered domains, and defects create energetic trap sites which limit carrier mobilities [15]. On the device scale, charge carriers must travel over distances of tens of nanometers to micrometers from the semiconducting active layer to an electrode within the device. On the mesoscale, the nature of interfaces and grain boundaries between ordered and
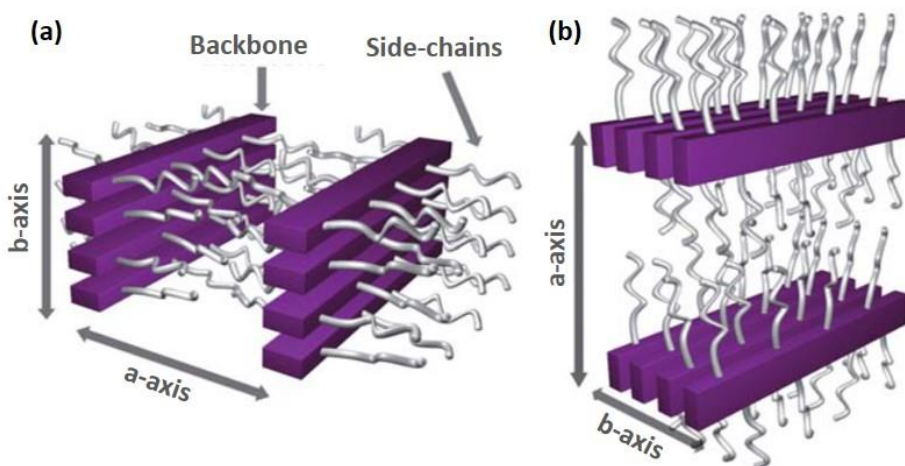
Figure 1-1. Schematic of lamellar packing for a conjugated polymer in the (a) face-on and (b) edge-on configuration. Reproduced with permission from Ref. [31]

disordered domains is of critical importance. On the scale of a single crystallite, the majority of semiconducting polymers adopt a lamellar packing structure in which the conjugated backbones align in closely packed π-stacks separated by the alkyl side-chains (Figure 1-1). This leads to anisotropic charge transport properties as the fastest transport direction is along

the backbone and the second fastest is in the direction of the π-stacking. Charge transport in the direction of the alkyl chain stacking is essentially slow due to the insulating nature of the single bonded carbon chains.

While the angstrom-scale packing details can be easily studied using X-ray scattering methods, an understanding of the mesoscale is much harder to achieve. Transport on the relies on the connectivity between adjacent ordered domains in order to form a coherent transport pathway[16]. This is particularly important in semiconducting polymers where the average grain size is on the order of 10-50 nm, which is much smaller than the total distance which charges must traverse in order to reach the electrodes in a device architecture. In the traditional model of a crystalline polymer, transport across grain boundaries occurs through bridging polymer chains called tie-chains [17]. While tie-chains are likely occurring in many systems,
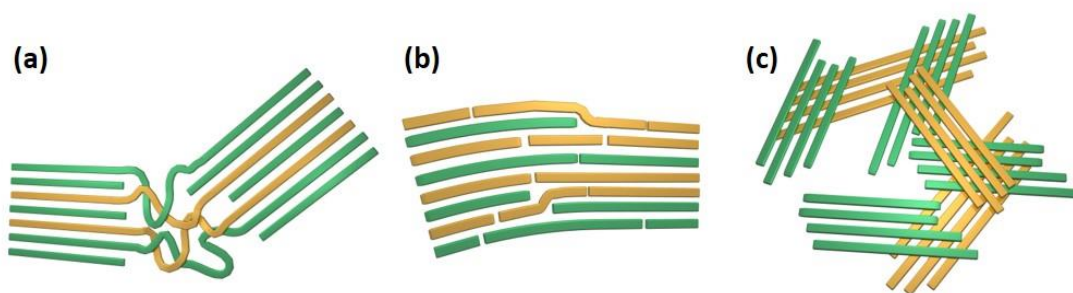
Figure 1-2. Types of grains boundaries encountered in semiconducting polymers. (a) tie-chains, (b) low-angle grain boundary, (c) quadrites or "special" high-angle grain boundaries. Figure adapted with permission from Ref. [21].

the situation may be more complex with the new class of D-A copolymers, which tend to have a more extended backbone due to the large conjugated monomers units and a lower number of degrees of freedom. Polymer thin films containing small grain sizes likely contain a significant number of defects in the form of low and high angle grain boundaries (Figure 1-2). Low angle grain boundaries can provide connections between crystallites without requiring

significant structural disorder of the polymer backbone, minimizing electronic disorder. High-angle grain-boundaries are usually considered high energy when a large bend in the conjugated backbone is required. However, if the grain boundary is created by two crystallites overlapping, then the energy of formation is likely lower.

"Special" high-angle grain-boundaries may electronically bridge crystallites by aiding transport around the insulating side-chains effectively increasing connectivity on the nanoscale. In the conventional structure of a lamellar crystal, each layer has anisotropic transport properties and can move charge carriers in 2 directions (Figure 1-3a). In the quadrite-type structure, a lamellar layer at a different orientation may become trapped within a crystallite either in solution or during deposition where there is a huge energetic barrier to rearranging (Figure 1-3b). This enables the 2D transport properties of each layer to be combined effectively creating 3D transport through use of an additional pathway at the interface between the π faces of the crossed chains.
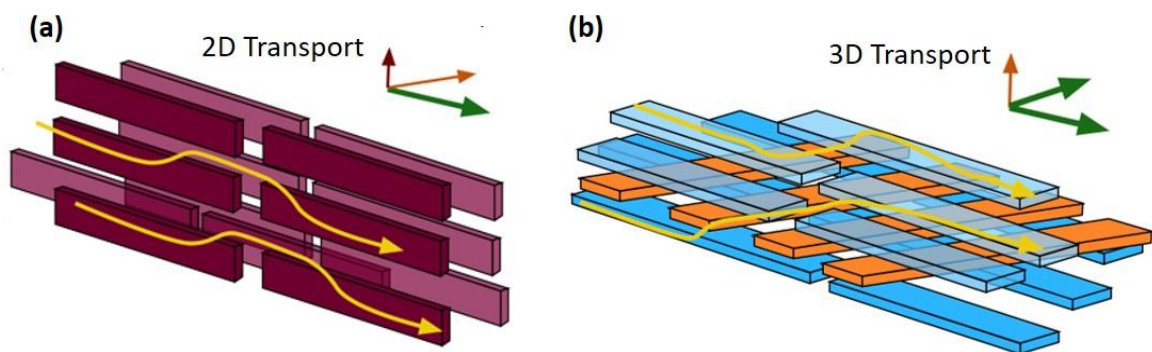
Figure 1-3. (a) 2D transport in a conventional lamellar crystal and (b) 3D transport for the quadrite structure with a nonparallel arrangement of the backbones.

Ordered high-angle grain boundaries formed by the coherent backbone overlap have been observed in insulating materials such as isotactic polypropylene (iPP) [18], poly(parapheny1ene benzobisoxazole) (PBZO) [19], pyromellitic dianhydrideoxydianiline

4

(PMD A-ODA) poly(imide) [20], and the donor-acceptor copolymer poly[(4,4′-bis(2-ethylhexyl)dithieno[3,2-b:2′,3′-d]silole)-2,6-diyl-alt-(2,1,3-benzothiadiazole)-4,7-diyl] (PSBTBT) [21]. Takacs et al. defined a unique geometrical relationship (Figure 1-4) between the crossing angle, θ, alkyl d-spacing, and the length of the repeating polymer unit, *b*.

$$\sin \theta = {}^{d}/_{b}$$

The *d*-spacing of the polymer can be obtained through X-ray scattering. This experiment highlights that an understanding of how different molecular designs lead to specific packing motifs in the solid state needs to be more rigorously explored. As previously discussed, many optical and electronic properties can be engineering into the molecular structure, but there is little current ability to design a molecule to adopt a particular packing motif.
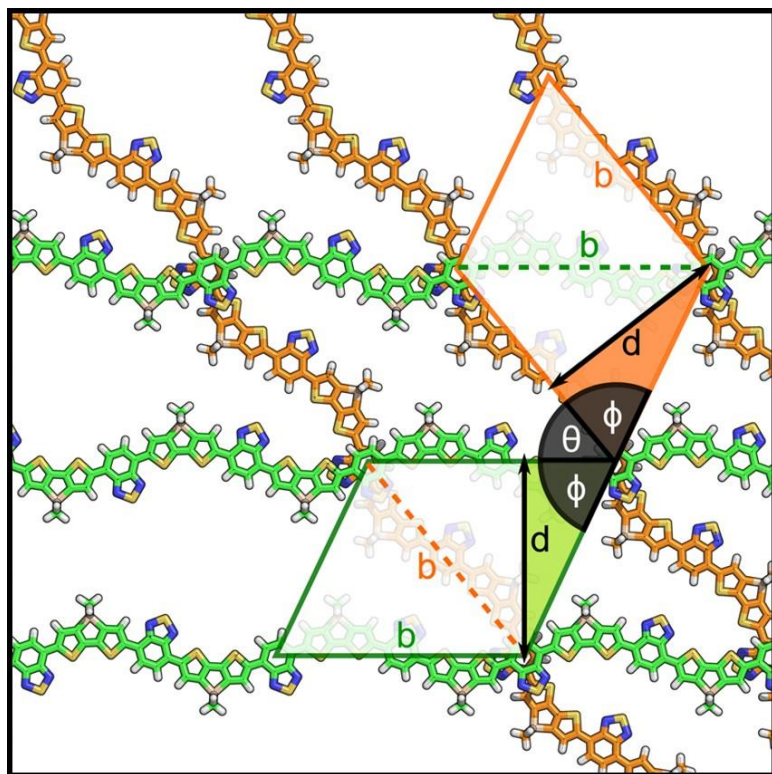
Figure 1-4. Schematic shows a proposed model for chains at the interface of two polymer lamellae along with the geometrical constraints for infinite tiling. The side-chains (omitted) at the surface of each lamella are thought to fit into pockets/voids of the other. Reproduced with permission from Ref. [21].

Evidence of cross-chain structures for another donor-acceptor copolymer, (poly[(benzo[1,2-b:4,5-b0]dithiophene)-alt-(4H-thieno[3,4-c]pyrrole-4,6(5H)-dione)]) (PBDTTPD) is presented in Chapter 4. The role of the alkyl side-chains on the intercrystallite order was probed through a study of three PBDTTPD derivatives. The crystalline structure and grain boundaries were examined using high-resolution transmission electron microscopy (HRTEM). Cross-chain structures may act as physical crosslinks and entanglements and will have an effect on the thermal and mechanical properties. The expansion and contraction of PBDTTPD thin films during thermal annealing and slow cooling was monitored through *in-situ* grazing incidence wide-angle X-ray scattering (GIWAXS) measurements.

1.2 GIWAXS and HRTEM to Study Thin Organization

GIWAXS is a synchrotron-based technique which is used to study organic systems and to determine details of the molecular packing (0.1-10 nm), crystalline order, crystallite coherence length and orientation[14], [22]. An incident x-ray beam impinges on the sample at a grazing angle, α, (usually about 0.10° for polymers) and is diffracted by the periodic lattice planes within the film[14]. Constructive inference of the exiting plane waves results in a spot of higher intensity on the detector (Figure 1-5). The scattering vector, q, exits the sample at angle 2θ and has a magnitude defined by equation.

$$q = \left(\frac{4\pi}{\lambda}\right)\sin\theta$$

where λ is the X-ray wavelength. Bragg's law describes the constructive interference of incoming waves reflecting off parallel planes of molecules separated by a distance d.

$$n\lambda = 2d\sin\theta$$

The *d*-spacing between the lattice planes (d_{hkl}) can be determined from the peak position, q.
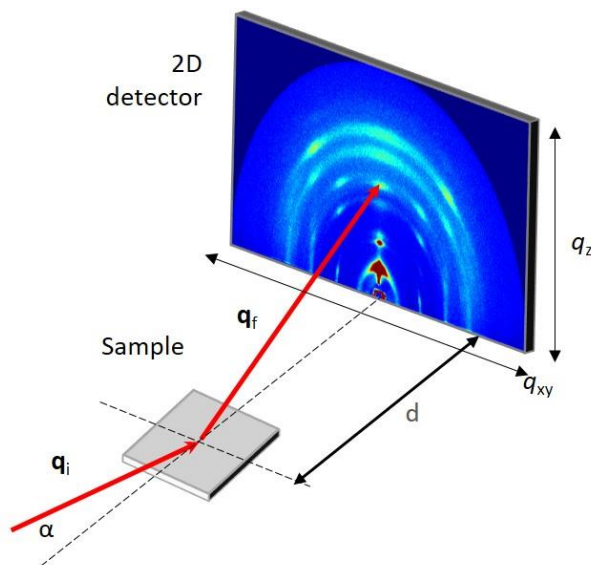
Figure 1-5. Scattering geometry for a GIWAXS experiment to study the nanostructure of a thin film.

$$q = \frac{2\pi}{d_{hkl}}$$

where the wave vector, q, is perpendicular to the periodic array of molecular spacings [14]. Depending on the orientation of the crystallites, the direction of the beam will change. Using a 2D detector, a map of q-space is generated containing information about the relative size and orientation of the crystalline regions within the film.

Transmission electron microscopy (TEM) probes the crystalline in-plane molecular packing of very thin films (<100 nm) with Angstrom resolution and is very complimentary to X-ray scattering. Chapter 2 describes the important concepts involved in high resolution transmission electron microscopy (HRTEM). In order to successfully use HRTEM to image the lattice fringes of crystalline regions of semiconducting polymers and small-molecules, the effects of radiation damage must be fully understood. In addition, the effect of the specific imaging conditions and sample damage on resolution, and data interpretability are discussed.

Chapter 3 outlines specific examples of the key morphological features that can be examined with HRTEM.

1.3 Thermal and Photostability of Semiconducting Polymer Thin Films

In Chapter 5, the stability of semiconducting polymer thin films as a function of both the chemical structure and the thin film morphology is discussed. The photostability of poly[[2,6′-4,8-di(5-ethylhexylthienyl)benzo[1,2-*b*;3,3-*b*] dithiophene] [3-fluoro-2[(2-ethylhexyl)carbonyl]thieno[3,4-*b*]thiophenediyl]] (PTB7-Th) in neat films and BHJs with $PC_{71}BM$ were examined as a function of the presence of the solvent additive, diiodooctane (DIO). Solvent additives are frequently used in BHJ processing to optimize the thin film morphology. GIWAXS was used to study the changes in the molecular packing as a result of photodegradation and revealed a reduction in the intensity of both primary and higher-order polymer reflections. This was correlated with the presence of residual DIO in the films after spin-casting. Additionally, PBDTTPD thin films were subjected to high-temperature thermal treatments below the polymer degradation temperature in order to improve structural order. GIWAXS and HRTEM showed evidence of a structural rearrangement, but extensive degradation was revealed upon examination of the absorption properties with ultraviolet-visible spectroscopy (UV-Vis). Degradation of both PTB7-Th and PBDTTPD was hypothesized to be initiated by damage to the alkyl side-chains resulting in the production of free-radical species which then attacked the backbone and reduced the polymer conjugation length. Overall, many processing steps such as thermal annealing and addition of solvent additives are used to optimize molecular packing and morphology. However, the effect of processing on material degradation must be thoroughly examined.

1.4 Non-fullerene Acceptors for OPVs

The morphology of BHJs containing a small-molecule acceptor is discussed is Chapter 6. In a BHJ solar cell, the active layer is comprised of a blend of an electron donating and electron accepting material[1]. Many high-efficiency OPVs use fullerene-based acceptor materials, however, fullerene derivatives generally have a high production cost, low absorption in the visible range, and limited synthetic variability of electronic and optical properties. Small-molecule acceptors are a promising alternative to fullerenes as they have an increased synthetic flexibility, which allows for fine-tuning of optical and electronic properties[23]– [27]. A promising fullerene alternative - 4,7-bis(4-(N-hexyl phthalimide)vinyl)benzo[c]1,2,5-thiadiazole (HPI-BT) [28] was blended with P3HT, a commonly used donor material.

The efficient conversion of light energy into electrical energy depends on the phase separated morphology and occurs through a number of discrete steps. These include absorption of light, generation of a bound electron-hole pair (exciton), exciton diffusion to the D-A interface, charge separation, and transport of charge carriers to the respective electrodes [29]. An ideal optimized solar cell is one which has good light absorption across the visible range, is able to generate a high number of free charges, and is then able to quickly transport all generated charges to the electrodes with little to no recombination[30]. An exciton can diffuse approximately 10-15 nm before recombining and therefore, the domain size should be comparable to this length scale[1].

Thermal processing can have a large effect on the morphology. In the HPI-BT:P3HT solar cells, the PCE doubled from 1 to 2% after thermal annealing at 100°C for 6 minutes. Changes in the morphology were monitored by GIWAXS *in-situ* annealing and were observed to occur on the same timescale that electrical properties improved. An increase in the PCE was

attributed to a crystalline acceptor phase which was buried beneath the cathode interface by a thin P3HT capping layer. A short anneal allowed diffusion of the HPI-BT crystallites to the cathode interface and improved the PCE, FF, and J_{SC}. However, micron-sized acceptor crystallites formed upon spin-casting which limited the performance. Ultimately, methods to suppress the acceptor crystallization should be adopted in the use of small-molecule acceptors and would be required to further improve the efficiency.

References

[1]   A. J. Heeger, "25th anniversary article: Bulk heterojunction solar cells: Understanding the mechanism of operation," *Adv. Mater.*, vol. 26, no. 1, pp. 10–28, 2014.

[2]   B. Russ, A. Glaudell, J. J. Urban, M. L. Chabinyc, and R. A. Segalman, "Organic thermoelectric materials for energy harvesting and temperature control," *Nat. Rev. Mater.*, vol. 1, no. 10, p. 16050, 2016.

[3]   A. P. Kulkarni, C. J. Tonzola, A. Babel, and S. A. Jenekhe, "Electron transport materials for organic light-emitting diodes," *Chem. Mater.*, vol. 16, no. 23, pp. 4556–4573, 2004.

[4]   A. Salleo, "Charge transport in polymeric transistors," *Mater. Today*, vol. 10, no. 3, pp. 38–45, 2007.

[5]   S. R. Forrest, "The path to ubiquitous and low-cost organic electronic appliances on plastic.," *Nature*, vol. 428, no. 6986, pp. 911–918, 2004.

[6]   J. Mei and Z. Bao, "Side Chain Engineering in Solution-Processable Conjugated Polymers," *Chem. Mater.*, vol. 26, no. 1, pp. 604–615, 2014.

[7]   A. C. Arias, J. D. MacKenzie, I. McCulloch, J. Rivnay, and A. Salleo, "Materials and applications for large area electronics: Solution-based approaches," *Chem. Rev.*, vol. 110, no. 1, pp. 3–24, 2010.

[8]   G. Odian, *Principles of Polymerization*, 4th ed. New Jersey: John Wiley & Sons, Inc., 2004.

[9]   A. J. Shirakawa, H.; Louis, E.J.; MacDiramid, A.G.; Chiang, C.K.; Heeger, "Synthesis of electrically conducting organic polymers: halogen derivatives of polyacetylene, (CH)," *J. Chem. Soc. Chem. Commun.*, no. 16, pp. 578–580, 1977.

[10]   D. Berthelot, "Sur le mélange des gaz," *Compt. Rendus*, vol. 126, pp. 1703–1706, 1898.

[11]   A. M. Saxman, R. Liepins, and M. Aldissi, "Polyacetylene: Its synthesis, doping and structure," *Prog. Polym. Sci.*, vol. 11, no. 1–2, pp. 57–89, 1985.

[12]   H. A. M. Van Mullekom, J. A. J. M. Vekemans, E. E. Havinga, and E. W. Meijer, *Developments in the chemistry and band gap engineering of donor-acceptor substituted conjugated polymers*, vol. 32, no. 1. 2001.

[13]   Z. Zhang and J. Wang, "Structures and properties of conjugated Donor–Acceptor copolymers for solar cell applications," *J. Mater. Chem.*, vol. 22, no. 10, p. 4178, 2012.

[14]   J. Rivnay, S. C. B. Mannsfeld, C. E. Miller, A. Salleo, and M. F. Toney, "Quantitative determination of organic semiconductor microstructure from the molecular to device scale," *Chem. Rev.*, vol. 112, no. 10, pp. 5488–5519, Oct. 2012.

[15]   H. Sirringhaus, "Device physics of solution-processed organic field-effect transistors," *Adv. Mater.*, vol. 17, no. 20, pp. 2411–2425, 2005.

[16]   R. Noriega *et al.*, "A general relationship between disorder, aggregation and charge transport in conjugated polymers.," *Nat. Mater.*, vol. 12, no. 11, pp. 1038–44, Nov. 2013.

[17]   R. A. Street, J. E. Northrup, and A. Salleo, "Transport in polycrystalline polymer thin-film transistors," *Phys. Rev. B - Condens. Matter Mater. Phys.*, vol. 71, no. 16, pp. 1–13, 2005.

[18]   F. Khoury, "The Spherulitic Crystallization of Isotactic Polypropylene From Solution : On the Evolution of Monoclinic Spherulites From," *J. Res. Natl. Bur. Stand. A*, vol. 70, no. 1, pp. 29–61, 1966.

[19]   D. C. Martin and Thomas, "Grain boundaries in extended-chain polymers Theory and Experiment," *Philos. Mag. A*, vol. 64, pp. 903–922, 1991.

[20]   J. R. Ojeda and D. C. Martin, "High Resolution Microscopy of PMDA-ODA Poly(imide) Single Crystals," *Macromolecules*, vol. 26, pp. 6557–6565, 1993.

[21]   C. J. Takacs, M. a Brady, N. D. Treat, E. J. Kramer, and M. L. Chabinyc, "Quadrites and crossed-chain crystal structures in polymer semiconductors.," *Nano Lett.*, vol. 14, no. 6, pp. 3096–101, Jun. 2014.

[22]   A. Salleo, R. J. Kline, D. M. DeLongchamp, and M. L. Chabinyc, "Microstructural characterization and charge transport in thin films of conjugated polymers.," *Adv. Mater.*, vol. 22, no. 34, pp. 3812–38, Sep. 2010.

[23]   Y. Sun, G. C. Welch, W. L. Leong, C. J. Takacs, G. C. Bazan, and A. J. Heeger, "Solution-processed small-molecule solar cells with 6.7% efficiency.," *Nat. Mater.*, vol. 11, no. 1, pp. 44–48, Jan. 2012.

[24]   A. Mishra and P. Bäuerle, "Small molecule organic semiconductors on the move: promises for future solar energy technology.," *Angew. Chem. Int. Ed. Engl.*, vol. 51, no. 9, pp. 2020–2067, Feb. 2012.

[25]   Y. Liu *et al.*, "Solution-processed small-molecule solar cells: breaking the 10% power conversion efficiency.," *Sci. Rep.*, vol. 3, p. 3356, Jan. 2013.

[26]   N. Shin *et al.*, "Vertically Segregated Structure and Properties of Small Molecule-Polymer Blend Semiconductors for Organic Thin-Film Transistors," *Adv. Funct. Mater.*, vol. 23, no. 3, pp. 366–376, Jan. 2013.

[27]   K. Cnops, B. P. Rand, D. Cheyns, B. Verreet, M. a Empl, and P. Heremans, "8.4% Efficient Fullerene-Free Organic Solar Cells Exploiting Long-Range Exciton Energy Transfer.," *Nat. Commun.*, vol. 5, p. 3406, Jan. 2014.

[28]   J. T. Bloking *et al.*, "Solution-Processed Organic Solar Cells with Power Conversion Efficiencies of 2.5% using Benzothiadiazole/Imide-Based Acceptors," *Chem. Mater.*, vol. 23, no. 24, pp. 5484–5490, 2011.

[29]   B. P. W. M. Blom, V. D. Mihailetchi, L. J. A. Koster, and D. E. Markov, "Device Physics of Polymer : Fullerene Bulk Heterojunction Solar Cells **," pp. 1551–1566, 2007.

[30]   B. C. Thompson and J. M. J. Fréchet, "Polymer-fullerene composite solar cells.," *Angew. Chem. Int. Ed. Engl.*, vol. 47, no. 1, pp. 58–77, Jan. 2008.

[31]   N. D. Treat, C. G. Shuttle, M. F. Toney, C. J. Hawker, and M. L. Chabinyc, "In situ measurement of power conversion efficiency and molecular ordering during thermal annealing in P3HT:PCBM bulk heterojunction solar cells," *J. Mater. Chem.*, vol. 21, no. 39, pp. 15224–15231, 2011.

Chapter 2

High Resolution Transmission Electron Microscopy of Organic Thin Films

2.1 Introduction

Transmission electron microscopy (TEM) is a technique in which a beam of electrons is transmitted through a sufficiently thin sample and characteristic signals from the interaction with the sample are used to produce an image. While TEM is widely used in the study of inorganic materials to understand grain boundaries and defects,[1] it is less widely used to study semiconducting organic materials. This lack of information about the morphology of organic semiconductors limits the understanding of many keys issues such as transport across grain boundaries and their connectivity to theory and simulations. One reason that it is not a more commonly used experimental method is due to the complicated nature of radiation damage in soft materials which can drastically reduce image quality, resolution, and interpretability [2]–[9].

Despite the difficulty of studying organic materials using TEM, there have been a number of exceptional studies of organic materials. For example, over the last few decades, many groups have examined the structure of isotactic polypropylene (iPP) in order to understand how to control its microstructure through processing methods [10]–[19]. Additionally, there has been excellent work on liquid crystalline polymers [20]–[24] and other stiff chain polymers [8], [25]–[27] using high-resolution imaging and electron diffraction. However, high-resolution TEM (HRTEM) of semiconducting polymers, where lattice fringes are produced by the periodic arrangement of the conjugated backbone, is highly underutilized

despite the ability to probe the molecular organization on a length scale that is critical for organic electronics.

Semiconducting polymers and small-molecules form the active layer in a variety of devices including organic thin-film transistors (OTFT), organic photovoltaics (OPV), and organic thermoelectrics (OTE). Grain sizes of organic materials tend (~50 nm) to be small compared to the total distance that charge carriers must travel. While bright-field TEM is commonly used to determine of phase separation between the donor and acceptor materials of a bulk-heterojunction (BHJ) solar cells through conventional bright-field [28]–[31] and energy-filtered TEM [32]–[35], there is a tremendous need for examination of how crystals assemble and connect on the molecular scale. There are only a handful of groups using HRTEM to study the molecular packing of small-molecules [36]–[39], oligomers [40], and polymers [41]–[47]. Even though there is significant variability in crystallite packing and connectivity with molecular structure, only a few semiconducting polymers have been thoroughly examined with HRTEM including P3HT [41], [43], [47], P(NDI2OD-T2) [42], [45], and derivatives of PCPDTBT [44], [46]. There have been fewer high-resolution imaging studies on grain boundaries in semiconducting polymers [44].

Here, the basics of TEM are discussed along with damage, resolution, and contrast considerations that are important for properly utilizing the technique to study organic materials. A focus is placed on high-resolution imaging of organic polymer and small-molecule thin films [8], [48]. Because of the significant potential for beam damage to organic samples, it is critical to understand the principles of operation of TEM and the particular requirements for imaging organic materials. The reader is directed to a number of published

15

resources for more information on the fundamental principles behind TEM and the interaction of electrons with matter [1], [49].

2.2 Basics of Image Formation

The TEM can be divided into four basic parts: electron source, condenser optics, objective lens/specimen mount, and projector lenses/viewing screen (Figure 2-). The electron gun, or electron emitter, is positioned at the top of the microscope and is composed of three main components which generate, focus, and accelerate the electrons. Electrons are generated by either thermionic emission or field electron emission in a field emission gun (FEG).
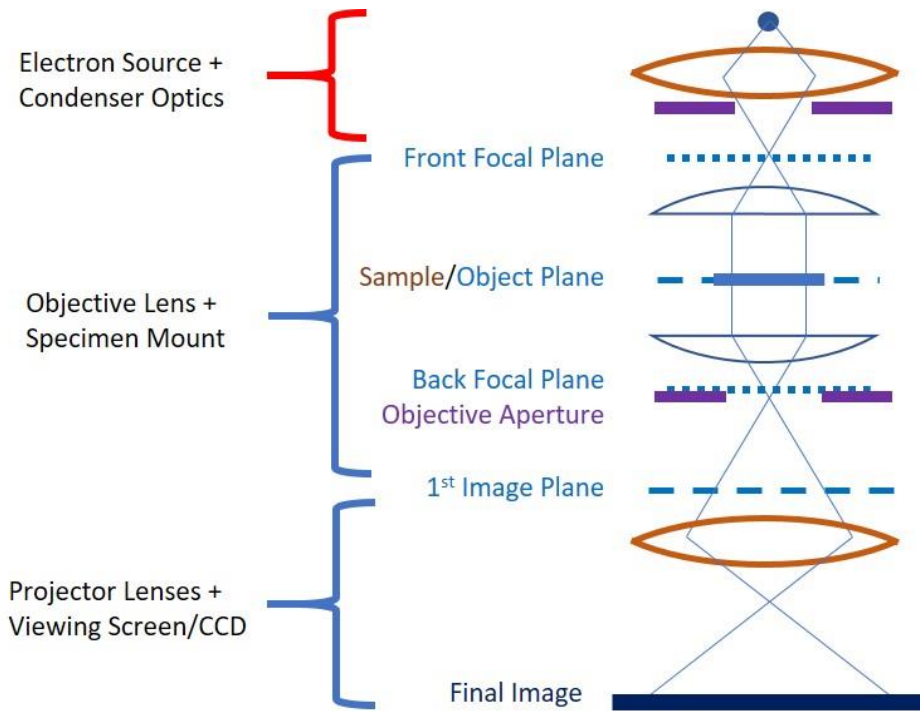
Figure 2-1. Diagram of the lenses and apertures of a TEM. Image courtesy of Dr. Christopher J. Takacs.

Thermionic sources generally have higher current and generate more electrons. On the other hand, Schottky FEG sources have a higher brightness and better electron focusing ability making them ideal for high-resolution imaging due to a high spatial coherency. A series of

electromagnetic lenses are used to focus and shape the electron beam. First, the condenser lenses control the spot size, brightness, and beam convergence angle. The sample sits in between the upper and lower components or "pole pieces" or the objective lens, which is used to form the image and diffraction patterns. Apertures can also be inserted into the beam path at various points to generate contrast by blocking different parts of the electron beam to form an image from only certain signals. An aperture is a hole drilled into a piece of metal such as Pt and Mo which allows certain electrons to pass while blocking others. Finally, the projector lenses magnify the image produced by the objective lens and project it onto a phosphor viewing screen.

2.3   Interaction Cross Section

The probability that an electron will interact with a single atom in the sample is expressed as the interaction cross section, σ, and is a function of both elastic and inelastic scattering events [49].

$$\sigma_{total} = \sigma_{elastic} + \sigma_{inelastic} = \pi r^2$$

where r is the radius of the scattering center. For elastic scattering of a particle, the electrons will interact with the atoms in the sample through Coulomb forces. The strength of the interaction with the nucleus and electron cloud surrounding the nucleus will affect the angle, θ, at which the incoming electrons scatter, and is related to the atomic number, Z, and the accelerating voltage, V. Lighter atoms, such as carbon ($Z=6$), will scatter electrons at much smaller angles than heavy elements, such as the transition metals. The electron-electron and electron-nucleus interactions were described by Hall in 1953 [50] in terms of a scattering field radius, r:

$$r_{electron} = r_e = e/V\theta$$
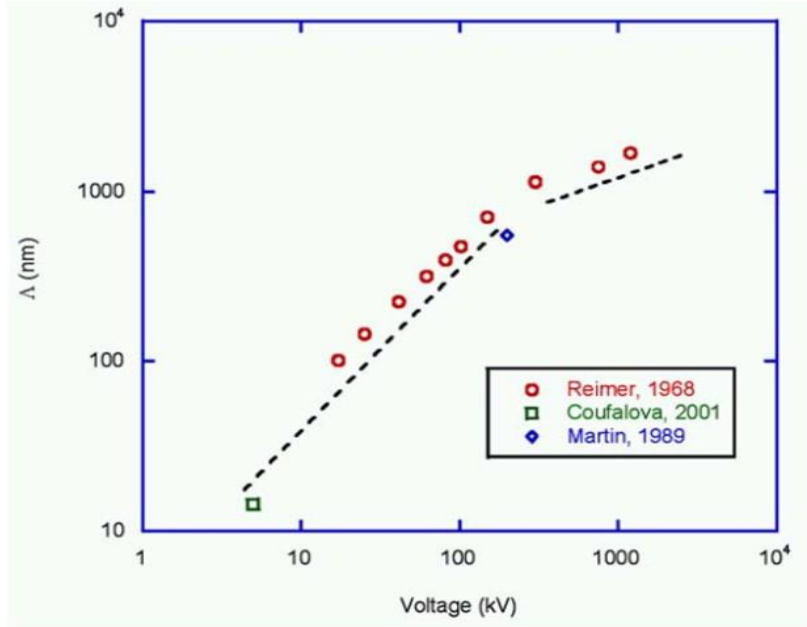
Figure 2-2. Electron mean free path as a function of operation voltage. Figure reproduced with permission from [52].

$$r_{nucleus} = r_n = Ze/V\theta$$

This indicates that elastic scattering with the nucleus is dictated by the atomic number, Z, but for electron-electron interactions is determined by the accelerating voltage, V. The total interaction cross section for the sample of N atoms/unit volume is:

$$Q_{total} = N\sigma_{total} = \frac{N_0\sigma_t\rho}{A}$$

where N_0 is Avogadro's number, ρ is the density, and A is the atomic weight of the atoms in the sample.

The sample thickness must be optimized as to only produce a single scattering event. The critical thickness at which this occurs is related to the atoms present and the operating voltage and is called the "Bremsdicke" value [51]. The probability, p, that an electron will scatter while traveling through a sample of thickness, t, is given by:

$$p = \frac{t}{\Lambda}$$

18

where Λ is the mean free path of the electron, or the distance the electron will travel before colliding with a particle.

$$\Lambda = \frac{1}{Q_{total}} = \frac{A}{N_0 \sigma_t \rho}$$

For organic samples with an assumed density of 1 g/cm^3, the evolution of the electron mean free path as a function of operating voltage is shown in Figure 2- [52] . As the sample gets thicker, more scattering will occur, and the resulting image will become less interpretable. Therefore, the sample thickness should be less than or equal to the mean free path of the electron for the chosen operating voltage. Figure 2- shows that thinner films are required for lower voltages because the scattering cross-section is higher.

In summary, the probability that an electron will scatter when passing through the sample increases with the atomic number and decreases with incident beam energy. Therefore, if the specimen is composed of high-Z elements such as gold, it needs to be much thinner than for a low-Z element like carbon.

2.4 Wavelength and Resolution

The de Broglie wavelength of a particle is expressed as [1]:

$$\lambda = \frac{h}{p} = \frac{h}{m_0 v}$$

where h is Planck's constant, p is the momentum, m is the resting particle mass, and v is the particle velocity. When an electron of charge e is accelerated from rest to a potential V, the kinetic energy is:

$$eV = \frac{1}{2} m_0 v^2$$

That equation can be rearranged to give:

$$v = \sqrt{\frac{2eV}{m_0}}$$

Therefore, the wavelength of an electron for an accelerating voltage, V, is:

$$\lambda = \frac{h}{\sqrt{2m_0eV}}$$

However, the particle will experience a relativistic mass change while it is moving which is expressed by the Lorentz factor, γ:

$$\gamma = \frac{m}{m_0} = \sqrt{1\text{-}v^2/c^2} = \left(1 + \frac{eV_0}{m_0c^2}\right)$$

where m is the mass of the particle in motion, m_0 is the resting mass, and c is the speed of light. Therefore, the relativistic wavelength of the electron is:

$$\lambda_R = \frac{h}{\sqrt{2m_0eV}}\frac{1}{\sqrt{1 + \frac{eV}{2m_0c^2}}}$$

These effects must be considered when an accelerating voltage great than 100 kV is used because the electron velocity approaches the speed of light [49]. For a 300kV microscope, the non-relativistic wavelength is 0.00223 nm, the relativistic wavelength is 0.00197 nm, and the electron velocity is 2.33×10^8 m/s.

The Rayleigh criterion states that the resolution of a microscope (light or electron) is based on the wavelength of the radiation [49].

$$\delta = \frac{0.61\lambda}{\mu \sin \beta} \approx \frac{1.22\lambda}{\beta}$$

where β is the "semi-angle of collection of the magnifying lens". The electron wavelength represents the ultimate resolution limit for the microscope. However, in reality, the image

resolution is decreased by a number of effects including lens aberrations caused by imperfections in the electromagnetic lenses, radiation damage, and sample drift.

2.5   Higher Energy Electrons Reduce Inelastic Scattering

Electron radiation damage to the sample is known to reduce image resolution and therefore is important to understand. Damage occurs primarily through two methods – ionization of the atoms and local heating [6]. Ionization results from the inelastic scattering of the electron with the atoms in the sample. The ionization energy is the energy required to remove an outer shell electron, which for hydrogen is 13.6 eV and carbon is 11.3 eV. The energy needed to displace a carbon atom is about 27 eV and occurs at a rate of approximately 1 in 525 atoms per second for accelerating voltage of 100 kV [3]. However, when a high-energy electron beam is transmitted through the sample, only a fraction of the energy will be absorbed. The amount of energy transferred to the sample can be understood as the energy lost by the incoming electron through the Bethe-Bloch relation [53].

$$\left(\frac{dE}{dx}\right)_{electron} = \frac{4\pi e^4}{m_e V^2} n_0 Z \ln\left\{\frac{m_e V^2}{2\bar{I}}\left(\frac{1}{2}e\right)^{1/2}\right\}$$

It is a function of the electron energy, V, atomic density, n_0, atomic number, Z, and ionization energy, $\bar{I}$. Therefore, the energy transfer to the sample will decrease as the energy of the electron increases. A higher electron energy also reduces sample damage by minimizing the scattering cross-section [5].

Early work by Thomas et al. examined the effect of the accelerating voltage (100-1000 kV) on the degradation of polyethylene (PE) and polyoxymethylene (POM) crystals and found that radiation damage of organic samples could be reduced by using a higher accelerating voltage [4]. However, not all organic materials damage in the same way and the molecular

structure and organization will also play a role [54], [55]. In a comparison of aliphatic, aromatic, and phthalocyanine molecules, aliphatic compounds required the lowest electron dose to induce damage whereas phthalocyanines are the most resistant. Initial ionization of the atoms in the sample occurs in 10^{-14} s [56], but additional ionization events by secondary electrons can lead to crosslinking between adjacent chains, chain scission, and radical formation [2]. The electron delocalization afforded by the double bonds in the aromatic compounds and phthalocyanines allows for quicker dissipation of the secondary electrons. Non-aromatic polymers like cellulose are particularly prone to damage and effects such as a change in the d-spacing due to radiation damage can occur [57].

A higher electrical conductivity of the sample will minimize the structural damage caused by the secondary electrons, and a conductive coating can be applied to take advantage of this effect [58], [59]. Fryer and Holland explained that damage occurs by the breaking of chemical bonds after excitation of the molecule by the electron beam [59]. This leads to the separation and diffusion of charged species which can react with other parts of the sample. The encapsulation layer and also a reduction of the temperature is thought to slow the diffusion of the charged species. However, the conductive coating method does not always reduce beam damage and damage has been suggested to also be related to a build-up of electrostatic charge [60].

2.6 Low Electron Dose Minimizes Radiation Damage

While an increase in electron energy can reduce damage effects, the electron dose, or number of electrons per sample area, must still be minimized. The critical dose is energy dependent and is defined as the number of electrons per sample area that lead to observable

structural changes. The critical dose, J_C, required to cause damage by ionization of electrons in the K-shell is:

$$J_C = fd = f\frac{e}{Q}$$

where f is the fraction of molecules that must be ionized to cause sample damage, d is the dose necessary to ionize a single electron from the K-shell, and Q is the scattering cross-section [61].

The critical dose can also be calculated by monitoring the decay in the intensity of peaks in the diffraction pattern. Polymers show an exponential decay in the intensity of spots in the diffraction pattern with damage through the following relation:

$$I = I_0 \exp\left(-\frac{J}{J_C}\right)$$

where I is the peak intensity, I_0 is the peak intensity before exposure, and J is the electron dose. The critical dose for a sample is the number of electrons per area that result in a reduction of the intensity of the strongest peak by a factor of $1/e$ [9]. Kumar and Adams also found that an increase in the polymer melting and/or degradation temperature was correlated with an increase in the critical dose. Therefore, the specific chemical bonding that makes polymers more thermally stable also increases the resistance to radiation damage. Figure 2- shows that the critical dose varies considerably for different types of organic molecules. However, different reflections will also fade at different rates. For example, in samples formed from polymer fibers smaller d-spacings are observed to fade faster such as the peak from the packing between chains versus the more stable along chain reflection [62]. This is also observed for semiconducting polymers where the π-π stacking peak tends to fade faster than
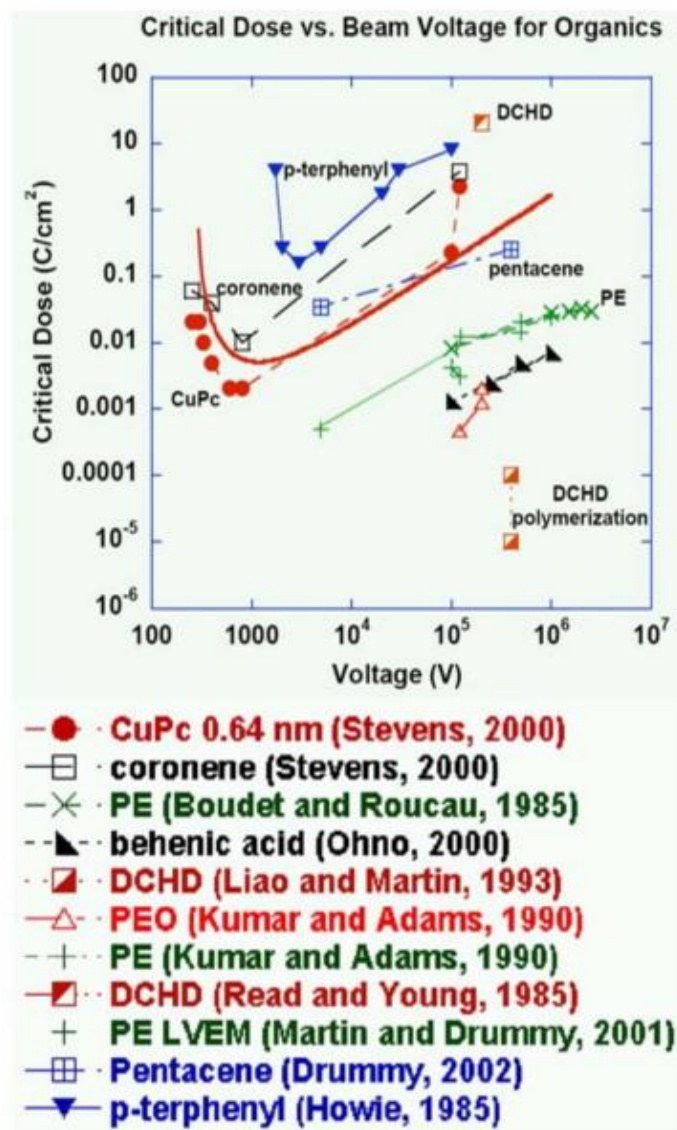
Figure 2-3. Critical electron dose as a function of beam damage for organics. Figure reproduced with permission from reference [52].

the alkyl stacking peak. Ultimately, dose rate considerations will limit how the TEM can be used to study organic thin films. For example, 3D reconstructions with a tilt series are more problematic due to damage effects and likely to exceed the critical dose.

2.7 Detecting Damage

A high energy electron beam can cause significant damage to an organic thin film if low-dose imaging conditions are not used, or if a certain area is subjected to repeated exposures.
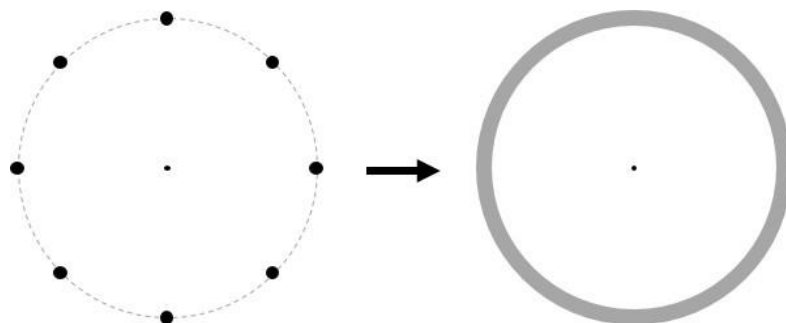
Figure 2-4. Change in the diffraction pattern observed as the sample is damaging. Discrete spots will slowly fade and become an isotropic ring.

These effects can be monitored by two main methods. First, through observation of the electron diffraction pattern and determining the electron dose required to cause discrete diffraction spots/arcs to turn into an amorphous ring or disappear altogether. When the main secondary reaction is crosslinking, the diffraction patterns will blur, whereas if scission is occurring then the intensity of spots in the diffraction pattern will fade out [2]. Often a combination of the two is observed. However, one should not assume the presence of blurred spots or rings is always due to electron irradiation damage. Inherent disorder and defects within the film will also produce these effects. The key is to determine how the diffraction pattern is *changing*. Often, the faint amorphous ring that remains in the diffraction pattern is from the carbon support film on the copper grid. Therefore, it is important to gain an understanding of the signal produced by a care carbon support film with no sample in order to prevent incorrect conclusions.

When observing changes to the diffraction pattern it is important to also check the condition of the film in imaging mode. Prolonged exposure of a particular area will not only result in the peaks in the diffraction pattern disappearing, but the sample may actually disappear in that location as well. Figure 2-5 shows how repeated exposures to a particular area can burn a hole in the film. Therefore, high-resolution images should always be collected
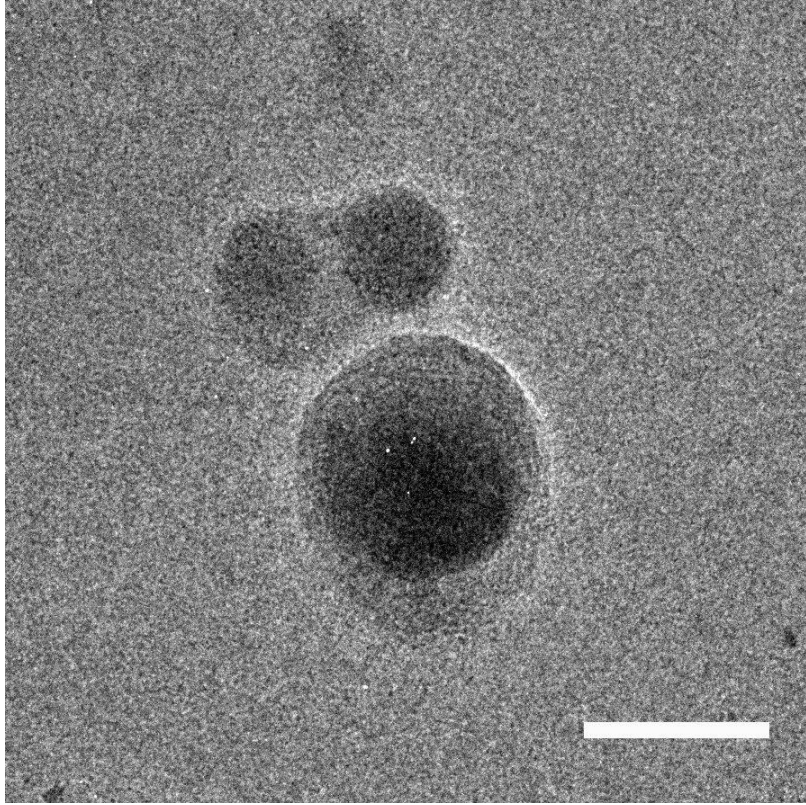
Figure 2-5. Bright-field image of a hole that formed in the film/grid after using that location for focusing and alignment. Imaging is always performed on a separate region away from any areas already exposed. Scale bar is 50 nm.

at a location far from where the sample may have been pre-exposed, such as during alignments.

Alternatively, when imaging an area that has not previously been exposed, the damage onset can be determined by the point when the image begins to "change" under the electron beam. "Changes" may come in many forms such as a twisting or warping of the sample structure or the reduction in observable crystalline features. These changes are then reflected in a fast Fourier transform (FFT) of the area.

2.8 Image Contrast

There are two main types of contrast in a TEM image: absorption and phase contrast [63]. Absorption contrast, or Z-contrast, *is* generated by a difference in scattering behavior for

atoms with different atomic numbers. Phase-contrast is generated by the interference of the scattered and unscattered electron waves. Absorption contrast tends to be poor for organic thin films composed mostly of carbon, but the signal can be enhanced through several methods including lowering the accelerating voltage and the use of energy-filters. Lowering the accelerating voltage improves the mass-thickness contrast, which may remove the need for sample staining [52], [64].
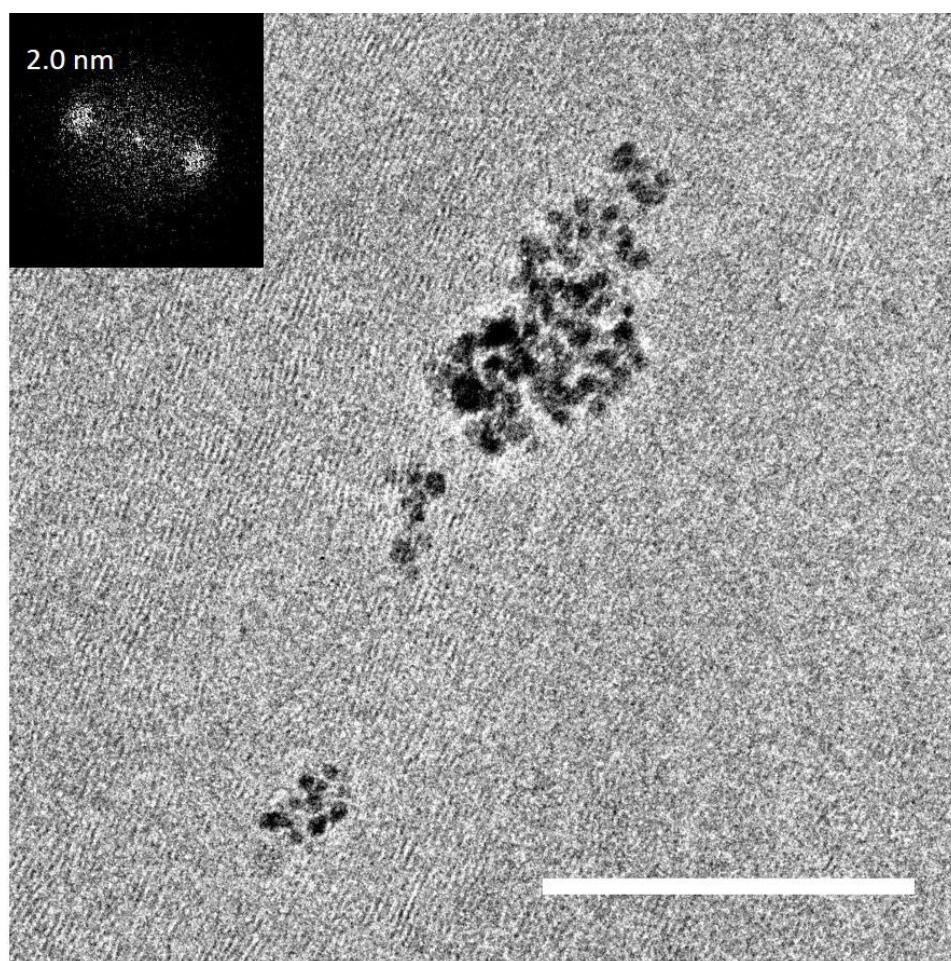
Figure 2-6. Bright-field TEM image of a thin film of DPPT-TT with both absorption contrast (dark catalyst aggregate) and phase-contrast (lattice fringes) are present. Scale bar is 100 nm.

2.8.1 Absorption Contrast
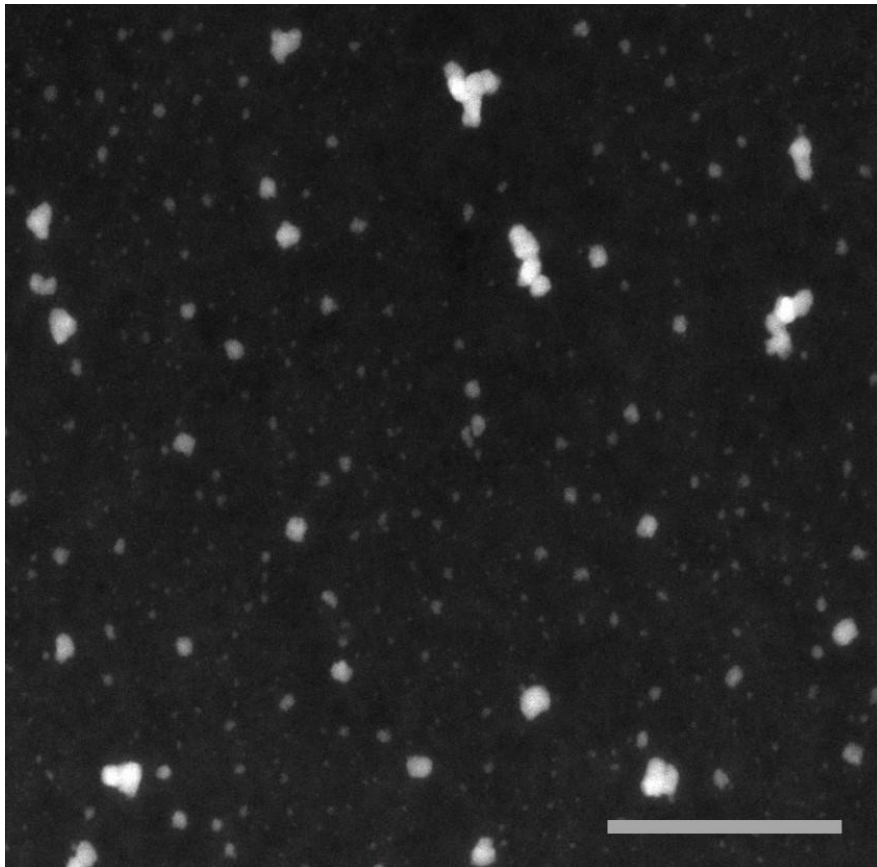
Figure 2-7. STEM image of a P3HT thin film containing a Ru-based dopant. Here the dopant atoms are aggregating (light areas). Scale bar is 500 nm.

The true power of TEM is in being able to specifically filter out which diffracted beams are used to generate the image. Amplitude contrast (or absorption contrast) is generated by the use of apertures to exclude scattered signal from the final image [1]. Absorption contrast scales with the atomic number, Z, differently depending on the imaging mode being used which determines whether the scattered or unscattered beam is being used to generate the image. In bright-field imaging mode, absorption contrast scales as Z^2 (Figure 2-6). The unscattered beam is used the generate the final image, which means that heavier atoms appear darker and lighter atoms appear brighter. STEM imaging is a dark-field technique so

the scattered beam is used to generate the image. Therefore, in STEM imaging mode, heavier atoms will appear brighter, and light atoms will appear darker (Figure 2-7).

TEM is often used in the study of phase separation in BHJs. The success relies on having an appreciable difference in electron density between the donor and acceptor materials, such as when a fullerene acceptor is used. [52]. Energy filtered TEM has been useful in differentiating between different phases in BHJs [32], [65], [66] and block copolymers [67].

2.8.2   Phase Contrast

Phase-contrast is generated due to the interference of the transmitted and diffracted waves. For high-resolution imaging of lattice fringes, where phase-contrast is the dominant contrast mechanism, it is desirable to reduce the amplitude contrast by using a higher electron energy. As the accelerating voltage increases, the absorption contrast decreases and the phase contrast increases due to the increase of the relativistic electron mass [1]. This means that the phase-contrast in thicker samples will be more interpretable at a higher voltage. However, a low electron dose is still required and high contrast relies on selection of the proper defocus value.

2.9   Process of High Resolution Imaging

The details of the process of high-resolution imaging are described in depth in Refs [1], [8], [49], however, the main concepts and equations are summarized (Figure 2-8).

The time-invariant function for the characteristic electron potential of the specimen is given by

$$\varphi(x_1, x_2, x_3)$$

where x_1, x_2, x_3 are the real-space positions of the atoms. When an incoming electron beam with a wavefunction of $\psi_{incident}$ passes through the sample with an electron potential of
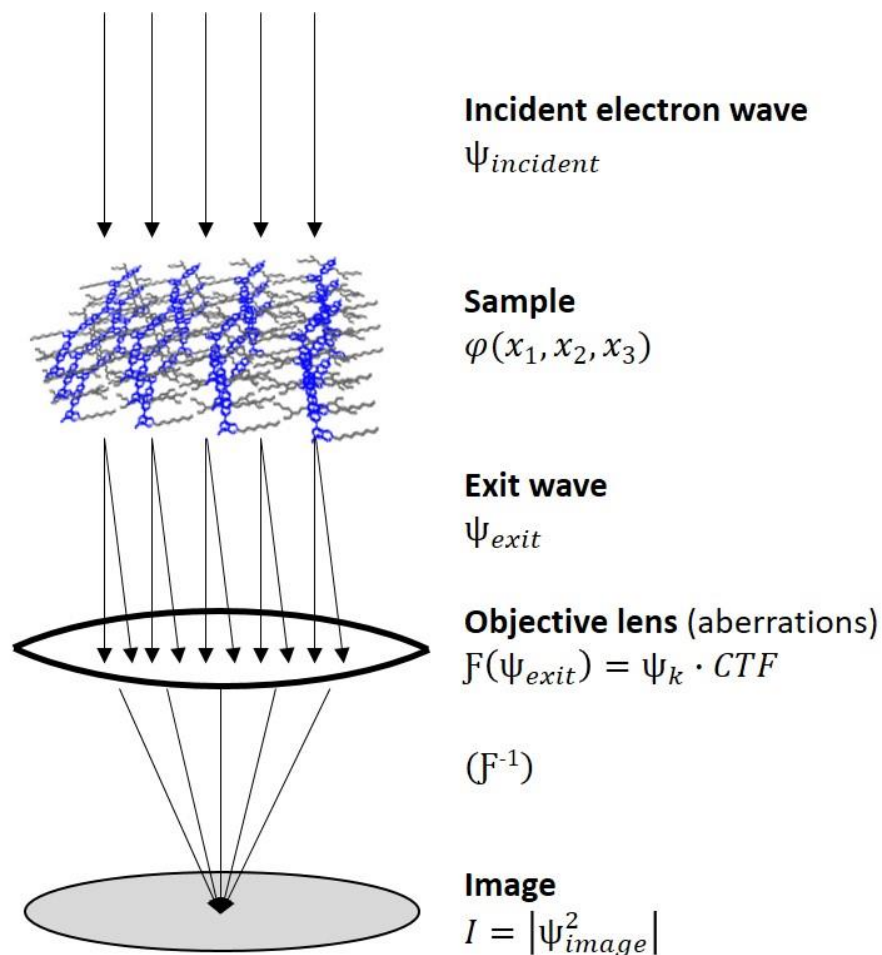
Figure 2-8. Summary of high-resolution imaging

$\varphi(x_1, x_2, x_3)$, it will experience a phase shift. The Fourier transform of the exit wave, ψ_{exit}, is ψ_k (k is the wavevector). In the objective lens, the Fourier transform of the exit wave is multiplied by the contrast transfer function (CTF), and then the product is inverse Fourier transformed to give the image wave, ψ_{image}. The intensity of the image is related to $\left|\psi_{image}^2\right|$.

For organic and biological samples, the weak-phase object approximation (WPOA) can be applied. This states that if the sample is sufficiently thin and composed light-weight atoms, then the phase shift experienced by the incident electron wave upon passing through the sample will be small such that:

$$\psi_{exit} = \psi_{incident}[1\text{-}i\sigma\varphi(x_1, x_2)]$$

where here σ is the interaction constant and is equal to $2\pi m e \lambda_R / h^2$. When the electron beam

passes through a weak-phase object, the scattered beam is assumed to be much weaker than

the unscattered beam.

The contrast transfer function (CTF) provides an understanding of how aberrations in the

microscope will modify the final image.

$$CTF = A(k)\ E(k)\ exp[i\chi(k, \Delta f)]$$

where k is the wave vector, $A(k)$ is the aperture function, $E(k)$ is the envelope function,

$exp[i\chi(k)]$ is the aberration function, and $\chi(k)$ is the phase-distortion function. Often, if the

sample is a weak-phase object, then the CTF is sometimes called the transfer function, T.

$$T = A(k)\ E(k)2\sin\chi(k)$$

For a weak phase object, the amplitude of the scattered frequency, k, is given by:
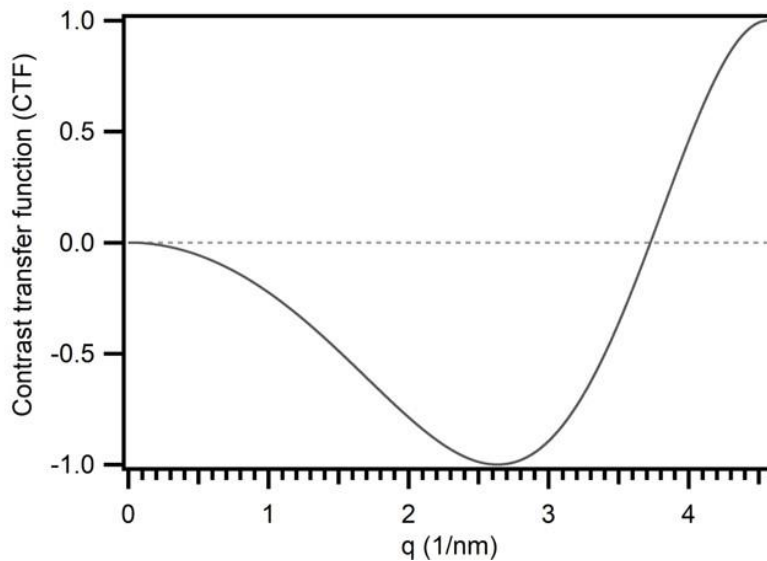
Figure 2-9. CTF for $\Delta f_{Scherzer}$ = -36 nm and λ of 0.002 nm. Here, the value of the CTF is only -0.02 for the polymer alkyl stacking distance of 2 nm (q ~ 0.3 nm^{-1}).

$$\sin \chi(k) = \sin\left[\pi\lambda\Delta f k^2 + \frac{1}{2}\pi C_S \lambda^3 k^4\right]$$

where C_S is the spherical aberration coefficient, and Δf is the defocus. The CTF has characteristic oscillations between 1 and -1 [1]. When the CTF is equal to zero, there is no contrast for that spatial frequency. Maximum contrast is achieved at the extremes of 1 and -1. Positive phase contrast occurs when the CTF is negative and the atoms will appear dark. For negative phase contrast, the CTF is positive and the atoms will appear light.

If the characteristic frequencies for a particular material are not known, the microscope should be operated at a defocus where the contrast transfer function is flat over a wide range
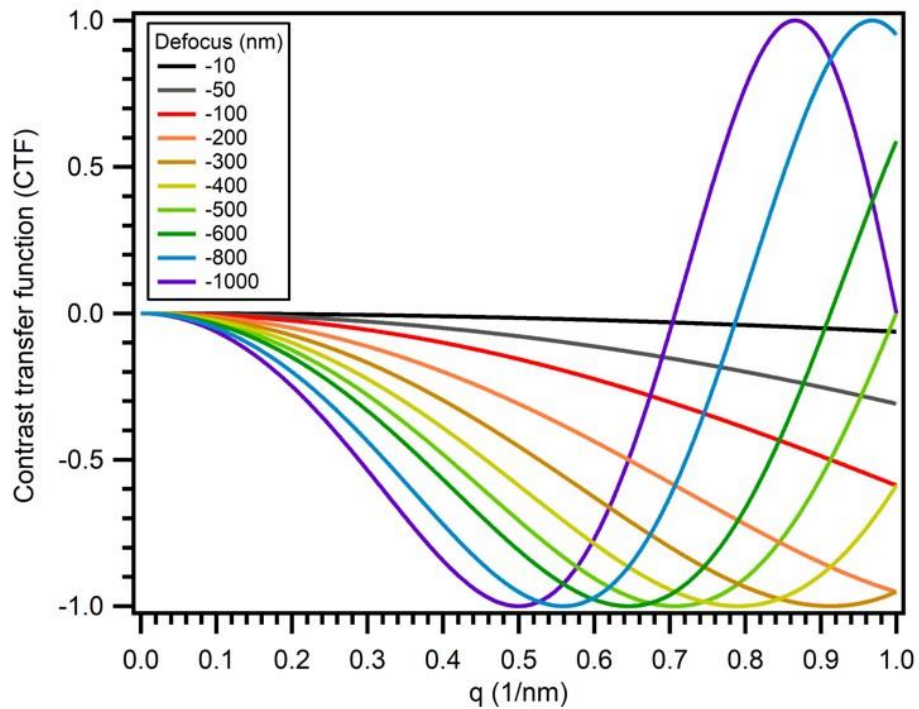
Figure 2-10. The maxima of the CTF shifts towards larger frequencies as the defocus increases.
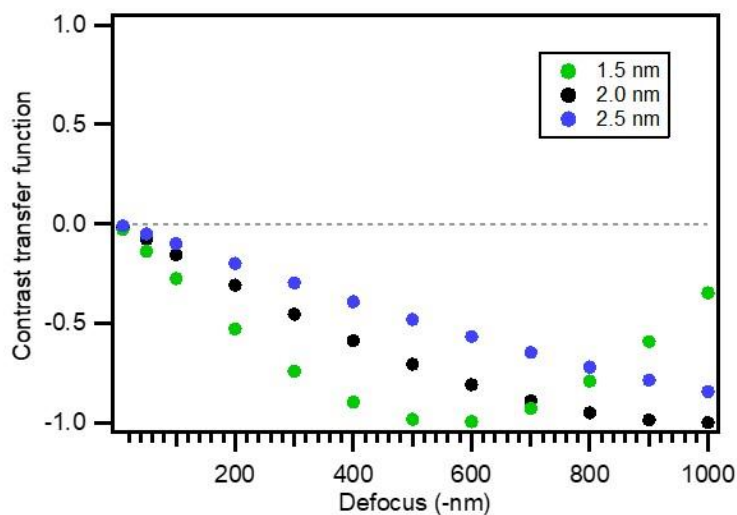
Figure 2-11. CTF as a function of defocus value for different d-spacings.

of spacings. A typical starting point is at the Scherzer defocus, where the optimal value is a function of the spherical aberration coefficient and the wavelength.

$$\Delta f_{Scherzer} = -1.2\sqrt{C_s\lambda}$$

For a 300 kV microscope with a λ of 0.002 nm and C_s of 0.65mm, the Scherzer defocus is around -36 nm. However, one must also ensure that the maximum in the CTF overlaps with peaks in the spatial frequency. For polymers that form lamellar crystals, the alkyl stacking distance ($k \sim 1-3$ nm, $q \sim 0.2-0.6$ nm^{-1}) will be the easiest to resolve because it is well above the resolution of most high-resolution microscopes. For example, the FEI Titan 300 kV microscope used for the HRTEM studies described here has a resolution of 1-2 Å. Therefore, if a typical conjugated polymer is primarily in a face-on orientation to the substrate/grid, then the alkyl stacking will be in the plane of the film and can be resolved with HRTEM at normal incidence. However, in order to correctly resolve the desired spatial frequency of $k \sim 2$ nm ($q \sim 0.3$ nm^{-1}), a defocus value must be selected to maximize the CTF at that value.

$$CTF \sim \sin(\pi\lambda\Delta fk^2)$$

33

Figure 2-9 shows the CTF at the Scherzer defocus, where the first maximum (-1) of the CTF is at $q \sim 2.2$ nm^{-1} or $k = 0.45$ nm. However, the CTF is at approximately 8% of the maximum value for $q = 0.5$ nm^{-1} or $k = 2.0$ nm. The defocus must be increased in order to increase the phase-contrast for the k of interest. Figure 2-10 shows a plot of the CTF for different defocus values. A defocus of -1000 nm results in the alignment of the first maximum in the CTF at $k = 2.0$ nm. Although it should be noted that the use of the defocus to increase phase-contrast should be used Ultimately, a defocus value between -200 and -500 nm was used during microscope operation as to increase contrast while minimizing image distortion. Figure 2-11 shows that a smaller defocus is better for smaller d-spacings. It can also be seen that around 50 nm, the contrast is close to zero and is not ideal when the periodic feature is large. Figure 2-12 shows a high-resolution phase-contrast image of a polymer crystallite where a defocus
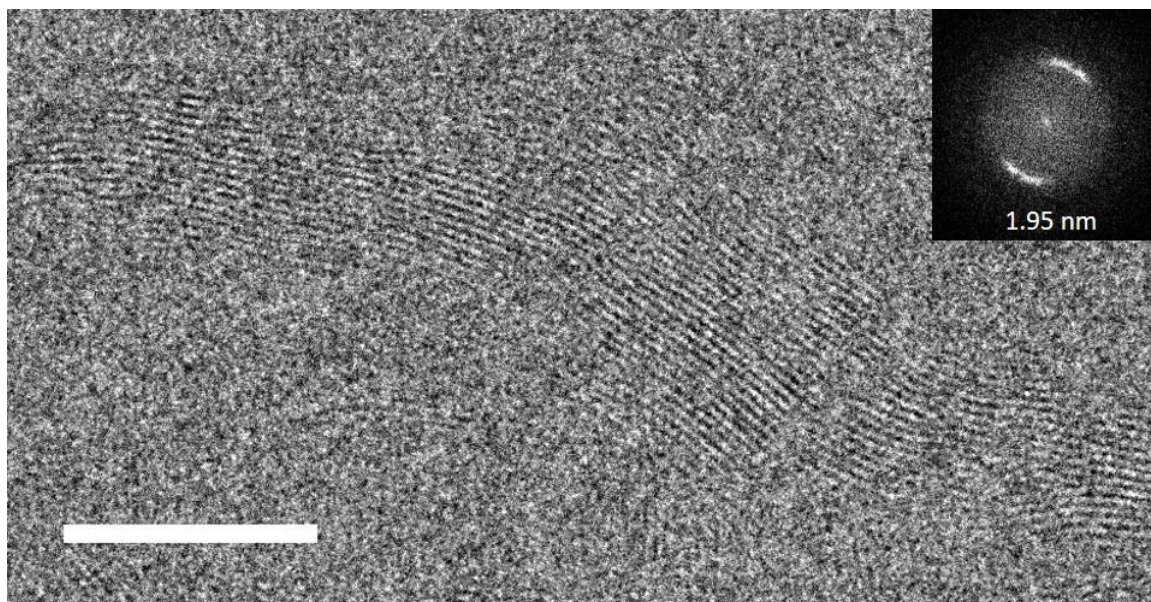
Figure 2-12. HRTEM image of a PBDTTPD (2EH/C8) crystallite after annealing at 275C. Scale bar is 50 nm.

of -500 nm was chosen to maximize the signal from the spatial frequency of 1.95 nm. Imaging conditions were optimized for a dose rate of 300 e/nm^2 to minimize damage.

2.10   Choosing a Magnification

A magnification should be selected such that the periodicity of interest is at least 5-6x larger than pixel size on the detector. For example, if the goal is to image a polymer alkyl stacking distance of 1.6 nm with a 2048x2048 pixel CCD camera, then a magnification of at least 43kx should be used. At that magnification, the pixel spacing is 2.42 Å, which is ~6.6x the d-spacing of 1.6 nm (16 Å). A continued increase in the magnification will only increase the image resolution until the point at which the pixel spacing is equal to the microscope resolution. For the FEI Titan 300 kV microscope at UCSB, the best achievable resolution is around 1 Å (because of aberrations). Therefore, increasing the magnification beyond approximately 87kx (pixel spacing = 1.23) will not increase the resolution. For this reason, the π-π stacking peak (~ 3-4 Å) is very difficult to directly image because drift and damage will further reduce the image resolution. The use of an aberration corrected TEM will improve the achievable resolution.

2.11   Reasons Lattice Fringes are not Present

A very common misconception is that the lack of lattice fringes indicates a sample is amorphous in that region. However, there are many reasons why lattice fringes would not be observed. The first reason is if the crystallites in the film are tipped out-of-plane. The periodic feature being imaged must be parallel to the incoming electron beam. For this reason,

35
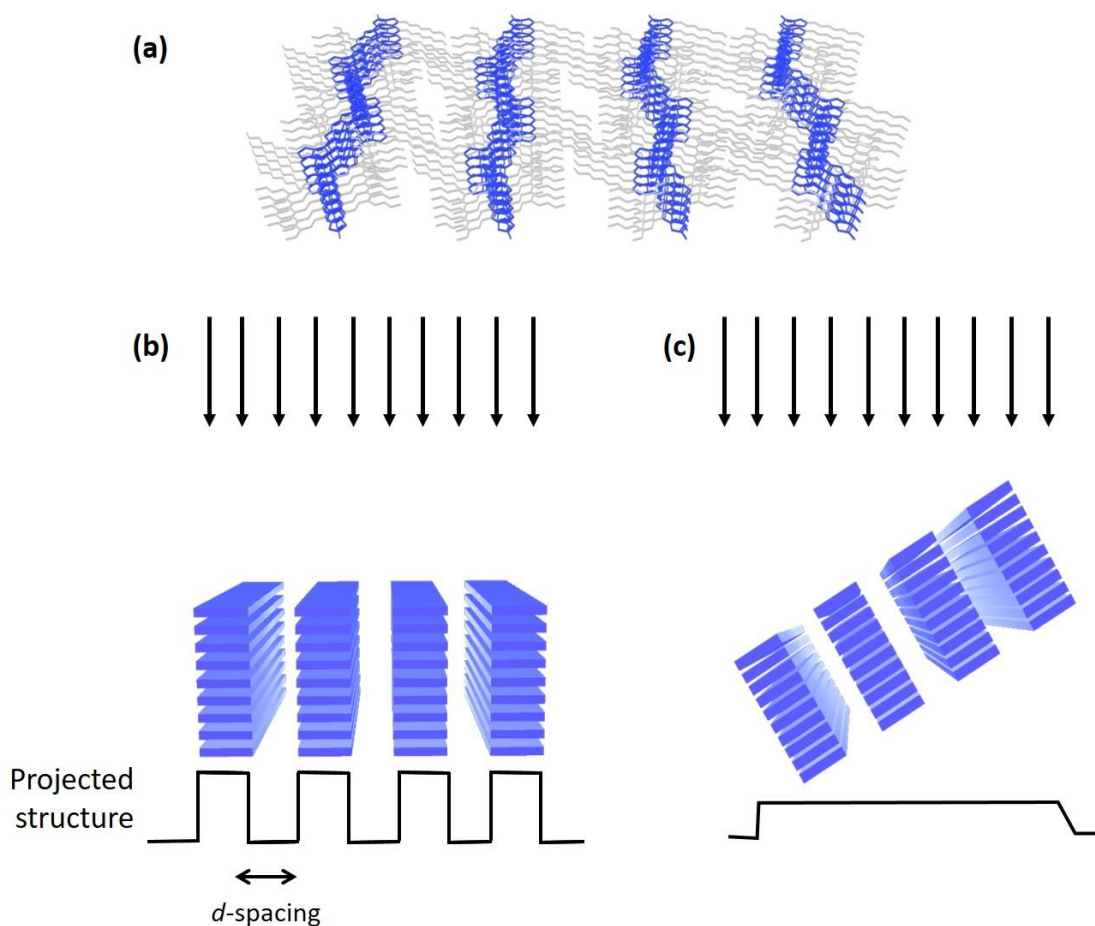
Figure 2-13. (a) Schematic of face-on polymer crystallite with parallel conjugated backbones (blue) and aliphatic side-chains (gray), (b,c) simplified drawing of polymer backbones in face-on crystallites. When the crystal planes being imaged are (b) parallel to the incoming electron beam the projected periodic structure is visible. However, when the crystallite is (c) tipped out of plane, lattice fringes will not be observed in the image.

predominantly face-on materials are easier to image (oriented ~0° to 5°). The amount that

crystallites can be tipped out of the plane and produce detectable signal will depend on the

crystallite thickness and d-spacing. If the crystallite is very thin with a large d-spacing, small

deviations in the orientation from perfectly in-plane (< 10°) will likely still be detected.

However, if the d-spacing is small or the crystallite is very thick then a small tip of the

crystallite by even a few degrees might prevent the signal from being collected in the image

(Figure 2-13).

Additionally, the sample may drift during imaging which would have a smearing effect and may result in no detectable signal. Drift can be caused by mechanical movement of the sample stage or from static charging of the sample, which is common for organic materials. Depending on the conductivity of the material, which can be low for organics, For the case of sample charging causing drift, a low and stable vacuum level is required. The mechanism of charging is described by Glaeser and Downing [68]. It is common to encounter a drift rate for polymer thin films on the order of 0.2 nm/s. Therefore, either steps must be taken to reduce the drift rate, or a shorter exposure time is required. A typical exposure time is between 3-10 seconds, and the drift will worsen image resolution for longer exposures.
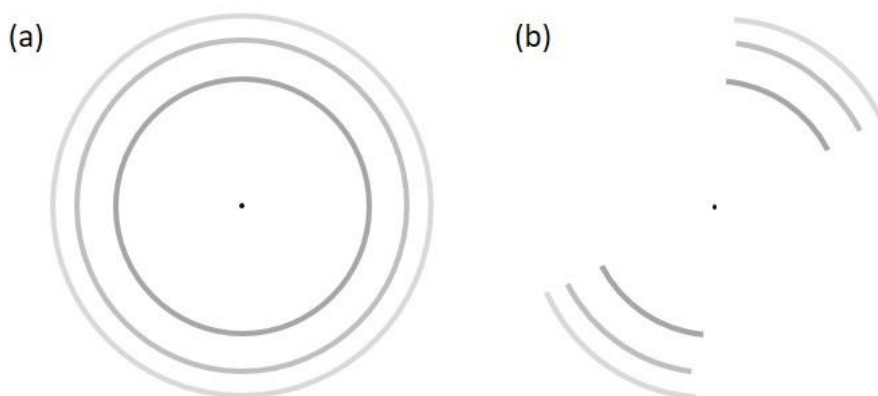
Figure 2-14. Example of the power spectrum of a defocused image for the case of (a) no drift and (b) drift.

When in bright-field imaging mode, sample drift can be observed in intensity distribution of the FFT. When drift is occurring, the power spectrum will appear stronger in one direction and washed out in another. Figure 2-14 shows an example of how to detect sample drift in an image. Drift will cause an asymmetry in the power spectrum that may resemble arcs as are commonly seen for polymer samples. In order to separate the two, the image defocus can be decreased so that several rings from the contrast transfer function (CTF) can be observed.

When the sample is not drifting, the power spectrum will appear as in Figure 2-14a. However, if there is appreciable drift, the rings will become arcs that are perpendicular to the drift direction (Figure 2-14b).

2.12 Sample Preparation - Materials Selection
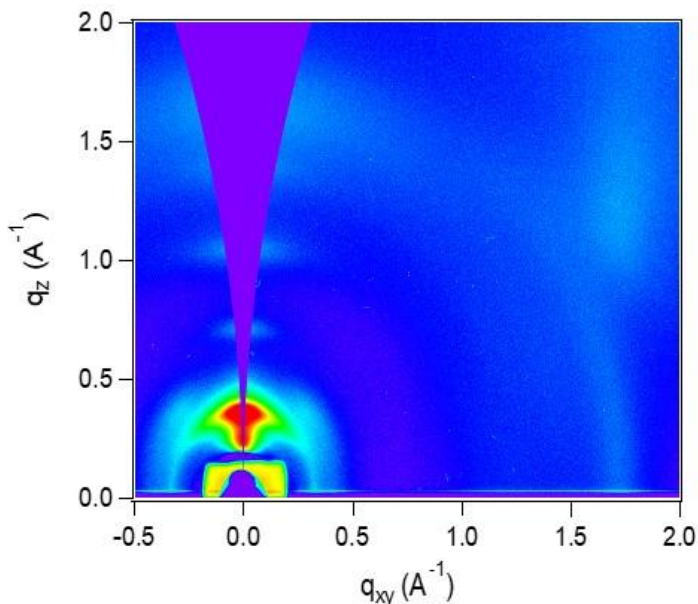
Figure 2-15. GIWAXS image of the polymer PBDTTPD (2EH/2EH) showing weak scattering features suggesting a glassy morphology.

Because TEM can be time-consuming and difficult to interpret on its own in some cases, it is important to use multiple methods to determine if a material is a good candidate for a particular imaging method and to formulate a specific question that could be answered. HRTEM is highly complementary to techniques such as grazing incidence wide-angle X-ray scattering (GIWAXS) which is able to determine the molecular packing details of a material in and out of the plane of the substrate. If the material has strong in-plane scattering then it is likely to be a good candidate for high-resolution imaging. For polymers and small-molecules, that corresponds to intense reflections between $q_{xy} \sim 0.2 - 0.6$ Å^{-1}. However, features outside of
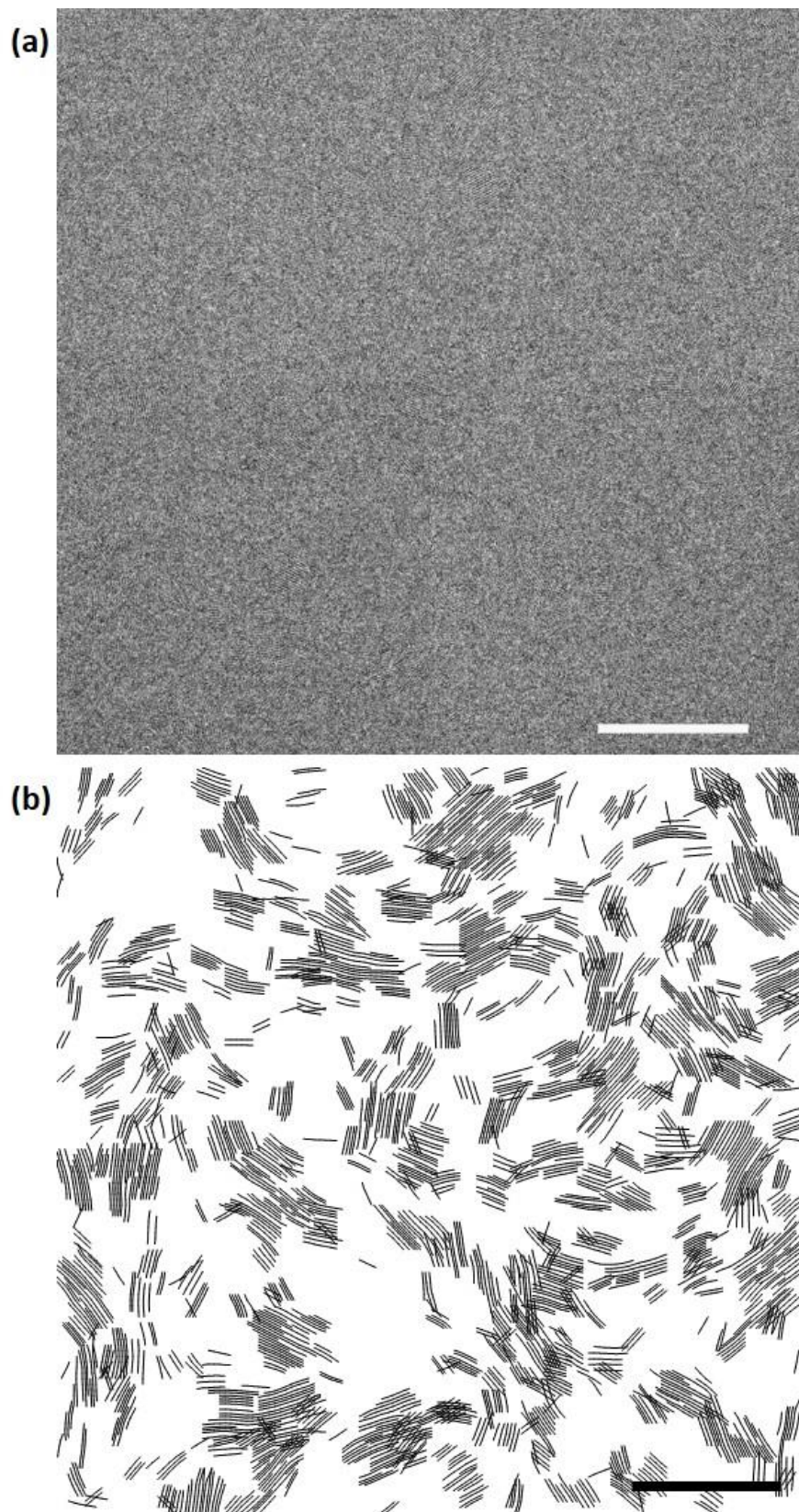
Figure 2-16. PBDTTPD (2EH/2EH) (a) HRTEM image and (b) line-drawing of raw image.

this range can still be studied using other techniques, such as electron diffraction, where many of the resolution challenges of direct imaging are not relevant.

Additionally, it is important to remember that many X-ray scattering methods such as GIWAXS will provide an average of the bulk thin film molecular packing. Therefore, if there is significant disorder or a high concentration of defects in the structure then X-ray diffraction peaks will appear broad. However, there are other contributing factors such as the potential for multiple polymorphs with similar packing or a small average crystallite size that will make a material appear more disordered on the macroscale. Examination of the local structure with HRTEM may show considerably more order than would be expected from the 2D X-ray pattern. Especially for semiconducting polymers which typically have very few peaks in a typical GIWAXS pattern, and therefore it is difficult to estimate the nature of the local packing structure. Many materials that are identified as 'glassy' with GIWAXS often appear highly crystalline with TEM. For example, Figure 2-16 shows a HRTEM of the same PBDTTPD film for which X-ray scattering data is presented in Figure 2-15. It is important to define the length scale over which a material goes from having isotropic to anisotropic packing. This can be accomplished through the use of HRTEM and selected area electron diffraction. When the grain size is small, an accurate assessment of the nanoscale morphology must include a characterization technique that is able to examine the local structure.

2.13 Microscope Operation

See Appendix A

2.14 Conclusions

High-resolution TEM is an incredibly valuable tool for the study of the nanoscale morphology in thin films of polymers and small-molecules. Knowledge of the molecular assembly on this length scale is required to better understand charge transport processes in organic electronic devices. For imaging of the lattice fringes formed by the crystalline molecular packing, phase-contrast contrast is the dominant mechanism. To increase the interpretability of the microscopy image, the polymer or small-molecule film should be less than 50 nm thick (~ 20 nm is even better). Additionally, a higher accelerating voltage is preferred for minimizing radiation damage and increasing resolution. An optimal defocus value should also be selected such that the CTF is maximized for the periodicity of interest. For the examination of phase separation of two materials in a blend (BHJ or even a polymer with a molecular dopant), the absorption contrast should be maximized. This is accomplished through the use of apertures, lowering the accelerating voltage, or operating in STEM imaging mode. Ultimately, through use of the appropriate imaging conditions and careful monitoring of damage effects, TEM can be an extremely valuable tool for examining the structural organization of organic thin films.

Bibliography

[1]   J. C. H. Spence, *High-Resolution Electron Microscopy*, 3rd ed. New York: Oxford University Press, 2003.

[2]   K. Kobayashi and K. Sakaoku, "The Changes of Polymer Crystals due to Irradiation with Electrons Accelerated at Various Voltages," *Bull. Inst. Chem. Res. Kyoto Univ.*, vol. 42, no. 6, pp. 473–493, 1965.

[3]   V. E. Cosslett, "Beam and Specimen: Radiation Damage and Image Resolution," *Berichte der Bunsengesellschaft für Phys. Chemie*, vol. 74, no. 11, pp. 1171–1175, 1970.

[4]   L. E. Thomas, C. J. Humphreys, W. R. Duff, and D. T. Grubb, "Radiation damage of polymers in the million volt electron microscope," *Radiat. Eff.*, vol. 3, no. 1, pp. 89–91, 1970.

[5]   D. T. Grubb and G. W. Groves, "Rate of damage of polymer crystals in the electron microscope: Dependence on temperature and beam voltage," *Philos. Mag.*, vol. 24, no. August, pp. 815–828, 1971.

[6]   D. T. Grubb, "Radiation damage and electron microscopy of organic polymers," *J. Mater. Sci.*, vol. 9, no. 10, pp. 1715–1736, 1974.

[7]   R. F. Egerton, "Control of radiation damage in the TEM," *Ultramicroscopy*, vol. 127, pp. 100–108, 2013.

[8]   C. Martin and L. Thomas, "Experimental high-resolution electron microscopy of polymers *," *Science (80-.).*, vol. 36, no. 9, pp. 1743–1759, 1995.

[9]   S. Kumar and W. W. Adams, "Electron beam damage in high temperature polymers," *Polymer (Guildf).*, vol. 31, no. 1, pp. 15–19, 1990.

[10]   F. Khoury, "The Spherulitic Crystallization of Isotactic Polypropylene From Solution : On the Evolution of Monoclinic Spherulites From," *J. Res. Natl. Bur. Stand. A*, vol. 70, no. 1, pp. 29–61, 1966.

[11]   F. J. Padden and H. D. Keith, "Crystallization in thin films of isotactic polypropylene," *J. Appl. Phys.*, vol. 37, no. 11, pp. 4013–4020, 1966.

[12]   F. L. Binsbergen and B. G. M. de Lange, "Morphology of polypropylene crystallized from the melt," *Polymer (Guildf).*, vol. 9, pp. 23–40, 1968.

[13]   F. J. Padden and H. D. Keith, "Mechanism for lamellar branching in isotactic polypropylene," *J. Appl. Phys.*, vol. 44, no. 3, pp. 1217–1223, 1973.

[14]   A. J. Lovinger, "Microstructure and unit-cell orientation in α-polypropylene," *J. Polym. Sci. Part B Polym. Phys.*, vol. 21, no. 1, pp. 97–110, 1983.

[15]   B. Lotz and J. C. Wittmann, "The molecular origin of lamellar branching in the α (monoclinic) form of isotactic polypropylene," *J. Polym. Sci. Part B Polym. Phys.*, vol. 24, no. 7, pp. 1541–1558, 1986.

[16]   S. Bruckner and S. V Meille, "Non-parallel chains in crystalline γ-isotactic

polypropylene," *Nature*, vol. 340, no. 6233, pp. 455–457, 1989.

[17] S. V Meille, S. Bruckner, and W. Porzios, "y-Isotactic Polypropylene. A Structure with Nonparallel Chain Axes," *Macromolecules*, vol. 23, pp. 4114–4121, 1990.

[18] B. Lotz, J. C. Wittmann, and A. J. Lovinger, "Structure and morphology of poly(propylenes): A molecular analysis," *Polymer (Guildf).*, vol. 37, no. 22, pp. 4979–4992, 1996.

[19] A. Romankiewicz, T. Sterzynski, and W. Brostow, "Structural characterization of α- and β-nucleated isotactic polypropylene," *Polym. Int.*, vol. 53, no. 12, pp. 2086–2091, 2004.

[20] I. G. Voigt-Martin, H. Durst, B. Reck, and H. Ringsdorf, "Structure Analysis of a Combined Main-Chain / Side-Group Liquid Crystalline Polymer by Electron Microscopy," *Society*, vol. 21, pp. 1620–1626, 1988.

[21] I. G. Voigt-Martin and H. Durst, "High-Resolution Images of Defects in Liquid Crystalline Polymers in the Smectic and Crystalline Phases," *Macromolecules*, vol. 22, pp. 168–173, 1989.

[22] I. G. Voigt-Martin, R. W. Garbella, and M. Schumacher, "Structure and defects in discotic crystals and liquid crystals as revealed by electron diffraction and high-resolution electron microscopy," *Macromolecules*, vol. 25, pp. 961–971, 1992.

[23] I. G. Voigt-Martin, P. Simon, S. Bauer, and H. Ringsdorf, "Structure and Defects in Sanidic Liquid Crystalline Polymers. 1," *Macromolecules*, vol. 28, pp. 236–242, 1995.

[24] I. G. Voigt-Martin, P. Simon, D. Yan, and A. Yakimansky, "Structure and Defects in Sanidic Liquid Crystalline Polymers. 2 . Structure Analysis of Sanidic Polymers by Simulation of Diffraction Patterns from Monomeric Analogs," *Macromolecules*, vol. 28, pp. 243–254, 1995.

[25] D. C. Martin and Thomas, "Grain boundaries in extended-chain polymers Theory and Experiment," *Philos. Mag. A*, vol. 64, pp. 903–922, 1991.

[26] D. C. Martin, "Intermolecular Twist Defects in Extended-Chain Polymers," pp. 5171–5177, 1992.

[27] J. R. Ojeda and D. C. Martin, "High Resolution Microscopy of PMDA-ODA Poly(imide) Single Crystals," *Macromolecules*, vol. 26, pp. 6557–6565, 1993.

[28] S. Van Bavel, E. Sourty, G. De With, K. Frolic, and J. Loos, "Relation between photoactive layer thickness, 3D morphology, and device performance in P3HT/PCBM bulk-heterojunction solar cells," *Macromolecules*, vol. 42, no. 19, pp. 7396–7403, 2009.

[29] J. S. Moon *et al.*, "Effect of processing additive on the nanomorphology of a bulk heterojunction material," *Nano Lett.*, vol. 10, no. 10, pp. 4005–4008, Oct. 2010.

[30] J. a. Bartelt *et al.*, "Controlling Solution-Phase Polymer Aggregation with Molecular Weight and Solvent Additives to Optimize Polymer-Fullerene Bulk Heterojunction Solar Cells," *Adv. Energy Mater.*, vol. 4, no. 9, Jun. 2014.

[31] W. Huang, E. Gann, L. Thomsen, C. Dong, Y.-B. Cheng, and C. R. McNeill, "Unraveling the Morphology of High Efficiency Polymer Solar Cells Based on the Donor Polymer PBDTTT-EFT," *Adv. Energy Mater.*, vol. 5, no. 7, p. n/a-n/a, Apr. 2015.

[32] M. Pfannmöller, H. Flügge, G. Benner, I. Wacker, W. Kowalsky, and R. R. Schröder, "Visualizing photovoltaic nanostructures with high-resolution analytical electron microscopy reveals material phases in bulk heterojunctions," *Synth. Met.*, vol. 161, no. 23–24, pp. 2526–2533, Jan. 2012.

[33] L. A. Perez *et al.*, "The Role of Solvent Additive Processing in High Performance Small Molecule Solar Cells," *Chem. Mater.*, vol. 26, no. 22, pp. 6531–6541, 2014.

[34] D. Leman *et al.*, "In situ characterization of polymer-fullerene bilayer stability," *Macromolecules*, vol. 48, no. 2, pp. 383–392, 2015.

[35] C. Guo *et al.*, "Probing Local Electronic Transitions in Organic Semiconductors through Energy-Loss Spectrum Imaging in the Transmission Electron Microscope," *Adv. Funct. Mater.*, vol. 25, no. 38, pp. 6071–6076, 2015.

[36] Y. Sun, G. C. Welch, W. L. Leong, C. J. Takacs, G. C. Bazan, and A. J. Heeger, "Solution-processed small-molecule solar cells with 6.7% efficiency.," *Nat. Mater.*, vol. 11, no. 1, pp. 44–48, Jan. 2012.

[37] K. A. O'Hara *et al.*, "Role of Crystallization in the Morphology of Polymer:Non-fullerene Acceptor Bulk Heterojunctions," *ACS Appl. Mater. Interfaces*, vol. 9, no. 22, pp. 19021–19029, 2017.

[38] M. Gao *et al.*, "Direct observation of liquid crystals using cryo-TEM: Specimen preparation and low-dose imaging," *Microsc. Res. Tech.*, vol. 77, no. 10, pp. 754–772, 2014.

[39] C. Zhang *et al.*, "Direct observation of smectic layers in thermotropic liquid crystals," *Phys. Rev. Lett.*, vol. 109, no. 10, pp. 1–5, 2012.

[40] L. Biniek *et al.*, "Zipper-like molecular packing of donor–acceptor conjugated co-oligomers based on perylenediimide," *J. Mater. Chem. C*, vol. 3342, no. 3, pp. 3342–3349, 2015.

[41] L. Hartmann *et al.*, "2D versus 3D crystalline order in thin films of regioregular poly(3-hexylthiophene) oriented by mechanical rubbing and epitaxy," *Adv. Funct. Mater.*, vol. 21, no. 21, pp. 4047–4057, 2011.

[42] K. Tremel *et al.*, "Charge transport anisotropy in highly oriented thin films of the acceptor polymer P(NDI2OD-T2)," *Adv. Energy Mater.*, vol. 4, no. 10, pp. 1–13, 2014.

[43] A. Hamidi-Sakr, L. Biniek, S. Fall, and M. Brinkmann, "Precise Control of Lamellar Thickness in Highly Oriented Regioregular Poly(3-Hexylthiophene) Thin Films Prepared by High-Temperature Rubbing: Correlations with Optical Properties and Charge Transport," *Adv. Funct. Mater.*, vol. 26, no. 3, pp. 408–420, 2016.

[44] C. J. Takacs, M. a Brady, N. D. Treat, E. J. Kramer, and M. L. Chabinyc, "Quadrites and crossed-chain crystal structures in polymer semiconductors.," *Nano Lett.*, vol. 14,

no. 6, pp. 3096–101, Jun. 2014.

[45] C. J. Takacs *et al.*, "Remarkable Order of a High-Performance Polymer," *Nano Lett.*, 2013.

[46] G. L. Schulz *et al.*, "The PCPDTBT Family: Correlations between Chemical Structure, Polymorphism, and Device Performance," *Macromolecules*, vol. 50, no. 4, pp. 1402–1414, 2017.

[47] M. J. M. Wirix, P. H. H. Bomans, F. Heiner, N. A. J. M. Sommerdijk, and G. De With, "Three-Dimensional Structure of P3HT Assemblies in Organic Solvents Revealed by Cryo-TEM," *Nano Lett.*, vol. 14, no. 4, pp. 2033–2038, 2014.

[48] D. C. Martin, J. Chen, J. Yang, L. F. Drummy, and C. Kübel, "High resolution electron microscopy of ordered polymers and organic molecular crystals: Recent developments and future possibilities," *J. Polym. Sci. Part B Polym. Phys.*, vol. 43, no. 14, pp. 1749–1778, Jul. 2005.

[49] D. B. Williams and B. C. Carter, *Transmission Electron Microscopy*, 2nd ed. 2009.

[50] C. E. Hall, *Introduction to Electron Microscopy*. New York: McGraw-Hill, 1953.

[51] B. von Borries and E. Ruska, "Der Einflufl der Strahlspannung auf das iibermikroskopische Bild," *Z. Phys.*, vol. 116, pp. 249–256, 1940.

[52] L. F. Drummy, J. Yang, and D. C. Martin, "Low-voltage electron microscopy of polymer and organic molecular thin films," *Ultramicroscopy*, vol. 99, no. 4, pp. 247–256, 2004.

[53] H. A. Bethe and J. Ashkin, "Passage of Radiations Through Matter," in *Experimental Nuclear Physics*, Vol. 1., E. Segre, Ed. New York: Wiley, 1953.

[54] P. Bernsen, L. Reimer, and P. F. Schmidt, "Investigation of Electron Irradiation Damage of Evaporated Organic Films by Laser Microprobe Mass Analysis," *Ultramicroscopy*, vol. 7, pp. 197–202, 1981.

[55] J. R. Fryer and F. Holland, "High resolution electron microscopy of molecular crystals III. Radiation processes at room temperature," *Proc. R. Soc. Lond. A*, vol. 393, pp. 353–369, 1984.

[56] H. A. Dewhurst, A. H. Samuel, and J. L. Magee, "A Theoretical Survey of the Radiation Chemistry of Water and Aqueous Solutions," *Radiat. Res.*, vol. 1, no. 1, pp. 62–84, 1954.

[57] J. F. Revol, "Change of the d spacing in cellulose crystals during lattice imaging," *J. Mater. Sci. Lett.*, vol. 4, no. 11, pp. 1347–1349, 1985.

[58] S. M. Salih and V. E. Cosslett, "Reduction in electron irradiation damage to organic compounds by conducting coatings," *Philos. Mag.*, vol. 30, no. 1, pp. 225–228, 1974.

[59] J. R. Fryer and F. Holland, "The Reduction of Radiation Damage in the Electron Microscope," *Ultramicroscopy*, vol. 11, pp. 67–70, 1983.

[60] G. Mihély and L. Zuppiroli, "Radiation effects in organic metals: The mechanisms of damage production," *Philos. Mag. A*, vol. 45, no. 3, pp. 549–562, 1982.

[61]   M. Gryziński, "Classical theory of atomic collisions. I. Theory of Inelestic collisions," *Phys. Rev.*, vol. 138, no. 2, pp. 336–358, 1965.

[62]   D. C. Martin and E. L. Thomas, "Observation of Defects in Crystalline Polymers by HREM," *MRS Bull.*, vol. 12, no. 8, pp. 27–35, 1987.

[63]   E. M. Belavtseva and K. Z. Gumargalieva, "Contrast Intensification in the Electron Microscopy of Polymers," *Russ. Chem. Rev.*, vol. 37, no. 4, pp. 298–309, 1968.

[64]   L. F. Drummy, J. Chen, J. Yang, and D. C. Martin, "Low voltage electron microscopy of organic materials," *Microsc. Microanal.*, vol. 12, no. SUPPL. 2, pp. 1434–1435, 2006.

[65]   L. F. Drummy, R. J. Davis, D. L. Moore, M. Durstock, R. A. Vaia, and J. W. P. Hsu, "Molecular-scale and nanoscale morphology of P3HT:PCBM bulk heterojunctions: Energy-filtered TEM and low-dose HREM," *Chem. Mater.*, vol. 23, no. 3, pp. 907–912, 2011.

[66]   W. Schindler, M. Wollgarten, and K. Fostiropoulos, "Revealing nanoscale phase separation in small-molecule photovoltaic blends by plasmonic contrast in the TEM," *Org. Electron. physics, Mater. Appl.*, vol. 13, no. 6, pp. 1100–1104, 2012.

[67]   F. I. Allen, P. Ercius, M. A. Modestino, R. A. Segalman, N. P. Balsara, and A. M. Minor, "Deciphering the three-dimensional morphology of free-standing block copolymer thin films by transmission electron microscopy," *Micron*, vol. 44, no. 1, pp. 442–450, 2013.

[68]   R. M. Glaeser and K. H. Downing, "Specimen charging on thin films with one conducting layer: discussion of physical principles.," *Microsc. Microanal.*, vol. 10, no. 6, pp. 790–796, 2004.

Chapter 3

Observation of Inter- and Intracrystallite Ordering in High Resolution TEM Images of Semiconducting Polymers and Small-molecules

3.1 Introduction

Both the morphology and local order of organic semiconductors must be precisely controlled to impart the desired transport properties for devices[1]. For semiconducting polymers, this includes minimizing the local energetic disorder due to their defective molecular ordering that determines, in part, the electronic density of states [2]. In addition, two other factors have an important effect on their ability to transport charge. First, the structural anisotropy in the direction of transport determines if the polymer chain is favorably aligned and second, the connectivity of adjacent domains through grain boundaries in (semi-) crystalline materials determines the barrier to move from domain to domain. The nature of the connectivity and the structure at domain boundaries is important for interpretation of transport data and the development of models that incorporate hierarchical ordering.

The basic features of charge transport in semiconducting polymers have been established [3]. Charge carriers can move more easily along the backbone of conjugated polymers than hopping between chains [4]. Thus, alignment of the conjugated backbones of semiconducting polymers with the direction of charge transport in a device can take advantage of the fastest transport direction. There have been considerable efforts to improve the connectivity of transport pathways in organic electronic devices by increasing the degree of structural anisotropy [5]. This has been accomplished through methods such as directional

crystallization [6], solution shearing [7], [8], use of mechanically rubbed substrates [9], [10], nano-grooved substrates [11], use of liquid crystalline polymers [9], [12], and control of molecular weight [13]–[15]. There is a critical need to understand how these averaged aligned domains connect to uncover the origin of barriers caused by imperfectly ordered regions.

Much of the understanding of the role of grain boundaries in semicrystalline polymers on charge transport comes from modeling of transport measurements [16]. For example, more ordered polymer semiconductors are predicted to have fast transport within an ordered domain that is limited by the ability to move between domains. Two primary mechanisms for transport between grains were described by Street, Northup and Salleo in 2005 [17]. The first is through a tie-chain or bridging polymer chain between domains, where transport is probable if there is a small degree of misorientation between two grains. The second is through thermally activated hopping where charge carriers can move between grains at high-temperatures at more disordered boundaries. In general, the energy required to traverse a grain-boundary increases with the amount of disorder.

The connectivity of polymer domains through tie-chains depends on molecular weight. Kline et. al [13] studied poly(3-hexylthiophene) (P3HT), and found that a lower molecular weight produced a more crystalline film, but a lower field-effect mobility. The higher molecular weight sample had lower crystallinity but higher mobility. It was hypothesized that the longer chains in the high molecular weight sample were able to connect adjacent crystalline domains. Noriega et al. stated that the crystalline regions contribute more to charge transport and must be well-connected to achieve high carrier mobilities[18]. Therefore, a higher-molecular weight promotes a network structure through an increase in tie-chains

between crystallites. However, molecular weight should only be increased until a high degree of connectivity is achieved, and further increases will promote structural disorder.

Structural disorder in the π-stacking of chains has been considered to be detrimental to transport and must be minimized[18]. Changes in the lattice spacing between π-stacked chains significantly modify their electronic coupling. A source of disorder in organic systems is often attributed to random fluctuations in the lattice parameter, or paracrystallinity, g. When g is large (>10%), the transport behavior follows that of an amorphous material (hopping between individual states). For a g of 5-10%, a multiple trapping and release model of transport is predicted. However, a high degree of order is not always a prerequisite for efficient charge transport, as there have been examples of glassier polymers producing high charge carrier
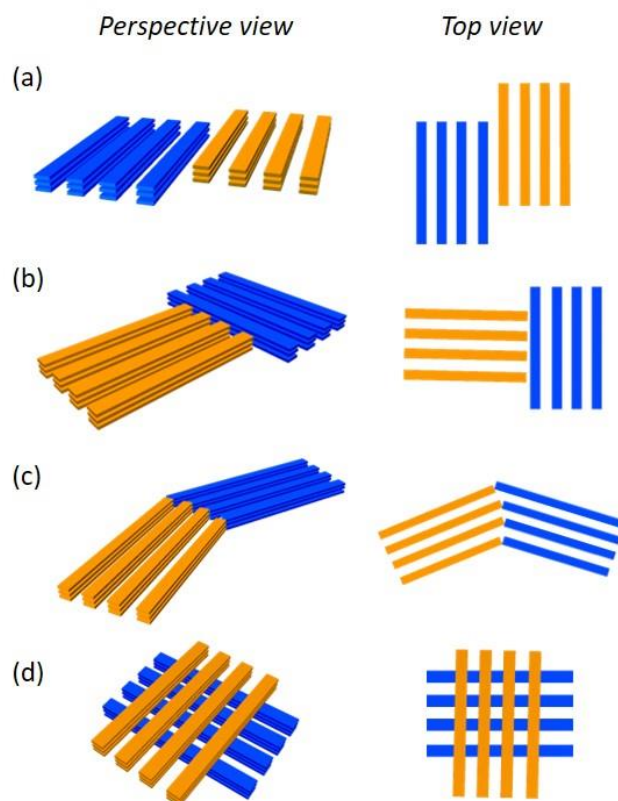
Figure 3-1. Common grain boundaries encountered in semiconducting polymers labeled according to the classification scheme by Martin and Thomas [22]. (a) lateral chain invariant, (b) axial chain rotation with chains not connected, (c) axial chain rotation with chains connected, and (d) lateral chain rotation.

mobilities[19], [20]. There are unfortunately no existing studies that can easily separate the contribution from morphology, i.e. tie chains, from disorder in the π-stacking of polymers.

Currently, the discussion of grain boundaries in semiconducting polymers is centered around the idea of isolated crystallites connected by tie-chains. Such models are generally applied to thin films where transport occurs along the direction of the substrate. In most cases, the backbones of semiconducting polymers lie along the substrate and are distributed in an edge-on or face-on orientation. The texture of ordered domains is imperfect, however, and the how such domains might connect to each other is not certain.

High resolution transmission electron microscopy (HRTEM) studies of grain boundaries of stiff-chain polymers in fibers showed that the potential types of grain boundaries can be much more complex than models typically drawn for semiconducting polymers [21], [22]. Four different types of grain boundaries for stiff-chain polymers were described by Martin and Thomas in a HRTEM study of the polymer PBZO: lateral chain invariant (LCI), lateral chain rotation (LCR), axial chain invariant (ACI), and axial chain rotation (ACR)[22]. Lateral versus axial describes the orientation of the grain boundary plane without respect to the chain axis, where lateral is parallel and axial is not. Invariant versus rotation indicates whether the chain axes of the two crystallites are parallel (invariant) or misoriented (rotation). There are structural differences between conventional fiber polymers and modern semiconducting polymers, such as the presence of extended solubilizing side-chains (Figure 3-1). Therefore for 'modern' polymers with lamellar packing, ACI boundaries will only occur for small twist angles due to the large difference in the lattice parameter for the alkyl and π-π stacking. Only recently were lateral chain rotation boundaries first observed in 'modern' semiconducting polymers [23]. In this study, crystallites of the donor-acceptor copolymer, PSBTBT, were

imaged with HRTEM and the backbones were observed to overlap at particular angles dictated by the molecular geometry. The crystallite overlap angle in PSBTBT was also confirmed by Schulz et al. [24].

3.2 Experimental Methods

Transmission Electron Microscopy: Electron micrographs were obtained using a FEI Titan 300 kV FEG TEM/STEM System. Spot sizes of 7-9 were used at a magnification of 43k. An average dose Spin-coated films were floated onto Ted Pella Cu grids with ultrathin carbon film on a lacey carbon support film (product # 01824) and Electron Microscopy Sciences (EMS) C-flat holey carbon grids (product # CF-4/1-4C). Film thickness ranged from 15 nm for thinnest samples to 60 nm for thicker films. Images were collected using the automated software SerialEM. Analysis was complete with a combination of ImageJ and MATLAB software.

3.3 Challenges of Imaging Polymer Grain Boundaries

High resolution TEM is useful in the study of local ordering of crystalline polymers and examination of grain boundaries. When there is a periodic feature present, the interference of the transmitted and diffracted waves passing through the sample will produce a characteristic 'phase contrast' image. Lattice fringes are observed in the image when the crystal is oriented parallel to the incoming electron beam. However, the absence of lattice fringes does not mean that the material in that location is amorphous (this is a common misconception). While that is a possibility, it is also likely that crystalline regions are oriented away from the optical axis. Additionally, damage and sample drift may wash out certain features, especially if the periodicity is small (such as π-π stacking which is ~3-5 Å).

One of the key challenges in the study of grain boundaries in organic systems has been the difficulty with direct imaging due to the high sensitivity of organic materials to electron irradiation[25]–[27]. The use low electron dose rates (e$^-$/nm^2) can help minimize these effects. Image quality is also dependent on a number of other factors such as accelerating voltage, aberrations, dose rate, damage, drift, proper alignment, defocus, magnification, and temperature fluctuations. Also, electron micrographs of polymer samples are often noisy due to the low-dose operating conditions and scattering from the amorphous carbon support grid.

In the present study, face-on crystallite populations (Figure 3-2) are examined to take advantage of the large periodicity of the alkyl side-chain stacking (~1-3 nm). Because HRTEM is a transmission imaging method, the final image is a projection of the structures present through the entire thickness, and samples must be very thin (< 20 nm) to best interpret the image.
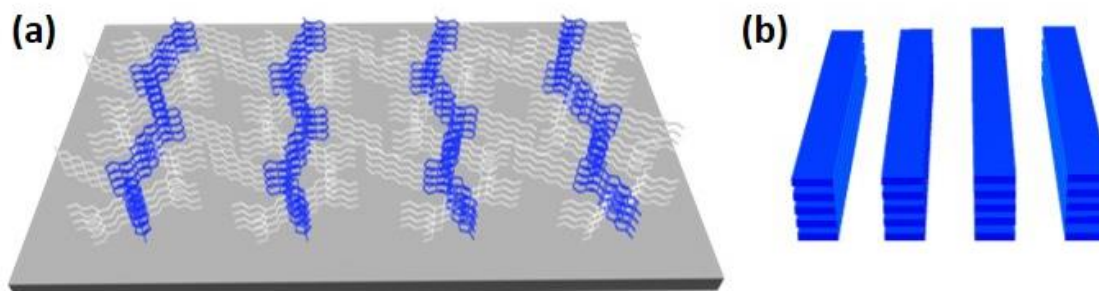
Figure 3-2. Schematic of a face-on crystallite on a substrate and (b) simplified schematic of face-on crystallite with side-chains omitted.

3.4 Analysis of Crystalline Structure and Grain Boundaries

Here, we examine three semiconducting polymers and two small-molecule used in organic electronics (Figure 3-3). HRTEM images of each are decomposed into simplified line drawings that serve as directors for the ordered domains, which allow for qualitative

52

observations about the molecular arrangements. The five materials examined show large differences in the molecular arrangement, and were chosen to show the range of nanoscale features that can be observed with HRTEM. 4,7-bis(4-(N-hexyl-phthalimide)vinyl)benzo[c]1,2,5-thiadiazole (HPI-BT) and (5Z,50Z)-5, 50-{(9,9-dioctyl-9H-fluorene-2,7-diyl)bis[2,1,3-benzothiadiazole-7, 4-diyl(Z)methylylidene]}bis(3-ethyl-2-thioxo-1,3-thiazolidin-4-one) (FBR) are both small-molecule acceptors used in OPVs[28]–[30], diketopyrrolopyrrole thieno[3,2-b]thiophene (DPPT-TT) is a donor-acceptor copolymer used in OPVs and OTFTs [19], [31], P3HT is a widely studied polymer for TFTs and OPV, and poly(benzo[1,2-b:4,5-b′]dithiophene−alt−thieno[3,4-c]pyrrole-4,6-dione) (PBDTTPD) is a donor-acceptor copolymer for OPVs[32].
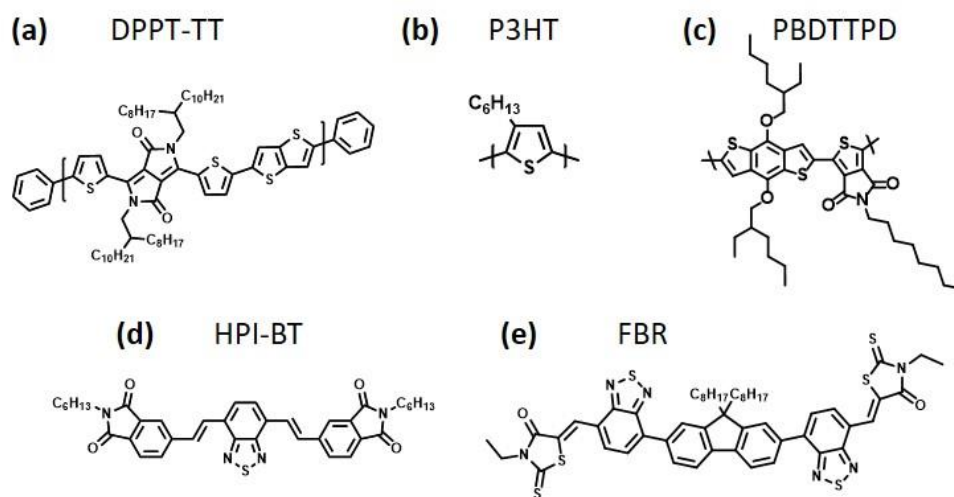
Figure 3-3. Molecular structures of (a) DPPT-TT, (b) P3HT, (c) PBDTTPD, (d) HPI-BT and (e) FBR.

The spatial arrangement of crystalline domains in a thin film can be understood by identifying the lattice fringes in a HRTEM image. The *d*-spacings correspond to the periodic stacking features along a particular crystallographic direction. It can be difficult to gain a sense of the crystalline packing from a raw TEM image because the signal is often weak and

significant amount of noise is present due to low-electron dose imaging methods. A Fourier transform-based analysis is better able to detect periodic features and is used to generate a reconstruction of the periodicities in the image.

Fluctuations in the local packing can affect the electronic properties through a reduction in the orbital overlap. This has been reported as most critical in the π-π stacking direction, however alkyl stacking fluctuations may affect crystallite connectivity. With HRTEM, images of the crystallite packing can be collected and Fourier transforming the image provides orientational information as well as the fluctuation in crystallite d-spacing. The ordering can also be probed through selected area electron diffraction, dark-field TEM[33] and X-ray nanodiffraction experiments[34]. However, the specific connectivity is better understood through a real-space image of the crystalline packing. We show here HRTEM images of a number of common polymers to show the representative behavior in each.

3.4.1 Long Range Order in High Performance Donor-acceptor Copolymer

A number of donor-acceptor copolymers, such as IDTBT and DPPTTT have been shown to exhibit high mobilities in OTFTs without pronounced crystallinity[20]. For example, DPPTTT derivatives can achieve high mobilities in OTFTs of 1.5-2.2 cm^2/Vs[31]. HRTEM of a DPPT-TT thin film shows that long range orientational order is present in face-on regions of the film (Figure 3-4). Examination of the thin film packing with GIWAXS shows that the film is mostly edge-on, however, isolated regions with a face-on orientation can be observed (Figure 3-5). A Fourier transform of the HRTEM image shows a set of diffuse peaks corresponding to the alkyl stacking distance centered around 2.0 nm (Figure 3-4c). The width of the peak is probed by a radial integration of the FFT intensity (Figure 3-4d) and shows a
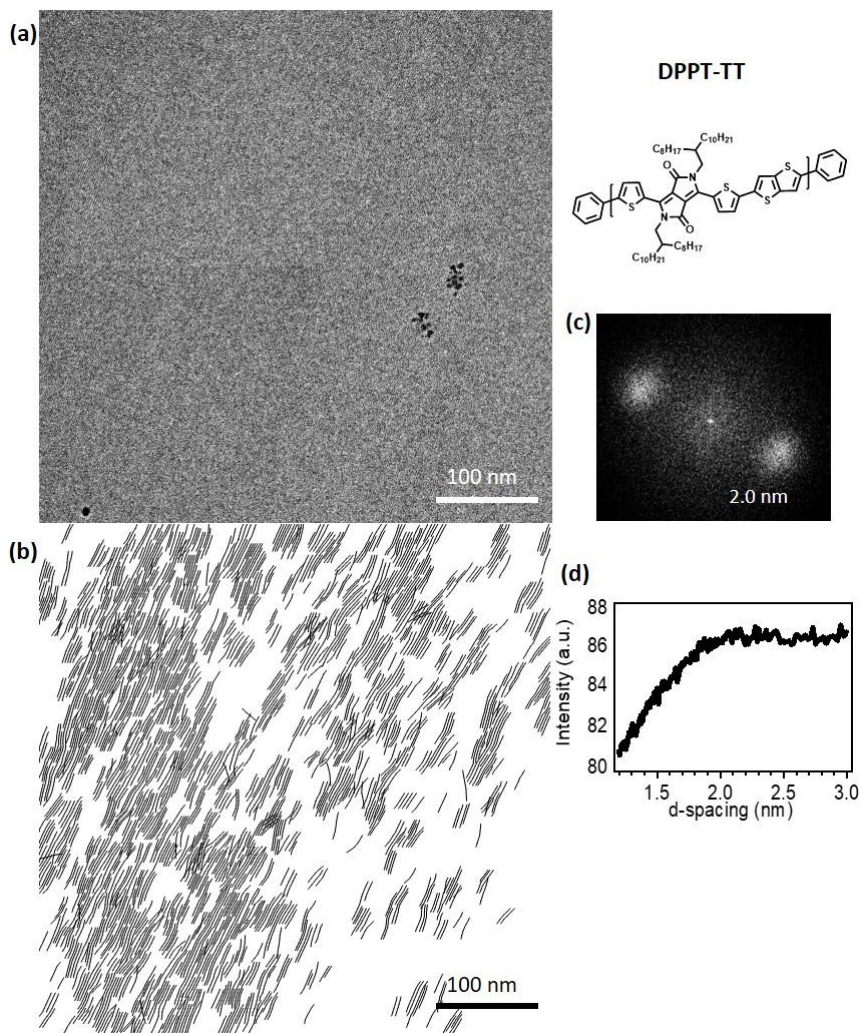
Figure 3-4. DPPT-TT (a) raw TEM image and (b) reconstructed line-drawing of the periodic lattice fringes within crystalline domains, (c) power spectrum, and (d) 1D profile of the FFT radially integrated intensity.

broad peak with a width of almost 1 nm over an area of just 300 x 300 nm. This indicates that there are local fluctuations in the alkyl stacking distance (Figure 3-4c). GIWAXS of the DPPT-TT film shows a similar diffuse alkyl in-plane stacking peak (Figure 3-5). The GIWAXs in-plane alkyl stacking peak is centered at 0.297 Å^{-1} ($d \sim 21.1$ Å) and a FWHM of 0.153 Å^{-1}. This corresponds to a range in the in-plane alkyl stacking distance of approximately 1.7 - 2.8 nm from GIWAXS. It is surprising that the same degree of fluctuation in the alkyl
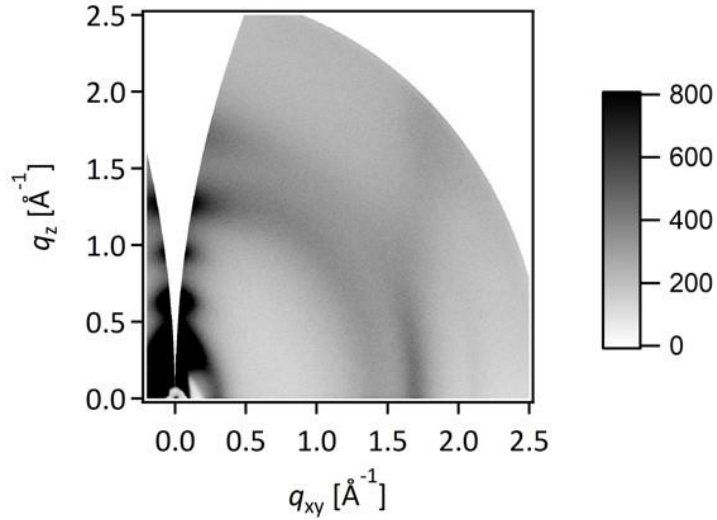
Figure 3-5. 2D GIWAXS pattern for a DPPT-TT thin film.

stacking distance (~ 1 nm) is observed both in small regions with TEM (300x300 nm) and in the bulk of the film as determined by GIWAXS. The local fluctuations in the *d*-spacing are likely what allows the polymer to extend in a particular direction without abrupt grain boundaries or turns. Molecular dynamics simulations of the polymer IDTBT, which has a similar structure and performance, show the backbone is highly planar and relatively torsion free which enables a high-resiliency to disorder in the side-chains[20]. IDTBT has a long persistence length of 28.2 nm[35], due to the extended backbone conformation. Long-range correlations of the backbones have been observed in other high-performance polymers such as poly{[N,N′- bis(2-octyldodecyl)-naphthalene-1,4,5,8-bis(dicarboximide)- 2,6-diyl]-alt-5,5′-(2,2′-bithiophene)} (P(NDI2OD-T2))[36]. Polymer chain and domain alignment over large length scales has been correlated with improved optical and electronic properties[9], [37]–[39].

3.4.2 HRTEM to Study BHJs

Bright-field TEM is often used to study the macroscale phase separation in BHJs by taking advantage of the contrast generated by a difference in density between most donor polymers and fullerene-based acceptors[40]. However, in the study of non-fullerene acceptors where the density differences are minimal, HRTEM can also be used to identify the location of each phase from the distinct periodic lattice fringes[29]. A understanding of the molecular stacking distances for each material can be gained through X-ray scattering or electron diffraction of neat films of the donor and acceptor.

3.4.2.1 Large Crystalline Domains in Small-molecule Acceptor Film

Small-molecules acceptors are a growing area in OPV research due to the high synthetic flexibility[41]–[43]. The "bulkiness" of the chemical structure will have a large effect on the crystallization behavior. For example, nonplanar or twisted structures can frustrate molecular packing and lead to a glassier morphology[44], [45]. On the other hand, linear molecular structures have been shown for form large crystalline regions [46]. Here, the small-molecule being examined is HPI-BT, which is utilized as an acceptor material in BHJs. The film is a blend with the polymer P3HT, however, extensive phase separation leads to areas that are donor and acceptor rich. Figure 3-6 shows a region where only HPI-BT crystallites are present. Large crystalline domains form that are approximately 80-250 (~60-190 layers) nm wide and 70-300 nm long. A large degree of arcing is observed in the peaks in the power spectrum due to a slight bend in the crystallites over distances of 10s of nm. This has been observed in HRTEM studies of liquid crystalline polymers[47]. In contrast to the polymer DPPT-TT which also shows extended regions of order, only small fluctuations in the d-spacing are observed for HPI-BT. The shape of the HPI-BT molecule
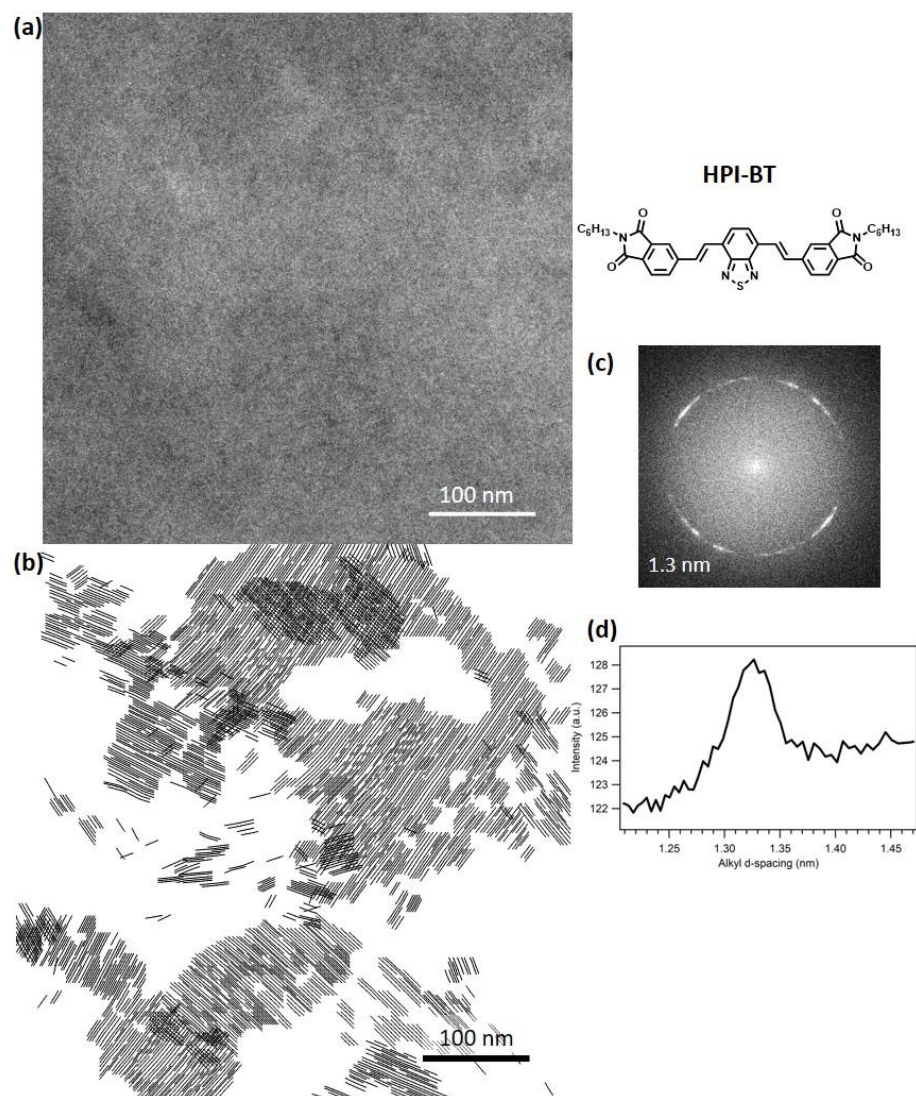
Figure 3-6. HPI-BT (a) HRTEM image and (b) reconstructed line-drawing of the periodic lattice fringes within crystalline domains, (c) power spectrum, and (d) lD plot of the radially integrated FFT intensity.

resembles that of a banana-shaped liquid crystal, which has been shown to enable a close packing of molecules [48]. The film is approximately 100 nm thick and therefore it is difficult to comment on the grain boundary structure. In thicker films, the resulting image is a projection of the structure through the entire thickness, however, processing conditions were kept identical to those for device fabrication to ensure consistency.

3.4.2.2   P3HT Forms Small Discrete Crystallites

Examination of the P3HT (donor) phase of the BHJ film is possible due to the difference in the in-plane *d*-spacings for each material. While the predominant in-plane stacking distance for HPI-BT is 1.3nm, the alkyl stacking distance of P3HT is 1.6 nm. The resolution of the microscope is approximately 1 Å and therefore the phases can be differentiated. A P3HT rich region is shown in Figure 3-7. An FFT of the image indicates that both materials (1.6 nm (P3HT), 1.3 nm (HPI-BT)). However, in this image only discrete crystallites of P3HT can be clearly observed due the lower resolution from the specific camera settings used (this enabled
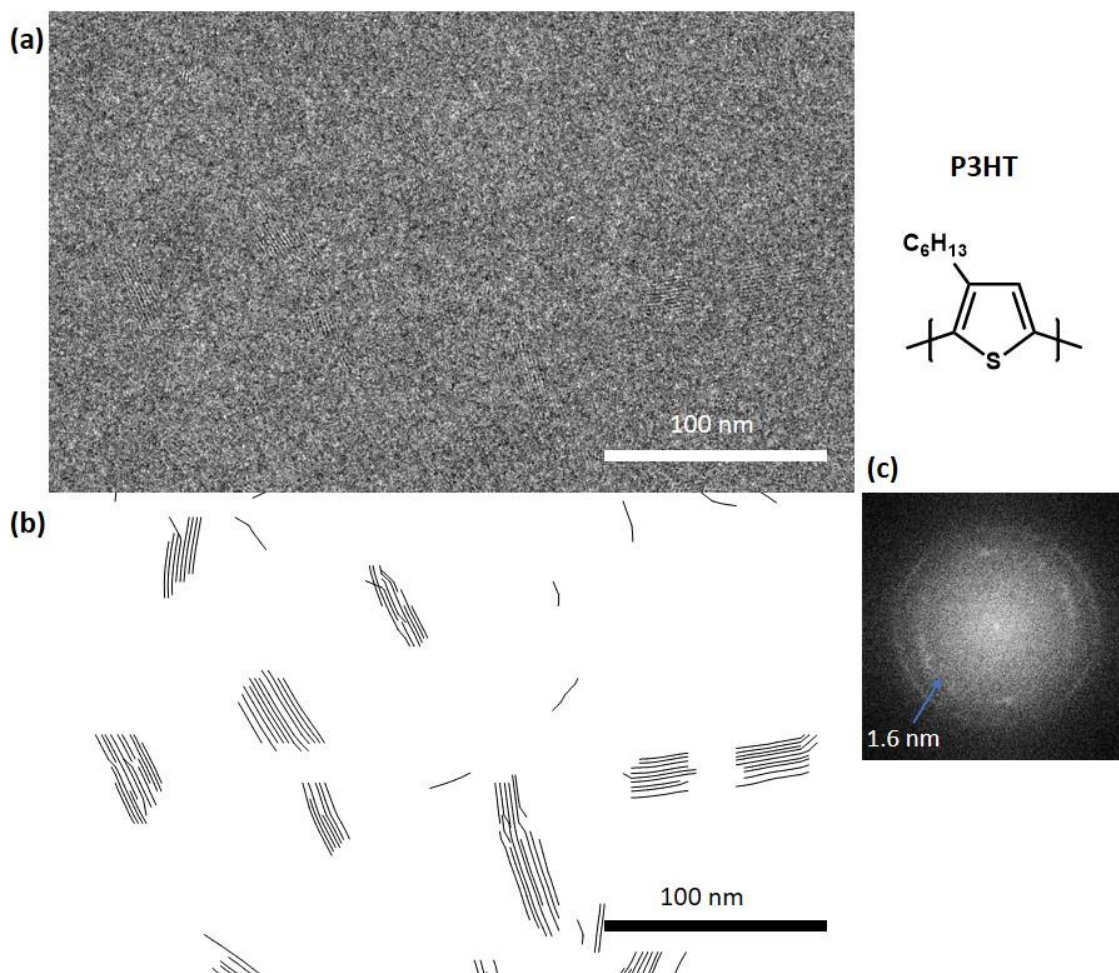
Figure 3-7. (a) HRTEM image of P3HT crystalline region, (b) line-drawing, and (c) FFT showing 1.6 nm peak from the crystallites in the image.

the use of shorter exposure times to minimize sample damage). P3HT forms small fiber-like crystallites that are approximately 20 nm wide (12 alkyl stacked chains) and 30-60 nm long. Small gaps of 10-15 nm can be observed between crystallites oriented in nominally the same direction. It is unclear whether these regions represent a single crystallite or two isolated crystallites. For the case of the single crystallite, it is possible that the region in the center is oriented slight out-of-plane such that the incoming electron beam is no longer parallel with the periodic spacing (see Section 2.11). P3HT behaves as a worm-like chain, and therefore backbone bending is possible over distances greater than the persistence length (3 nm) [35]. Additionally, two discrete crystallites could be connected by tie-chains which bridge the crystallites. Here, the P3HT has a molecular weight between 20 and 40 kDa. For a monomer unit length of approximately 0.40 nm, this corresponds to estimated chain lengths between 50 and 100 nm. Therefore, it is possible that the ordered domains are connected by tie-chains. Both scenarios are plausible, but it is not possible to determine from HRTEM alone. Although for the purposes of charge percolation, it has been suggested that the tie-chains model is most successful when the crystallite separation distance is on the order of the persistence length [49]. Overall, there is a large difference in the size, shape, and organization of the donor and acceptor crystallites. A HRTEM study of the BHJ enables an understanding of the crystalline domain size for each material which is an important parameter in OPVs[50].

3.4.2.3 Not Always Possible to Distinguish Between Phases by *d*-spacing Alone

Distinguishing between phases based on the *d*-spacing is not always possible as many materials share similar stacking distances and patterns of molecular organization. HRTEM of a BHJ containing the donor polymer P3HT and the small-molecule FBR [30] show small crystallites which are 10-20 nm wide and 30-100 nm long, however, the two phases are
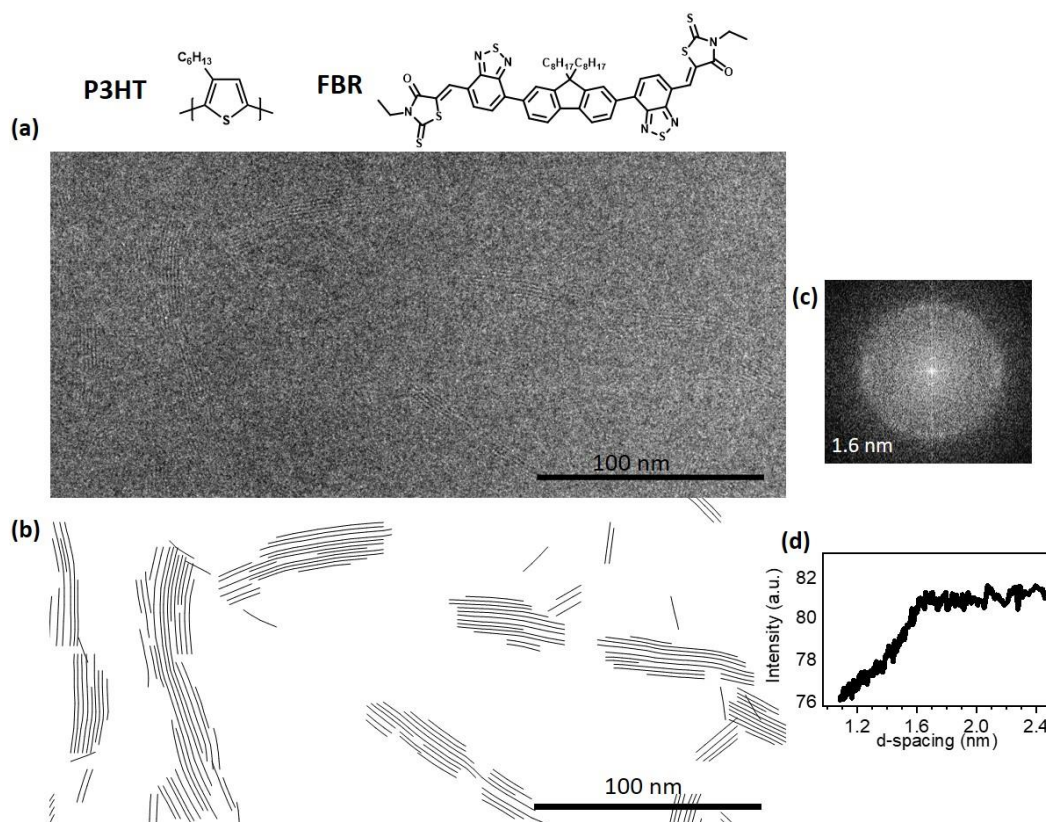
Figure 3-8. P3HT:FBR BHJ (a) HRTEM image, (b) line-drawing, (c) FFT, and (d) radial integration of FFT intensity showing the distribution in *d*-spacing.

indistinguishable (Figure 3-8). This is because both materials have an in-plane diffraction peak corresponding to the stacking distance of around 1.6 nm. In this case, HRTEM is not a good technique to use to understand the phase separation. Instead, energy filtered TEM could be used to identify each material due to the different elements present in each[51], [52]. For example, FBR contains both nitrogen and oxygen and this will generate contrast between the donor and acceptor phases.

3.4.3 Crystallite Connectivity

In a HRTEM image, while it is useful to qualitatively locate crystalline regions, it is more useful to quantify those regions with parameters that can be used to assess their detailed local structure and connectivity, such as crystallite *d*-spacings and orientational distribution.
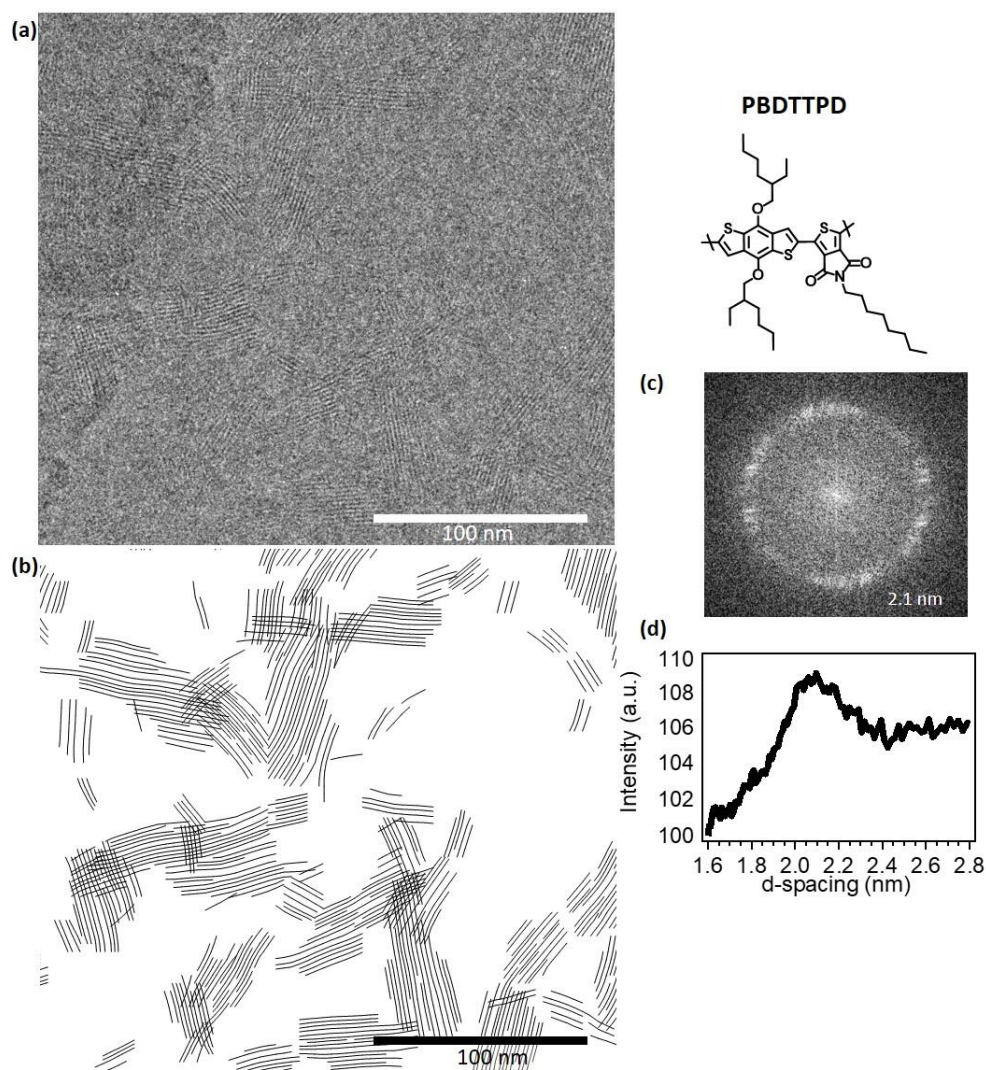
Figure 3-9. PBDTTPD (a) HRTEM image and (b) reconstructed line-drawing of the periodic lattice fringes within crystalline domains, (c) power spectrum, and (d) 1D profile of the FFT radially integrated intensity.

Frequently, grain boundaries in semiconducting polymers are mostly understood in terms of tie-chains, but more ordered structures have been observed[23]. The polymer PBDTTPD (EH/C8 derivative) is observed to form similarly sized crystalline domains to P3HT but with very different connectivity at the grain boundaries. Here, we show evidence of highly ordered high-angle grain boundaries forming between PBDTTPD crystallites through the overlap of adjacent crystallites at a preferred angle.
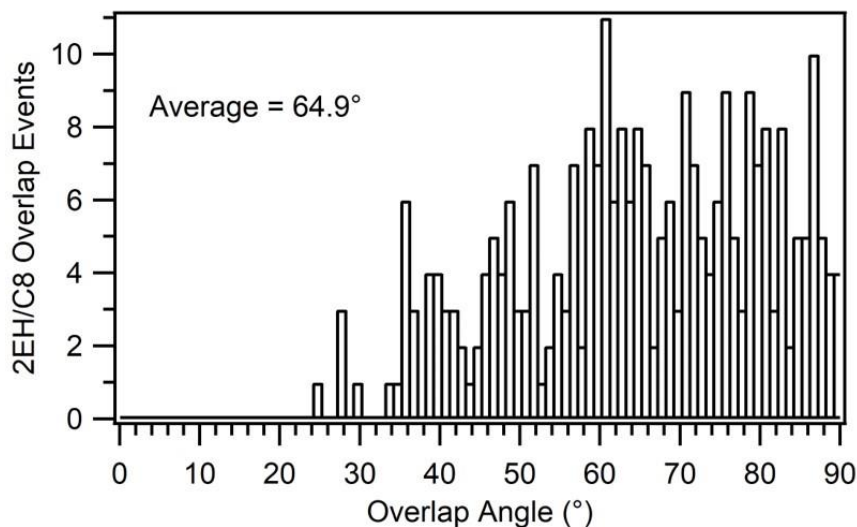
Figure 3-10. Histogram of the crystallite crossing angles for PBDTTPD.

Very thin films of PBDTTPD were prepared (~10-15 nm) so that they were only a few crystallites thick and the grain boundary structure could be studied. PBDTTPD has a predominantly face-on texture, which means that the alkyl stacking occurs in the plane of the substrate (Figure 3-9). The periodicity of this feature is approximately 2 nm and can be easily viewed with HRTEM.

A relationship was developed by Takacs et al.[23] to describe the geometry of the overlap between two adjacent crystallites:

$$\sin\theta = \frac{d}{b}$$

where θ is the angle of offset between the backbones in each crystallite, d is the alkyl spacing for the material, and b is the repeat unit length. Here, an area of approximately 30 μm^2 was manually examined using ImageJ and regions showing crystallite overlap were Fourier transformed to determine the crossing angle. PBDTTPD shows an average overlap angle of 64.9°, but a range of angles is observed (Figure 3-10). It is likely that the statistics will continue to improve as larger areas are examined.

3.4.4   Image Defect Structure with HRTEM

The origin of disorder is debated semiconducting polymer thin films. Paracrystallinity, or the gradual loss in molecular stacking correlations over a certain distance, is the widely accepted explanation for the loss higher reflections in diffraction experiments[18]. However, a high density of defects and dislocations will also result in the loss of higher order reflections. Defects in the crystalline packing of polymers and small-molecules can be imaged with
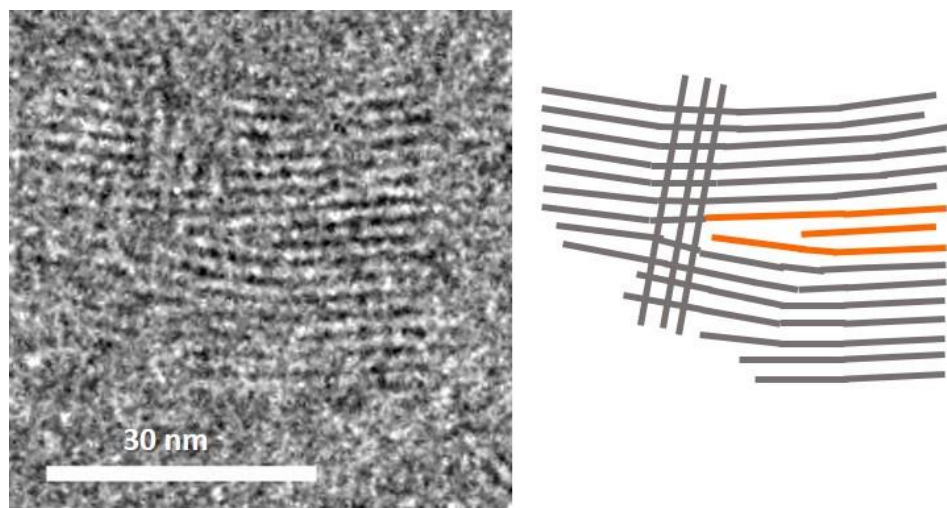
Figure 3-11. Edge dislocation within a polymer crystallite.

HRTEM. Point (0-D), line (1-D), and planar (2-D) defects all occur in crystalline polymers and they are easily studied through direct imaging [53]. Edge dislocations were observed in the smectic layer packing of a polymalonate and azobenzene-based liquid crystalline polymer using HRTEM [54]. While the smectic layers were relatively straight before the dislocation, a distortion of the structure resulted from the addition of the extra layers. Additionally, HRTEM was used to examine defects in the grain boundary structure of the crystalline and liquid crystalline phases of a hexakis(heptyloxy)triphenylene polymer [55]. Here, defects are also observed in the donor-acceptor copolymer, PBDTTPD. Figure 3-11 shows an edge dislocation in a PBDTTPD thin film. A distortion can be observed in the molecular packing

due to the addition of the extra chain. The density of edge dislocations in the film likely scales with the polydispersity. For a large distribution in the molecular weight, a distribution of chain lengths will be present and will lead to dislocations when chains of varying length form a crystallite. Here, PBDDTPD has a number-average molecular weight of 17.6 kDa and weight average molecular weight of 55.5 kDa (polydispersity = 3.2). This will result in an average range of the chain length between 30-100 nm. While DFT calculations of the PBDTTPD backbone showed a mostly planar conformation, a high number of edge dislocations may enable the crystallites to bend over larger distances.

3.5 Outlook

HRTEM can be used for direct visualization of grain boundaries and defects in semiconducting polymers and small-molecules. Due to software advancements enabling fast automated collection of images, it is possible to collect large quantities of high-resolution data over the length scales that are relevant for transport in organic electronic devices (10s to 100s of µm). However, analysis methods need to be improved to keep up with the large datasets that can easily be acquired. A user-friendly program, GRATE (GRaph based Analysis of
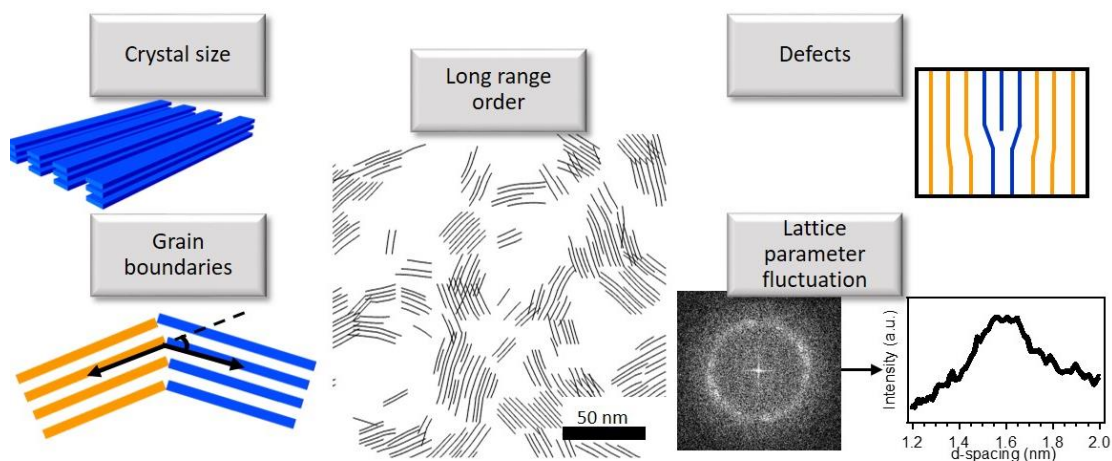
Figure 3-12. Summary of HRTEM and GRATE capabilities

Transmission Electron microscopy images), is being developed in collaboration with Baskar Ganapathysubramanian's group at Iowa State University to extend HRTEM image analysis capabilities and enable the long-range study of grain boundaries and connectivity in polymers and small-molecules. While many studies using HRTEM rely on manual interpretation of images, we are developing a framework for analysis that can be tailored for specific features encountered in the study of ordered semiconducting polymers. Quantitative information about crystallite ordering will be extracted including the spatial arrangement of ordered domains, domain orientation, local fluctuation in d-spacing, and angle of misorientation between grains.

3.5.1   There is a Need for Improved Computational Power

Large quantities of high resolution TEM data can be easily acquired with software for automated data collection and ultrafast CCD cameras. However, this often leads to a bottleneck with data analysis. Robust computational methods are needed to streamline the analysis of large image sets, thereby increasing the amount of sample area that can be studied without sacrificing resolution.

Computational power has been improving recently with programs to analyze orientational correlations in images from high resolution bright-field TEM[23], STEM nanobeam diffraction[56], and AFM[57]. Panova et. al. used STEM nanobeam diffraction to map out the orientation of P3HT domains over areas of up to 1 micron with a resolution of 20 nm[56]. Additionally, Persson et. al. developed a MATLAB-based program to analyze AFM images of materials with fiber-like morphologies and generate a fiber orientation map[57]. However, there is a lack of user-friendly programs to analyze HRTEM images.

3.5.2 Utilize GRATE for Analysis of High-resolution TEM Images

GRATE utilizes both image processing filters and fast Fourier-transforms (FFT) to construct line drawings of HRTEM images. Line-drawings provide a qualitative understanding of molecular organization and determination of grain size. Additional decomposition of the image through FFT allow for quantification of d-spacing, grain boundaries orientation and lattice parameter fluctuation. GRATE will provide high throughput analysis of data sets covering 10s of microns with nanometer-scale resolution. The goal in the development of GRATE is to compile common analysis methods into a single user-friendly program to make HRTEM characterization of sample structure more accessible.

The program has a modular design that enables the user to decide the type of analysis that is performed. The two main modules operate independently and include a contrast-based line-drawing and large-scale FFT-based image decomposition. Each requires varying degrees of user input, but built-in functions complete the bulk of the analysis.
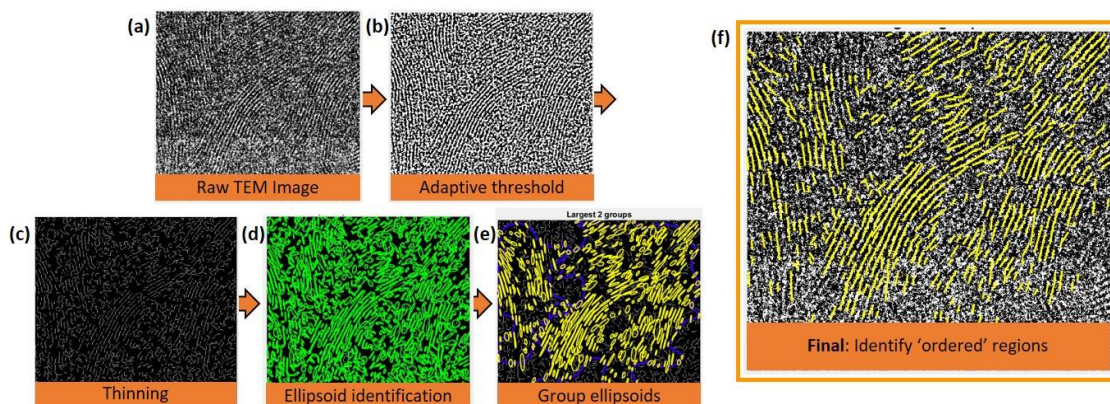
Figure 3-13. Step-by-step output of line-drawing module. Starting with the (a) raw TEM image, (b) adaptive threshold, (c) thinning or skeletonization, (d) ellipsoid identification, (e) ellipsoid group, and (f) final identification of ordered regions in TEM image through line drawing.

In order to understand how the nanometer scale order changes over tens to hundreds of micrometers, HRTEM must be converted into an easier to visualize format. This enables one

to make qualitative observations about the structure such as liquid crystalline-type ordering, isotropic orientation of discrete crystals, etc. This is accomplished with 2 different modules within GRATE. The first module converts the raw images into a set of line-drawings of the lattice fringes present by taking advantage of the contrast present in the image (Figure 3-13).

3.5.2.1 Fourier Transform-based Image Decomposition
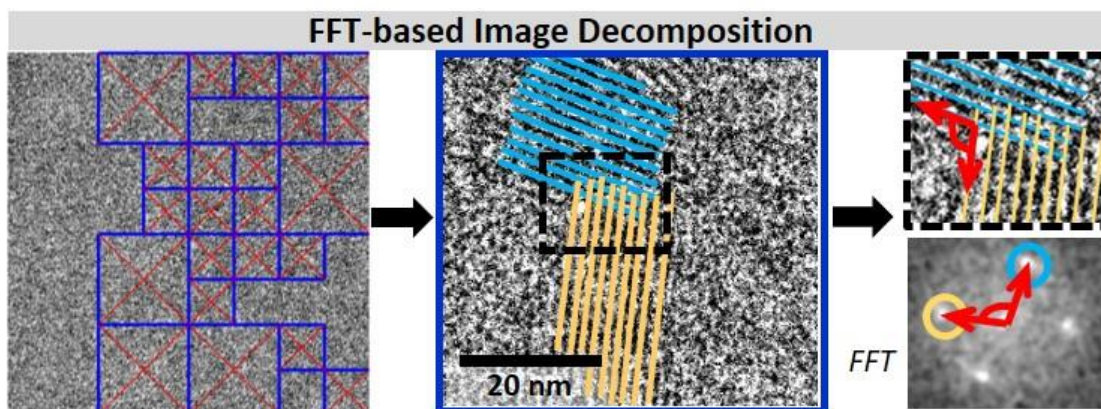
Figure 3-14. Diagram illustrating the basic processed in the FFT-based image decomposition.

The second module uses FFTs to analyze regions of order. GRATE uses an algorithm called quad-tree decomposition to successively reduce the size of sub-image that is analyzed. The general procedure is illustrated in Figure 3-14. The image is halved in size (i.e. made into 4 equal sub-images) until a termination criterion is reached. The smallest sub-image that will be analyzed can be understood in terms of the lower limit on the average crystallite size:

$$\text{sub image size}_{\text{termination value}} = 4d$$

where d, is the average d-spacing present in the image. The final product is a plotted line-drawing along with identified lattice spacings, orientations, and crystallite crossing angles.

3.6 Conclusions

HRTEM can be used to investigate the inter- and intracrystallite ordering in semicrystalline polymers and small-molecules. An FFT-based MATLAB program is being developed to analyze TEM images of crystalline domains to produce line drawings depicting the backbone structure and determine local order and connectivity information. The ultimate goal is to have information on the local correlations and nanometer scale order over length scales relevant for charge transport and device operation. In the future, GRATE connectivity maps could be used as inputs into transport simulations to understand the effect of certain morphologies on the charge carrier mobilities.

References

[1]   J. Rivnay, S. C. B. Mannsfeld, C. E. Miller, A. Salleo, and M. F. Toney, "Quantitative determination of organic semiconductor microstructure from the molecular to device scale," *Chem. Rev.*, vol. 112, no. 10, pp. 5488–5519, Oct. 2012.

[2]   V. Coropceanu, J. Cornil, D. A. da Silva Filho, Y. Olivier, R. Silbey, and J.-L. Bredas, "Charge Transport in Organic Semiconductors," *Chem. Rev.*, vol. 107, pp. 926–952, 2007.

[3]   A. Salleo, "Charge transport in polymeric transistors," *Mater. Today*, vol. 10, no. 3, pp. 38–45, 2007.

[4]   D. S. Pearson, P. A. Pincus, G. W. Heffner, and S. J. Dahman, "Effect of Molecular Weight and Orientation on the Conductivity of Conjugated Polymers," *Macromolecules*, vol. 26, no. 7, pp. 1570–1575, 1993.

[5]   H. N. Tsao and K. Müllen, "Improving polymer transistor performance via morphology control," *Chem. Soc. Rev.*, vol. 39, no. 7, p. 2372, 2010.

[6]   L. H. Jimison, M. F. Toney, I. McCulloch, M. Heeney, and A. Salleo, "Charge-Transport Anisotropy Due to Grain Boundaries in Directionally Crystallized Thin Films of Regioregular Poly(3-hexylthiophene)," *Adv. Mater.*, vol. 21, no. 16, pp. 1568–1572, 2009.

[7]   H. A. Becerril, M. E. Roberts, Z. Liu, J. Locklin, and Z. Bao, "High-performance organic thin-film transistors through solution-sheared deposition of small-molecule organic semiconductors," *Adv. Mater.*, vol. 20, no. 13, pp. 2588–2594, 2008.

[8]   R. L. Headrick, S. Wo, F. Sansoz, and J. E. Anthony, "Anisotropic mobility in large grain size solution processed organic semiconductor thin films," *Appl. Phys. Lett.*, vol. 92, no. 6, 2008.

[9]   H. Sirringhaus *et al.*, "Mobility enhancement in conjugated polymer field-effect transistors through chain alignment in a liquid-crystalline phase," *Appl. Phys. Lett.*, vol. 77, no. 3, pp. 406–408, 2000.

[10]   H. Heil, T. Finnberg, N. Von Malm, R. Schmechel, and H. Von Seggern, "The influence of mechanical rubbing on the field-effect mobility in polyhexylthiophene," *J. Appl. Phys.*, vol. 93, no. 3, pp. 1636–1641, 2003.

[11]   H. Tseng *et al.*, "High-Mobility Field-Effect Transistors Fabricated with Macroscopic Aligned Semiconducting Polymers," pp. 2993–2998, 2014.

[12]   W. Pisula *et al.*, "A zone-casting technique for device fabrication of field-effect transistors based on discotic hexa-perihexabenzocoronene," *Adv. Mater.*, vol. 17, no. 6, pp. 684–688, 2005.

[13]   R. J. Kline, M. D. McGehee, E. N. Kadnikova, J. Liu, and J. M. J. Fréchet, "Controlling the field-effect mobility of regioregular polythiophene by changing the molecular weight," *Adv. Mater.*, vol. 15, no. 18, pp. 1519–1522, 2003.

[14]   R. J. Kline, M. D. McGehee, E. N. Kadnikova, J. Liu, J. M. J. Fréchet, and M. F.

Toney, "Dependence of regioregular poly(3-hexylthiophene) film morphology and field-effect mobility on molecular weight," *Macromolecules*, vol. 38, no. 8, pp. 3312–3319, 2005.

[15]   R. Joseph Kline, M. D. McGehee, and M. F. Toney, "Highly oriented crystals at the buried interface in polythiophene thin-film transistors," *Nat. Mater.*, vol. 5, no. 3, pp. 222–228, Feb. 2006.

[16]   R. Noriega, A. Salleo, and A. J. Spakowitz, "Chain conformations dictate multiscale charge transport phenomena in disordered semiconducting polymers.," *Proc. Natl. Acad. Sci. U. S. A.*, vol. 110, no. 41, pp. 16315–20, Oct. 2013.

[17]   R. A. Street, J. E. Northrup, and A. Salleo, "Transport in polycrystalline polymer thin-film transistors," *Phys. Rev. B - Condens. Matter Mater. Phys.*, vol. 71, no. 16, pp. 1–13, 2005.

[18]   R. Noriega *et al.*, "A general relationship between disorder, aggregation and charge transport in conjugated polymers.," *Nat. Mater.*, vol. 12, no. 11, pp. 1038–44, Nov. 2013.

[19]   W. Zhang *et al.*, "Indacenodithiophene semiconducting polymers for high-performance, air-stable transistors," *J. Am. Chem. Soc.*, vol. 132, no. 33, pp. 11437–11439, 2010.

[20]   D. Venkateshvaran *et al.*, "Approaching disorder-free transport in high-mobility conjugated polymers," *Nature*, vol. 515, no. 7527, pp. 384–388, Nov. 2014.

[21]   M. Bevis, "Chain-axis invariant and chain-axis rotation twins in polymer crystals," *Colloid Polym. Sci. Kolloid-Zeitschrift Zeitschrift f??r Polym.*, vol. 256, no. 3, pp. 234–240, 1978.

[22]   D. C. Martin and Thomas, "Grain boundaries in extended-chain polymers Theory and Experiment," *Philos. Mag. A*, vol. 64, pp. 903–922, 1991.

[23]   C. J. Takacs, M. a Brady, N. D. Treat, E. J. Kramer, and M. L. Chabinyc, "Quadrites and crossed-chain crystal structures in polymer semiconductors.," *Nano Lett.*, vol. 14, no. 6, pp. 3096–101, Jun. 2014.

[24]   G. L. Schulz *et al.*, "The PCPDTBT Family: Correlations between Chemical Structure, Polymorphism, and Device Performance," *Macromolecules*, vol. 50, no. 4, pp. 1402–1414, 2017.

[25]   K. Kobayashi and K. Sakaoku, "The Changes of Polymer Crystals due to Irradiation with Electrons Accelerated at Various Voltages," *Bull. Inst. Chem. Res. Kyoto Univ.*, vol. 42, no. 6, pp. 473–493, 1965.

[26]   D. T. Grubb, "Radiation damage and electron microscopy of organic polymers," *J. Mater. Sci.*, vol. 9, no. 10, pp. 1715–1736, 1974.

[27]   R. F. Egerton, "Control of radiation damage in the TEM," *Ultramicroscopy*, vol. 127, pp. 100–108, 2013.

[28]   J. T. Bloking *et al.*, "Solution-Processed Organic Solar Cells with Power Conversion Efficiencies of 2.5% using Benzothiadiazole/Imide-Based Acceptors," *Chem. Mater.*,

vol. 23, no. 24, pp. 5484–5490, 2011.

[29] K. A. O'Hara *et al.*, "Role of Crystallization in the Morphology of Polymer:Non-fullerene Acceptor Bulk Heterojunctions," *ACS Appl. Mater. Interfaces*, vol. 9, no. 22, pp. 19021–19029, 2017.

[30] S. Holliday *et al.*, "A rhodanine flanked nonfullerene acceptor for solution-processed organic photovoltaics.," *J. Am. Chem. Soc.*, vol. 137, no. 2, pp. 898–904, Jan. 2015.

[31] Z. Chen *et al.*, "High-performance ambipolar diketopyrrolopyrrole-thieno[3,2-b]thiophene copolymer field-effect transistors with balanced hole and electron mobilities," *Adv. Mater.*, vol. 24, no. 5, pp. 647–652, 2012.

[32] A. El Labban *et al.*, "Dependence of Crystallite Formation and Preferential Backbone Orientations on the Side Chain Pattern in PBDTTPD Polymers," *ACS Appl. Mater. Interfaces*, vol. 6, no. 22, pp. 19477–19481, Nov. 2014.

[33] X. Zhang, S. D. Hudson, D. M. Delongchamp, D. J. Gundlach, M. Heeney, and I. McCulloch, "In-plane liquid crystalline texture of high-performance thienothiophene copolymer thin films," *Adv. Funct. Mater.*, vol. 20, no. 23, pp. 4098–4106, 2010.

[34] C. Gutt, L. Grodd, E. Mikayelyan, U. Pietsch, R. J. Kline, and S. Grigorian, "Local orientational structure of a P3HT π-π Conjugated network investigated by X-ray nanodiffraction," *J. Phys. Chem. Lett.*, vol. 5, no. 13, pp. 2335–2339, 2014.

[35] B. Kuei and E. D. Gomez, "Chain conformations and phase behavior of conjugated polymers," *Soft Matter*, vol. 114, pp. 10087–10088, 2016.

[36] C. J. Takacs *et al.*, "Remarkable Order of a High-Performance Polymer," *Nano Lett.*, 2013.

[37] M. Grell, D. D. C. Bradley, M. Inbasekaran, and E. P. Woo, "A glass-forming conjugated main-chain liquid crystal polymer for polarized electroluminescence applications," *Adv. Mater.*, vol. 9, no. 10, pp. 798–802, 1997.

[38] M. Redecker, D. D. C. Bradley, M. Inbasekaran, and E. P. Woo, "Mobility enhancement through homogeneous nematic alignment of a liquid-crystalline polyfluorene," *Appl. Phys. Lett.*, vol. 74, no. 10, pp. 1400–1402, 1999.

[39] I. McCulloch *et al.*, "Liquid-crystalline semiconducting polymers with high charge-carrier mobility.," *Nat. Mater.*, vol. 5, pp. 328–333, 2006.

[40] J. a. Bartelt *et al.*, "Controlling Solution-Phase Polymer Aggregation with Molecular Weight and Solvent Additives to Optimize Polymer-Fullerene Bulk Heterojunction Solar Cells," *Adv. Energy Mater.*, vol. 4, no. 9, Jun. 2014.

[41] Y. Lin, Y. Li, and X. Zhan, "Small molecule semiconductors for high-efficiency organic photovoltaics," *Chem. Soc. Rev.*, vol. 41, no. 11, p. 4245, Jun. 2012.

[42] J. Roncali, P. Leriche, and P. Blanchard, "Molecular materials for organic photovoltaics: small is beautiful.," *Adv. Mater.*, vol. 26, no. 23, pp. 3821–38, Jun. 2014.

[43] A. Mishra and P. Bäuerle, "Small molecule organic semiconductors on the move: promises for future solar energy technology.," *Angew. Chem. Int. Ed. Engl.*, vol. 51,

no. 9, pp. 2020–2067, Feb. 2012.

[44] Y. Lin, P. Cheng, Y. Li, and X. Zhan, "A 3D star-shaped non-fullerene acceptor for solution-processed organic solar cells with a high open-circuit voltage of 1.18 V," *Chem. Commun.*, vol. 48, no. 39, pp. 4773–4775, 2012.

[45] J. Lee, R. Singh, D. H. Sin, H. G. Kim, K. C. Song, and K. Cho, "A Nonfullerene Small Molecule Acceptor with 3D Interlocking Geometry Enabling Efficient Organic Solar Cells," *Adv. Mater.*, vol. 28, no. 1, pp. 69–76, 2016.

[46] S. Rajaram, R. Shivanna, S. K. Kandappa, and K. S. Narayan, "Nonplanar perylene diimides as potential alternatives to fullerenes in organic solar cells," *J. Phys. Chem. Lett.*, vol. 3, no. 17, pp. 2405–2408, 2012.

[47] I. G. Voigt-Martin, H. Durst, B. Reck, and H. Ringsdorf, "Structure Analysis of a Combined Main-Chain / Side-Group Liquid Crystalline Polymer by Electron Microscopy," *Society*, vol. 21, pp. 1620–1626, 1988.

[48] M. B. Ros, J. L. Serrano, M. R. de la Fuente, and C. L. Folcia, "Banana-shaped liquid crystals: a new field to explore," *J. Mater. Chem.*, vol. 15, no. 48, p. 5093, 2005.

[49] D. T. Duong *et al.*, "Mechanism of crystallization and implications for charge transport in poly(3-ethylhexylthiophene) thin films," *Adv. Funct. Mater.*, vol. 24, no. 28, pp. 4515–4521, 2014.

[50] A. J. Heeger, "25th anniversary article: Bulk heterojunction solar cells: Understanding the mechanism of operation," *Adv. Mater.*, vol. 26, no. 1, pp. 10–28, 2014.

[51] M. Pfannmöller, H. Flügge, G. Benner, I. Wacker, W. Kowalsky, and R. R. Schröder, "Visualizing photovoltaic nanostructures with high-resolution analytical electron microscopy reveals material phases in bulk heterojunctions," *Synth. Met.*, vol. 161, no. 23–24, pp. 2526–2533, Jan. 2012.

[52] L. A. Perez *et al.*, "The Role of Solvent Additive Processing in High Performance Small Molecule Solar Cells," *Chem. Mater.*, vol. 26, no. 22, pp. 6531–6541, 2014.

[53] D. C. Martin and E. L. Thomas, "Observation of Defects in Crystalline Polymers by HREM," *MRS Bull.*, vol. 12, no. 8, pp. 27–35, 1987.

[54] I. G. Voigt-Martin and H. Durst, "High-Resolution Images of Defects in Liquid Crystalline Polymers in the Smectic and Crystalline Phases," *Macromolecules*, vol. 22, pp. 168–173, 1989.

[55] I. G. Voigt-Martin, R. W. Garbella, and M. Schumacher, "Structure and defects in discotic crystals and liquid crystals as revealed by electron diffraction and high-resolution electron microscopy," *Macromolecules*, vol. 25, pp. 961–971, 1992.

[56] O. Panova *et al.*, "Orientation mapping of semicrystalline polymers using scanning electron nanobeam diffraction," *Micron*, vol. 88, pp. 30–36, 2016.

[57] N. E. Persson, M. A. McBride, M. A. Grover, and E. Reichmanis, "Automated Analysis of Orientational Order in Images of Fibrillar Materials," *Chem. Mater.*, p. acs.chemmater.6b01825, 2016.

[58]   H. Sirringhaus, "Device physics of solution-processed organic field-effect transistors," *Adv. Mater.*, vol. 17, no. 20, pp. 2411–2425, 2005.

Chapter 4

The Effect of the Alkyl Side-chains on Intercrystallite Ordering in Semiconducting Polymers

4.1 Introduction

Organic electronic devices such as bulk-heterojunction (BHJ) solar cells and thin-film transistors (OTFTs) often utilize semiconducting polymers. Charge transport within thin films of semiconducting polymers heavily relies on the nanoscale organization of polymers to ensure electronic coupling through overlap of molecular orbitals and to provide continuous transport pathways[1], [2]. On a molecular level, the two fastest transport directions for polymers are the intermolecular direction along the backbone and between molecules when the conjugated planes overlap. Because of these issues, understanding how the long-range morphology connects to local order is critical to develop structure property relationships.

Thiophene-based polymers frequently exhibit lamellar packing where their semiconducting π-conjugated backbones arrange into parallel closely packed stacks separated by the insulating alkyl side-chains [3]–[6]. Because of this structure, the molecular orientation relative to the transport direction has been shown to affect transport properties. It was suggested in early reports on poly(3-hexylthiophene) (P3HT) that for efficient in-plane charge transport in organic thin film transistors (OTFs), the backbone should be aligned parallel with the substrate in an edge-on configuration [3]. However, subsequent studies have achieved high charge carrier mobilities for chains in the face-on orientation as well [7]–[9].

There are many open questions in the field pertaining to both the factors influencing crystallite orientation as well as crystallite connectivity on the nanoscale. While there is a large focus in the on the design of new materials[10], there is less of an understanding of

intracrystallite ordering. Both will have a large influence on the electronic properties and require further study. Much of the understanding of the processing strategies and resulting morphologies in semiconducting polymers comes from studies of semiflexible polymers such as P3HT. However, the numerous donor-acceptor copolymers being developed for OPVs and OTFTs typically have much larger and bulkier monomer units, which can lead to a more extended backbone structure[11]. As the molecular structures become more complex, it is expected that the morphology will also vary. Detailed studies of the crystallite connectivity enable a greater understanding of the connection between the chemical structure and thin film organization.

4.1.1 Transport Sensitive to Grain Boundary Structure

Due to the small average grain (domain) size in many semiconducting polymers (~30-50 nm), the connectivity of ordered and disordered domains will also dictate the electrical properties. While the connection between charge transport and molecular alignment has been extensively studied mainly in transistors[12]–[16], there are considerably less studies on the detailed connectivity of ordered domains in polymers. Both vertical and lateral charge transport in semiconducting polymers relies on the connectivity of the polymer chains in three dimensions beyond the alignment of domains parallel to this main transport direction.

Gaining detailed information about the structure of grain boundaries in semiconducting polymers is difficult due to their inherent structural disorder. Therefore, the effect of structure and processing changes on grain boundaries is often inferred from transport measurements and modeling [17], [18]. For example, tie-chains have been cited as the main way to transport charge between domains in polymers such as P3HT, inferred by the improvement in carrier mobility by increasing the molecular weight[19], [20]. Additionally, transport measurements

parallel and perpendicular to aligned grain structures have led to the conclusion that electrical properties suffer as the angle of misorientation between adjacent grains increases [21]. However, direct imaging methods will be required to fully understand the complexities of molecular arrangement on the nanoscale.

High resolution transmission electron microscopy (HRTEM) is a powerful tool for directly imaging the crystalline grain boundaries in polymer and small-molecule thin films [22]. Recently, structures comparable to quadrites were discovered in the semiconducting polymer, Si-PCPDTBT [23]. It was observed that the backbones of the polymer in ordered domains tend to overlap at a preferred angle of ~52°. This quasi-epitaxial relationship is driven by the geometry molecular arrangement through the polymer repeat unit length, b, and alkyl stacking distance, d. The ratio of these two parameters is a major factor which determines the angle, θ, at which the chains will cross through the following equation:

$$\sin \theta = b/d$$

Therefore, the formation of such cross-chain structures is highly dependent on the nature of the alkyl side-chains. A cross-hatched morphology in PBSTBT was also confirmed by Schulz et al., but the origin of the structure is not fully understood[24]. Possible explanations include defects (twinning) and aggregation in solution prior to solidification. Nonparallel chain packing and homoepitaxy has been observed in other rigid-rod systems such as isotactic polypropylene (iPP)[25]–[29], poly(parapheny1ene benzobisoxazole) (PBZO) [22], and pyromellitic dianhydrideoxydianiline (PMD A-ODA) poly(imide) [30]. The benefit of cross-chain structures in polymers such as iPP was to enhance the mechanical properties, but in semiconducting polymers, it may enable 3D transport through connected grains. Sterics and

geometrical relationships drive the formation of such structures and therefore the nature of the side-chains is likely to have a large effect on how the backbones assemble.

4.1.2   Role of Side-chains in Determining Microstructure

It is known that strong π-π interactions between the conjugated backbones are required for efficient charge transport properties [31], [10], [32], however, aliphatic side-chains are necessary to increase the solubility and improve the ease of purification and device fabrication. While the single bonded carbon chains are insulating and thus do not serve as charge transport pathways, they can have a large effect on the nanoscale structure which effects the electronic processes. Alkyl side-chains, both linear and branched, are the most commonly used, but there are many other variations [33], [34]. The length and placement of linear side-chains can lead to closer packing of the main chain through interdigitation [35], [36], but branched chains are generally too bulky for this to occur. The backbones have a separation of > 1 nm in the direction of the alkyl stacking, and therefore a more interdigitated structure does not increase electronic coupling along the a-axis. However, the side-chains will also affect the self-assembly and crystallization. The side-chain density has been correlated with the film texture in diketo pyrrolo-pyrrole (DPP)-bithiophene copolymers where a higher density promotes a more face-on orientation of the crystallites [37]. Several studies have aimed to determine the relationship between side-chain length and field-effect mobility for poly(3-alkylthiophenes) (P3AT)-based field-effect transistors (FETs) [38], [39]. However, inferences about morphology and transport can vary between studies as there are many other factors to consider including processing conditions, differences in molecular weight. For example, changing the side-chains will affect how the material responds to processing

methods because both order-to-disorder transition temperatures [39] and solubility will be affected.

The type of side-chain has been shown to have an effect on the electrical properties of bulk heterojunction solar cells. For the low band-gap polymer poly[naphtho[2,1-*b*:3,4-*b′*]dithiophene–4,7-di(thiophen-2-yl)benzothiadiazole] (PNDTDTBT), bulkier side-chains were correlated with a higher open-circuit voltage (V_{OC}) in BHJs, but a decreased short-circuit current (J_{SC}) due to greater disorder in the π-π stacking direction [40]. Similar studies of PBDTTPD showed a negligible effect on the V_{OC}, but a similar decrease in J_{SC}, when the TPD acceptor unit was substituted with an ethyl hexyl versus linear side-chain [41]. Additionally for PBDTTPD, the length of the linear side-chain on the TPD unit affects the BHJ power conversion efficiency (PCE), as an octyl chain results in a 7.5% efficiency and 8.5% for a heptyl chain [42].   However, BHJs are phase separated blends of donors and acceptors, so it is difficult to determine if the change in performance are due to transport properties of the polymer or changes in the domain size between the donor and the acceptor.

Here, it has been determined that another semiconducting polymer, PBDTTPD, forms face-on cross-chain structures in thin films. PBDTTPD is a low band-gap donor-acceptor copolymer which can achieve PCEs of up to 8.5%[42] in BHJs with PC$_{71}$BM[43], [44]. There have been many studies on the effect of the side-chains on the solar cell performance. Side-chain induced steric hindrance of the donor and acceptor units has been correlated with electrical properties, with bulkier side-chains on the donor unit and a less sterically hindered acceptor unit leading to high efficiencies [45]. The specific PBDTTPD backbone substitutions also affect the texture of the neat polymer films [46]. Large variations in packing were observed when the donor and acceptor units were substituted with various branched and linear

side-chains, however, the factors driving crystallite orientation are still not well understood. We determined the effect of the alkyl side-chains on intercrystallite order by examining the three different derivatives of the PBDTTPD polymer. Results show that minor variations in side-chain structure drive both texture and the formation of crossed structures. The angle at which crossing occurs can be predicted through the geometrical relationship defined by Takacs et al. [23], however, when side-chains are present on both the donor and acceptor units, a range of angles will be observed. Additionally, the formation of cross-chains structures appears to be related to aggregation in solution as more concentrated films lead to a denser cross-hatched morphology. The same effect is not observed in the more edge-on derivatives which do not form cross-chain structures.

4.2 Results

4.2.1 Computational Studies of Molecular Structure using DFT

The backbone conformation and crystallographic repeat unit of PBDTTPD were modeled using density functional theory (DFT) calculations with a B3LYP 6-31G(d,p) level of theory. DFT calculations were carried out with a model of the main chain composed of 4 monomer
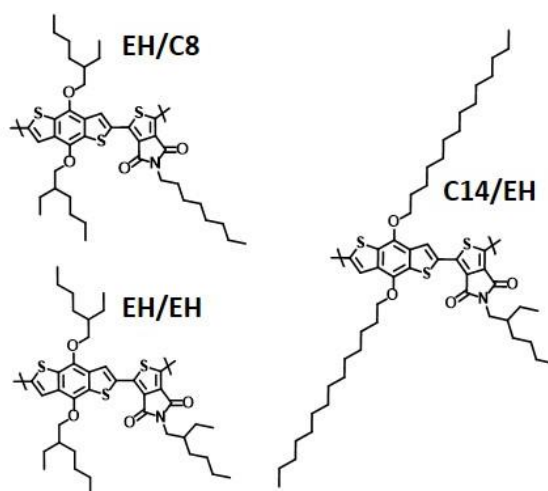
Figure 4-1. Molecular structures of the three PBDTTPD derivatives for the study.
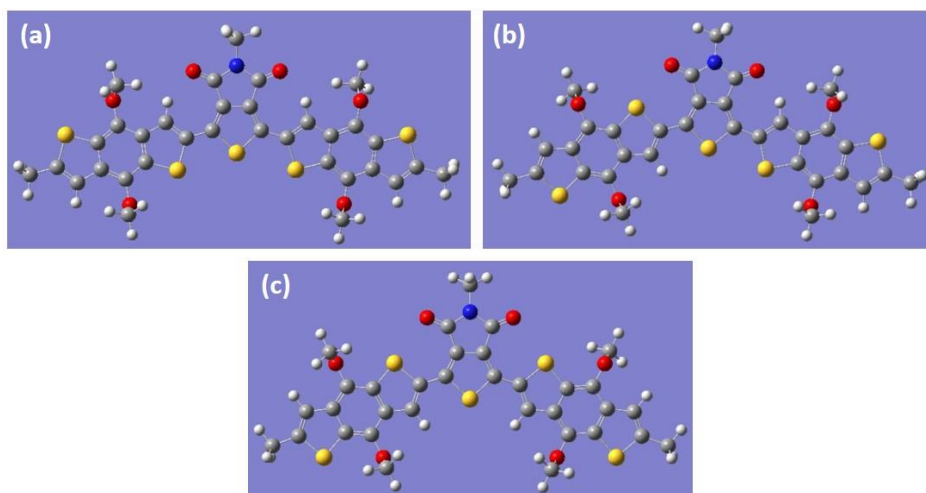
Figure 4-2. The energy of the conformation depends on the S-C-C-S dihedral angle between the donor and acceptor moieties. For a donor-acceptor-donor unit, the lowest energy is achieved when the dihedral angles are (a) 8°, (b) 0.0738 eV higher for angles of 179° and 9°, and (c) 0.155 eV higher for angles of 176 and 178°.

repeat units and methyl groups at the position of side-chain attachment. The initial dihedral angle between functional groups was varied to determine the effect of the conformation on the overall structure of the backbone. The energy-minimized structures show a mostly planar backbone with an undulating, yet linear, structure along the chain axis. While, the energy minima are close to 0 and 180°, slight deviations (Table 4-1) prevent the backbone from being perfectly planar as can be observed in Figure 4-3.

DFT calculations indicate that for a monomer unit, the lowest energy configuration is for a dihedral angle close to 0°, but for an angle of approximately 180° the energy difference is 0.08 eV. For a donor-acceptor-donor unit, when both S-C-C-S dihedral angles are close to 180° the energy is 0.155 eV, and 0.0738 eV for one angle close to 180° and the other near 0°. Therefore, for every dihedral angle close to 180°, the conformational energy increases by ~ 0.07-0.08 eV. Our results are consistent with DFT calculations by Chen et a. where planarity of the backbone was attributed to interactions between the hydrogen atoms on the benzodithiophene (BDT) donor unit and oxygen atoms on the thienopyrroledione (TPD)

acceptor unit [47]. This interaction was suggested to restrict the rotation of the donor and acceptor units such that the lowest energy configuration was for a dihedral angle close to 0° and a second minimum was located close to 180°. The energy difference between the two configurations was approximately 3.2 kcal/mol (0.14 eV) [47].

Variation in the dihedral angle also leads to slight differences in the length of the crystallographic repeat unit. For a chain composed of 7 monomer units, if all the dihedral angles are initially set to 0°, then the repeat unit length is 2.44 nm. For alternating angles of 0
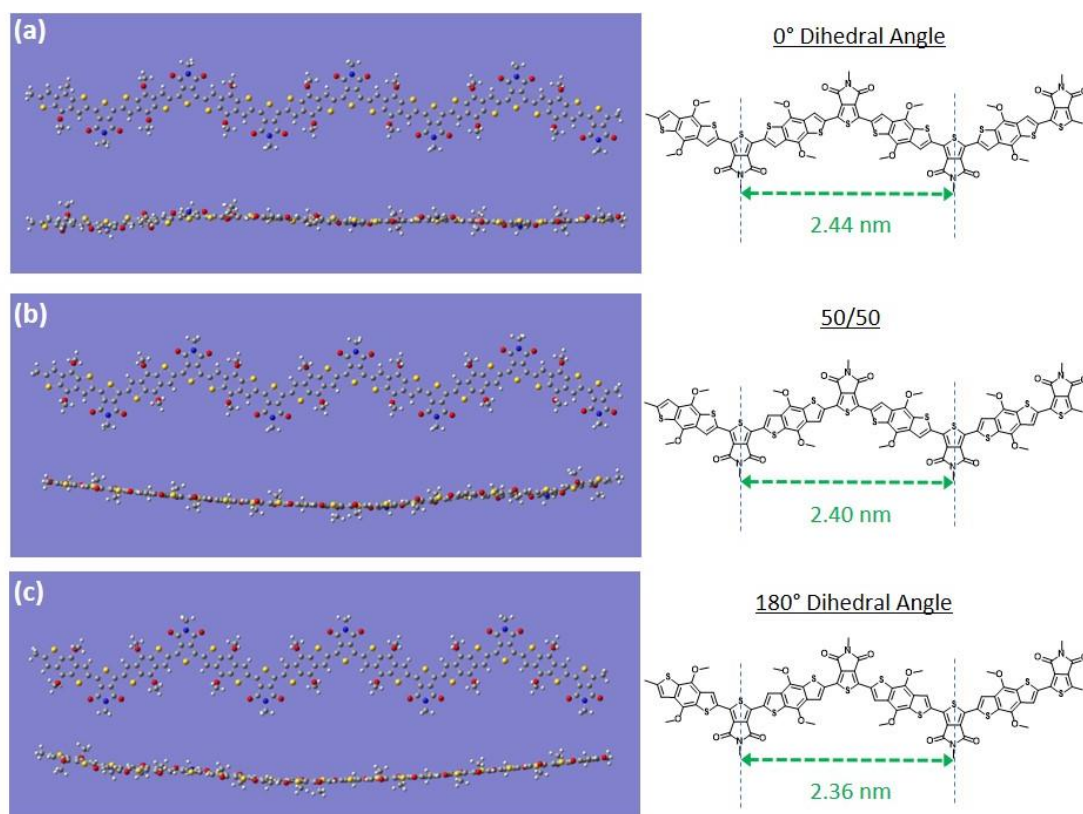
Figure 4-3. Results of DFT calculations of PBDTTPD backbones where variations in repeat unit length result from variations in the S-C-C-S dihedral angle.

Table 4-1. Average S-C-C-S dihedral angles for the backbone configurations in (Figure 4-3).

	Average S-C-C-S Dihedral Angles (°)
(a)	9
(b)	9, 177
(c)	178

82

and 180°, the length decreases to 2.40 nm. The shortest repeat unit length of 2.36 nm results

when all the S-C-C-S dihedral angles are close to 180°. It should be noted that while the energy

minima are close to 0 and 180°, slight deviations (Table 4-1) prevent the backbone from being

perfectly planar as can be observed in Figure 4-3. Due to the inherent disorder present in the

film, a distribution of dihedral angles and crystallographic repeat unit length may be observed,

but the average should be close to 2.36 nm.

4.2.2   GIWAXS Shows Differences in Molecular Packing and Texture

Grazing incidence wide-angle X-ray scattering (GIWAXS) was used to study the

molecular packing of the three derivatives. GIWAXS is widely used in the study of

semiconducting polymers to determine crystallographic order, texture, and coherence length

of ordered domains [48]. The scattering geometry limits the collection of data for perfectly

out-of-plane periodicities due to the so-called "missing wedge" of inaccessible reciprocal

space, however, structural disorder often leads to the broadening of out-of-plane peaks such
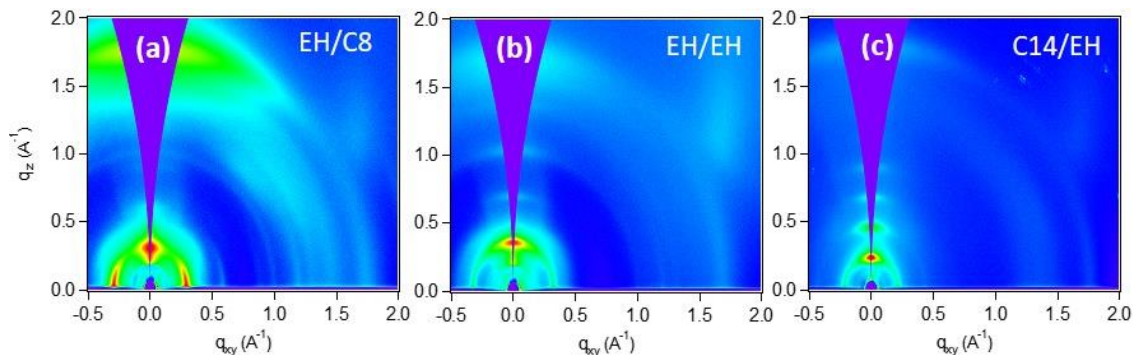
Figure 4-4. GIWAXS of the as-cast PBDDTPD films: (a) EH/C8, (b) EH/EH, and (c) C14/EH.

Table 4-2. Molecular packing details of as-cast films. (All values in Å)

	EH/C8		EH/EH		C14/EH	
Peak	face-on	edge-on	face-on	edge-on	face-on	edge-on
Alkyl	21.24	20.50	19.14	17.76	28.78	26.72
π-π stacking	3.61	3.57	3.73	3.68	3.55	3.53

83

that they can still be observed [49]. The location of a diffraction peak on the 2D detector is related to the interplanar spacing, d_{hkl}, and orientation along a specific crystallographic direction and the shape of a diffraction peak can be used to determine the presence of defects and degree of disorder[50].

GIWAXS shows that the three derivatives show a lamellar stacking configuration, but with differences in the alkyl stacking distance depending on the side-chains. The 2D scattering patterns for the PBDTTPD films are shown in Figure 4-4. The alkyl stacking peaks can be observed in the low-q region of 0.2 to 0.3 Å^{-1} and the π-π stacking at q of 1.7 to 1.8 Å^{-1}. Face-on crystallites are characterized by an in-plane alkyl stacking peak and out-of-plane π-π stacking peak, whereas edge-on crystallites produce out-of-plane alkyl and in-plane π-π stacking peaks. As expected, the different side-chain attachments result in different alkyl stacking distances: C14/2EH (27 - 29 Å) > 2EH/C8 (20 – 21 Å) > 2EH/2EH (18 – 19 Å).

Differences in alkyl stacking distances are observed for the edge-on and face-on crystallite populations within each film (Table 4-2). The 2EH/2EH derivative with ethyl-hexyl side-chains on BDT and TPD units has face-on crystallites with an alkyl d-spacing of 19.14 Å (0.33 Å^{-1}) and out-of-plane of 17.76 Å (0.35 Å^{-1}). The EH/C8 derivative has an in-plane alkyl d-
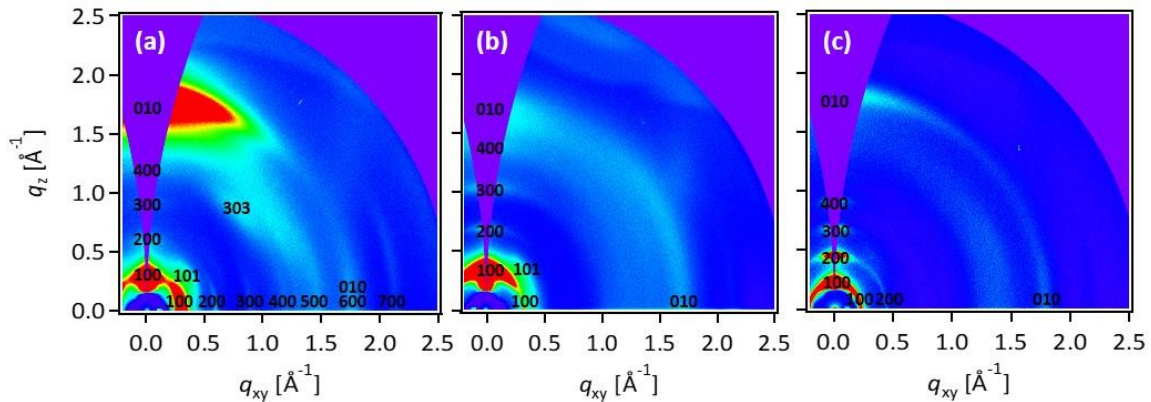
Figure 4-5. Assignment of peaks for 2D GIWAXS images of thicker films (60 nm) (a) 2EH/C8, (b) 2EH/2EH, and (c) C14/2EH.

spacing of 21.24 Å (0.30 Å^{-1}) and out-of-plane of 20.50 Å (0.31 Å^{-1}). Finally, for C14/EH, the

face-on crystallites have an alkyl *d*-spacing of 28.78 Å (0.22 Å^{-1}) and 26.72 Å (0.24 Å^{-1}) for

edge-on. In the edge-on crystallite population, the alkyl stacking distances of the four

derivatives are 4-11% smaller suggesting that there is a structural difference between the two

populations. There is a negligible difference of ≈1% in the π-π stacking distances between

the edge-on and face-on populations. It is not typical to see such large variations between the

in-plane and out-of-plane populations and they are generally assumed to be the same.

However, here a difference in packing is observed which is dependent on the crystallite

orientation. Additionally, the number of observable *a*-axis higher order peaks vary in-plane

and out-of-plane (Figure 4-5). All three derivatives show four orders of diffraction out-of-

plane, but in-plane 2EH/C8 shows seven orders of diffraction, C14/2EH shows two orders

and 2EH/2EH has only a first order alkyl stacking peak in-plane.

The width of the diffraction peak is a function of the finite crystallite size, lattice strain,

defects (stacking faults, anti-phase boundaries) and instrumental effects. The interpretation of

the peak width depends on the type of disorder present. In highly crystalline materials, the

Scherrer equation can be used to determine a crystallite or grain size from the width of a

diffraction peak [51]. However, peak width is also related to the amount of lattice disorder

present in a system, which the Scherrer equation does not consider. In disordered solids, an

approximate crystallite coherence length, L_c, can instead be estimated[52]. This is often

considered to be a lower bound on the actual crystallite size. Therefore, for disordered systems

such as organic materials:

$$\text{coherence length} = L_c = \frac{2\pi K}{\Delta_q}$$

where K is a dimensionless shape factor and Δ_q is the diffraction peak FWHM. Using the alkyl stacking peak width, the in-plane crystallite coherence length for the 3 derivatives is around 30 nm, while the out-of-plane coherence length varies between 15 and 30 nm providing a lower bound on the domain size (Table 4-3).

Table 4-3. Calculated in and out-of-plane crystallite coherence length from the alkyl stacking peak.

Derivative	In-plane Coherence Length (nm)	Out-of-Plane Coherence Length (nm)
2EH/C8	33	15
C14/2EH	27	31
2EH/2EH	28	26

A characterization of the approximate crystallite texture distribution was computed through analysis of the orientations adopted by the alkyl stacking peak. A cake segment placed at the upper and lower bounds of the alkyl stacking peak is integrated over all crystallite orientations, χ. After the appropriate background subtractions and sinχ intensity correction[53] an approximate texture distribution can be determined. The edge-on crystalline population is defined by a χ of 0 to 30° whereas the face-on crystallites have an orientation between 60-90°. However, using a grazing incidence technique, the specular scattering cannot be collected and thus the texture determination be slightly underestimate the proportion of edge-on crystallites. [54]

Large variations in the texture are observed when the side-chain attachments are varied. The EH/C8 derivative is predominately face-on with 66% face-on and 19% edge-on crystallites. The EH/EH and C14/EH derivatives have a similar distribution with EH/EH
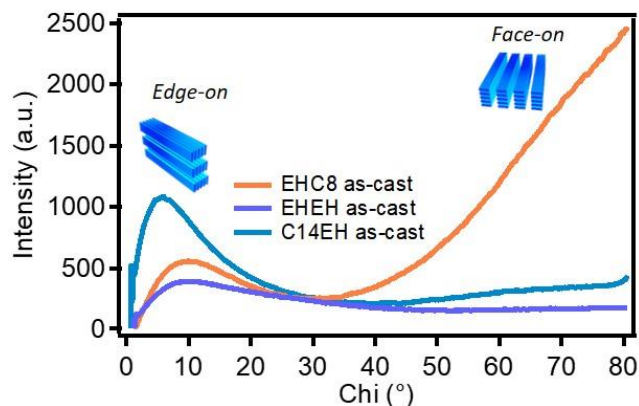
Figure 4-6. Intensity distribution of the alkyl stacking peak for the as-cast film showing the relative percentage of edge-on and face-on oriented crystallite populations.

Table 4-4. Crystallite texture distribution for the as-cast films.

	As-cast		
Derivative	**Edge-on** (%)	**Face-on** (%)	**Off-axis** (%)
EH/C8	19	66	15
EH/EH	49	28	23
C14/EH	62	24	14

containing 27% face-on and 49% edge-on crystallites, and C14/EH with 24% face-on and 62% edge-on crystallites. A similar examination of the crystallite texture as a function of side-chain attachment was conducted with GIWAXS for ten PBDTTPD derivatives by Labban et al. [46]. The presence of a branched chain on the BDT donor unit promoted a more face-on texture, while a linear side-chain on the BDT resulted in a more edge-on orientation. The strongest face-on texture was also observed for an ethylhexyl substituted donor and octyl substituted acceptor unit. However, the face-on character decreased when the side-chain on the acceptor unit was modified from a linear chain to bulkier ethylhexyl and butyloctyl chains[46]. Here, a similar conclusion is reached as the most face-on derivative, 2EH/C8, has a branched side-chain on the donor unit and linear on the acceptor unit. The most edge-on material is C14/EH, which has a linear chain on the donor and branched on the acceptor.

4.2.3 HRTEM Reveals Chain Crossing in Crystalline Domains

The chain connectivity within face-on crystalline domains can be observed with HRTEM. Phase-contrast images of the lattice fringes from the packing of the alkyl side-chains provide a real-space picture of how crystallites arrange and connect. By working at a magnification where the pixel spacing of the camera is much lower than the periodicity of interest, the lattice planes within the in-plane crystallites can be directly imaged. The HRETM images were further processed using a MATLAB code to convert the raw image into a set of lines corresponding to the location of the lattice fringes, which facilitates visualization of the structure.
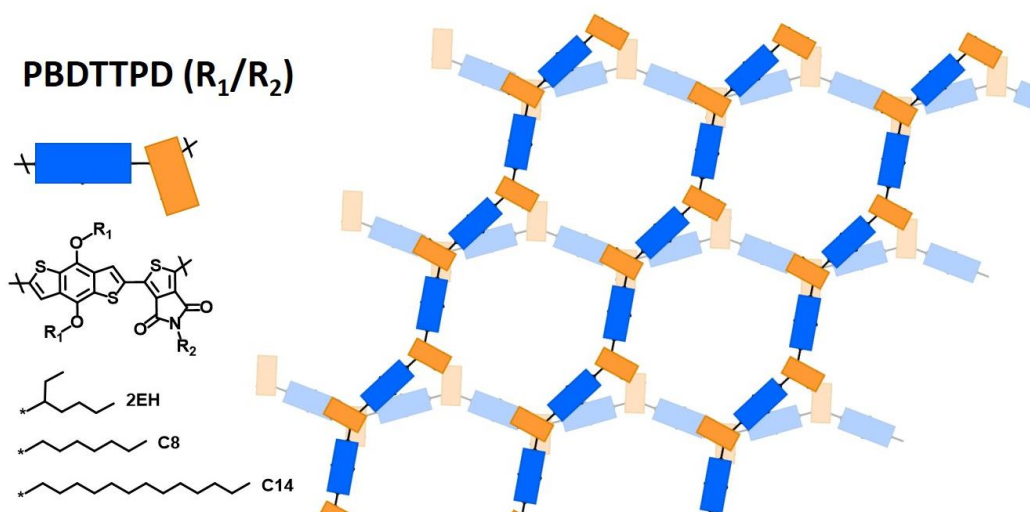
Figure 4-7. Schematic of the cross-chain structure.

The 2EH/C8 derivative shows a large degree of crystallite overlap, which occurs at an average of 60°, although other angles are also observed. Overlap was observed in nearly every image (500x500 nm) during examination of data sets covering over 50 µm². HRTEM images of the as-cast thin films (~15 nm) is shown in Figure 4-8b. The structure is reminiscent of the dendritic structure that forms in iPP due to homoepitaxy of crystallites on one another [55].

Face-on PBDTTPD lamellar crystallites are observed to connect in such a way that they overlap at particular angles.
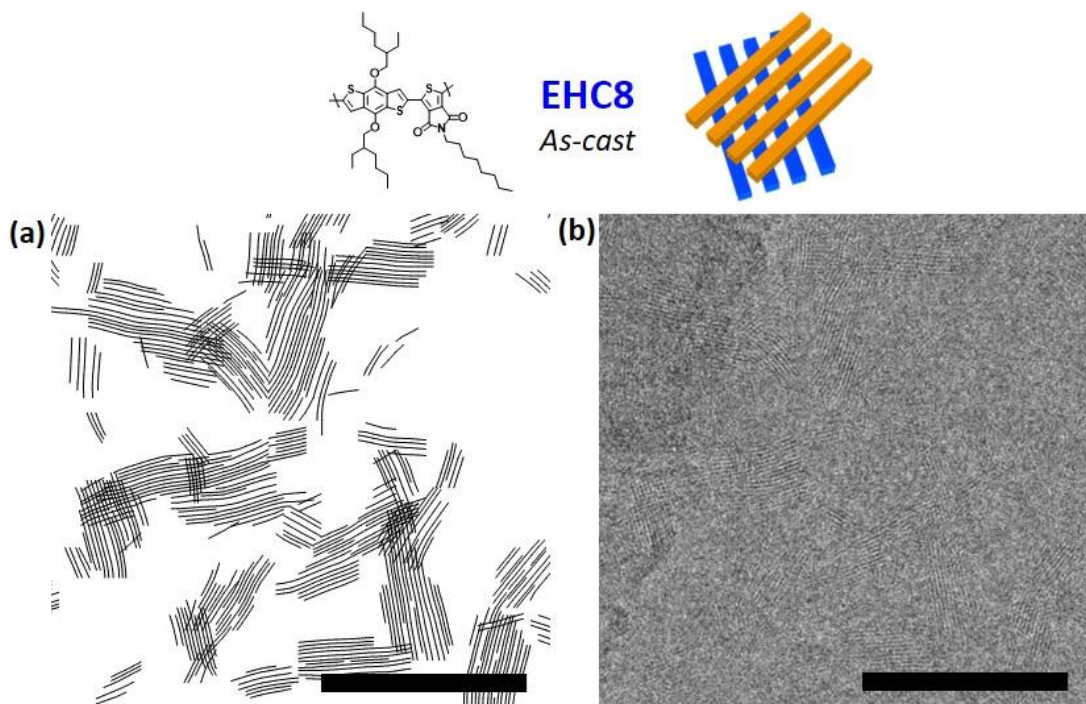
Figure 4-8. Crystallite overlap observed in 2EH/C8 thin film (15 nm) from 2 mg/ml solution. (a) Crystallite connectivity line-drawing and (b) HRTEM image. Scale bars are 100 nm.

The heavily cross-hatched structure is not observed for the 2EH/2EH and C14/2EH derivatives. The amount of face-on character is lower and therefore crystallites are only observed in about 25% of images. The face-on crystallites tend to be found in discrete, highly ordered regions. However, crystallite overlap occurring over smaller distances (~10 nm) at the crystallite edges is observed for 2EH/2EH instead of overlap over the entire crystallite width (~30 nm) as observed for 2EH/C8. An overlap angle of 51-53° was predicted based on the geometric model, which is observed in addition to other angles. The bulkiness of the branched ethyl-hexyl side-chain on the TPD acceptor unit may frustrate the packing required for efficient overlap. This explains why the crystallites cross but only for short distances. While the overlap assumes that each segment is a discrete crystallite, it is

also possible that these regions are defect induced bends in the backbone. Because the polymers are not monodisperse, there will be a distribution of chain lengths within the crystallites, which will lead to defects such as edge dislocations.

The addition of tetradecyl chains onto the polymer donor unit results in crystallites which do not show a preferential crossing. The geometrical model from Takacs et al.[23] predicts that chain crossing would not occur as the alkyl stacking distance (2.9 nm) is larger than the crystallographic repeat unit (2.4 nm). However, high resolution images were collected from an area of 15 μm^2 showed even coverage of face-on crystallites consistent with the image in Figure 4-10. A texture analysis from X-ray scattering indicated that the film was 24% face-on. The crystallites could also be very thin and therefore the edge-on
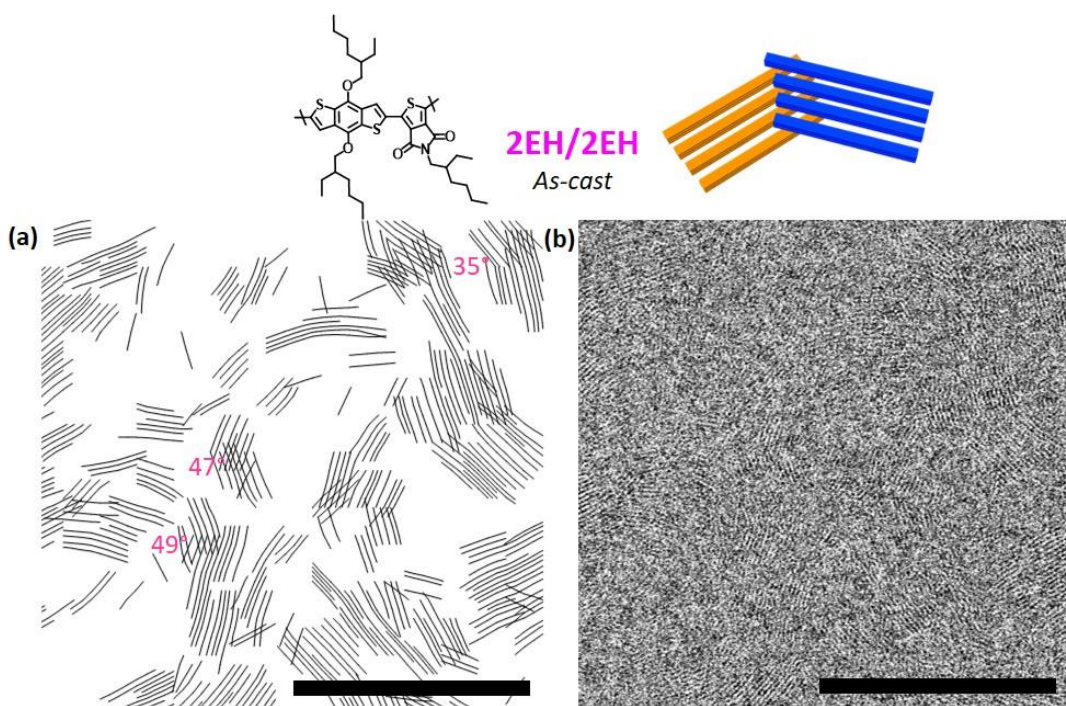

Figure 4-9. Moderate crystallite overlap observed in 2EH/2EH thin film from 5 mg/ml solution(a) crystallite connectivity line-drawing and (b) HRTEM image. Scale bars are 100 nm.

crystallites could be present above or below. An estimate of the thickness of the face-on crystallites is provided by the width of the out-of-plane π-π stacking peak centered at q_z ~

1.78 Å. With a FWHM of 0.18 Å, the crystallite coherence length is 6.3 nm. For a film thickness of around 15 nm, it is plausible that a thin layer of face-on crystallites form. It may also be possible that the areas examined with TEM were from a more face-on region and variations likely occur across the entire film.
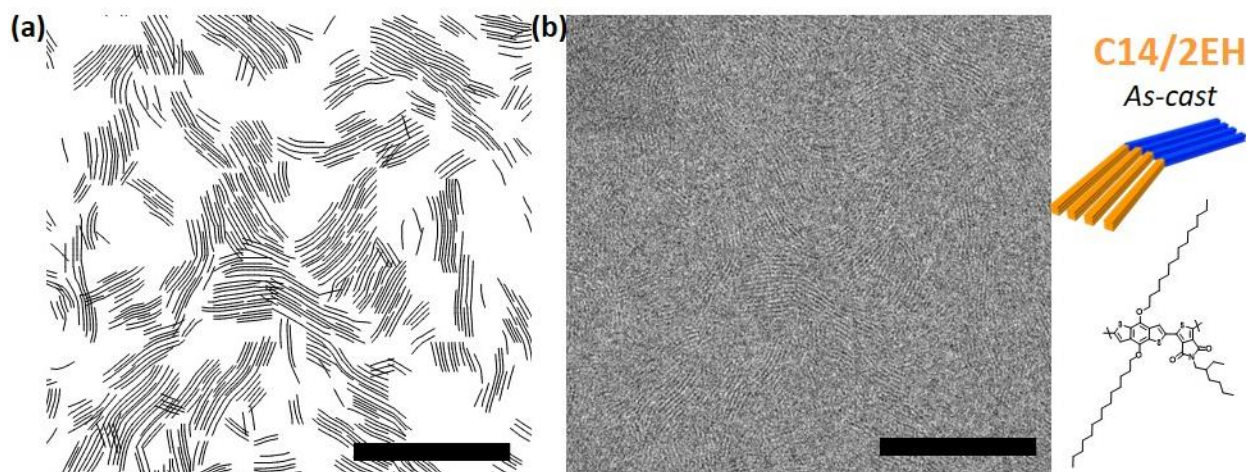
Figure 4-10. C14/2EH thin film from 2 mg/ml solution (a) crystallite connectivity line-drawing and (b) HRTEM image. Scale bars are 100 nm.

Chain-crossings may act as physical crosslinks which are known to have a significant impact on the mechanical properties of polymers, generally increasing their modulus and increasing their fracture toughness. While sufficient material was not available for quantitative mechanical testing, the process of floating the thin films onto TEM grids provided some insight into the mechanical behavior. Floating of the thinnest films (10-15 nm) was more successful for 2EH/C8, which has significant crystallite overlap versus 2EH/2EH and C14/2EH which both shattered while delaminating into a water bath. 2EH/C8 films remained intact, whereas 2EH/2EH films immediately shattered upon contact with the water. Therefore, a more concentration solution (5 mg/ml versus 2 mg/ml) was used for the HRTEM images of 2EH/2EH in Figure 4-9. The thinnest C14/2EH films only partially shattered and were able to be floated. This may be explained by the uniformly distributed face-on crystallites that were

observed in the HRTEM images. The thin layer of face-on crystallites may be sufficiently entangled to increase the film toughness. On the other hand, the 2EH/2EH face-on regions were more discrete and covering smaller areas (~ 0.50 μm^2 versus 15 μm^2 for C14/2EH). The coherence length of the 2EH/2EH out-of-plane π-π stacking is 9.3 nm (q_z ~ 1.71 Å, FWHM ~ 0.12 Å), therefore the face-on regions may have been thicker which explains the difference in lateral coverage.

4.2.4 Does the PBDTTPD system obey the geometric rule?

Because each derivative should have approximately the same repeat unit length, it was hypothesized that different crossing angles should be observed due to the difference in alkyl stacking distance. Predicted and measured values of the crossing angle are shown in Table 4-5. Predicted angles were calculated using the model equation which states that if two polymer crystallites may approach closely and overlap through a registration of the backbones and alkyl side-chains [23]. The angle of overlap is driven by the ratio of the alkyl stacking distance, d, to the polymer repeat unit length, b, through the following equation:

$$\sin \theta = b/d$$

In order to satisfy this equation, the d-spacing must be smaller than the crystallographic repeat unit length. Therefore, extended side-chains which increase the alkyl stacking distance will prevent overlap.

The geometric model of chain overlap is an excellent starting point for understanding how cross-chain structures may form and fit together. However, it is likely an oversimplification of chain-crossing as it 1) assumes a planar conjugated backbone and 2) assumes that there is enough volume to accommodate the sidechains. In the case of PSBTBT, the acceptor unit did

not have side-chains which minimized steric congestion at the proposed point of overlap. In addition, the longer Si-C bond created more distance between the side-chains and backbone which allowed for close packing of the π-faces [24]. The situation becomes more complex for polymers with side-chains on both the donor and acceptor units.

While the model predicts the single most probable overlap angle, local fluctuations in *d*-spacing and overlap site will lead to a distribution of angles. The predicted and measured overlap angles for each of the derivatives is shown in Table 4-5. A range of angles is predicted to occur due to the variation in the crystallographic repeat unit length observed from simple modifications of the dihedral angle between the donor and acceptor units (Figure 4-3).
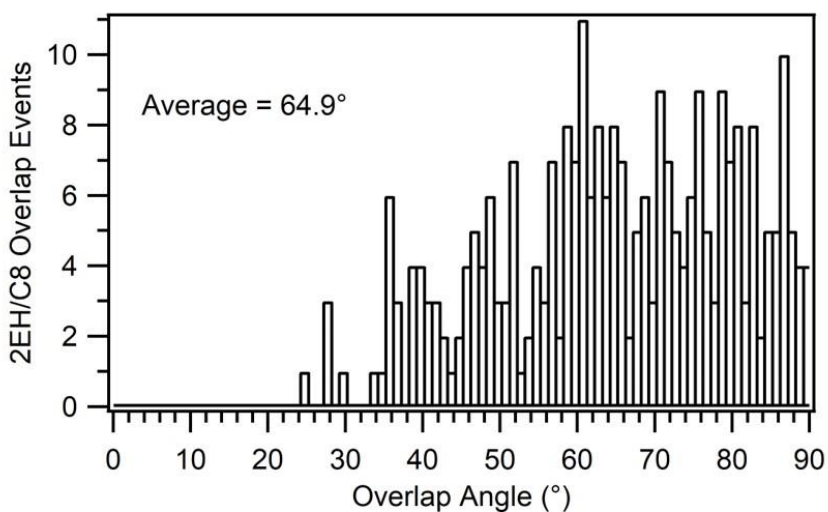
Figure 4-11. Crossing statistics for the 2EH/C8 thin film (from 2 mg/ml solution) for an area of $31\mu m^2$.

Table 4-5. Predicted and measured values of the chain crossing angle for each derivative.

Derivative	Predicted Angle (°)	Measured Angle (°)
EH/C8	59-63	64-66
C14/EH	Not possible	n/a
EH/EH	51-53	50

93

Statistics are only collected for the thinnest film made from the 2 mg/ml solution where the film is approximately 2-3 crystallites thick. In the thicker films, the true crystallite overlap angle is difficult to discern because it is a projection image. 2EH/C8 is predicted to have an overlap between 59-63°. However, in the thin film, a range of angles is observed (Figure 4-11). A distribution in angle has been observed in other systems which exhibit crystallite crossing such as lamellar crystals of pyromellitic dianhydride-oxydianiline (PMDA-ODA)[30]. With PMDA-ODA, fluctuations in the crystallographic angle, γ, of the unit cell resulted a modification of the crossing angle in order to minimize the energy.

A templating effect can be observed in the crystallite overlap for 2EH/C8 thin films. The crystallite crossing is related to specific polymer-polymer interactions leading to an average overlap angle of 64.9°. Figure 4-12b shows the overlap of three crystallites where the relative angle between each is ~60°. This suggests that chains are epitaxially arranging on one another.
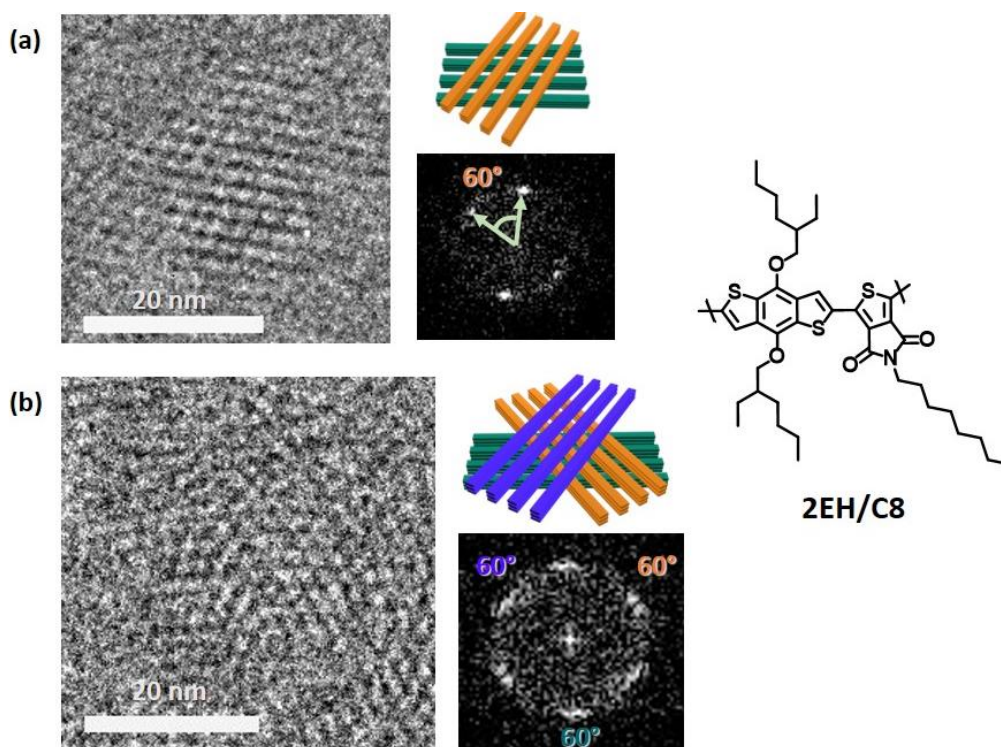
Figure 4-12. Templating of 2EH/C8 (a) 2 crystallites and (b) 3 crystallites where each is oriented at a relative angle of 60°.

94

The presence of branched versus linear side-chains will affect the ability of the π-faces to pack closely in a non-parallel chain arrangement. Here, the 2EH/C8 and 2EH/2EH are both predicted to overlap based on the in-plane alkyl d-spacings of 2.1 and 1.9 nm, respectively. However, only 2EH/C8 shows a strong cross-hatched structure. Therefore, the ability of the chains to "fit together" also depends on the bulkiness of the side-groups. The only difference between 2EH/C8 and 2EH/2EH is substitution on the TPD acceptor unit, where 2EH/C8 has a linear octyl chain and 2EH/2EH has an ethyl hexyl group. This suggests that a sterically unhindered acceptor unit is an important determinant of whether efficient crystallite overlap will occur. Therefore, the lack of overlap in the C14/2EH thin film can be explained by both an alkyl d-spacing that is too large and the presence of a branched side-chain on the TPD unit.

4.2.5 Estimation of Chain Length from Molecular Weight

Variations in the crystallite size and chain length are observed as all the derivatives have a polydispersity greater than 1 (Table 4-6). Two peaks can be observed in the molecular weight distribution for 2EH/C8, whereas both 2EH/2EH and C14/2EH have a single peak (Figure B-1). An estimation of average chain length can be computed by considering the molecular weight of each derivative and the repeat unit length. If the crystallographic repeat unit is 2.40 nm and is composed of 2 monomer units, then each monomer unit contributes 1.2 nm to the length.

$$\begin{array}{c} estimated \\ chain\ length \end{array} = \left(\frac{\begin{array}{c} polymer \\ molecular\ weight \end{array}}{\begin{array}{c} monomer \\ molecular\ weight \end{array}} \right) (monomer\ length) = \frac{M}{M_0} l_{monomer}$$

A range in the chain length is estimated from the number average (M_n) and weight average (M_w) molecular weights. Therefore, 2EH/C8 should have a chain length of 31-98 nm, 35-79

95

Table 4-6. Molecular weight results from GPC.

Derivative	M_n (kDa)	M_w (kDa)	PDI
2EH/C8	17.6	55.5	3.2
2EH/2EH	20.0	44.5	2.2
C14/2EH	17.9	39.4	2.2

nm for 2EH/2EH, and 25-56 nm for C14/2EH. From HRTEM, crystallites have an average width of 20-50 nm and length of 30-100 nm, which matches the estimated values.

4.2.6 Changes in Overlap Density with Solution Concentration

The overlap density of face-on crystallites increases in 2EH/C8 as the film thickness increases and is likely connected to aggregation in solution. The thickness of the films was increased by using more concentrated solutions while keeping spin-casting conditions identical. The film thickness varied from ~10 to 60 nm by varying solution concentration between 1 and 10 mg/ml, respectively. For thin films (~15 nm) from a 2 mg/ml solution of 2EH/C8 in chlorobenzene, individual crystallites are observed to overlap and intersect (Figure 4-8,Figure *4-14*. Doubling the thickness to 30 nm with a 5 mg/ml solution increases the overlap (Figure 4-15). The crystallites have an overall isotropic orientation as can be seen from the ring in the power spectrum, but overlap at angles around 60° can still be observed. Doubling the thickness again to 60 nm with a 10 mg/ml solution results in a very and densely crosshatched morphology (Figure 4-16). For all film thicknesses, the cross-hatch structure in 2EH/C8 is not a random occurrence and is observed in almost every image across areas of 10s of µm, but the density of the overlap increases with thickness.

The percentage of face-on and edge-on character also changes in the 2EH/C8 solid film as the solution used for spin-casting becomes more concentrated (Figure 4-13, Table 4-7). When the solution is the most concentrated (10 mg/ml), the film is 73% face-on and 14%

edge-on. As the solution becomes more dilute, the face-on character decreases and edge-on increases. The most dilute solution (1 mg/ml) makes a solid film that is 26% face-on and 64% edge-on. The texture distribution may be related to differences in chain interactions in solution. Tournebize et al. looked at the molecular packing of PBDTTPD (2EH/C8) films spun cast from hot (130°C) and cold solutions (50°C) [56]. A more pronounced π-stacking peak for the films was observed for the cold solution, and it was suggested that the π-stacking was stabilized by a unique overlap of the donor units at an angle of 64° due to sulfur-oxygen interactions [57]. While in general, the occurrence of aggregation in solution does not automatically indicate that cross-chain structures are forming, a certain solution concentration or degree of chain interaction is required for the structures to form.
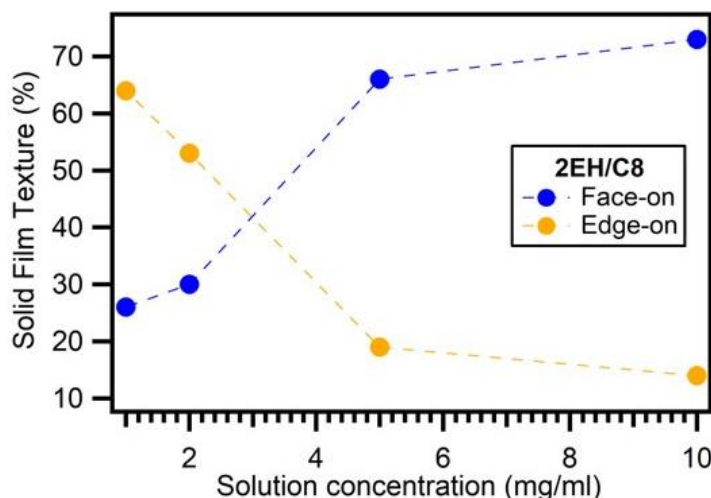
Figure 4-13. Change in 2EH/C8 solid film texture when spun cast from solutions of different concentrations. (The off-axis population is excluded from the plot)

Table 4-7. Change in 2EH/C8 solid film texture by varying solution concentration.

2EH/C8			
Solution concentration (mg/ml)	Edge-on (%)	Face-on (%)	Off-axis (%)
10	14	73	13
5	19	66	15
2	53	30	17
1	64	26	10
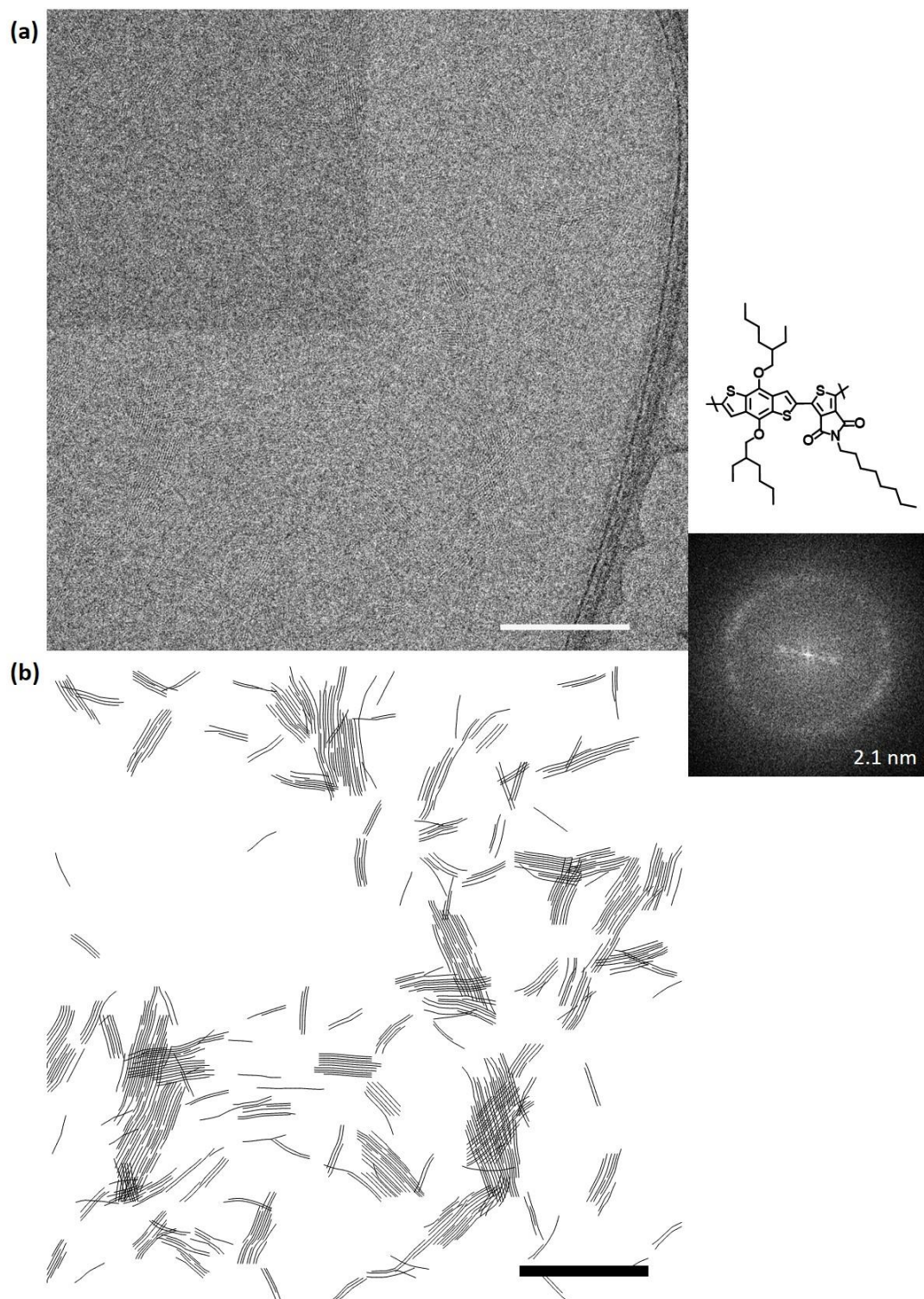
Figure 4-14. (a) HRTEM image of 15 nm thick as-cast film of 2EH/C8 from 2 mg/ml solution showing isolated regions of crystallite overlap, and (b) line-drawing of HRTEM image. Scale bars are 100 nm.
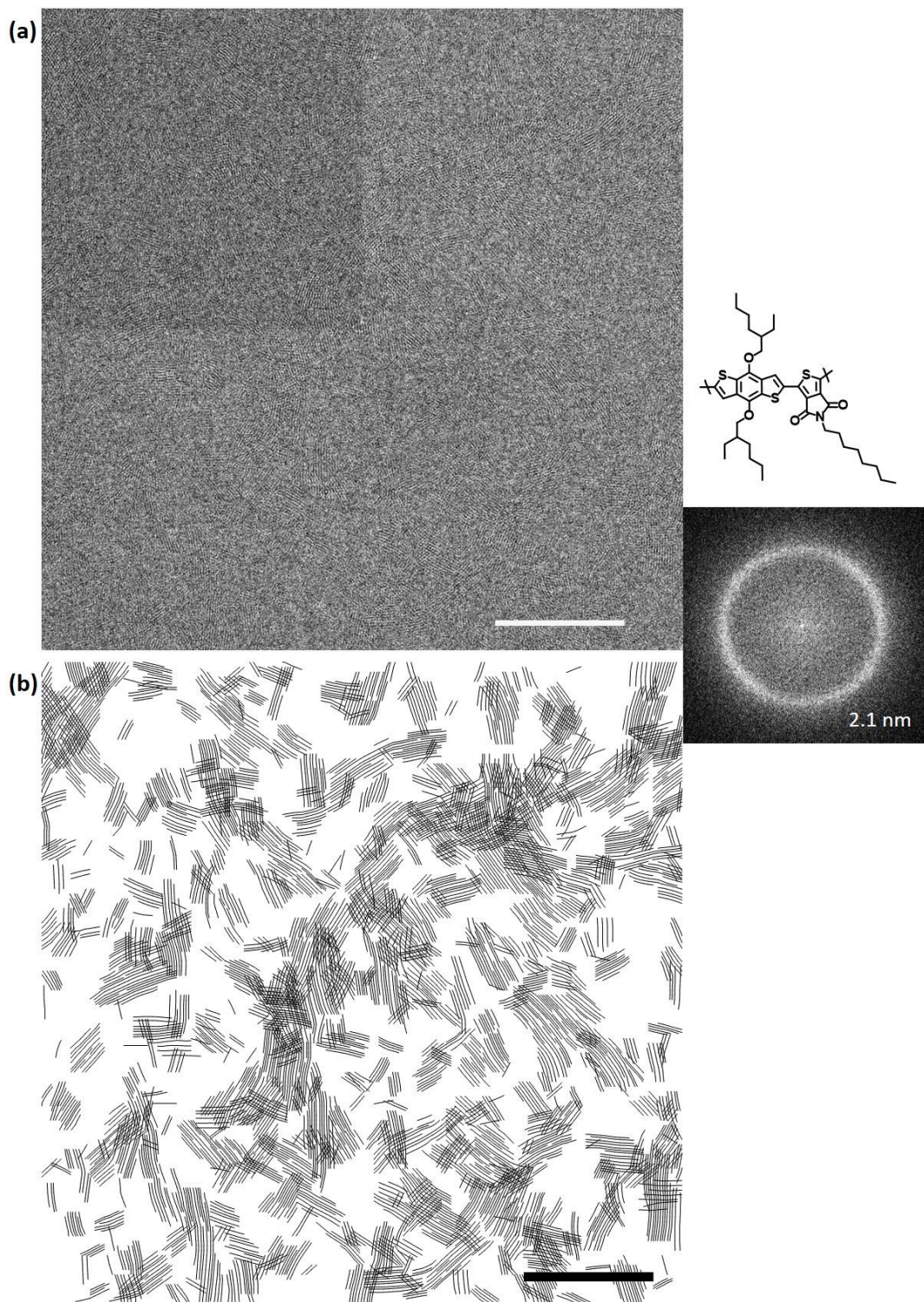
Figure 4-15. (a) HRTEM image of 30 nm thick as-cast film of 2EH/C8 from 5 mg/ml thick solutions showing crystallite overlap, and (b) line-drawing of HRTEM image. Scale bars are 100 nm.
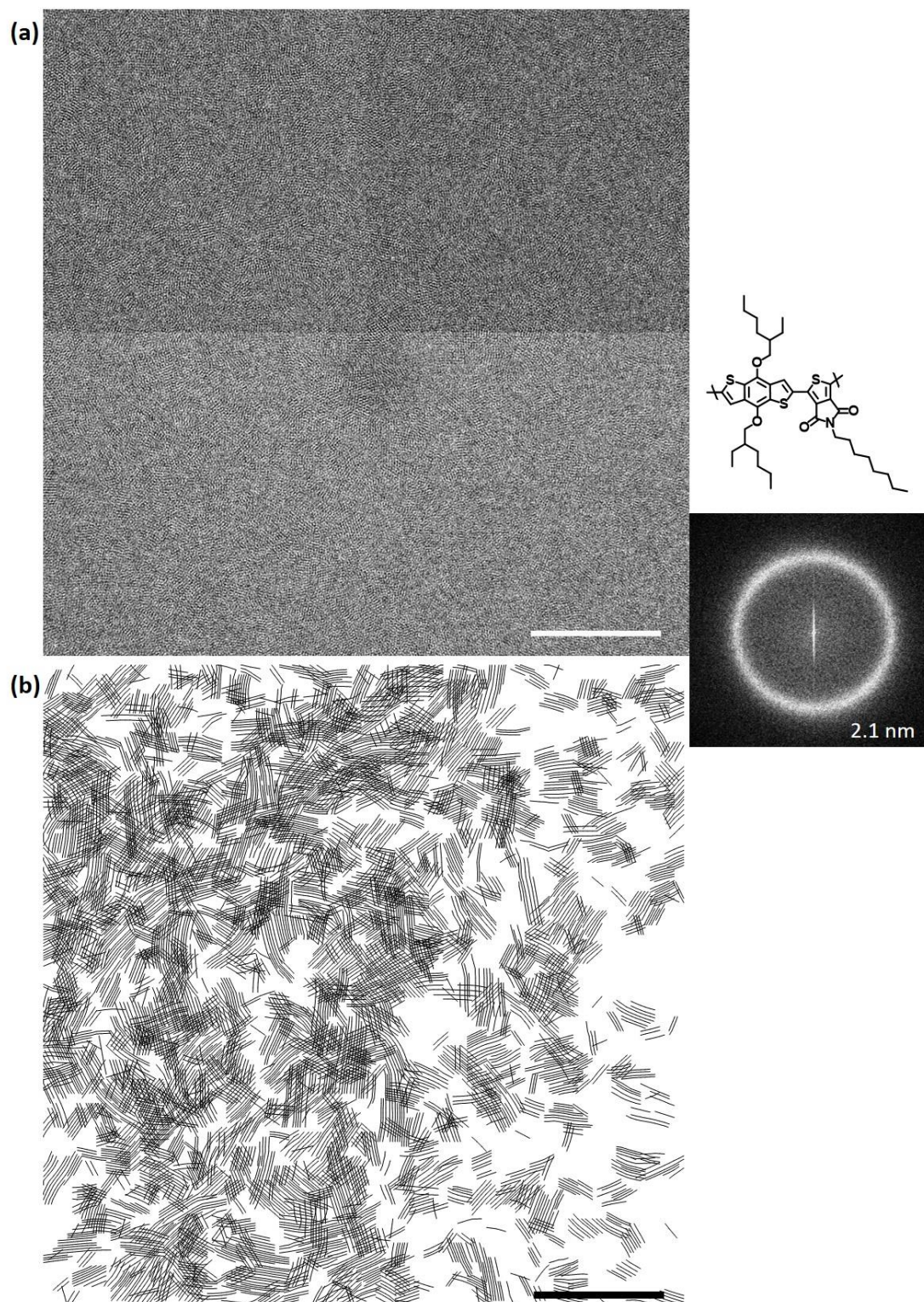
Figure 4-16. (a) HRTEM of thick (60 nm) as-cast 2EH/C8 film from 10 mg/ml solution where the structure is highly complex due to multiple crystallite overlap, and (b) line-drawing of HRTEM image. Scale bars are 100 nm.

Increasing the film thickness through the use of more concentrated solutions does not result in an increase in crystallite overlap for the 2EH/2EH and C14/2EH derivatives (Figure 4-18, Figure *4-19*). However, 2EH/2EH and C14/2EH also have a lower percentage of face-on character compared to 2EH/C8. There were slight differences in the solubility between the derivatives which could affect the spun-cast morphology. Both 2EH/2EH and C14/2EH were soluble in chlorobenzene at room temperature, whereas the 2EH/C8 solution had to be heated before complete dissolution.
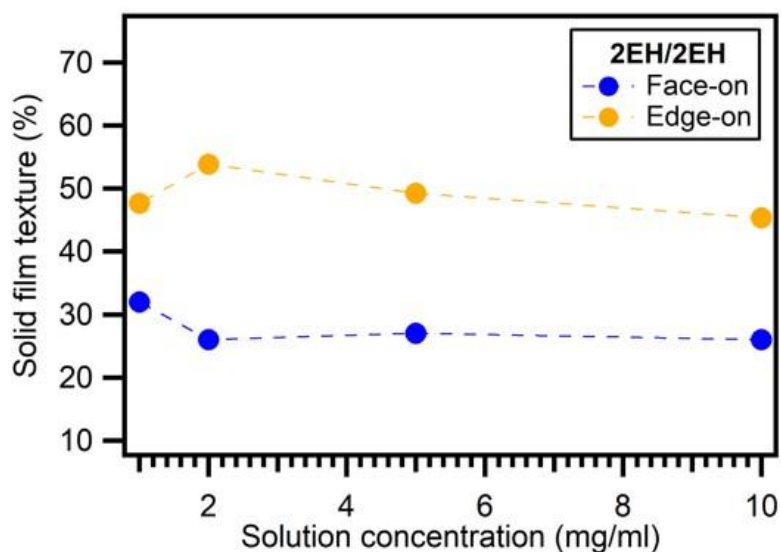
Figure 4-17. Change in face-on and edge-on character for the 2EH/2EH thin film as solution concentration increases.

Table 4-8. 2EH/2EH thin film texture as a function of solution concentration.

2EH/2EH			
Solution concentration (mg/ml)	Edge-on (%)	Face-on (%)	Off-axis (%)
10	45	27	28
5	49	28	23
2	54	26	20
1	48	32	20

Examination of the change in thin film texture with solution concentration for 2EH/2EH revealed only minor changes compared to 2EH/C8 (Table 4-8). Spin casting a thin film from the most concentrated solution (10 mg/ml) leads to a 45% edge-on and 27% face-on character. Decreasing the concentration to 5 mg/ml showed a very similarly textured thin film that was 49% edge-on and 28% face-on. The 2 mg/ml solution produced the most edge-on solid film at 54%, however there is not a clear trend between texture and solution concentration. This is likely within the error expected between different spin-cast thin films. There are clearly differences in the 2EH/C8 derivative afforded by a simple change in the side-chain on the acceptor unit which lead to variations in solution properties and solid film organization.
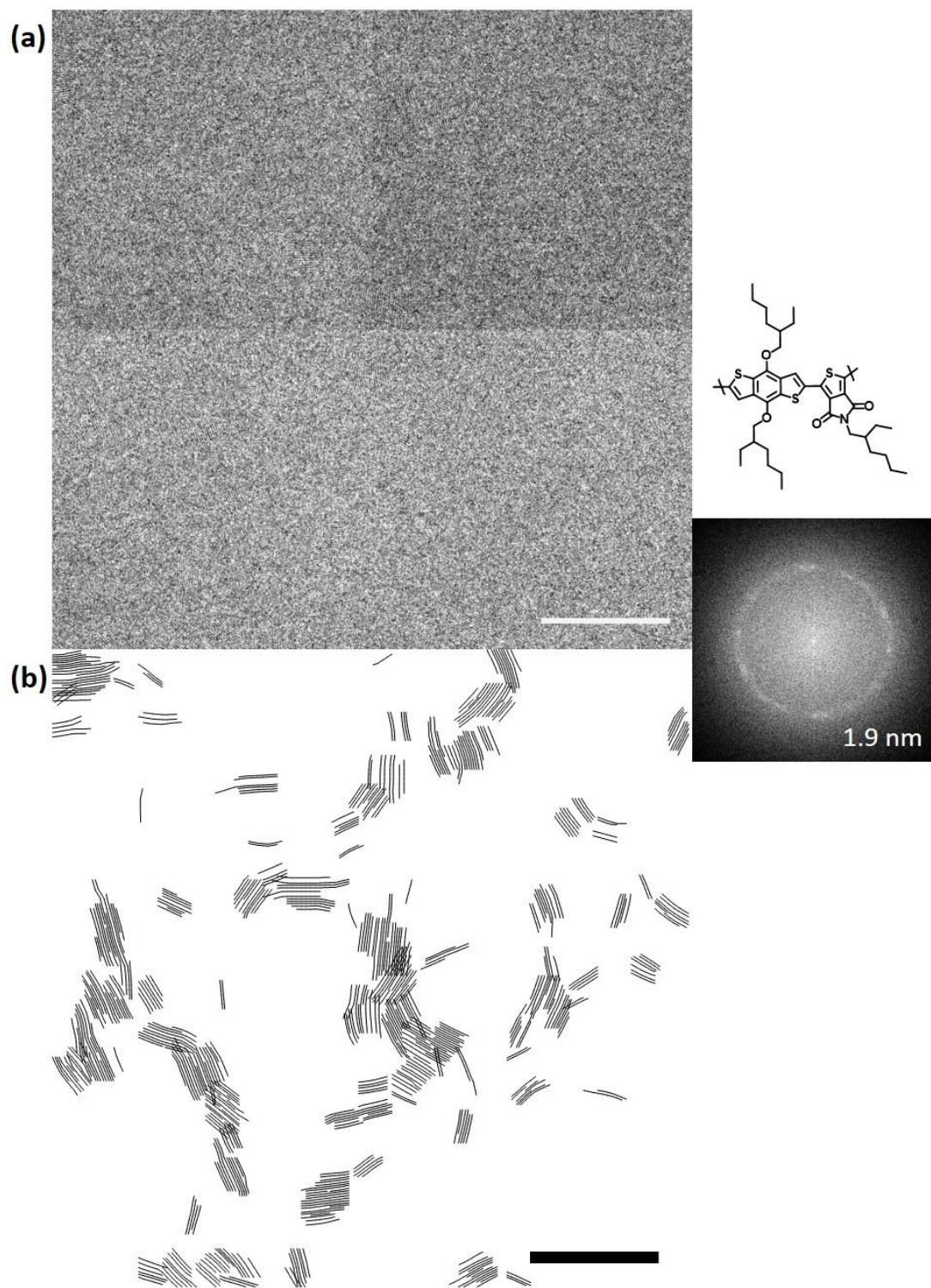
Figure 4-18. 2EH/2EH thick film from 10 mg/ml solution. (a) HRTEM image and (b) line-drawing. Scale bars are 100 nm.
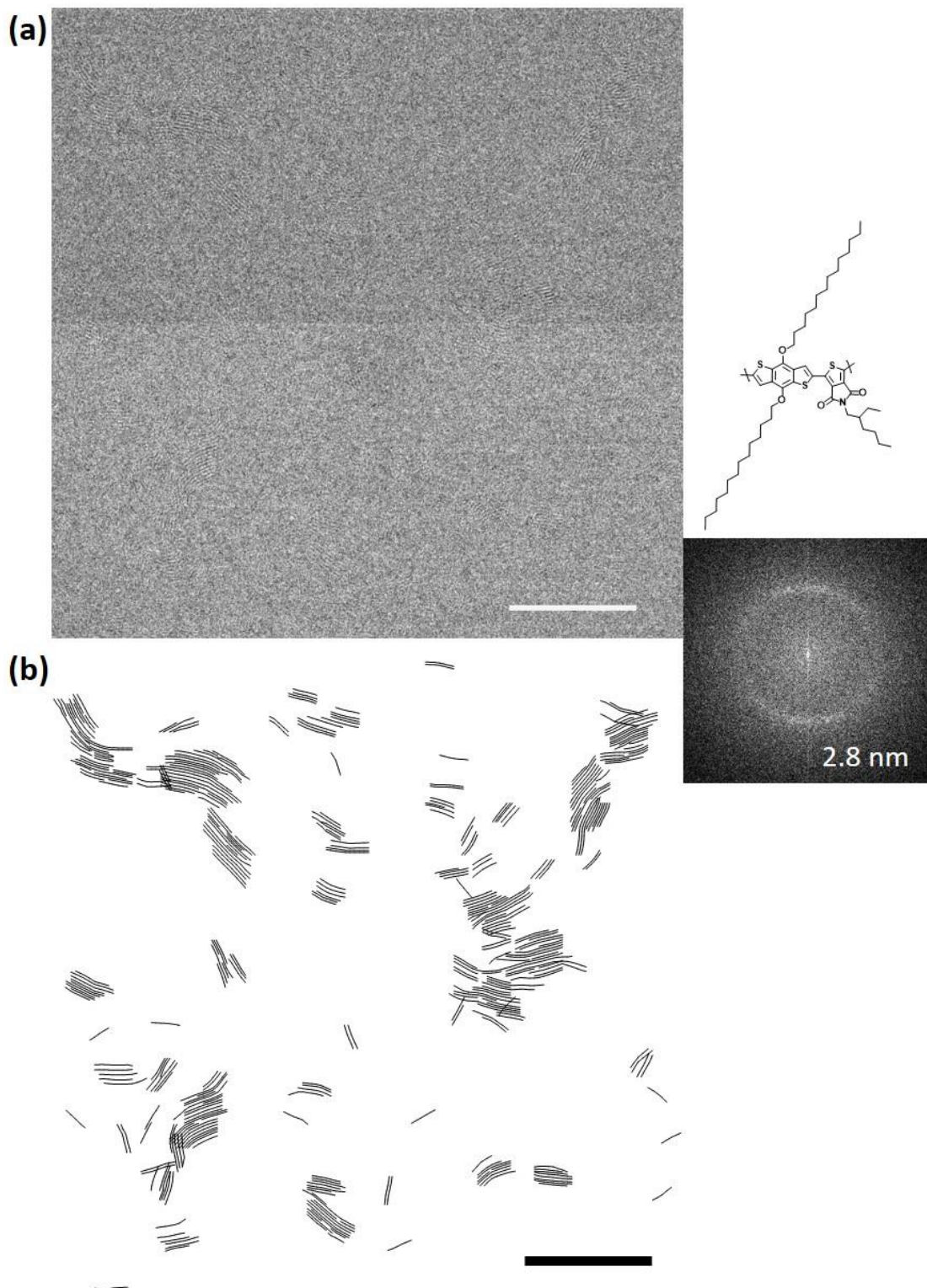
Figure 4-19. C14/2EH thick film from 10 mg/ml solution. (a) HRTEM image and (b) line-drawing. Scale bars are 100 nm.

4.2.7 Response to Thermal Annealing Dependent on Side-Chains

Cross-chain structures have been suggested to be a metastable state[23] and therefore it was unclear whether the structures would persist after a high temperature, long time annealing step. In many polymer and small-molecule systems thermal annealing has been shown to increase structural ordering and allows for rearrangement of the chains [58]. In many studies annealing is only done for short times, e.g. several minutes, due to the technical consideration of fast processing for printed electronic devices. Fewer studies have examined longer time scale annealing to attempt to fully relax the as-cast structure.

Thin film UV-Vis absorption measurements were used to determine the stability of films after annealing at various temperatures and times. Differential scanning calorimetry (DSC) and thermogravimetric analysis (TGA) are frequently used to show thermal stability of bulk
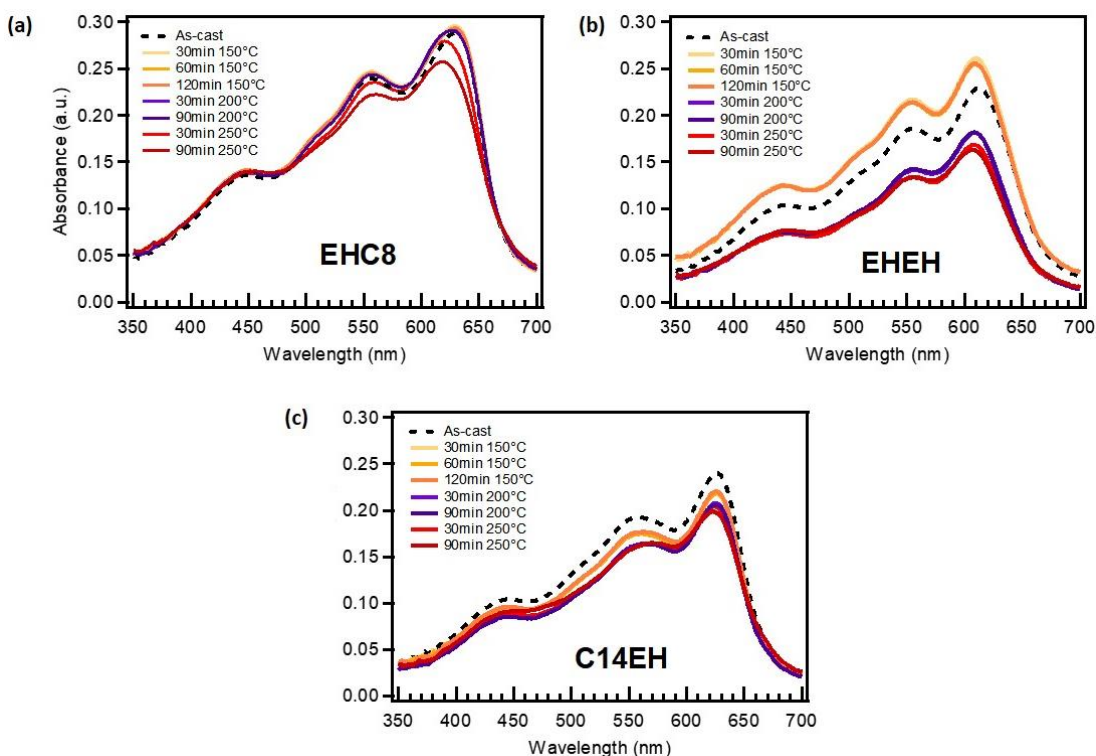
Figure 4-20. UV-Vis absorption spectra for (a) 2EH/C8, (b) 2EH/2EH, and (c) C14/2EH after annealing at different temperatures.

materials. However, previous studies on PBDTTPD, including the EH/C8 derivative, reported no observable phase transitions during DSC scans from room temperature to 300°C[59], [60]. TGA shows that PBDTTPD begins to decompose at high temperature with a less than 2% weight-loss at 300°C[60] and 5% weight-loss temperature at 335°C[59]. However, the length of time spent at each temperature in the various techniques is usually much shorter than the length of typical thermal anneal used during film processing. Additionally, there were restrictions in the amount of material available, which meant that extended DSC and TGA experiments were not possible. Therefore, ultraviolet-visible (UV-Vis) spectroscopy was used to test the thermal stability of the PBDTTPD films. UV-Vis is commonly used to detect degradation to the conjugated backbone [61]. Changes in the absorption spectra of the films were monitored before and after annealing at various temperatures. Upon annealing the films at an elevated temperature for varying periods of time, small shifts occur in the position and intensity of the absorbance peaks. However, it can be observed that overall the absorption features are preserved (Figure 4-20).

4.2.8 Effect of Thermal Annealing on Molecular Packing and Texture

In-situ annealing GIWAXS measurements was used to determine changes in the local packing structure of the neat PBDTTPD films during thermal annealing. The use of synchrotron based X-ray scattering methods allows for much shorter exposure times to be used then would be required for a traditional laboratory X-ray source. The high flux of a synchrotron enables the design of *in-situ* experiments where fast structural rearrangements can be observed such as during spin-coating[62] or thermal annealing[63]–[65]. Here, the polymer films were heated to 250°C for 30 min followed by slow cooling to room temperature. This temperature was observed to be both below the decomposition temperature and films
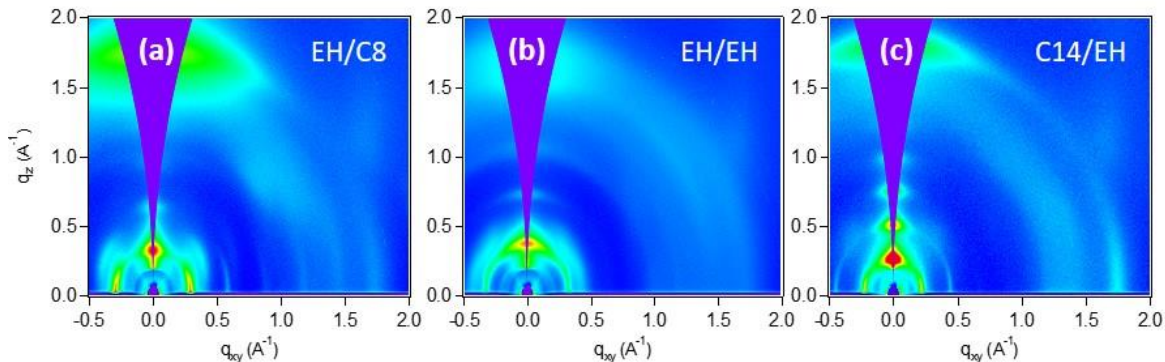
Figure 4-21. GIWAXS images of (a) EH/C8, (b) EH/EH, and (c) C14/EH after annealing at 250°C for 30 min followed by slow cooling.

Table 4-9. Contraction in alkyl d-spacing after thermal annealing at 250C.

	% Contraction in alkyl spacing after annealing 250°C		
	EH/C8	**EH/EH**	**C14/EH**
face-on	-0.02	0.09	-3.4
edge-on	-4.2	-4.5	-9.2

were stable as examined through UV-Vis measurements after annealing. It was expected that structural rearrangements would occur during thermal annealing, however, the edge-on and face-on alkyl stacking distances showed different responses to the heating and slow cooling (Table 4-9). The in-plane alkyl stacking for 2EH/C8 and 2EH/2EH show a change of less than 1%, while out of plane a contraction of 4.2 and 4.5% is observed, respectively. For C14/2EH, a 3.4% contraction is observed in plane and 9.2% out-of-plane. The texture of the annealed films is calculated from the alkyl stacking peak by looking at the distribution of intensity for from $\chi = 0°$ (edge-on) to $\chi = 90°$ (face-on). The films become more textured after annealing and slow cooling as evidenced by the decrease intensity of the off-axis alkyl stacking peaks
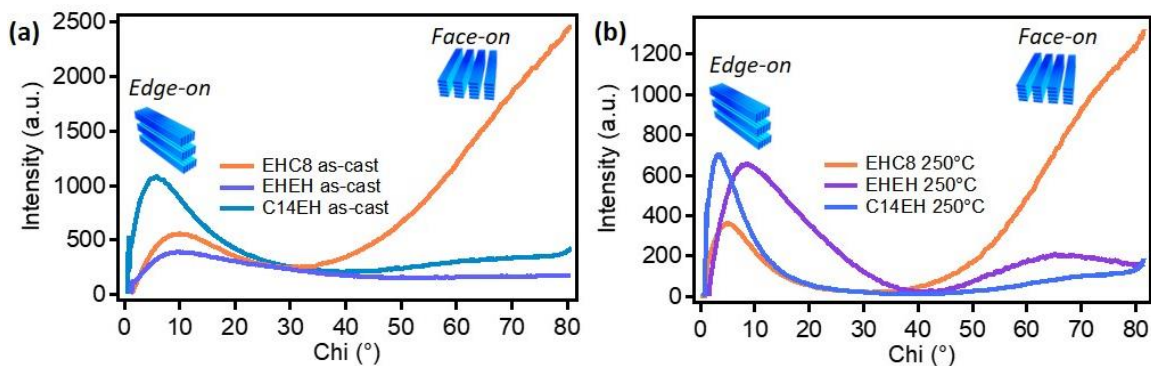
Figure 4-22. Integrated intensity distribution of the alkyl stacking peak showing crystallite texture for the (a) as-cast and (b) annealed films. Sinχ corrections were applied to the data.

Table 4-10. Crystallite texture distribution for the three derivatives before and after annealing. Edge on (χ=0-30°), face-on (χ=60-90°), off-axis (χ=30-60°).

	As-cast			Annealed		
	Edge-on (%)	*Face-on* (%)	*Off-axis* (%)	*Edge-on* (%)	*Face-on* (%)	*Off-axis* (%)
EH/C8	19	66	15	14	80	6
EH/EH	49	28	23	47	33	20
C14/EH	62	24	14	65	28	7

(χ = 30-60°). The 2EH/2EH and C14/2EH films show only a minor change in the texture with annealing.

4.2.9 Anisotropic Crystallite Strain Observed with GIWAXS

Differences in the side-chains attachments affect the crystallite connectivity and may also affect the way the films respond to thermal annealing. The crossed crystallites may act as physical crosslinks and change the way the film expands and contracts during heating and cooling. To test this hypothesis, GIWAXS measurements were conducted while heating the films to 250°C *in-situ* for 30 min followed by slow cooling at 5-10°C/min. The change in the alkyl stacking distance in and out of the plane of the substrate was monitored throughout.
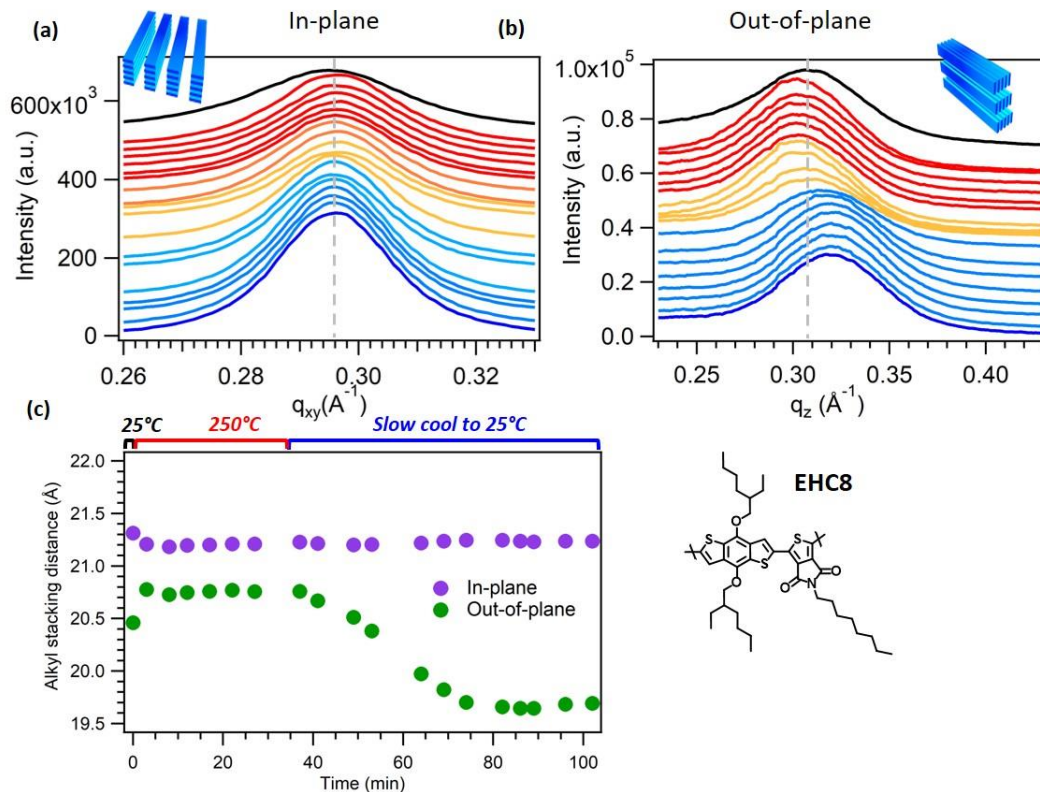
Figure 4-23. Results of GIWAXS in-situ heating of 2EH/C8 at 250°C for 30 min followed by slow cooling to room temperature. 1D line-cuts of the alkyl stacking peak (a) in-plane and (b) out-of-plane, and (c) evolution of alkyl stacking during heating and cooling for the in- and out-of-plane direction.

For the 2EH/C8 derivative, the face-on and edge-on crystallites show a different response to thermal annealing as evidenced by the change in *d*-spacing during heating and cooling (Figure 4-23). 1-D linecuts of the 2D GIWAXS images during *in-situ* annealing are shown in Figure 4-23a and b for the in- and out-of-plane direction, respectively. Minimal change is observed in the in-plane direction as the alkyl stacking distance is 2.13 nm before annealing and 2.12 nm after slow cooling. The out-of-plane alkyl stacking shows an initial expansion from 2.05 to 2.08 nm during heating followed by a contraction to 1.97 nm. However, the overall 4% reduction in *d*-spacing is still a relatively small change. Thermal expansion has been observed during the initial annealing of other semiconducting polymers such as P3HT, but was reversible upon cooling [63], [66].
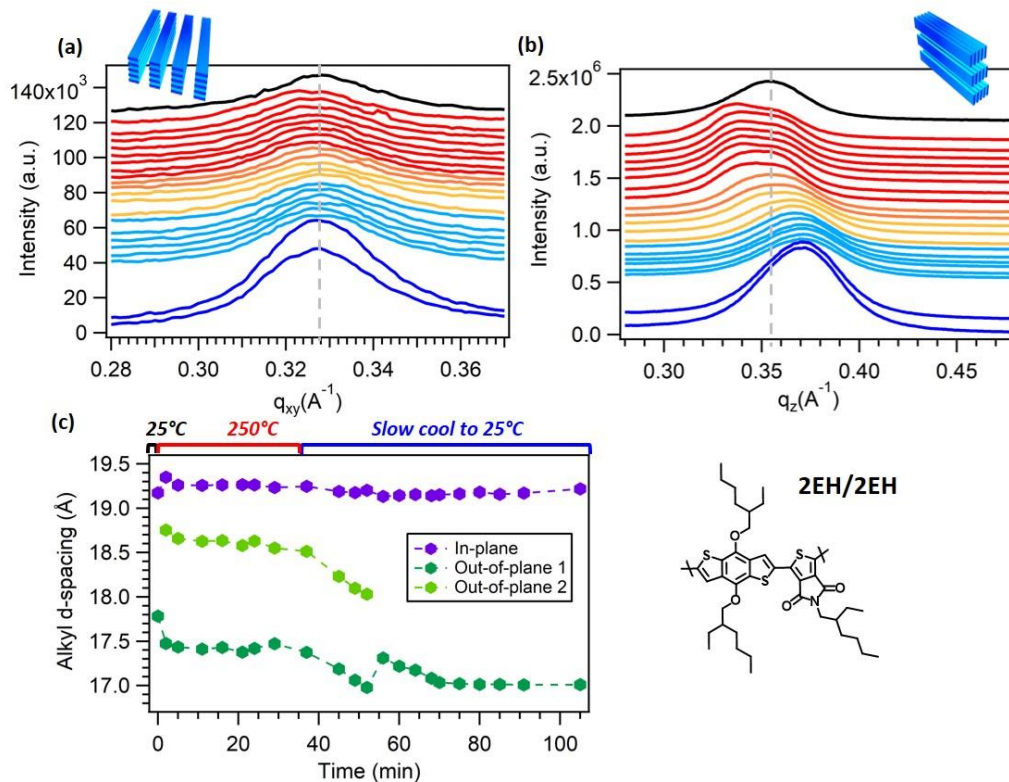
Figure 4-24. Results of GIWAXS in-situ heating of 2EH/2EH at 250°C for 30 min followed by slow cooling to room temperature. 1D line-cuts of the alkyl stacking peak (a) in-plane and (b) out-of-plane, and (c) evolution of alkyl stacking during heating and cooling for the in- and out-of-plane direction.

A similar in-plane stability in response to thermal annealing is also observed for the 2EH/2EH derivative. In-plane there is very little change in the *d*-spacing during heating and cooling as the as-cast and post-annealed in-plane alkyl stacking at both 1.92 nm (Figure 4-24). On the other hand, the out-of-plane alkyl stacking exhibits a larger change (distance is 1.78 nm ($q\sim0.353$ Å^{-1}). While heating at 250°C, the out-of-plane alkyl stacking peak splits into 2 peaks at $q\sim0.336$ Å^{-1} and $q\sim0.360$ Å^{-1}, corresponding to *d*-spacings of 1.86 and 1.74 nm, respectively. The lower *q* peak at 0.336 Å^{-1} slowly shifts towards a high *q* until it disappears during the final stages of cooling. The final out-of-plane alkyl *d*-spacing is 1.70 nm ($q\sim0.369$ Å^{-1}).
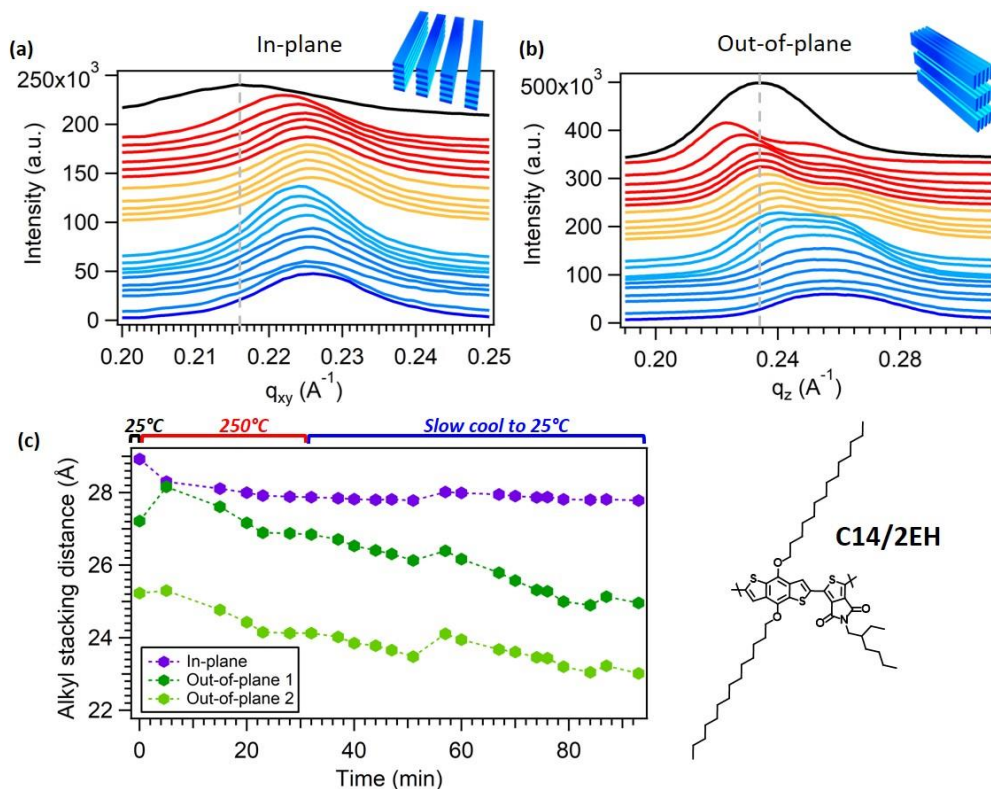
Figure 4-25. Results of GIWAXS in-situ heating of C14/2EH at 250°C for 30 min followed by slow cooling to room temperature. 1D line-cuts of the alkyl stacking peak (a) in-plane and (b) out-of-plane, and (c) evolution of alkyl stacking during heating and cooling for the in- and out-of-plane direction.

The C14/2EH derivative shows fluctuations in alkyl stacking distance in both the in- and out-of-plane directions. The in-plane alkyl stacking exhibits a 4% contraction during annealing from 2.89 to 2.78 nm. The immediate contraction in response to annealing is likely due to minor rearrangements of the linear tetradecyl side-chains on the TPD donor unit. In the out-of-plane direction, the alkyl stacking peak at $q \sim 0.234$ Å^{-1} ($d \sim 2.68$ nm) is observed to immediately split into 2 peaks at $q \sim 0.228$ Å^{-1} ($d \sim 2.82$ nm) and $q \sim 0.248$ Å^{-1} ($d \sim 2.53$ nm). Both peaks show an overall contraction in d-spacing from 2.82 to 2.55 nm ($q \sim 0.247$ Å^{-1}) for the lower-q peak and 2.53 to 2.35 nm ($q \sim 0.266$ Å^{-1}) for the higher-q peak. The 2 peaks appear to eventually merge into a single broad peak in the slow-cooled film (Figure 4-25b). It is

111

unclear if the peak around 2.4 nm is due to the presence of a polymorph or if it is the backbone (*c*-axis) reflection, which was determined by DFT calculations to be approximately 2.4 nm.
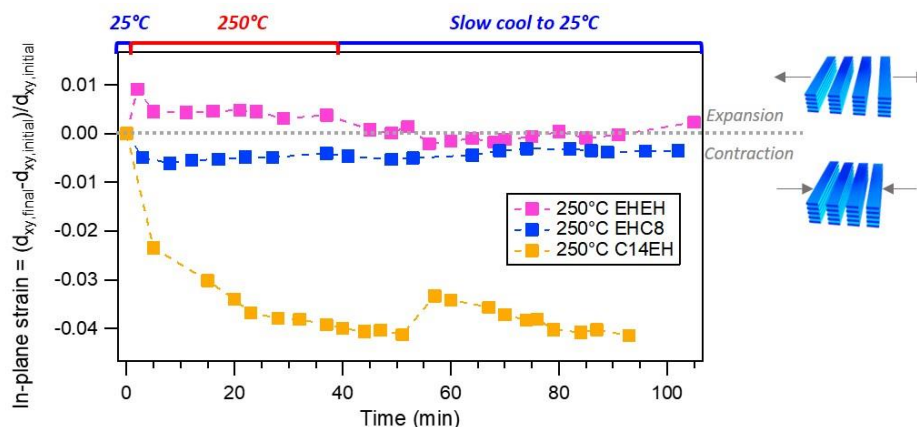
Figure 4-26. Comparison of the in-plane strain in the alkyl stacking direction for each derivative during heating at 250° for 30 minutes following by slow cooling for room temperature at 5-10°C/min.

4.2.10 Crossed chains structures are less sensitive to thermal annealing

The three PBDTTPD derivatives all show a contraction in the out-of-plane alkyl stacking with annealing, but different behavior in-plane. A value for the crystallite strain in the direction of the alkyl stacking was determined through the following equation:

$$\text{strain} = \frac{d_{alkyl,final} - d_{alkyl,initial}}{d_{alkyl,initial}}$$

2EH/C8 and 2EH/2EH have the most stable in-plane packing with minimal changes in the alkyl stacking distance. 2EH/C8 shows an initial expansion of the lattice, while both 2EH/2EH and C14/2EH are observed to contract. Variations in the in-plane molecular packing were also observed with HRTEM. 2EH/C8 showed strong intercrystallite overlap in-plane while 2EH/2EH mostly had overlap at the crystallite edges. C14/2EH was predicted to not have coherent crystallite overlap due to steric restrictions by the linear tetradecyl side-chains.

112

Therefore, it is possible that the in-plane stacking is stabilized by the intercrystallite overlap observed in HRTEM.

4.3 Discussion

4.3.1 Expansion and Contraction in PBDTTPD Thin Films

Thermal annealing is a common processing method used to optimize the thin film morphology and electrical properties. The effects of annealing on the molecular packing structure of semiconducting polymers and small-molecules and subsequent charge transport properties have been extensively studied in the literature[63], [67]. Gann et al. used in-situ GIWAXS measurements to reveal the evolution of the dominant stacking distances in a series of naphthalene diimide based small-molecules while annealing [65]. Thermal expansion coefficients in the in- and out-of-plane stacking direction were extracted from GIWAXS measurements and correlated with the OTFT mobility, which revealed that significant in-plane thermal expansion with annealing is detrimental to performance. A low in-plane thermal expansion coefficient was determined to be strongly correlated with higher OTFT mobilities. It has also been shown that the crystallographic texture of the polymer N2200 can be tuned from face-on to edge-on by annealing to the polymer melting temperature followed by slow cooling [54]. Additionally, melt-annealed resulted in a slight contraction of the average lamellar spacing from 2.50 to 2.44 nm. In-plane transport in bottom gate TFTs was largely unaffected however, a lower electron-only diode current density indicated poorer transport in the out-of-plane direction after annealing.

Here, GIWAXS *in-situ* annealing was used to examine the effects of thermal annealing on the PBDTTPD thin film structure in real time. While the three materials studied share the same conjugated backbone, modifications of the alkyl side-chains have a large effect on the

key stacking distances, texture, and the response to thermal annealing. The face-on and edge-on populations show differences in the expansion and contraction of the lattice in response to heating and slow cooling. The 2EH/C8 film, which is mostly face-on on, shows an expansion in the edge-on alkyl stacking followed by contraction during slow cooling (Figure 4-23). However, the in-plane alkyl stacking remains relatively constant throughout thermal processing. The 2EH/2EH derivative also shows a stable in-plane alkyl stacking distance during annealing (Figure 4-26). In the out-of-plane direction the alkyl stacking also expands during heating and contracts during cooling. Surprisingly, a split peak forms during annealing which then goes away during cooling (Figure 4-24b). The emergence of a split peak is also observed for C14/2EH (Figure 4-25b). However, a large contraction of the *d*-spacing is observed in-plane, which may be due to the rearrangement of the tetradecyl side-chains.

Small changes in the alkyl side-chain can have a large effect on how the material expands and contracts in response to annealing. Expansion and contraction in-plane may also be limited by the presence of the substrate, whereas in the out-of-plane direction there is not a physical restriction. The thermal response is also a function of film thickness [68], and there were likely slight differences between the derivatives because even though identical solution concentrations and spin conditions were used, each material has a different molecular weight (Table 4-6). Differences in the molecular weight are known to affect the film morphology[69]. Often it is assumed that several derivatives of the same polymer can be processed identically, but small changes to the structure will affect the solubility and film forming behavior. Therefore, it is difficult to say with certainty how to control certain morphological features because relationship between the chemical structure, processing, morphology, and electrical properties is highly complex and will vary from system to system.

The presence of cross-chain structures also likely plays a role in stabilizing the molecular packing in response to temperature fluctuations. Crossed chains may act as physical crosslinks or entanglements which limit the conformational degrees of freedom (Figure 4-27). The presence of crosslinks has been shown to affect how organic thin films expand and contract [70], [71].

4.3.2 Lattice Strain at the Crystallite Overlap

There is a question of whether there is a difference in the molecular packing at the overlap interface and how this contributes to the overall disorder of the system. It is not difficult to imagine that there may a slightly larger separation distance between the alkyl side-chains or the π-faces of the backbone when the chains are in a nonparallel arrangement. Therefore, the stacking distances between the crystallites at overlap points will not necessarily be the same
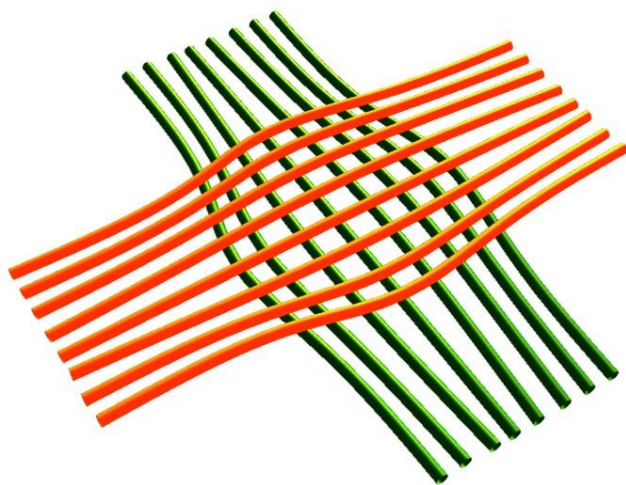
Figure 4-27. Crystallite overlap may act as a physical crosslink to stabilize the packing in response to thermal annealing

as that within an isolated crystallite and would lead to a broadening of the alkyl stacking peak. If there was a fluctuation in the molecular packing at the overlap interface this would generate a strain in the chains right at the overlap which would then be translated through the crystallite. The degree of strain allowed would depend on the flexibility of the polymer backbone.

115

While peak-shape is valuable for distinguishing between broadening caused by disorder versus finite crystallite size, it has been stated that is very difficult to identify the exact origin of the disorder [50], [52], [72]. Lattice disorder can be either non-cumulative (disorder of the 1st kind) or cumulative (disorder of the 2nd kind). In non-cumulative disorder, long-range order is preserved but local perturbations of the structure can occur such as thermal fluctuations, defects, and lattice strain. This type of disorder causes the intensity of diffraction peaks to weaken but not necessarily broaden. On the other hand, with cumulative disorder, long-range order is not preserved due to compounding of small distortions. This leads to a gradual loss of correlation between molecules as the distance between them increases. Distortions can result from a number of effects including polymer backbone twist, dislocations, and positional/orientational fluctuations in the packing of small-molecules. In organic systems, paracrystallinity is considered the dominant type of cumulative disorder resulting from small random fluctuations in the lattice spacings [73].

Lattice strain at the grain boundary between overlapping crystallites would be an example of non-cumulative disorder as the different in molecular packing would not be due to random fluctuations. This can also be observed through the expansion and contraction of the lattice during thermal annealing. The change in peak position for key features such as the π-π and alkyl stacking show how the structure accommodates fluctuations in temperature.

Strain in a particular direction is defined as the lattice distortion along that direction divided by the ideal lattice spacing.

$$e = \frac{\Delta L}{L}$$

Strain can be categorized as uniform or non-uniform. In uniform strain, the deformation is isotropic (extends equally in all directions) and typically caused by effects such as lattice

116

expansion and contraction [74]. This type leads to peak shifts but not peak broadening. However, if there are many isolated populations each with a slightly different lattice parameter, the peaks may overlap to produce a single broadened peak where it can be difficult to deconvolute the contributions of each population. Non-uniform strain is caused by point defects, which will not affect peak position but will lead to peak broadening[75]. Point defects distributed throughout a material will add a degree of cumulative disorder. However. the crossover from uniform to non-uniform strain can be difficult to identify when crystallite size is very small in comparison to the sample size.

Strain caused by the slight expansion or contraction of the lattice at grain boundaries, interfaces, or impurities can lead to variations in the lattice spacing at specific sites within the material. It may be possible to identify this type of disorder through peak-shape analysis when these inhomogeneities are contained within particular areas. However, the "probe" size and resolution of the diffraction technique being used must be considered. If the distorted regions are very small then it will be difficult to decouple their presence from general disorder when averaging over a large sample size. In organic samples, it is reasonable to imagine the formation of regions of inhomogeneous strain during the swelling of a material with solvent and subsequent removal of that solvent through evaporation. Especially when a concentrated solution is used such that molecular interactions in solution lead to aggregation before removal of the solvent.

4.3.3 Origin of Crossed Chain Grain Boundaries

The observation of cross-chain structures in the solid film is likely affected by several factors including the molecular geometry, processing, and aggregation in solution. Simple estimates of geometry and space-filling provide a sense of how the backbones and side-chains

117

could fit together and whether such structures are even possible. However, other factors may play a role such as molecular weight and processing details including the solution temperature and concentration. The origin of the crossing is debated, but it was proposed by Schulz et al. to be a different crystal structure, the result of defects (twinning), as well as related to the degree of aggregation.

The formation of cross-chain structures is likely related to the molecular geometry and the ability of the side-chains to efficiently pack. Quadrites in Si-PCPDTBT were first observed by Takacs et al. [23] and the angle of overlap was found to be related to the crystallographic repeat unit, b, and alkyl stacking distance, d, through the simple equation: $\sin \theta = d/b$. An angle of ~52° was observed with HRTEM, which was also confirmed by Schulz et al. [24]. Additionally, a slightly higher angle between the donor and acceptor units on the polymer backbone was suggested to provide additional room between layers for the side-chains to pack. In early studies of homoepitaxy in isotactic polypropylene, the γ-phase was observed to deposit on the α-phase at a preferred angle of 80° [76] and it was suggested that the methyl groups interdigitate at the overlap point [27]. In the present study, only the 2EH/C8 derivative showed a high degree of coherent overlap around the predicted angle of 60° even though the 2EH/2EH derivative was also predicted to overlap. The lack of overlap in the latter may be due to the presence of branched instead of linear chain on the acceptor unit. Therefore, the bulkiness of the side-chains at the predicted overlap location (acceptor unit) must be considered as well in the picture of the three-dimensional packing.

The specific processing conditions may also affect the formation of cross-chain structures. The cross-hatched morphology in Si-PCPDTBT was found to develop after spin-coating, but was not present after high-temperature (HT) rubbing [24]. HT rubbing is used to align polymer

118

chains in a thin film without the use of a specialized substrate. A cylinder covered in a microfiber cloth is rubbed along the film at high temperatures and is hypothesized to induce alignment by removing chain entanglements [77]. When the crossed structure was suppressed, thermal annealing at 280° led to a change in texture from predominantly face-on to edge-on. This suggests that the absence of the cross-hatched structure makes the crystallites less resistant to reorientation during thermal annealing. However, high temperature annealing of the spun-cast Si-PCPDTBT was not performed and therefore this is simply speculation. Although, in the present study, it was observed that high temperature annealing (250°) of 2EH/C8 film, which forms a heavily cross-hatched structure, caused the percentage of face-on character to increase. The presence of crystallite overlap also makes the structure more stable by minimizing lattice parameter fluctuations in the direction of the alkyl stacking (Figure 4-26). In the PBDTTPD study, the film concentration in 2EH/C8 could be directly related to the density of the overlap, with more concentration films showing extensive overlap.

It is likely that the formation of cross-chain structures and the resulting crystallite texture in thin films is related to molecular interactions in solution. In solution, chains would have a higher number of degrees of freedom than in the solid state. Therefore, the nonparallel arrangement may be one of several metastable states that can form where the likelihood of formation is related to the steric interactions between the backbone and side-chains. Tournebize et al. hypothesized that strong interactions between the π-stacked backbones in PBDTTPD through the sulfur and oxygen atoms on the donor unit would result in a non-parallel stacking where the angle between chains is approximately 64° [56], [57]. However, crossing at the BDT donor unit would also be the most sterically hindered due to the presence of side-chains on both sides. Schulz et al. investigated the formation of the cross-

hatched structure in C-, F-, and Si-PCPDTBT and only the Si derivative formed the face-on crystallites with coherent overlap, which was hypothesized to occur because Si-PCPDTBT aggregated more strongly in solution [24]. Additionally, early work by Khoury [25] showed that interwoven crystallites of the α-phase of iPP form during solution crystallization due to the epitaxial deposition of lamellae off the surface of another lamellae.

4.4 Conclusions

In semiconducting polymers, there is a large gap in the understanding of how ordered regions connect on the nanoscale to form clear charge transport pathways. Often, the main considerations in the backbone design are the absorption properties and energy levels. However, in the future it may also be possible to design for particular modes of crystallite connectivity beyond tie-chains. Because it is often not possible to grow single crystals, thin films with smaller crystallites will inherently have a large number of defects in the form of grain boundaries. This will require additional systematic studies on the effects of small changes to the molecular structure on the resulting mesoscale morphology. HRTEM is a powerful tool for studying grain boundaries in polymers and small-molecules and can help elucidate the connection between molecular structure, processing, and thin film morphology.

References

[1]   M. Samanta, W. Tian, S. Datta, J. Henderson, and C. Kubiak, "Electronic conduction through organic molecules.," *Phys. Rev. B. Condens. Matter*, vol. 53, no. 12, pp. R7626–R7629, 1996.

[2]   H. Sirringhaus, "Device physics of solution-processed organic field-effect transistors," *Adv. Mater.*, vol. 17, no. 20, pp. 2411–2425, 2005.

[3]   H. Sirringhaus *et al.*, "Two-Dimensional Charge Transport in Self-Organized, High-Mobility Conjugated Polymers," *Nature*, vol. 401, no. 6754, pp. 685–688, 1999.

[4]   B. S. Ong, Y. Wu, P. Liu, and S. Gardner, "High-Performance Semiconducting Polythiophenes for Organic Thin-Film Transistors," *J. Am. Chem. Soc.*, vol. 126, no. 11, pp. 3378–3379, 2004.

[5]   I. McCulloch *et al.*, "Liquid-crystalline semiconducting polymers with high charge-carrier mobility.," *Nat. Mater.*, vol. 5, pp. 328–333, 2006.

[6]   D. M. DeLongchamp *et al.*, "High carrier mobility polythiophene thin films: Structure determination by experiment and theory," *Adv. Mater.*, vol. 19, no. 6, pp. 833–837, 2007.

[7]   H. Yan *et al.*, "A high-mobility electron-transporting polymer for printed transistors.," *Nature*, vol. 457, no. 7230, pp. 679–86, Feb. 2009.

[8]   J. Rivnay *et al.*, "Unconventional face-on texture and exceptional in-plane order of a high mobility n-type polymer.," *Adv. Mater.*, vol. 22, no. 39, pp. 4359–63, Oct. 2010.

[9]   W. Zhang *et al.*, "Indacenodithiophene semiconducting polymers for high-performance, air-stable transistors," *J. Am. Chem. Soc.*, vol. 132, no. 33, pp. 11437–11439, 2010.

[10]   P. M. Beaujuge and J. M. J. Fréchet, "Molecular design and ordering effects in π-functional materials for transistor and solar cell applications.," *J. Am. Chem. Soc.*, vol. 133, no. 50, pp. 20009–29, Dec. 2011.

[11]   D. Venkateshvaran *et al.*, "Approaching disorder-free transport in high-mobility conjugated polymers," *Nature*, vol. 515, no. 7527, pp. 384–388, Nov. 2014.

[12]   H. Heil, T. Finnberg, N. Von Malm, R. Schmechel, and H. Von Seggern, "The influence of mechanical rubbing on the field-effect mobility in polyhexylthiophene," *J. Appl. Phys.*, vol. 93, no. 3, pp. 1636–1641, 2003.

[13]   W. Pisula *et al.*, "A zone-casting technique for device fabrication of field-effect transistors based on discotic hexa-perihexabenzocoronene," *Adv. Mater.*, vol. 17, no. 6, pp. 684–688, 2005.

[14] H. A. Becerril, M. E. Roberts, Z. Liu, J. Locklin, and Z. Bao, "High-performance organic thin-film transistors through solution-sheared deposition of small-molecule organic semiconductors," *Adv. Mater.*, vol. 20, no. 13, pp. 2588–2594, 2008.

[15] R. L. Headrick, S. Wo, F. Sansoz, and J. E. Anthony, "Anisotropic mobility in large grain size solution processed organic semiconductor thin films," *Appl. Phys. Lett.*, vol. 92, no. 6, 2008.

[16] H. Tseng *et al.*, "High-Mobility Field-Effect Transistors Fabricated with Macroscopic Aligned Semiconducting Polymers," pp. 2993–2998, 2014.

[17] R. A. Street, J. E. Northrup, and A. Salleo, "Transport in polycrystalline polymer thin-film transistors," *Phys. Rev. B - Condens. Matter Mater. Phys.*, vol. 71, no. 16, pp. 1–13, 2005.

[18] R. Noriega, A. Salleo, and A. J. Spakowitz, "Chain conformations dictate multiscale charge transport phenomena in disordered semiconducting polymers.," *Proc. Natl. Acad. Sci. U. S. A.*, vol. 110, no. 41, pp. 16315–20, Oct. 2013.

[19] R. J. Kline, M. D. McGehee, E. N. Kadnikova, J. Liu, and J. M. J. Fréchet, "Controlling the field-effect mobility of regioregular polythiophene by changing the molecular weight," *Adv. Mater.*, vol. 15, no. 18, pp. 1519–1522, 2003.

[20] R. Noriega *et al.*, "A general relationship between disorder, aggregation and charge transport in conjugated polymers.," *Nat. Mater.*, vol. 12, no. 11, pp. 1038–44, Nov. 2013.

[21] L. H. Jimison, M. F. Toney, I. McCulloch, M. Heeney, and A. Salleo, "Charge-Transport Anisotropy Due to Grain Boundaries in Directionally Crystallized Thin Films of Regioregular Poly(3-hexylthiophene)," *Adv. Mater.*, vol. 21, no. 16, pp. 1568–1572, 2009.

[22] D. C. Martin and Thomas, "Grain boundaries in extended-chain polymers Theory and Experiment," *Philos. Mag. A*, vol. 64, pp. 903–922, 1991.

[23] C. J. Takacs, M. a Brady, N. D. Treat, E. J. Kramer, and M. L. Chabinyc, "Quadrites and crossed-chain crystal structures in polymer semiconductors.," *Nano Lett.*, vol. 14, no. 6, pp. 3096–101, Jun. 2014.

[24] G. L. Schulz *et al.*, "The PCPDTBT Family: Correlations between Chemical Structure, Polymorphism, and Device Performance," *Macromolecules*, vol. 50, no. 4, pp. 1402–1414, 2017.

[25] F. Khoury, "The Spherulitic Crystallization of Isotactic Polypropylene From Solution : On the Evolution of Monoclinic Spherulites From," *J. Res. Natl. Bur. Stand. A*, vol. 70, no. 1, pp. 29–61, 1966.

[26] F. J. Padden and H. D. Keith, "Crystallization in thin films of isotactic

polypropylene," *J. Appl. Phys.*, vol. 37, no. 11, pp. 4013–4020, 1966.

[27]   F. L. Binsbergen and B. G. M. de Lange, "Morphology of polypropylene crystallized from the melt," *Polymer (Guildf).*, vol. 9, pp. 23–40, 1968.

[28]   B. Lotz and J. C. Wittmann, "The molecular origin of lamellar branching in the α (monoclinic) form of isotactic polypropylene," *J. Polym. Sci. Part B Polym. Phys.*, vol. 24, no. 7, pp. 1541–1558, 1986.

[29]   A. J. Lovinger, "Microstructure and unit-cell orientation in α-polypropylene," *J. Polym. Sci. Part B Polym. Phys.*, vol. 21, no. 1, pp. 97–110, 1983.

[30]   J. R. Ojeda and D. C. Martin, "High Resolution Microscopy of PMDA-ODA Poly(imide) Single Crystals," *Macromolecules*, vol. 26, pp. 6557–6565, 1993.

[31]   B. C. Thompson and J. M. J. Fréchet, "Polymer-fullerene composite solar cells.," *Angew. Chem. Int. Ed. Engl.*, vol. 47, no. 1, pp. 58–77, Jan. 2008.

[32]   J. Mei, Y. Diao, A. L. Appleton, L. Fang, and Z. Bao, "Integrated materials design of organic semiconductors for field-effect transistors," *J. Am. Chem. Soc.*, vol. 135, no. 18, pp. 6724–6746, 2013.

[33]   J. Mei and Z. Bao, "Side Chain Engineering in Solution-Processable Conjugated Polymers," *Chem. Mater.*, vol. 26, no. 1, pp. 604–615, 2014.

[34]   T. Lei, J. Wang, and J. Pei, "Roles of Flexible Chains in Organic Semiconducting Materials," *Chem. Mater.*, vol. 26, no. 1, pp. 594–603, 2014.

[35]   W. P. Hsu, K. Levon, K. S. Ho, A. S. Myerson, and T. K. Kwei, "Side-chain order in poly(3-alkylthiophenes)," *Macromolecules*, vol. 26, pp. 1318–1323, 1993.

[36]   R. J. Kline *et al.*, "Critical role of side-chain attachment density on the order and device performance of polythiophenes," *Macromolecules*, vol. 40, no. 22, pp. 7960–7965, 2007.

[37]   X. Zhang *et al.*, "Molecular packing of high-mobility diketo pyrrolo-pyrrole polymer semiconductors with branched alkyl side chains.," *J. Am. Chem. Soc.*, vol. 133, no. 38, pp. 15073–84, Sep. 2011.

[38]   A. Babel and S. A. Jenekhe, "Alkyl chain length dependence of the field-effect carrier mobility in regioregular poly(3-alkylthiophene)s," *Synth. Met.*, vol. 148, no. 2, pp. 169–173, 2005.

[39]   Y. D. Park *et al.*, "Effect of side chain length on molecular ordering and field-effect mobility in poly(3-alkylthiophene) transistors," *Org. Electron. physics, Mater. Appl.*, vol. 7, no. 6, pp. 514–520, 2006.

[40]   L. Yang, H. Zhou, and W. You, "Quantitatively Analyzing the Influence of Side

Chains on Photovoltaic Properties of Polymer-Fullerene Solar Cells," *J. Phys. Chem. C*, vol. 114, pp. 16793–16800, 2010.

[41] C. Piliego, T. W. Holcombe, J. D. Douglas, C. H. Woo, P. M. Beaujuge, and J. M. J. Fre, "Synthetic Control of Structural Order in N -Alkylthieno [3 , 4- c] pyrrole-4 , 6-dione-Based Polymers for Efficient Solar Cells," pp. 7595–7597, 2010.

[42] C. Cabanetos *et al.*, "Linear Side Chains in Benzo[1,2-b:4,5-b′]dithiophene−Thieno[3,4-c]pyrrole-4,6-dione Polymers Direct Self-Assembly and Solar Cell Performance," *J. Am. Chem. Soc.*, vol. 135, no. 12, p. 4656−4659, 2013.

[43] C. Piliego, T. W. Holcombe, J. D. Douglas, C. H. Woo, P. M. Beaujuge, and J. M. J. Fréchet, "Synthetic Control of Structural Order in N -Alkylthieno[3,4-c]pyrrole-4,6-dione-Based Polymers for Efficient Solar Cells," *J. Am. Chem. Soc.*, vol. 132, no. 22, pp. 7595–7597, 2010.

[44] Y. Zou *et al.*, "A Thieno[3, 4-c]pyrrole-4, 6-dione-Based Copolymer for Efficient Solar Cells," *J. Am. Chem. Soc.*, vol. 132, no. 15, pp. 5330–5331, 2010.

[45] K. R. Graham *et al.*, "Importance of the Donor:Fullerene Intermolecular Arrangement for High-Efficiency Organic Photovoltaics," *J. Am. Chem. Soc.*, vol. 136, no. 27, pp. 9608–9618, 2014.

[46] A. El Labban *et al.*, "Dependence of Crystallite Formation and Preferential Backbone Orientations on the Side Chain Pattern in PBDTTPD Polymers," *ACS Appl. Mater. Interfaces*, vol. 6, no. 22, pp. 19477–19481, Nov. 2014.

[47] X.-K. Chen, T. Wang, and J.-L. Brédas, "Suppressing Energy Loss due to Triplet Exciton Formation in Organic Solar Cells: The Role of Chemical Structures and Molecular Packing," *Adv. Energy Mater.*, p. 1602713, 2017.

[48] M. L. Chabinyc, *X-ray Scattering from Films of Semiconducting Polymers*, vol. 48, no. 3. 2008.

[49] J. Rivnay, S. C. B. Mannsfeld, C. E. Miller, A. Salleo, and M. F. Toney, "Quantitative determination of organic semiconductor microstructure from the molecular to device scale," *Chem. Rev.*, vol. 112, no. 10, pp. 5488–5519, Oct. 2012.

[50] J. Rivnay, R. Noriega, R. J. Kline, A. Salleo, and M. F. Toney, "Quantitative analysis of lattice disorder and crystallite size in organic semiconductor thin films," *Phys. Rev. B*, vol. 84, no. 4, p. 45203, 2011.

[51] D. M. Smilgies, "Scherrer grain-size analysis adapted to grazing-incidence scattering with area detectors," *J. Appl. Crystallogr.*, vol. 42, no. 6, pp. 1030–1034, 2009.

[52] A. Guinier, *X-ray diffraction in crystals, imperfect crystals, and amorphous bodies*. Courier Corporation, 1994.

[53] J. L. Baker *et al.*, "Quantification of thin film crystallographic orientation using X-ray diffraction with an area detector.," *Langmuir*, vol. 26, no. 11, pp. 9146–51, Jun. 2010.

[54] J. Rivnay *et al.*, "Drastic control of texture in a high performance n-type polymeric semiconductor and implications for charge transport," *Macromolecules*, vol. 44, no. 13, pp. 5246–5255, 2011.

[55] B. Lotz, S. Graff, and J. C. Wittmann, "Crystal morphology of the γ (triclinic) phase of isotactic polypropylene and its relation to the α phase," *J. Polym. Sci. Part B Polym. Phys.*, vol. 24, no. 9, pp. 2017–2032, 1986.

[56] A. Tournebize *et al.*, "Is there a photostable conjugated polymer for efficient solar cells?," *Polym. Degrad. Stab.*, vol. 112, pp. 175–184, 2015.

[57] S. Lois *et al.*, "How to build fully π-conjugated architectures with thienylene and phenylene fragments," *European J. Org. Chem.*, no. 24, pp. 4019–4031, 2007.

[58] M. L. Chabinyc, M. F. Toney, R. J. Kline, I. McCulloch, and M. Heeney, "X-ray scattering study of thin films of poly(2,5-bis(3-alkylthiophen-2-yl)thieno[3,2-b]thiophene).," *J. Am. Chem. Soc.*, vol. 129, no. 11, pp. 3226–3237, 2007.

[59] X.-Q. Chen *et al.*, "Long-Term Thermally Stable Organic Solar Cells Based on Cross-linkable Donor-Acceptor Conjugated Polymers," *J. Mater. Chem. A*, vol. 4, p. 9286, 2016.

[60] T. L. D. Tam and T. T. Lin, "Tuning Energy Levels and Film Morphology in Benzodithiophene-Thienopyrrolodione Copolymers via Nitrogen Substitutions," *Macromolecules*, vol. 49, no. 5, pp. 1648–1654, 2016.

[61] B. J. Tremolet De Villers *et al.*, "Removal of Residual Diiodooctane Improves Photostability of High-Performance Organic Solar Cell Polymers," *Chem. Mater.*, vol. 28, no. 3, pp. 876–884, 2016.

[62] L. A. Perez *et al.*, "Solvent additive effects on small molecule crystallization in bulk heterojunction solar cells probed during spin casting," *Adv. Mater.*, vol. 25, no. 44, pp. 6380–6384, 2013.

[63] E. Verploegen, R. Mondal, C. J. Bettinger, S. Sok, M. F. Toney, and Z. Bao, "Effects of thermal annealing upon the morphology of polymer-fullerene blends," *Adv. Funct. Mater.*, vol. 20, no. 20, pp. 3519–3529, 2010.

[64] N. D. Treat *et al.*, "Interdiffusion of PCBM and P3HT Reveals Miscibility in a Photovoltaically Active Blend," *Adv. Energy Mater.*, vol. 1, no. 1, pp. 82–89, Jan. 2011.

[65] E. Gann, X. Gao, C. Di, and C. R. McNeill, "Phase transitions and anisotropic thermal expansion in high mobility core-expanded naphthalene diimide thin film transistors," *Adv. Funct. Mater.*, vol. 24, no. 45, pp. 7211–7220, 2014.

[66]   N. D. Treat, C. G. Shuttle, M. F. Toney, C. J. Hawker, and M. L. Chabinyc, "In situ measurement of power conversion efficiency and molecular ordering during thermal annealing in P3HT:PCBM bulk heterojunction solar cells," *J. Mater. Chem.*, vol. 21, no. 39, pp. 15224–15231, 2011.

[67]   J. Huang *et al.*, "Annealing effect of polymer bulk heterojunction solar cells based on polyfluorene and fullerene blend," *Org. Electron.*, vol. 10, no. 1, pp. 27–33, 2009.

[68]   L. Singh, P. J. Ludovice, and C. L. Henderson, "Influence of molecular weight and film thickness on the glass transition temperature and coefficient of thermal expansion of supported ultrathin polymer films," *Thin Solid Films*, vol. 449, no. 1–2, pp. 231–241, 2004.

[69]   J. a. Bartelt *et al.*, "Controlling Solution-Phase Polymer Aggregation with Molecular Weight and Solvent Additives to Optimize Polymer-Fullerene Bulk Heterojunction Solar Cells," *Adv. Energy Mater.*, vol. 4, no. 9, Jun. 2014.

[70]   D. J. Broer and G. N. Mol, "Anisotropic thermal expansion of densely cross-linked oriented polymer networks," *Polym. Eng. Sci.*, vol. 31, no. 9, pp. 625–631, 1991.

[71]   S. A. Vaselabadi, D. Shakarisaz, P. Ruchhoeft, J. Strzalka, and G. E. Stein, "Radiation damage in polymer films from grazing-incidence X-ray scattering measurements," *J. Polym. Sci. Part B Polym. Phys.*, vol. 54, no. 11, pp. 1074–1086, 2016.

[72]   B. E. Warren, *X-ray Diffraction*. Mineola, NY, 1969.

[73]   P. H. Lindenmeyer and R. Hosemann, "Application of the theory of paracrystals to the crystal structure analysis of polyacrylonitrile," *J. Appl. Phys.*, vol. 34, no. 1, pp. 42–45, 1963.

[74]   R. W. Balluffi, *Introduction to Elasticity Theory for Crystal Defects*, 2nd ed. World Scientific Publishing, 2017.

[75]   H. Takahashi, "Fourier Coefficients of Line Profiles of Debye-Scherrer Rings Broadened by Lattice Distortion," *J. Phys. Soc. Japan*, vol. 27, no. 3, pp. 708–712, 1969.

[76]   F. J. Padden and H. D. Keith, "Mechanism for lamellar branching in isotactic polypropylene," *J. Appl. Phys.*, vol. 44, no. 3, pp. 1217–1223, 1973.

[77]   L. Biniek *et al.*, "High-temperature rubbing: A versatile method to align π-conjugated polymers without alignment substrate," *Macromolecules*, vol. 47, no. 12, pp. 3871–3879, 2014.

Chapter 5

Studies of Thermal and Photostability of Semiconducting Polymers

5.1 Introduction

The successful commercialization of organic photovoltaics (OPVs) and organic thin-film transistors (OTFTs) will require a clear understanding of both chemical degradation mechanisms and the morphological response of the active layer to common processing methods. Device lifetimes vary considerably depending the chemical photostability of the active layer [1], which is also highly connected to the molecular structure [2], processing methods, and illumination conditions [3]. Ultimately, achieving a high solar power conversion efficiency or high charge carrier mobility is meaningless unless it is also accompanied by a stable operation of the device.

The photo- and thermal stability of semiconducting polymers is affected by both the specific moieties contained in the conjugated backbone as well as the nature of the aliphatic side-chains. Manceau et al. found that the photo and thermal degradation of P3HT is driven by radical oxidation of the side-chains which leads to thiophene ring degradation and a reduction in the conjugation length [4]. A similar conclusion was reached by Hintz et al., however, degradation of P3HT by ozonolysis occurs primarily in the thiophene rings and not the side-chains [5]. Sivula et al. found that the thermal stability of P3HT is increased by decreasing the regioregularity without changing the chemical nature of the conjugated backbone [6]. The photochemical stability of dithienylbenzothiadiazole (DBT) and cyclopentadithiophene based copolymers improved by substituting a silicon atom for the carbon atom at the bridgehead group of the cyclopentadithiophene and the effect was

rationalized by the tendency of the carbon derivative to be more readily oxidized [7]. Manceau et al. examined over 20 different conjugated polymers to determine the effect of the backbone structure. Several moieties were shown to reduce the photochemical stability including exocyclic double bonds, cyclopentadithiophene units, and bonds that can be easily cleaved such as C-O and C-N [8]. The side-chain attachments along the conjugated backbone also play a role [9]. The use of linear over branched side-chains was found to afford greater thermal stability of polymers such as PCPDTBT [10].

There is evidence that the polymer morphology and degree of crystallinity affect the degradation mechanism. For example, in BHJs, the photostability of P3HT and dithienylthiazolo[5,4-d]thiazole (DTZ) and silolodithiophene (SDT) based copoloymers improved when blended with PCBM compared to the pristine films [11]. This was attributed to the ability of PCBM to scavenge free-radicals. However, photodegradation is enhanced when PBCM is blended with poly[2,6-(4,4-bis(2-ethylhexyl)-4H-cyclopenta[2,1-b;3,4-b′]-dithiophene)-alt-4,7-(2,1,3-benzothiadiazole)] (C- PCPDTBT) [12]. In P3HT, the rate of photodegradation was directly linked to the polymer regioregularity, which affects the degree of crystallinity [13]. This was also observed for small-molecules used in BHJs where highly crystalline materials were more resistant to degradation from heat and light [14]. The photochemical stability was examined for several materials including PBDTTPD, PCDTBT, and P3HT, by measuring the rate of change in the absorption spectra during illumination [15]. It was found that amorphous materials degrade faster than crystalline, and PBDTTPD was the polymer with the lowest rate of photobleaching indicating a more stable structure. A higher crystalline content protects the structure from degradation by radical chain oxidation, which

128

is known to occur primarily in the amorphous regions of the material. This is because the diffusion of oxygen is higher in the amorphous than crystalline domains [16], [17].

In many cases, the electrical performance can be strongly affected even in the absence of changes in the chemical structure. A number of techniques are used to optimize the morphology of organic semiconductors including varying the deposition method [18], thermal annealing [19], [20], and the use of solvent additives [21]–[23]. In bulk-heterojunction (BHJ) solar cells, processing methods affect the degree of phase separation between the donor and acceptor in the BHJ, which is highly complex [24], [25]. Because of the large variation in donor and acceptor molecular structure, there is not a set of universal rules for producing high efficiency solar cells. Frequently high temperature anneals between 100-200° C are used to optimize the morphology but every system responds differently. For example, in the study of alternative acceptor materials, annealing can both decrease [26] and increase [27] the power conversion efficiency (PCE).

Because both the morphology and chemical stability of organic semiconductors modify the performance of devices, it is critical to use a variety of characterization methods to understand how such changes manifest. Here, the photo- and thermal degradation is the studied in polymers PTB7-Th and PBDDTPD, respectively. It was found that the side-chains can easily damage to form radical species which lead to a reduction in the polymer conjugation length. However, that process can be accelerated by the presence of impurities in the active layer[28], [29]. Additionally, thermal processing is a common processing step but both the temperature and length of the annealing treatment contribute to degradation. Often, testing of the thermal stability of the material with differential scanning calorimetry (DSC) or thermogravimetric analysis (TGA) is conducted over a timescale that is shorter than will be

129

used during processing. This can lead to unexpected polymer degradation during longer periods of thermal annealing. Steps must be taken to ensure that the processing steps used during device fabrication do not damage the organic materials.

5.2 Residual Diiodooctane (DIO) Facilitates Light-induced Degradation of Semiconducting Polymers

Section adapted from Ref. [30]:

Tremolet De Villers, B. J.; O'Hara, K. A.; Ostrowski, D. P.; Biddle, P. H.; Shaheen, S. E.;

Chabinyc, M. L.; Olson, D. C.; Kopidakis, N. *Chem. Mater.* **2016**, *28* (3), 876–884.)

5.2.1 Background

Solvent additives are a common processing method to improve the efficiencies of BHJ solar cells. The power conversion efficiency (PCE) of BHJs is highly dependent on their phase separated morphology due to the need to form bicontinuous nanoscale domains that enable efficient charge generation and extraction [31]. Solvent additives have been found to affect the morphology that forms upon solvent evaporation by preferentially solvating either the donor or acceptor [32]–[34]. This change can lead to increases in the crystallinity of the donor and acceptor which improves charge carrier generation and extraction [35].

A variety of co-solvents, or additives, have been explored to improve the performance of BHJs. The benefits of using solvent additives were first discovered by adding small amounts of alkyl thiols to the donor-acceptor solution before casting [32], [33]. This change resulted in an increase in the efficiency of PCPDTBT:PC$_{71}$BM solar cells from 2.8 to 5.5% [33]. Lee et al. examined the use of 1,8-di(R)octanes on BHJ morphology and efficiency, where an R group of iodine of bromine produced the best results [36]. High boiling point solvents such as

1,8-diiodooctane (DIO), have been used to improve device efficiencies for BHJs containing

PCBM blended with PCPDTBT [37], PCDTBT [38], P3HT [39], PTB7 [40], and PTB7-Th.

DIO is widely used in many BHJs, but its impact on the longevity of BHJs has not been widely

examined.

The use of low-bandgap polymers with a high HOMO energy level as the donor material

is a strategy to achieve higher PCEs by increasing the efficiency of light harvesting [41]–[43].

The PTB family of donor polymers were initially designed to have enhanced light absorption

and increased backbone planarity and π-π stacking to improve charge carrier mobilities [44],
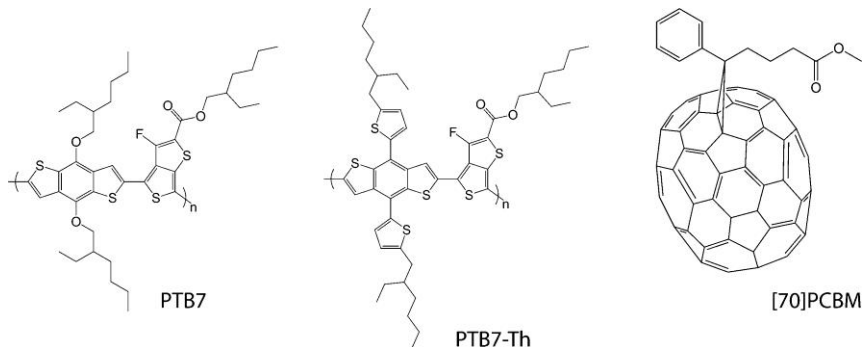
Figure 5-1. Molecular structures for PTB7, PTB7-Th, and PB$_{71}$BM. Figure
reproduced with permission from Ref. [30].

[45]. The low-bandgap polymer thieno[3,4-b]-thiophene/benzodithiophene (PTB7), is a

successful donor material and has been combined with PC$_{71}$BM to routinely achieve PCEs of

around 9% [40], [46], [47]. The PCE has been shown to increase with the use of DIO as a

processing additive [40]. An analogue of PTB7 was developed, PTB7-Th, which has

alkylthienyl side-groups off the benzodithiophene (BDT) unit on the backbone [48]. PCEs of

10.8% are achieved with a fullerene acceptor and through the addition of DIO [49]. It is

therefore of great interest to understand if materials such as PTB7-Th maintain their

performance under operational conditions.

Here, BHJs were formed by a blend of the low-bandgap donor polymer PTB7-Th and the small-molecule acceptor $PC_{71}BM$ (Figure 5-1). The active layer was deposited from a chlorobenzene solution with 3% volume of DIO, and achieved a PCE of 9%. However, illumination over a period of 12 hours resulted in a worsening of the solar cell performance. Several methods were used to characterize the morphology of the active layer before and after illumination both with residual DIO present and after removal. These included optical microscopy (OM), ultraviolet-visible (UV-Vis) absorption measurements, and grazing incidence wide-angle X-ray scattering (GIWAXS).

5.2.2 Probing Structure with GIWAXS Before and After Illumination

Changes in the nanostructure of the films upon illumination were measured using grazing
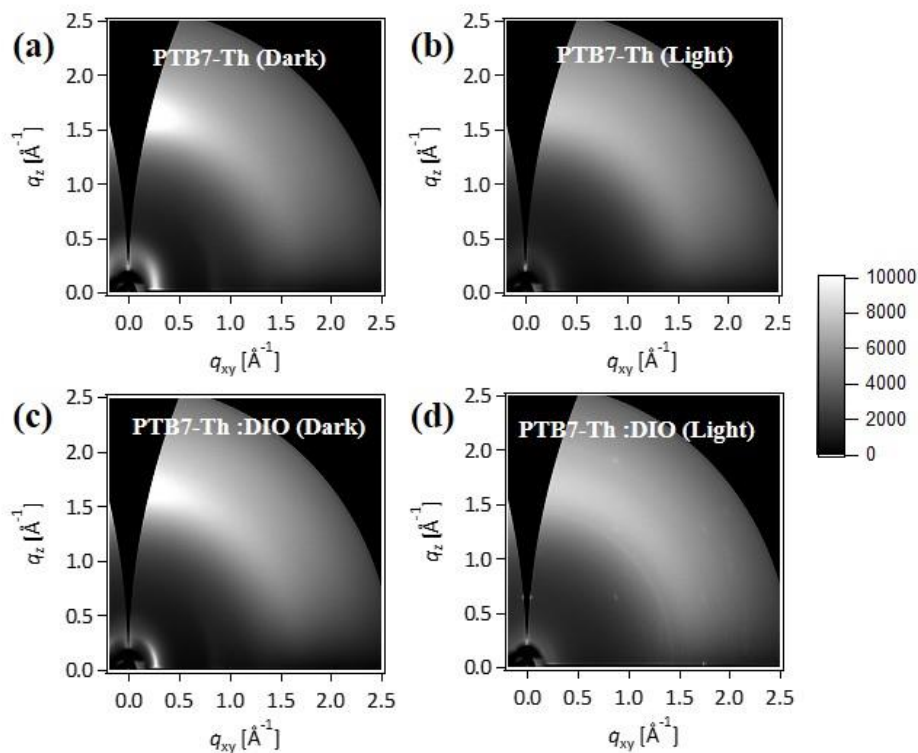
Figure 5-2. GIWAXS 2D scattering images of neat PTB7-Th films with and without DIO and either kept in the dark or exposed to ambient white light illumination for three hours. Reprinted with permission from Ref. [30].

132

incidence wide angle X-ray scattering (GIWAXS) (Figure 5-3: line profiles; Figure 5-2 & Figure 5-4: 2D scattering images; Table 5-1: Peak fitting parameters). Irradiation of the neat polymer and blend under 1 sun illumination leads to several structural changes in the polymer, most noticeably in the alkyl stacking distance. Before illumination, the neat PTB7-Th film has an in-plane peak at $q = 0.26$ Å^{-1} corresponding to an alkyl stacking distance of 24 Å. After exposure to light, the alkyl stacking distance shifts to 23 Å. Similar variations in the alkyl stacking distance ($\sim$1 Å) are commonly observed between as-cast and annealed polymer films and can be attributed to relatively small changes in the geometry of the side chains.[50] When DIO is added to the neat polymer, the alkyl stacking distance is 23 Å prior to illumination and
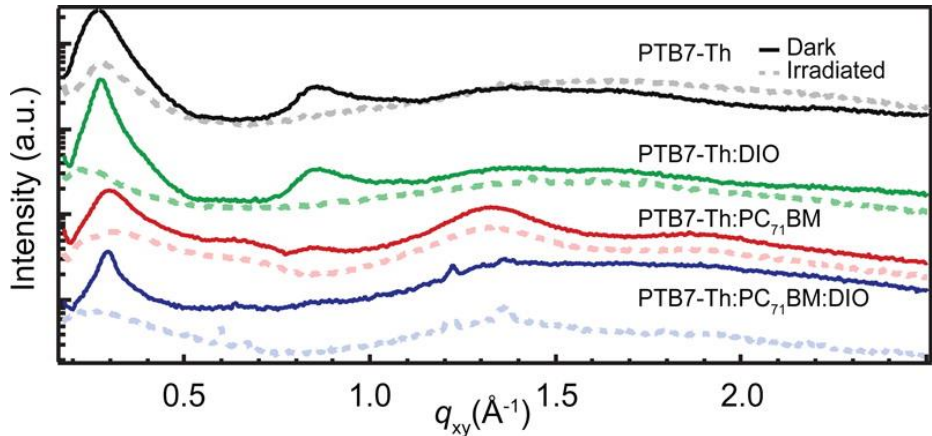
Figure 5-3. In-plane GIWAXS line profiles of PTB7-Th and PTB7-Th:PC71BM thin films. Samples were processed with or without DIO and either kept in the dark or exposed to ambient white light illumination for 3 h. 2D. Reprinted with permission from Ref. [30].

Table 5-1. GIWAXS peak fitting parameters.

Sample	q=0.20				q=0.26			
	center pos. q_{xy} (Å^{-1})	d-spacing (Å)	FWHM (Å^{-1})	Area	center pos. q_{xy} (Å^{-1})	d-spacing (Å)	FWHM (Å^{-1})	Area
PTB7-Th Dark					0.26	24	0.085	7210
PTB7-Th Light					0.27	23	0.094	2017
PTB7-Th :DIO_dark					0.27	23	0.053	7409
PTB7-Th :DIO_light	0.21	30	0.052	579	0.26	24	0.082	833
PTB7-Th :PC$_{71}$BM_dark					0.29	21	0.094	3234
PTB7-Th :PC$_{71}$BM_light	0.22	29	0.035	110	0.28	22	0.14	1468
PTB7-Th :PC$_{71}$BM:DIO_dark					0.29	22	0.053	962
PTB7-Th :PC$_{71}$BM:DIO_light	0.20	31	0.061	218	0.28	23	0.15	944

133

24 Å after illumination, again relatively small shifts. Larger changes occur when PTB7-Th is blended with PC71BM; the alkyl stacking distance shifts to 22 Å for blends with DIO and 21 Å without DIO. The distance increases by ~1 Å for each blend after light exposure. More significant is the emergence of a new in-plane peak at $q = 21 Å^{-1}$ for samples exposed to light, which corresponds to a *d*-spacing of about 30 Å. This feature is present for PTB7-Th with DIO and the blend PTB7-Th:PC71BM with and without DIO and is attributed to formation of products from photodegradation rather than a simple shift in structure.

The process of degradation of PTB7-Th in going from dark to light appears to be exaggerated when DIO is present. There is a noticeable drop in intensity for the in-plane alkyl stacking peak at $q = 0.26 Å^{-1}$ and the out-of-plane $\pi-\pi$ stacking at $q \sim 1.63 Å^{-1}$ after PTB7-Th films with and without DIO are illuminated. This result is expected because light has been
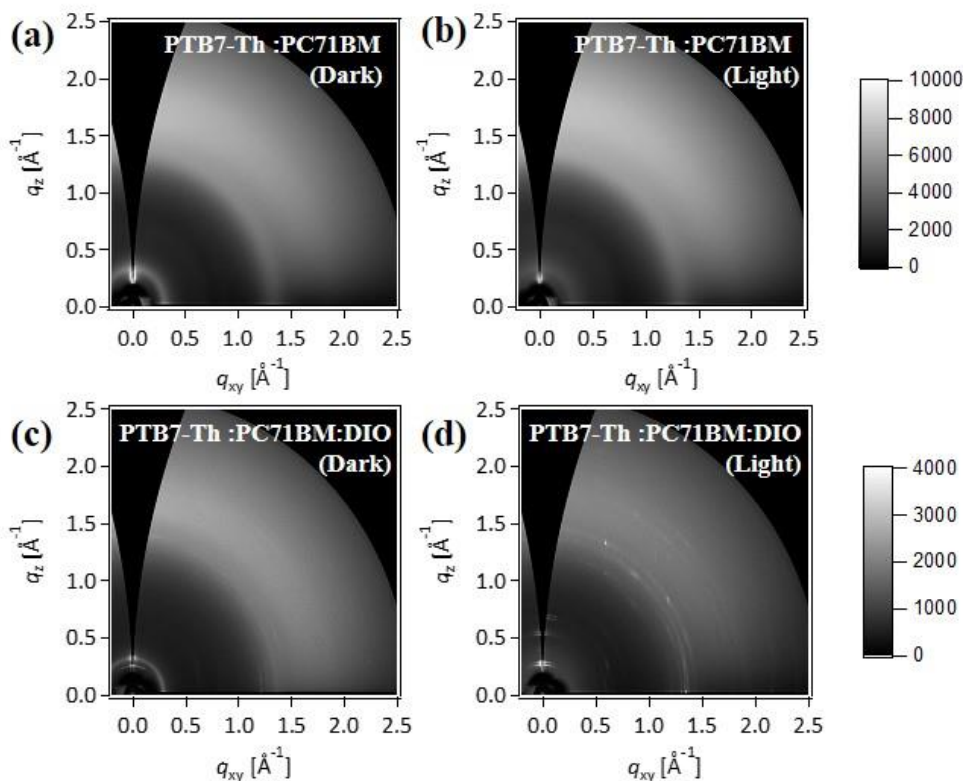
Figure 5-4. GIWAXS 2D scattering images of neat PTB7-Th:PC$_{71}$BM blend films with and without DIO and either kept in the dark or exposed to ambient white light illumination for three hours. Reprinted with permission from Ref. [30]

Films after 1 hr of light exposure
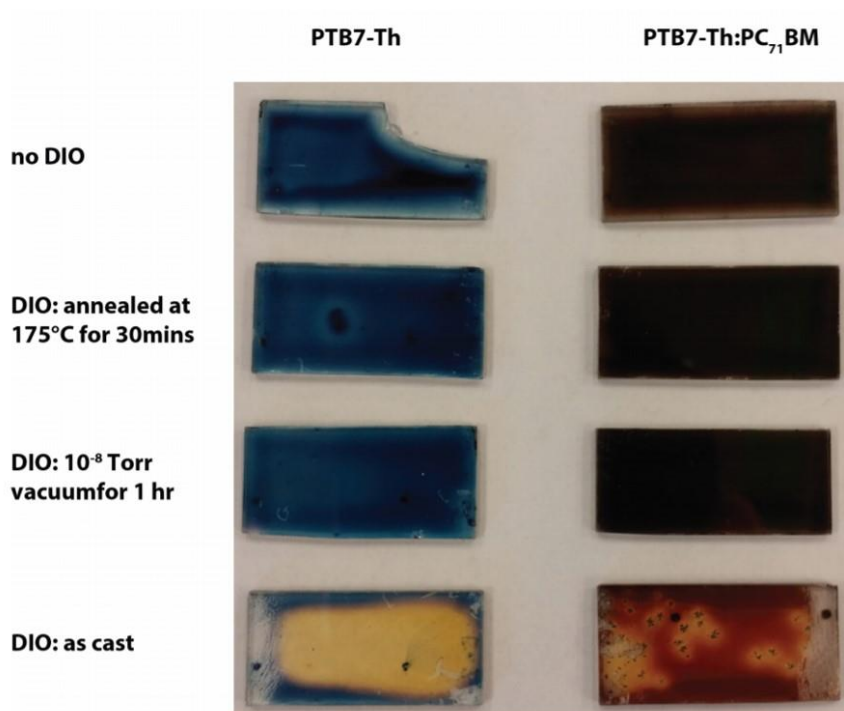
Figure 5-5. Photographs of PTB7-Th and PTB7-Th:PC71BM films after one hour of ambient. Reproduced with permission from Ref. [30].

shown to cause degradation of PTB7-Th without the presence of additives;[51] however, the effect is more pronounced in the film cast with DIO. This greater degradation is evidenced by the change in the polymer alkyl peak full-width- half-maximum (FWHM) value, which was used to calculate the lower limit on the coherence length of crystallites in the in- plane direction of PTB7-Th (Table 5-1).[52], [53] Before illumination, the neat polymer film had an average coherence length of 134 Å, which increased to 212 Å when DIO was added. After ambient white light illumination for 3 hours, the polymer coherence length decreased by 10% to 121 Å, compared to a 35% decrease to 138 Å with DIO present. Additionally, the coherence length of PBT7-Th in the blend without DIO decreased by ~33% after illumination, while the blend with DIO showed a 66% decrease.

The formation of photodegradation byproducts can also be observed in the GIWAXS patterns. The dark PTB7-Th:DIO film has the characteristic alkyl stacking peak at 0.26 Å^{-1} and $\pi-\pi$ stacking at $q \sim 1.63$ Å^{-1}. However, after exposure to light, discrete spots and arcing are present throughout the diffraction pattern. This same effect is observed in the DIO containing blend; however, it is unclear which peaks arise from the crystallization of PC$_{71}$BM versus the polymer photodegradation byproduct, but both are likely present. Optical micrographs of the PTB7-Th:PCBM:DIO film show the film is inhomogeneous with large aggregates present after irradiation, which are likely PC$_{71}$BM (Figure 5-5). Liu et al. noted that DIO was a good solvent for PCBM, but a poor solvent for PTB7; thus, after the chlorobenzene in the film evaporates and the PTB7 solidifies, the DIO provides the PCBM with increased mobility to diffuse through the film and crystallize.[51]

5.2.3   Conclusions

Solvent additives such as diiodooctane (DIO) are nearly ubiquitous in processing high performance organic photovoltaic (OPV) active layers. Here, the effects of DIO on the long-term stability of neat PTB7-Th thin films and BHJs with PC$_{71}$BM were investigated. It was found that residual DIO was present in the thin film after deposition, which accelerated polymer photodegradation during solar cell operation and decreased the performance. A mechanism for the degradation was proposed (Figure 5-6). The degradation was initiated by photolysis of the DIO which resulted in the production of an iodooctane radical, which then reacted with the polymer backbone leading to the formation of more highly reactive radical species. Optical microscopy results indicated that a decrease in performance was accompanied

Radical initiation:
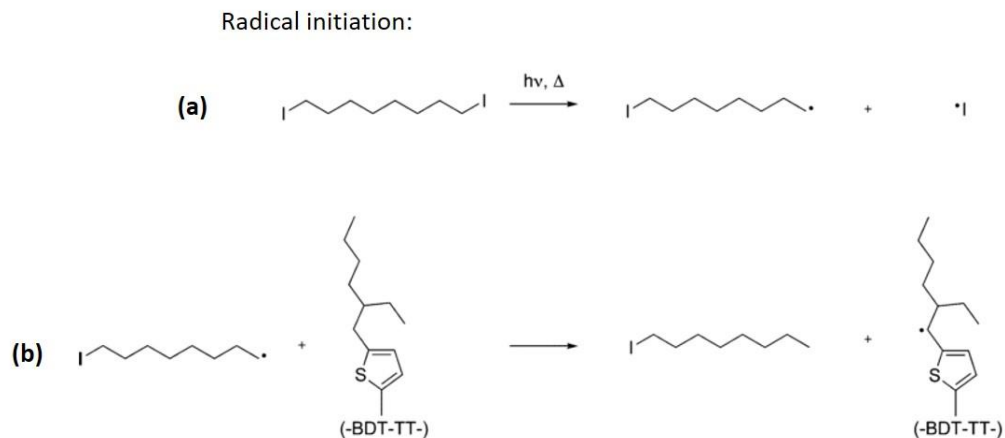
Figure 5-6. Proposed degradation mechanism. (a) Photolysis of diiodooctane (DIO) results in the formation of an iodooctane radical and (b) PTB7-Th radical photo-oxidation initiated when the iodooctane radical abstract a hydrogen atom from the α-carbon of the ethylhexylthienyl side chain of the polymer BDT unit. Adapted with permission from Ref. [30].

by a coarsening of the blend morphology, which is known to occur in BHJs over time [54]. In addition, a decrease in the in the ordering of the polymer was observed with GIWAXS through a reduction in the alkyl stacking peak intensity. Ultimately, when processing polymer solar cells with DIO-containing solutions, it is imperative to remove any trace amounts of DIO from deposited films. It was demonstrated that residual DIO could be removed and photodegradation delayed by post-processing methods such as a high vacuum (10^{-8} Torr) treatment for 60 min or a high-temperature thermal anneal at 175 °C for 30 min. These additional steps must be included during solar cell fabrication to extend lifetimes of solar cell devices using PTB7 and PTB7-Th.

5.3 Thermal Annealing Induced Degradation of Semiconducting Polymer, PBDTTPD

PBDTTPD is a successful donor material in BHJ solar cells due to its low-lying HOMO level [55], [56]. It is another example of a donor-acceptor or "push-pull" copolymer, named

for the presence of both electron rich and electron poor moieties in the monomer unit. This molecular design is an effective way to lower the polymer bandgap to increase the overlap with the solar spectrum [57]. BHJs with PCBM achieve a PCE of 7.5% for an octyl chain on the TPD acceptor unit and 8.5% for a heptyl [58]. In these BHJs, PBDTTPD has a face-on texture (the conjugated π-faces of the backbone are oriented parallel to the substrate) which is has also been observed for other polymers in the PTB family [59]. The side-chain substitution has been shown to have a large effect on the BHJ morphology and resulting solar cell properties [60], [61].

The thermal and photostability of PBDTTPD has been the subject of various studies in an effort to understand and control the lifetimes of solar cells. While thermal annealing results in an increase in PCE for many materials such as P3HT [19], that is not always the case for some D-A copolymers [62], and it may be related to degradation. PBDTTPD is reported to have a high photostability, which is related to strong intermolecular interactions in the π-stacking direction [63]. Degradation of the aliphatic sidechains of PBDTTPD in the solid state was monitored with IR spectroscopy and it was found that the rate of photo-ageing was dependent on the temperature that solutions were heated to before spin-casting [63]. Thin film deposition from cold solutions (50°C) made the aliphatic groups more stable to photooxidation compared to hot solutions (130°C). The high photostability may also be due to the presence of the alkoxy side-chains instead of alkyl side-chains on the BDT unit; it has been proposed that the oxygen atom can destabilize the radical species which may form [64]. Additionally, stability has been shown to improve in BHJs through extra purification steps to remove impurities from the polymer [29].

During microstructural analysis of neat films of PBDTTPD, it was found that multiple techniques including GIWAXS, HRTEM, UV-Vis spectroscopy, and fluorescence spectroscopy were necessary to understand the thermal stability. Thermal analysis including DSC and thermogravimetric analysis (TGA) is commonly used a predictive method to determine appropriate thermal annealing temperatures for organic electronic devices. Previous studies of this polymer using differential scanning calorimetry (DSC) showed no obvious thermal transitions between room temperature and 300°C, and a degradation temperature around 330°C by TGA [65]. Here we find that under typical processing conditions that degradation can indeed occur despite the apparent lack of change by TGA.

5.3.1 Change in Absorption Properties with Thermal Annealing

Thin films were prepared by spin-casting a solution of PBDTTPD (Figure 5-7) from chlorobenzene. In an effort to increase film ordering and enable the polymer to find a more stable microstructure, films were annealed in a nitrogen glovebox at 275°C for 20 hours. A comparison of the as-cast and annealed morphology was made. Additionally, a color change
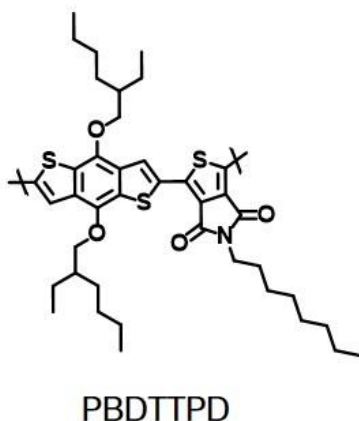
PBDTTPD

Figure 5-7. Molecular structure of PBDTTPD.
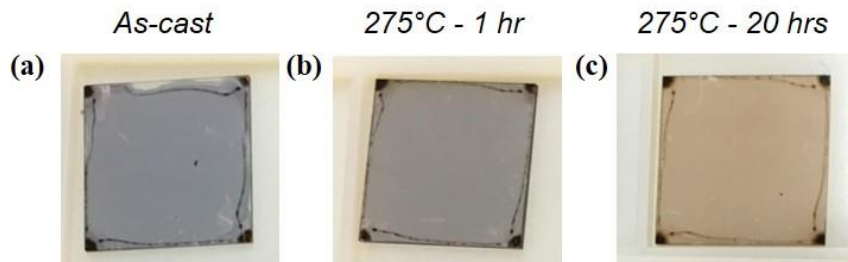
Figure 5-8. Visible color change in the film (a) before annealing and after for (b) 1 hour and (c) 20 hours at 275°C.

occurred after annealing, a common occurrence with changes in structural ordering, although, it can also indicate chemical degradation [2]. Significant material degradation was detected with UV-Vis and fluorescence spectroscopy measurements. Surprisingly, obvious signs of chemical damage were not evident in GIWAXS and HRTEM. The structural measurements suggested a change in the molecular packing, but the films did not appear to become more disordered as might be expected for significantly degraded sample. While GIWAXS is a useful tool for detecting degradation when a loss of order results, it can be misleading if degradation results in a transformation that does not strongly change the ordering.

Deposition of the polymer films onto transparent quartz substrates allowed for observation of color changes occurring with annealing. Figure 5-8 shows that the as-cast film is blue and eventually turns orange after annealing for 20 hours at 275°C. This temperature is below the temperature of weight loss by TGA, which is a commonly used metric for the stability of thin polymer films. This spectral shift towards the blue is often indicative of a reduction in the conjugation length of the polymer backbone [2].

The effect of thermal annealing at 275°C under inert conditions on the absorption properties is made clear through UV-Vis and fluorescence spectroscopy measurements (Figure 5-9a, b). Here subtle changes are observed in the absorbance spectra after only 10 minutes of annealing such as a reduction in absorbance and a shift of the 630nm peak to 620
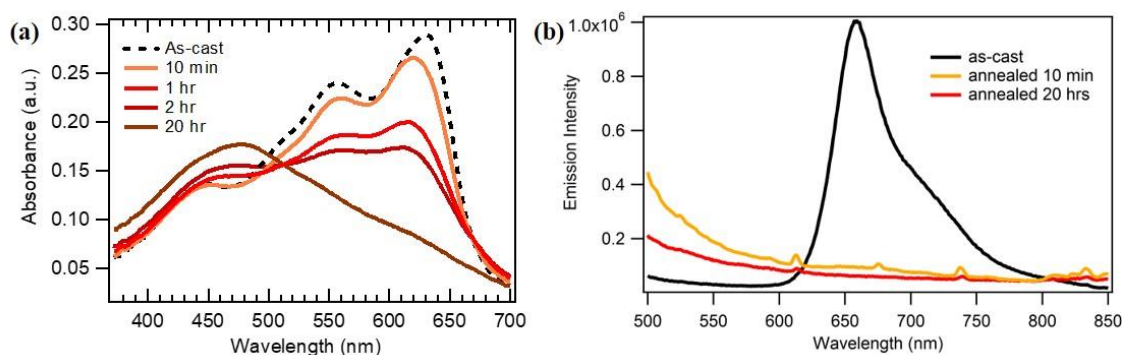
Figure 5-9. (a) UV-Vis absorption and (b) emission of the PBDTTPD film before and after annealing.

nm. Annealing for 1 and 2 hours results in additional loss of absorbance. Additionally, a new peak emerges around 475 nm, which increases in intensity with annealing time. After 20 hours, the lower energy peaks (620 and 560nm) are almost completely quenched. The absorbance feature at 475 nm peak becomes more intense, and is likely a product of the degradation. Overall, the blue-shift observed with annealing indicates a decrease in the polymer conjugation length. The original structure in the film appears entirely degraded after 20 hours and the new peak at 475 nm indicates that there is a chemical change to the conjugated backbone.

Fluorescence spectroscopy can be used to detect photooxidation of polymers. The fluorescence spectra of the PBDTTPD film is quenched after only 10 minutes of annealing even though the absorbance spectrum shows minimal change under these conditions. There are a variety of reasons why the fluorescence would quench before major structural changes occur. Changes in the emission spectra after thermal annealing have been attributed to degradation and crosslinking [66]. Oxidative stability is also a function of molecular weight, with lower molecular weight samples being less stable to the higher number of chain ends [67]. However, the fluorescence of conjugated polymers is highly sensitive to the formation of defects or any small changes in the molecular packing [68].

141

5.3.2 GIWAXS Shows a Contraction in Molecular Packing with Annealing
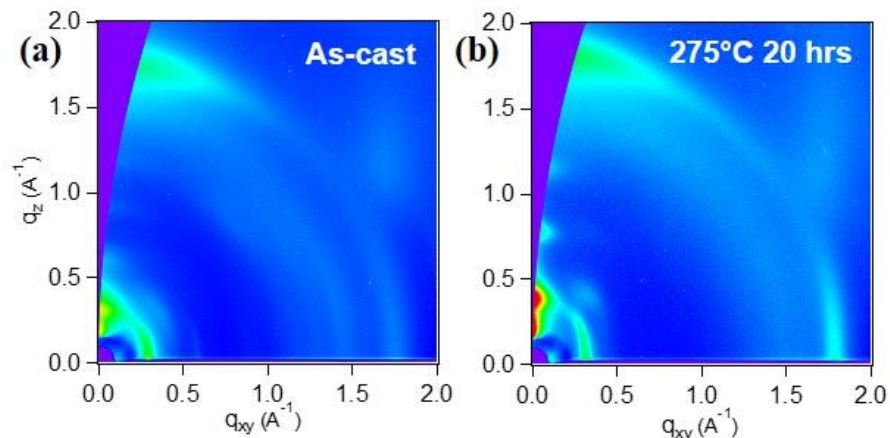
Figure 5-10. 2D GIWAXS images of PBDTTPD thin films in the (a) as-cast state and (b) after annealing at 275°C for 20 hours.

PBDTTPD thin films were examined with GIWAXS to probe the molecular packing, and a structural transformation was observed. The as-cast film has a predominantly face-on texture as can be seen from the out-of-plane π-stacking peak at a $q_z = 1.76$ Å^{-1} (d= 3.57 Å) and in-plane alkyl stacking peak at $q_{xy} = 0.30$ Å^{-1} (d= 21.2 Å). The evolution of the structure with increasing annealing time at 275°C can be observed through 1D linecuts of the 2D GIWAXS images in the in-plane and out-of-plane directions (Figure 5-11). After 20 hours, subtle shifts in the in-plane stacking are observed through a 6.9% contraction in the alkyl stacking from 21.2 to 19.8 Å. More dramatic shifts occur in the out-of-plane direction with an 18.5% contraction in the alkyl d-spacing from 20.5 to 16.7 Å. Annealing can often lead to ordering of the side-chains enabling closer packing. The π-stacking peaks show a smaller contraction with a 3.6% out-of-plane from 3.57 to 3.45 Å and 2.6% in-plane from 3.61 to 3.52 Å. The very small out-of-plane π-stacking distance of 3.45 Å was one of the first signs that something unusual was occurring. The van der Waals radii of carbon is 1.7 Å and sulfur is 1.8 Å suggesting that a stacking distance of less than 3.5 Å is highly improbable without specific
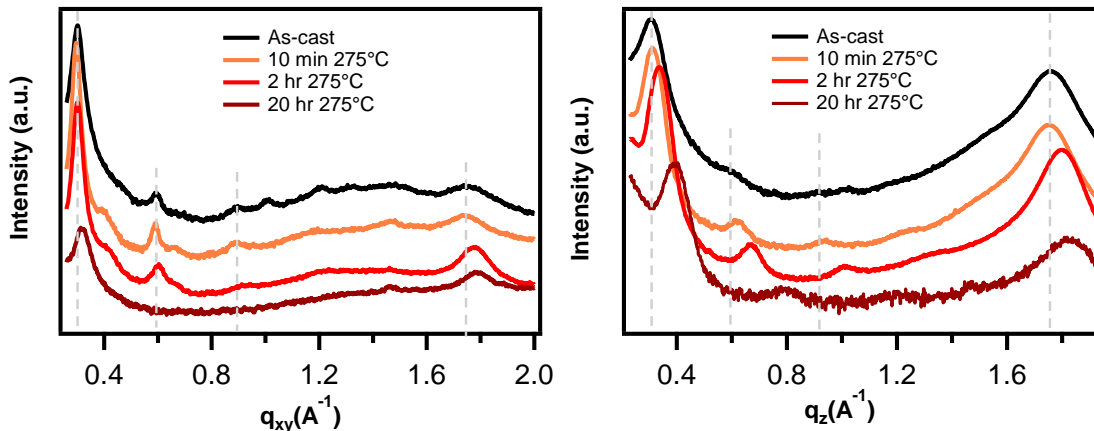
Figure 5-11. GIWAXS 1D linecuts of (a) in-plane and (b) out-of-plane peaks with increasing annealing time at 275°C.

Table 5-2. Summary of GIWAXS data showing the change in alkyl and π-π stacking distances for the face-on and edge-on crystallite populations before and after annealing

Hours	Face-on		Edge-on	
	Alkyl stacking (Å)	π-π stacking (Å)	Alkyl stacking (Å)	π-π stacking (Å)
0	21.2	3.6	20.5	3.6
0.16	21.2	3.6	20.1	3.6
2	20.8	3.5	18.7	3.5
20	19.8	3.4	16.7	3.5
% Δ	-6.9	-3.6	-18.5	-2.6

electronic interactions stabilizing the structure. However, a small π-π stacking distance could also indicate that the backbones are slipped relative to one another [69].

5.3.3 HRTEM Shows Increase in In-plane Ordering

Despite the reduction in the conjugation length and evidence of chemical damage observed with UV-Vis, HRTEM shows that the chains in the crystalline domains are nominally intact. Before and after annealing crystallites were observed to have an average width of 20-30 nm and length of 60-100 nm. GIWAXS, which collects an average of the molecular stacking distances over a large area, showed a contraction of the in-plane alkyl stacking from 21.2 to

143

19.8 Å after annealing. However, looking locally with HRTEM at the annealed film, areas where the crystallites overlap do not show a *d*-spacing contraction. The difference in the *d*-
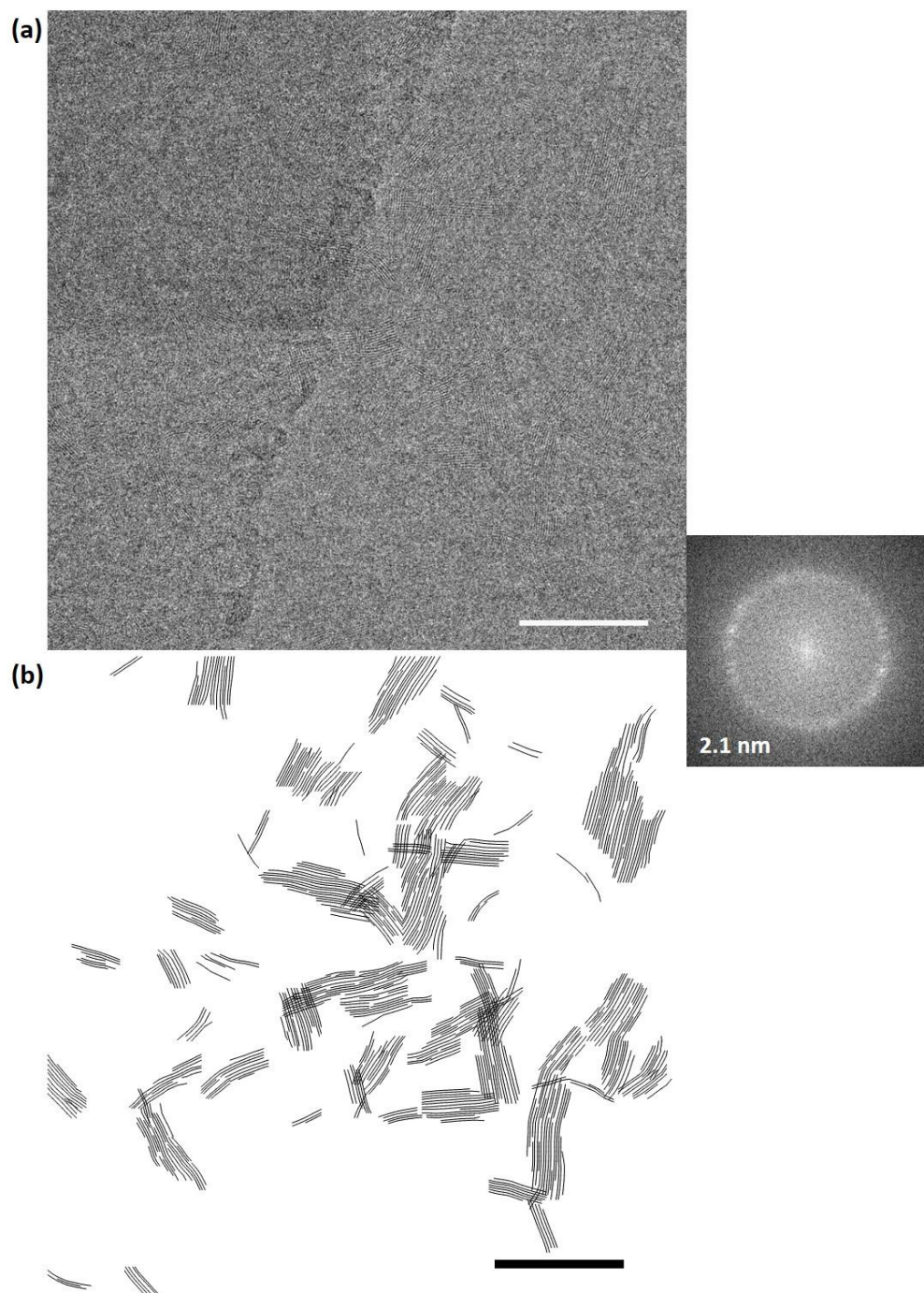
Figure 5-12. As-cast PBDTTPD thin film (~10-15 nm) (a) HRTEM image and (b) line-drawing of lattice fringes. Scale bar is 100 nm.
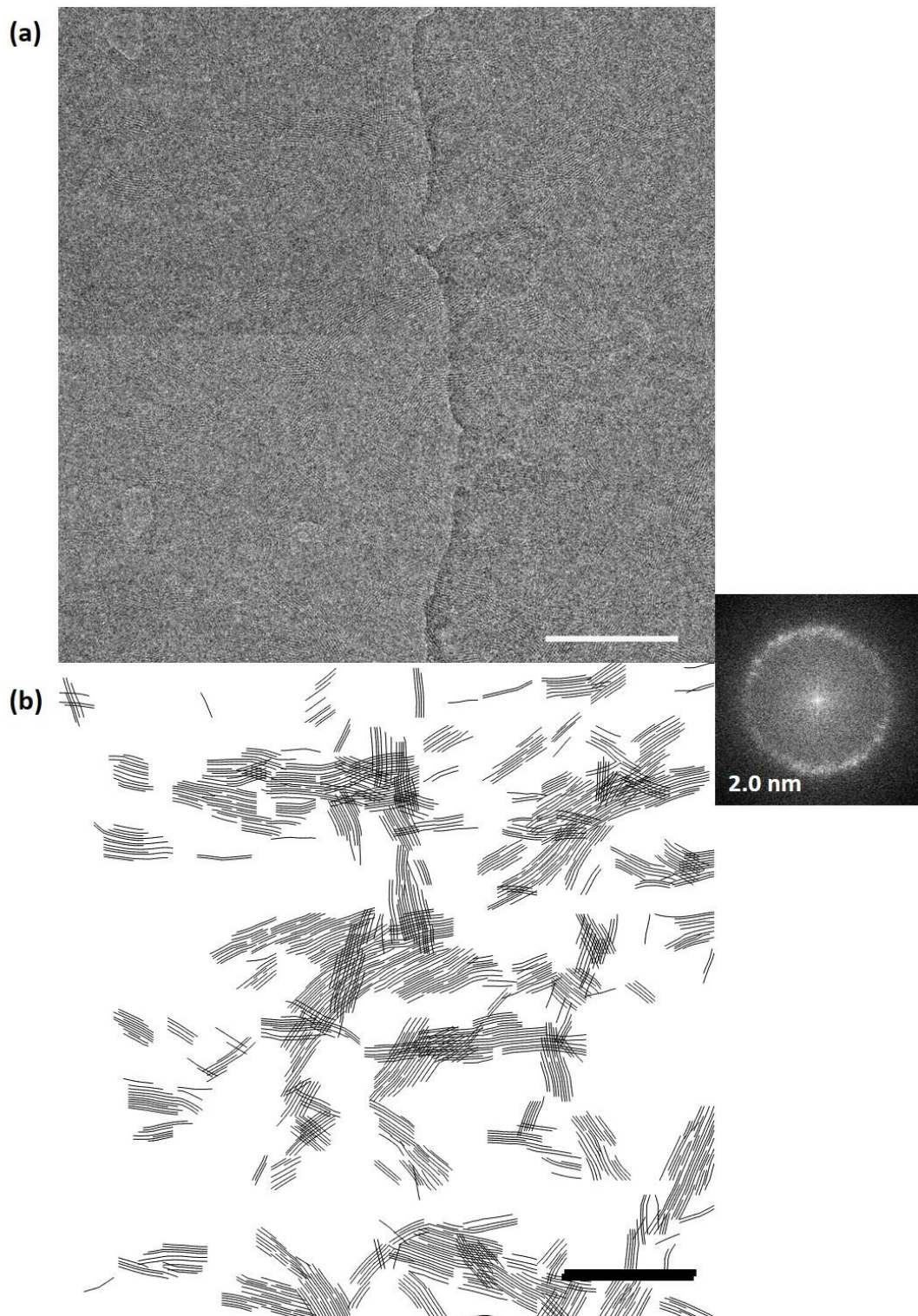
Figure 5-13. Annealed PBDTTPD thin film (~ 10-15 nm) (a) HRTEM image and (b) line-drawing of lattice fringes. Scale bars are 100 nm.

spacing is determined by Fourier transforming smaller regions of the image to determine the periodic spacing (Figure 5-14b). The alkyl stacking contraction is seen only in the uncrossed
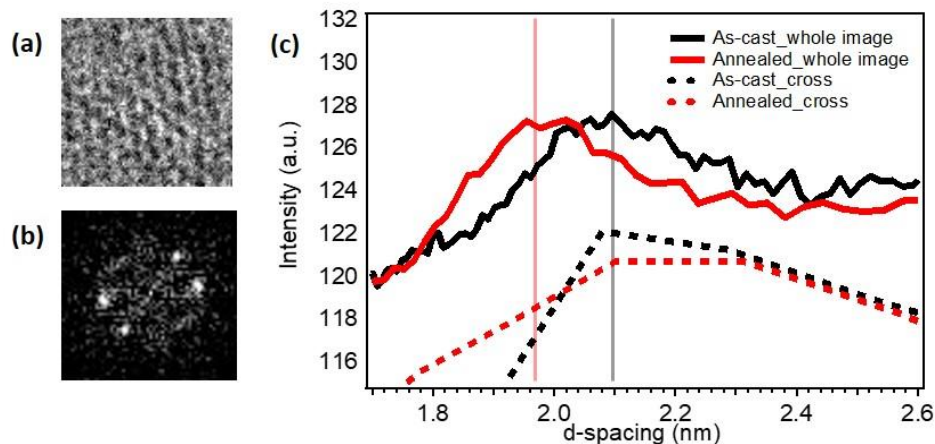
Figure 5-14. (a) HRTEM of a crossed region, (b) FFT of the crossed region, and (c) azimuthally integrated intensity profile showing distribution in d-spacing for the whole image versus the crossed areas for as-cast and annealed at 275°C.

regions (Figure 5-14c). One explanation is that the crossed regions are somehow more resistant because the d-spacing within the cross remains fixed during annealing. The formation of physical crosslinks at the overlap points probably increased the stability of those domains.

While the exact mechanism of the chemical degradation of PBDTTPD during annealing is unclear, it is also possible that the crystalline and amorphous portions of the film damaged differently. The film is semicrystalline and therefore GIWAXS and HRTEM, which probe the ordered domains, do not show the structure of the entire film. However, Fourier transforms to determine the d-spacing of the crossed regions show that they appear to be resistant to a contraction in the direction of the alkyl stacking than the uncrossed regions (Figure 5-14). Knowing the sample is degraded, the significant decrease in the alkyl stacking distance in and out of the plane observed with GIWAXS suggests that side-chains damage/loss may have occurred. Because annealing occurred in the absence of oxygen, it is

146

likely that the side-chain degradation resulted in the production of radical species that attack the backbone, as was observed for PTB7-Th. During thermal processing, the side-chains will degrade first followed by the conjugated backbone [10].This could explain how the chains were able to packing more closely if the side-chains had degraded [70]. However, heating may have led to decomposition of the conjugated units in the backbone, which would reduce the conjugation length, or loss of the side-chains.

In conclusion, thermal annealing is a commonly used processing technique to control the degree of crystallinity and phase separation in BHJs. However, even in systems where heat treatments are not used, the thermal stability must be considered as temperature fluctuations are expected to occur during normal device operation. Here, neat films of the donor polymer PBDTTPD were examined to understand the structural resistance of the material on its own. The morphology of solution processed thin films for organic electronics is often metastable and cannot be precisely maintained for long periods of time. Overall, efforts to increase the morphological and chemical stability are important for improving device lifetimes.

5.4 Conclusions

The mechanism through which damage occurs in semiconducting polymers will differ depending on the molecular structure, the presence of O_2 and other impurities. However, it is clear that the aliphatic side-chains are the least resistant functionalities to degradation and can readily form radical species during photoxidation and thermal annealing. In the case of photo-degradation of the polymer PTB7, the production of an iodooctane radical from the photolysis of DIO led to the degradation of the polymer backbone. For the thermal degradation of PBDTTPD, films were annealed in an inert environment and thus damage to the side-chains

at high temperatures likely promoted the formation of free radicals which then reacted with the conjugated backbone.

Various characterization techniques are used to detect damage but it is important to remember that each system will degrade differently. For example, the degradation of the PTB7 polymer could be observed with GIWAXS because it resulted in a broadening and loss of intensity of scattering peaks. This is makes intuitive sense that damage would reduce the polymer ordering and crystallinity. However, degradation of the PBTTPD sample resulted in a structural change, but damage was not immediately evident by examination with GIWAXS and HRTEM, which only probe the ordered material. This suggests that the amorphous and crystalline components of the film damage differently because the quenching of the absorption and emission spectra after annealing indicated major chemical damage that decreased the polymer conjugation length. Careful monitoring of changes in the optical properties with processing and choosing techniques which probe both the amorphous and crystalline parts of the film ensure that any damage effects can be properly detected.

References

[1]   M. Jørgensen, K. Norrman, and F. C. Krebs, "Stability/degradation of polymer solar cells," *Sol. Energy Mater. Sol. Cells*, vol. 92, no. 7, pp. 686–714, 2008.

[2]   S. Alem, S. Wakim, J. Lu, G. Robertson, J. Ding, and Y. Tao, "Degradation mechanism of benzodithiophene-based conjugated polymers when exposed to light in air," *ACS Appl. Mater. Interfaces*, vol. 4, no. 6, pp. 2993–2998, 2012.

[3]   T. Tromholt, M. Manceau, M. Helgesen, J. E. Carlé, and F. C. Krebs, "Degradation of semiconducting polymers by concentrated sunlight," *Sol. Energy Mater. Sol. Cells*, vol. 95, no. 5, pp. 1308–1314, 2011.

[4]   M. Manceau, A. Rivaton, J. L. Gardette, S. Guillerez, and N. Lemaître, "The mechanism of photo- and thermooxidation of poly(3-hexylthiophene) (P3HT) reconsidered," *Polym. Degrad. Stab.*, vol. 94, no. 6, pp. 898–907, 2009.

[5]   H. Hintz, H. J. Egelhaaf, H. Peisert, and T. Chass??, "Photo-oxidation and ozonization of poly(3-hexylthiophene) thin films as studied by UV/VIS and photoelectron spectroscopy," *Polym. Degrad. Stab.*, vol. 95, no. 5, pp. 818–825, 2010.

[6]   K. Sivula, C. K. Luscombe, B. C. Thompson, and J. M. J. Fréchet, "Enhancing the thermal stability of polythiophene:fullerene solar cells by decreasing effective polymer regioregularity," *J. Am. Chem. Soc.*, vol. 128, no. 43, pp. 13988–13989, 2006.

[7]   M. Helgesen, T. J. Sørensen, M. Manceau, and F. C. Krebs, "Photochemical stability and photovoltaic performance of low-band gap polymers based on dithiophene with different bridging atoms," *Polym. Chem.*, vol. 2, p. 1355, 2011.

[8]   M. Manceau *et al.*, "Photochemical stability of π-conjugated polymers for polymer solar cells: a rule of thumb," *J. Mater. Chem.*, vol. 21, no. 12, p. 4132, 2011.

[9]   S. Chambon, A. Rivaton, J. L. Gardette, M. Firon, and L. Lutsen, "Aging of a Donor Conjugated Polymer: Photochemical Studies of the Degradation of Poly[2-methoxy-5- (30,70-dimethyloctyloxy)-1,4-phenylenevinylene]," *Am. Chem. Soc. Polym. Prepr. Div. Polym. Chem.*, vol. 45, pp. 317–331, 2007.

[10]   L. Marin *et al.*, "In situ monitoring the thermal degradation of PCPDTBT low band gap polymers with varying alkyl side-chain patterns," *J. Polym. Sci. Part A Polym. Chem.*, vol. 51, no. 22, pp. 4912–4922, 2013.

[11]   M. Helgesen *et al.*, "Thermally reactive Thiazolo[5,4-d]thiazole based copolymers for high photochemical stability in polymer solar cells," *Polym. Chem.*, vol. 2, no. 11, p. 2536, 2011.

[12]   A. Distler *et al.*, "Effect of PCBM on the photodegradation kinetics of polymers for

organic photovoltaics," *Chem. Mater.*, vol. 24, no. 22, pp. 4397–4405, 2012.

[13]   A. Dupuis, P. Wong-Wah-Chung, A. Rivaton, and J. L. Gardette, "Influence of the microstructure on the photooxidative degradation of poly(3-hexylthiophene)," *Polym. Degrad. Stab.*, vol. 97, no. 3, pp. 366–374, 2012.

[14]   R. Cheacharoen *et al.*, "Assessing the stability of high performance solution processed small molecule solar cells," *Sol. Energy Mater. Sol. Cells*, vol. 161, no. December 2016, pp. 368–376, 2017.

[15]   W. R. Mateker *et al.*, "Molecular Packing and Arrangement Govern the Photo-Oxidative Stability of Organic Photovoltaic Materials," *Chem. Mater.*, vol. 27, no. 18, pp. 6345–6353, 2015.

[16]   J. B. Knight, P. D. Calvert, and N. C. Billingham, "Localization of oxidation in polypropylene," *Polymer (Guildf).*, vol. 26, pp. 1713–1718, 1985.

[17]   N. C. Billingham, P. Prentice, and T. J. Walker, "Some Effects of Morphology on Oxidation and Stabilization of Polyolefins," *J. Polym. Sci. Symp.*, vol. 57, no. 57, pp. 287–297, 1976.

[18]   J. Peet, M. L. Senatore, A. J. Heeger, and G. C. Bazan, "The role of processing in the fabrication and optimization of plastic solar cells," *Adv. Mater.*, vol. 21, no. 14–15, pp. 1521–1527, 2009.

[19]   W. Ma, C. Yang, X. Gong, K. Lee, and A. J. Heeger, "Thermally stable, efficient polymer solar cells with nanoscale control of the interpenetrating network morphology," *Adv. Funct. Mater.*, vol. 15, no. 10, pp. 1617–1622, 2005.

[20]   E. Verploegen, R. Mondal, C. J. Bettinger, S. Sok, M. F. Toney, and Z. Bao, "Effects of thermal annealing upon the morphology of polymer-fullerene blends," *Adv. Funct. Mater.*, vol. 20, no. 20, pp. 3519–3529, 2010.

[21]   P. Cheng, L. Ye, X. Zhao, J. Hou, Y. Li, and X. Zhan, "Binary additives synergistically boost the efficiency of all-polymer solar cells up to 3.45%," *Energy Environ. Sci.*, vol. 7, no. 4, pp. 1351–1356, 2014.

[22]   M. Li *et al.*, "Cooperative effects of solvent and polymer acceptor co-additives in P3HT:PDI solar cells: simultaneous optimization in lateral and vertical phase separation.," *Phys. Chem. Chem. Phys.*, vol. 16, no. 10, pp. 4528–37, Mar. 2014.

[23]   J. a. Bartelt *et al.*, "Controlling Solution-Phase Polymer Aggregation with Molecular Weight and Solvent Additives to Optimize Polymer-Fullerene Bulk Heterojunction Solar Cells," *Adv. Energy Mater.*, vol. 4, no. 9, Jun. 2014.

[24]   C. Müller *et al.*, "Binary organic photovoltaic blends: A simple rationale for optimum compositions," *Adv. Mater.*, vol. 20, no. 18, pp. 3510–3515, 2008.

[25] B. Lei, Y. Yao, A. Kumar, Y. Yang, and V. Ozolins, "Quantifying the relation between the morphology and performance of polymer solar cells using Monte Carlo simulations," *J. Appl. Phys.*, vol. 104, no. 2, 2008.

[26] G. M. Su *et al.*, "Linking morphology and performance of organic solar cells based on decacyclene triimide acceptors," *J. Mater. Chem. A*, vol. 2, pp. 1781–1789, 2014.

[27] K. A. O'Hara *et al.*, "Role of Crystallization in the Morphology of Polymer:Non-fullerene Acceptor Bulk Heterojunctions," *ACS Appl. Mater. Interfaces*, vol. 9, no. 22, pp. 19021–19029, 2017.

[28] W. L. Leong *et al.*, "Role of trace impurities in the photovoltaic performance of solution processed small-molecule bulk heterojunction solar cells," *Chem. Sci.*, vol. 3, p. 2103, 2012.

[29] W. R. Mateker *et al.*, "Improving the long-term stability of PBDTTPD polymer solar cells through material purification aimed at removing organic impurities," *Energy Environ. Sci.*, vol. 6, no. 8, p. 2529, 2013.

[30] B. J. Tremolet De Villers *et al.*, "Removal of Residual Diiodooctane Improves Photostability of High-Performance Organic Solar Cell Polymers," *Chem. Mater.*, vol. 28, no. 3, pp. 876–884, 2016.

[31] G. Dennler *et al.*, "Charge carrier mobility and lifetime versus composition of conjugated polymer/fullerene bulk-heterojunction solar cells," *Org. Electron. physics, Mater. Appl.*, vol. 7, no. 4, pp. 229–234, 2006.

[32] J. Peet *et al.*, "Method for increasing the photoconductive response in conjugated polymer/fullerene composites," *Appl. Phys. Lett.*, vol. 89, no. 25, pp. 5–8, 2006.

[33] J. Peet *et al.*, "Efficiency enhancement in low-bandgap polymer solar cells by processing with alkane dithiols," *Nat. Mater.*, vol. 6, no. 7, pp. 497–500, 2007.

[34] J. Peet, N. S. Cho, S. K. Lee, and G. C. Bazan, "Transition from solution to the solid state in polymer solar cells cast from mixed solvents," *Macromolecules*, vol. 41, pp. 8655–8659, 2008.

[35] J. T. Rogers, K. Schmidt, M. F. Toney, E. J. Kramer, and G. C. Bazan, "Structural order in bulk heterojunction films prepared with solvent additives.," *Adv. Mater.*, vol. 23, no. 20, pp. 2284–8, May 2011.

[36] J. K. Lee *et al.*, "Processing additives for improved efficiency from bulk heterojunction solar cells.," *J. Am. Chem. Soc.*, vol. 130, no. 11, pp. 3619–23, 2008.

[37] Y. Gu, C. Wang, and T. P. Russell, "Multi-Length-Scale Morphologies in PCPDTBT/PCBM Bulk-Heterojunction Solar Cells," *Adv. Energy Mater.*, vol. 2, no. 6, pp. 683–690, Jun. 2012.

[38]   Z. Liu, H. Ju, and E. C. Lee, "Improvement of polycarbazole-based organic bulk-heterojunction solar cells using 1,8-diiodooctane," *Appl. Phys. Lett.*, vol. 103, no. 13, pp. 1–5, 2013.

[39]   X. Huang *et al.*, "Enhanced performance for polymer/fullerene solar cells by using bromobenzene/1,8-diiodooctane co-solvent," *Appl. Phys. Lett.*, vol. 104, no. 21, 2014.

[40]   Y. Liang *et al.*, "For the bright future-bulk heterojunction polymer solar cells with power conversion efficiency of 7.4%," *Adv. Mater.*, vol. 22, no. 20, pp. 135–138, 2010.

[41]   F. Wang, J. Luo, K. Yang, J. Chen, F. Huang, and Y. Cao, "Conjugated fluorene and silole copolymers: Synthesis, characterization, electronic transition, light emission, photovoltaic cell, and field effect hole mobility," *Macromolecules*, vol. 38, no. 6, pp. 2253–2260, 2005.

[42]   F. Zhang, W. Mammo, L. M. Andersson, S. Admassie, M. R. Andersson, and O. Inganäs, "Low-bandgap alternating fluorene copolymer/methanofullerene heterojunctions in efficient near-infrared polymer solar cells," *Adv. Mater.*, vol. 18, no. 16, pp. 2169–2173, 2006.

[43]   N. Blouin, A. Michaud, and M. Leclerc, "A low-bandgap poly(2,7-carbazole) derivative for use in high-performance solar cells," *Adv. Mater.*, vol. 19, no. 17, pp. 2295–2300, 2007.

[44]   Y. Liang *et al.*, "Highly efficient solar cell polymers developed via fine-tuning of structural and electronic properties," *J. Am. Chem. Soc.*, vol. 131, no. 22, pp. 7792–7799, 2009.

[45]   L. Lu and L. Yu, "Understanding low bandgap polymer PTB7 and optimizing polymer solar cells based on IT," *Adv. Mater.*, vol. 26, no. 26, pp. 4413–4430, 2014.

[46]   Z. He, C. Zhong, S. Su, M. Xu, H. Wu, and Y. Cao, "Enhanced power-conversion efficiency in polymer solar cells using an inverted device structure," vol. 6, no. September, pp. 591–595, 2012.

[47]   H. Zhou *et al.*, "Conductive conjugated polyelectrolyte as hole-transporting layer for organic bulk heterojunction solar cells.," *Adv. Mater.*, vol. 26, no. 5, pp. 780–5, 2014.

[48]   S.-H. Liao, H.-J. Jhuo, Y.-S. Cheng, and S.-A. Chen, "Fullerene derivative-doped zinc oxide nanofilm as the cathode of inverted polymer solar cells with low-bandgap polymer (PTB7-Th) for high performance," *Adv. Mater.*, vol. 25, no. 34, pp. 4766–4771, 2013.

[49]   Q. Wan *et al.*, "10.8% Efficiency Polymer Solar Cells Based on PTB7-Th and PC 71 BM via Binary Solvent Additives Treatment," *Adv. Funct. Mater.*, vol. 26, no. 36, pp. 6635–6640, 2016.

[50] M. L. Chabinyc, *X-ray Scattering from Films of Semiconducting Polymers*, vol. 48, no. 3. 2008.

[51] F. Liu *et al.*, "Understanding the Morphology of PTB7:PCBM Blends in Organic Photovoltaics," *Adv. Energy Mater.*, vol. 4, no. 5, p. 1301377, Apr. 2014.

[52] B. E. Warren, *X-ray Diffraction*. Mineola, NY, 1969.

[53] J. Rivnay, S. C. B. Mannsfeld, C. E. Miller, A. Salleo, and M. F. Toney, "Quantitative determination of organic semiconductor microstructure from the molecular to device scale," *Chem. Rev.*, vol. 112, no. 10, pp. 5488–5519, Oct. 2012.

[54] J. U. Lee, J. W. Jung, J. W. Jo, and W. H. Jo, "Degradation and stability of polymer-based solar cells," *J. Mater. Chem.*, vol. 22, no. 46, p. 24265, 2012.

[55] C. Piliego, T. W. Holcombe, J. D. Douglas, C. H. Woo, P. M. Beaujuge, and J. M. J. Fréchet, "Synthetic Control of Structural Order in N -Alkylthieno[3,4-c]pyrrole-4,6-dione-Based Polymers for Efficient Solar Cells," *J. Am. Chem. Soc.*, vol. 132, no. 22, pp. 7595–7597, 2010.

[56] Y. Zou *et al.*, "A Thieno[3, 4-c]pyrrole-4, 6-dione-Based Copolymer for Efficient Solar Cells," *J. Am. Chem. Soc.*, vol. 132, no. 15, pp. 5330–5331, 2010.

[57] P. L. T. Boudreault, A. Najari, and M. Leclerc, "Processable low-bandgap polymers for photovoltaic applications," *Chem. Mater.*, vol. 23, no. 3, pp. 456–469, 2011.

[58] C. Cabanetos *et al.*, "Linear Side Chains in Benzo[1,2-b:4,5-b′]dithiophene−Thieno[3,4-c]pyrrole-4,6-dione Polymers Direct Self-Assembly and Solar Cell Performance," *J. Am. Chem. Soc.*, vol. 135, no. 12, p. 4656−4659, 2013.

[59] J. Guo *et al.*, "Structure, dynamics, and power conversion efficiency correlations in a new low bandgap polymer: PCBM solar cell," *J. Phys. Chem. B*, vol. 114, no. 2, pp. 742–748, 2010.

[60] A. El Labban *et al.*, "Dependence of Crystallite Formation and Preferential Backbone Orientations on the Side Chain Pattern in PBDTTPD Polymers," *ACS Appl. Mater. Interfaces*, vol. 6, no. 22, pp. 19477–19481, Nov. 2014.

[61] J. Warnan *et al.*, "Ring substituents mediate the morphology of PBDTTPD-PCBM bulk-heterojunction solar cells," *Chem. Mater.*, vol. 26, no. 7, pp. 2299–2306, 2014.

[62] T. Y. Chu *et al.*, "Morphology control in polycarbazole based bulk heterojunction solar cells and its impact on device performance," *Appl. Phys. Lett.*, vol. 98, no. 25, pp. 2009–2012, 2011.

[63] A. Tournebize *et al.*, "Is there a photostable conjugated polymer for efficient solar cells?," *Polym. Degrad. Stab.*, vol. 112, pp. 175–184, 2015.

[64] H. S. Silva *et al.*, "A universal route to improving conjugated macromolecule photostability," *RSC Adv.*, vol. 4, no. 97, pp. 54919–54923, 2014.

[65] X.-Q. Chen *et al.*, "SI: Long-Term Thermally Stable Organic Solar Cells Based on Cross-linkable Donor-Acceptor Conjugated Polymers," *J. Mater. Chem. A*, vol. 4, no. 23, pp. 9286–9292, 2016.

[66] W. Zhao, T. Cao, and J. M. White, "On the origin of green emission in polyfluorene polymers: The roles of thermal oxidation degradation and crosslinking," *Adv. Funct. Mater.*, vol. 14, no. 8, pp. 783–790, 2004.

[67] J. Lee, G. Klaerner, and R. D. Miller, "Oxidative Stability and Its Effect on the Photoluminescence of Poly(Fluorene) Derivatives: End Group Effects," *Chem. Mater.*, vol. 11, no. 4, pp. 1083–1088, 1999.

[68] A. Alvarez, J. M. Costa-Fernández, R. Pereiro, A. Sanz-Medel, and A. Salinas-Castillo, "Fluorescent conjugated polymers for chemical and biochemical sensing," *TrAC - Trends Anal. Chem.*, vol. 30, no. 9, pp. 1513–1525, 2011.

[69] C. J. Takacs *et al.*, "Remarkable Order of a High-Performance Polymer," *Nano Lett.*, 2013.

[70] R. Abbel *et al.*, "Side-chain degradation of ultrapure π-conjugated oligomers: Implications for organic electronics," *Adv. Mater.*, vol. 21, no. 5, pp. 597–602, 2009.

Chapter 6

Role of Crystallization in the Morphology of Polymer:Non-fullerene Acceptor Bulk Heterojunctions

Abstract

Many high efficiency organic photovoltaics use fullerene-based acceptors despite their high production cost, weak optical absorption in the visible range, and limited synthetic variability of electronic and optical properties. To circumvent this deficiency, non-fullerene small-molecule acceptors have been developed that have good synthetic flexibility, allowing for precise tuning of optoelectronic properties, leading to enhanced absorption of the solar spectrum and increased open-circuit voltages (V_{OC}). We examined the detailed morphology of bulk heterojunctions of poly(3-hexylthiophene) and the small-molecule acceptor HPI-BT to reveal structural changes that lead to improvements in the fill factor of solar cells upon thermal annealing. The kinetics of the phase transformation process of HPI-BT during thermal annealing were investigated through in situ grazing incidence wide-angle X-ray scattering studies, atomic force microscopy, and transmission electron microscopy. The HPI-BT acceptor crystallizes during film formation to form micron-sized domains embedded within the film center and a donor rich capping layer at the cathode interface reducing efficient charge extraction. Thermal annealing changes the surface composition and improves charge extraction. This study reveals the need for complementary methods to investigate the morphology of BHJs.

6.1 Introduction

Since early reports,[1]–[3] organic photovoltaics (OPVs) have reached the commercialization stage with power conversion efficiencies (PCEs) of 13.2% and lifetimes in lab cells of 25 years.[4] Solution-processed bulk heterojunction (BHJ) structures, where electron donating and electron accepting materials form a bicontinuous nanoscale network in a thin film, have shown great promise.[5]–[8] The majority of efforts to increase the PCE of OPVs have focused on designing new donor materials for use with fullerene-based acceptors.[9]–[13] While fullerene derivatives can form efficient BHJs with many classes of donors due to their high electron affinity and ultrafast electron transfer kinetics,[14]–[16] they also have several known limitations. These limitations include a high production cost, weak optical absorption in the visible range, and limited synthetic variability of electronic and optical properties.[17]

The need to further improve the performance of OPVs has led to investigation of non-fullerene acceptors (NFAs)[18]–[30] with the most successful utilizing naphthalene diimide (NDI),[18] perylene diimide (PDI),[20], [21], [24]–[26], [29], [30] spirobifluorene (SF),[22], [28] and indacenodithiophene (IDT)[27], [31]–[34] core units. So far, device PCEs of over 11%[32], [33] have been achieved for a polymer donor and small-molecule NFA and 9.08%[35] for an all-SM cell. In contrast to fullerenes, SM acceptors offer increased synthetic flexibility that allows for fine-tuning of optical and electronic properties. The challenge is to optimize device performance through control over the morphology that develops during casting, a topic that has been extensively studied for polymer−fullerene blend BHJs.[36]–[38] In particular, the role of crystallization has been studied in several

156

systems as a driving force for nanoscale domain formation,[39] and subsequently for charge carrier separation in the operating device.[40]

Many studies on NFA systems aim to find the balance between suppressing large-scale crystallization while preserving π-stacking in order to achieve high-electron mobilities. The geometry and planarity of the molecule have a large effect on aggregation that ultimately affects phase separation and domain size. There are a number of molecular design strategies that have been explored to influence molecular organization such as highly planar structures, which tend to promote crystallization,[20] and bulky 3D structures, which frustrate packing and promote formation of an amorphous phase.[19], [26], [28]–[30]

Self-aggregation is particularly problematic with commonly used PDI-based acceptors as PDI monomer units have a strong tendency to π-stack.[20] However, this can be reduced through formation of dimers that introduce torsion at the connection point and lead to nonplanar/twisted structures.[25], [41] Furthermore, by incorporating four PDI units into the molecular structure, acceptors with 3D conformations have been observed[26], [29], [30] and are able to match the isotropic transport qualities of fullerenes and achieve comparable efficiencies.[29] The placement of alkyl substituents can have a large effect on the aggregation. For example, self-aggregation of PDIs can be reduced by attachment of branched alkyl chains on the nitrogen atom of the PDI core,[42] whereas suppression of the donor phase crystallization can be accomplished by using core- alkylated PDIs.[43] Structures which induce a backbone twist have also been explored to restrict π−π stacking such as with SF linkages.[22], [28]

The use of processing additives is also a beneficial method for controlling the phase-separated morphology. Binary additives were used to increase the PCE in a PBDTTT-C-T:

PPDIDTT system by selectively suppressing aggregation of the acceptor and increasing aggregation of the donor.[44] Aggregation can also be induced in less crystalline materials through the use of additives. Wu et al. used the solvent additive 1,8-diiodooctane (DIO) along with thermal annealing to increase crystallization of the SF-based acceptor.[22] However, too much additive can also result in excessive phase separation through crystallization of the acceptor.[18]

Here, we examine the morphology of the NFA 4,7-bis(4-(N-hexylphthalimide)vinyl)-benzo[c]-1,2,5-thiadiazole (HPI-BT), to reassess the origin of its performance in BHJs. Previously, BHJs of HPI-BT and poly(3-hexylthiophene) (P3HT) were shown to achieve a maximum PCE of about 3.7%.[45], [46] OPVs with HPI-BT were suggested to be limited by insufficient mixing of the donor and acceptor phases upon annealing, leading to inefficient charge generation and separation.[46] Here, we describe an in-depth investigation into the evolution of the morphology of the BHJ with thermal annealing. While the electronic performance of the as-cast and annealed devices agrees with previous studies, we find features in the morphology by grazing incidence wide-angle X-ray scattering (GIWAXS) along with high resolution and scanning trans- mission electron microscopy (HRTEM and STEM) that reveal significant phase separation in the as-cast films that is not significantly changed by thermal annealing.

6.2 Experimental Section

6.2.1 Materials

The synthesis of 5,5′-(2,1,3-benzothiadiazole-4,7-diyldi-2,1-ethenediyl)bis[2-hexyl-1H-isoindole-1,3(2H)-dione], HPI-BT, is described in a previous publication,[45] and the compound is also commercially available now (Sigma-Aldrich).

158

6.2.2 Device Fabrication

Devices are prepared using glass-ITO substrates prepatterned from thin film devices. A thin layer of molybdenum oxide (MoO_3) ($\sim$20 nm) was thermally evaporated on top of the ITO as a hole transport layer. The active layer was formed from a 1:2 ratio of P3HT:HPI-BT dissolved in chlorobenzene at a concentration of 20 mg/mL total and spun-cast onto the ITO/MoO_3 substrate with a thickness of $\sim$100 nm. Thermal annealing at 100 °C in an inert atmosphere was performed on some of the samples in the study. After the active layer deposition and annealing, a thin layer of LiF (1 nm) was thermally deposited, and a subsequent layer of Al (80 nm) was added as the top electrode. Thermal annealing at 100 °C in an inert atmosphere was performed on some of the devices in the study.

6.2.3 Characterization

GIWAXS. X-ray scattering experiments on both the blended films and the pure components were performed at Stanford Synchrotron Radiation Lightsource (SSRL) beamline 11-3 with a 12 keV beam in a sample chamber with flowing helium to reduce air scatter. In situ annealing studies were carried out by heating samples to 100 °C and collecting diffraction patterns every 2 min for 10 min, followed by 10 min of cooling to room temperature (23.5 °C). Analysis of the 2D images was conducted using WxDiff and Igor.

AFM. Data were collected in tapping mode using silicon FORTA AFM tips. The top and bottom surface of the pure and blended films were scanned. Because the active layer was deposited on a layer of MoO_3, the interfacial layer could be dissolved in water to remove the film from the substrate. Films were then flipped and relaminated onto a Si (and glass) substrate.

159

TEM. Blended films were delaminated from the glass substrate by dissolving the MoO$_3$ layer in a water bath. The active layer was then relaminated onto a copper TEM grid with a carbon support. Imaging was carried using an FEI Titan 300 kV FEG TEM/STEM microscope at the California NanoSystems Institute (CNSI) at UCSB.

6.3   Results and Discussion

6.3.1   Thermal Processing Conditions Modify Power Conversion Efficiency

The current−voltage characteristics under illumination conditions of BHJs of P3HT:HPI BT are shown in Figure 6-1 and summarized in Table 6-1 external quantum efficiency measurements are shown in Figure C-1. The highest performing devices were formed using a (1:2) P3HT: HPI-BT blend ratio and were tested in the as-cast state and after annealing at 100 °C for 2.5, 6, and 21 min. In the as-cast state, devices have a V_{OC} of 0.91 ± 0.02 V, *FF* of 0.40 ± 0.01, J_{SC} of 2.5 ± 0.10 mA/cm^2, and PCE of 0.93 ± 0.1%. Higher performance was achieved after 6 min of annealing, marked by an increase in *FF* to 0.62 ± 0.01, in JSC to 3.5 ± 0.1 mA/cm2, and in PCE to 1.95 ± 0.1%. Additional annealing at 100 °C for 21 min resulted in a small decline in performance with the V_{OC} and *FF* remaining constant, and the J_{SC} decreasing from 3.5 ± 0.1 to 3.3 ± 0.1 mA/cm^2. These results are generally consistent with previous studies[45], [46] of the HPI-BT acceptor.

Previous studies explored the effect of both annealing time and temperature on the PCE of P3HT:HPI-BT devices,[45], [46] but did not fully examine the evolution of the morphology as a function of time. Similar to our results here, the highest PCE was achieved with a (1:2) P3HT:HPI-BT blend ratio annealed for 100 °C for 5 min. The low J_{SC} and PCE values were explained by a lack of a significant mixed phase between the HPI-BT and P3HT. The appearance of an HPI-BT scattering peak in GIWAXS images was used as a

measure related to the miscibility of HPI-BT in the amorphous P3HT phase.[46] However, there was no investigation into the details of the morphology, such as size of donor and acceptor domains and how structure evolved with annealing. In order to fully understand the bottlenecks in the PCE of P3HT:HPI-BT BHJs, here we have carried out a more detailed study of the structure in the as-cast state and the time dependence on structure evolution with annealing, and we have made a determination of the domain sizes via in situ GIWAXS.[47]–[52]
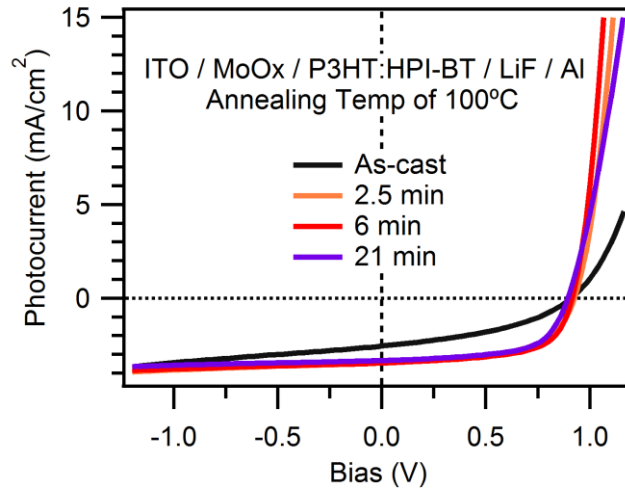
Figure 6-1. J-V curves for devices at various stages of thermal annealing.

Table 6-1. Device performance characteristics as a function of time of thermal annealing at 100 °C. Error in the measurements is 0.02 V in V_{oc}, 0.10 mA/cm^2 in J_{sc}, 0.5% in FF and 0.10% in efficiency.

Anneal (min)	V_{OC} (V)	J_{SC} (mA/cm^2)	FF (%)	Efficiency (%)
0	0.91	2.55	40.3	0.93
2.5	0.93	3.43	57.8	1.82
6	0.91	3.45	62.0	1.95
21	0.89	3.32	62.1	1.83

6.3.2 X-ray Scattering Reveals Kinetics of Structure Evolution

The increase in the PCE of P3HT:HPI-BT BHJs with annealing can be attributed to the increase in the *FF*, which depends heavily on the morphology of the photoactive layer. Thus, it was expected that significant changes in the morphology were occurring during thermal processing. In situ annealing X-ray scattering is a valuable tool for studying the time dependence of thermally induced structural changes.[47]–[52] In order to correlate changes in the local packing structure on the same timescale over which device performance shows significant change, a (1:2) P3HT:HPI-BT film was investigated with this technique. Scattering patterns were collected every 2 min while the film was heated to 100 °C, remained at 100 °C for 10 min, and was slow cooled back to room temperature (23.5 °C) for 10 min (Figure 6-2c,d).
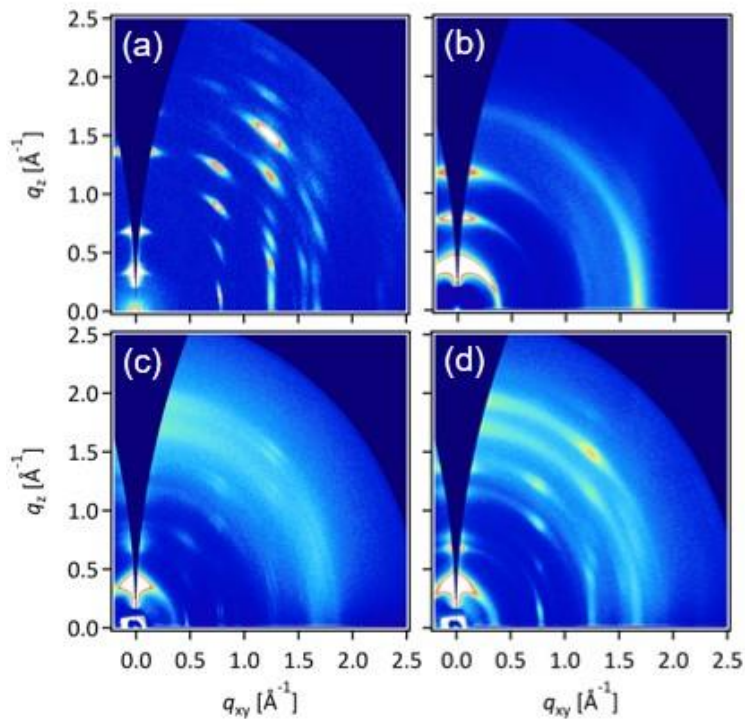
Figure 6-2. GIWAXS scattering patterns for (a) as-cast HPI-BT, (b) as-cast P3HT, (c) as-cast (1:2) P3HT:HPI-BT blend, (d) blend annealed at 100°C for 10 minutes followed by 10 minutes of slow cooling to 23.5 °C.
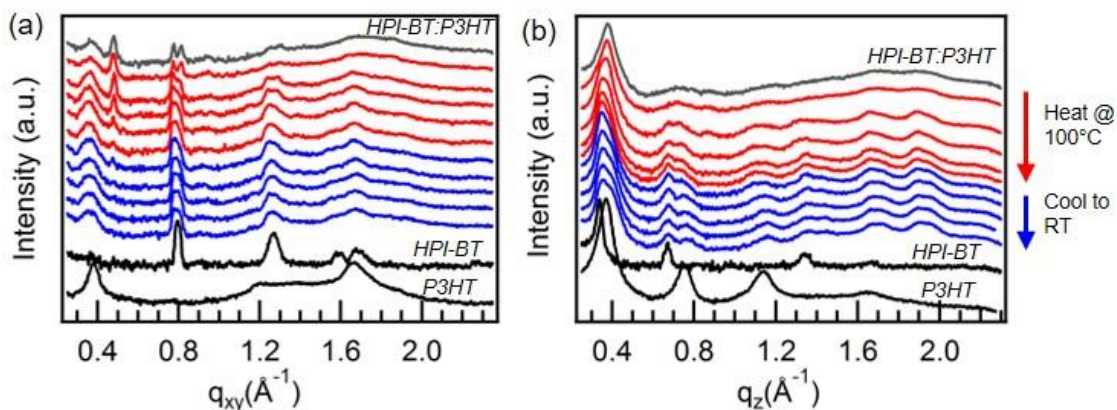
**Figure 6-3.** Results of GIWAXS in-situ annealing showing evolution of P3HT and HPI-BT film morphology while heating film for 10 minutes at 100°C (red) followed by 10 minutes cooling down to room temperature (23.5°C, blue). Line-cuts from the 2D GIWAXS images in the (a) In-plane and (b) out-of-plane direction.

The X-ray scattering from neat films and BHJs shows significant differences (Figure 6-2a,b). Films of P3HT show a peak in the out-of-plane direction corresponding to the alkyl stacking at $q \sim 0.38$ Å^{-1} ($d = 1.65$ nm) and a π-stacking feature at $q \sim 1.66$ Å^{-1} ($d = 3.78$ Å) (Figure 6-2a). The pure HPI-BT acceptor has sharper diffraction peaks indicative of a more crystalline film. The scattering pattern for the as-cast BHJ shows distinct peaks from P3HT and HPI-BT with the latter having different peak positions than in the neat as-cast film (Figure 6-2c). After annealing at 100 °C for 10 min and then cooling back to room temperature, the intensity of the features and arcs corresponding to each phase increase, leading to the pattern resembling the superposition of the two pure films in the as-cast state (Figure 6-2d). These data from before and after annealing show that the P3HT is less ordered in the as-cast BHJ than in the annealed film and that the HPI-BT forms a distinct polymorph in the as-cast state that transforms to the structure in the neat film upon annealing.

The X-ray scattering of the structural transformation occurring in the nominal out-of-plane and the in-plane direction during thermal annealing shows the coexistence of two

163

phases of HPI-BT. In the in-plane direction, the as-cast polymorph of HPI-BT can be observed at $q_{xy} = 0.47$ Å^{-1}, and a split peak is observed at 0.77 and 0.7 9 Å^{-1} (Figure 6-3). The percentage change in integrated peak intensity of the polymorph peaks is tracked during heating and cooling (Figure 6-4). The peak at $q = 0.47$ Å^{-1} increases in intensity during the first 2 min of annealing, but quickly decreases with further annealing until it disappears during cooling. The split peak evolves on the same timescale with an increase in intensity of peaks at 0.77 and 0.79 Å^{-1} for the first 6 min of annealing, after which the intensity at 0.79 Å^{-1} rapidly increases and 0.77 Å^{-1} decreases (Figure 6-4). In the out-of-plane direction, overlapping P3HT and HPI-BT peaks are present at 0.34 and 0.38 Å^{-1} and it is difficult to deconvolute the two in the early stages of annealing. However, annealing leads to an increase in intensity of the HPI-BT 0.34 Å^{-1} peak, and the peaks can be distinguished from one another during cooling (Figure 6-3b). A pronounced shoulder is observed after the film reaches room temperature corresponding to the P3HT peak. There are no new polymorph peaks in the nominally out-of-plane direction, but both acceptor and donor peaks increase in
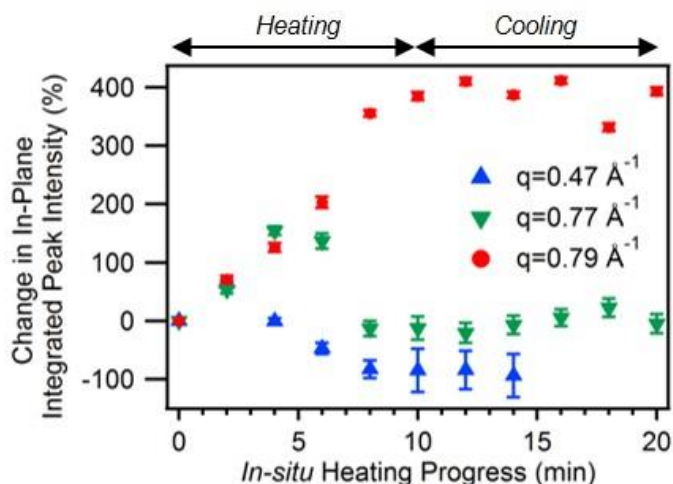

Figure 6-4. Time evolution of the change in integrated intensity of HPI- BT in-plane peaks during heating/cooling of active layer.

intensity as P3HT and HPI-BT crystallize. Both phases have increasing order as the films are annealed.

A Scherrer analysis was performed to provide an estimate of the crystallite coherence length using the FWHM of the scattering peaks during heating and cooling. The in-plane P3HT alkyl stacking peak at $q \sim 0.38$ Å^{-1} had an FWHM of 0.056 Å^{-1} corresponding to a coherence length of approximately 20 nm in the as-cast film and remained constant after annealing. The HPI-BT polymorph peak at $q \sim 0.47$ Å^{-1} had an FWHM of 0.023 Å^{-1} before annealing and decreased to 0.014 Å^{-1} during cooling, giving a lower bound on the polymorph crystallite coherence length of 50 nm in the as-cast film and about 80 nm after 10 min at 100 °C. Ultimately, the calculated coherence length provides a limit on how small a crystallite can be, but does not indicate how large it is.[53], [54] It is possible that the change of polymorph of HPI-BT during annealing of the BHJ could influence charge generation and extraction. The change in morphology during annealing on longer length scales is not given by the GIWAXS, and we further examined these changes as described in the following sections.

6.3.3 Surface Analysis Shows Large Change in Morphology with Thermal Annealing

The results of the GIWAXS analysis suggest that textured crystallites are present in the as-cast and annealed state; however, it is unclear where they are located within the film. The microstructural features of the top and bottom surfaces of the BHJ were examined with tapping mode atomic force microscopy (AFM) after thermal annealing to determine whether the top and bottom surfaces were donor or acceptor rich.

165
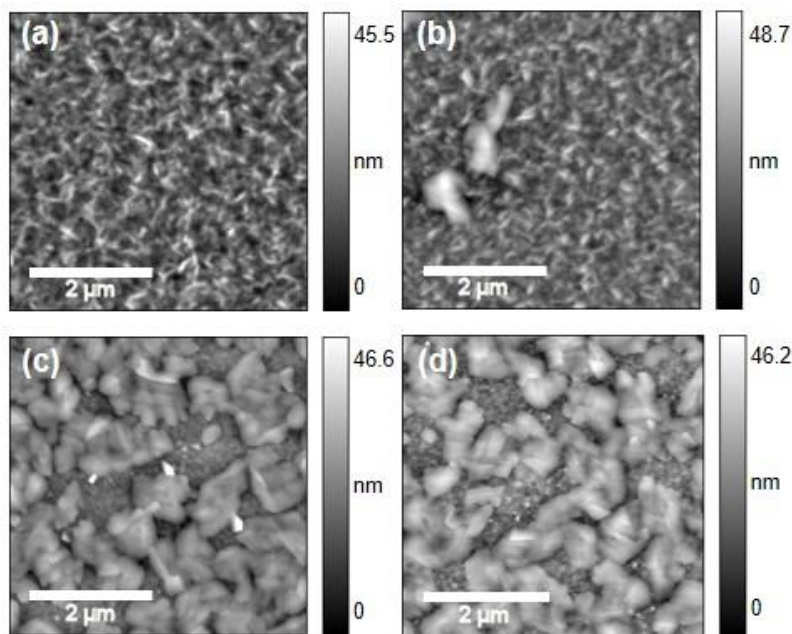
Figure 6-5. AFM topography images of active layer a) as-cast top surface, b) as-cast bottom surface, c) annealed top surface, and d) annealed bottom surface.

Examination of the as-cast film with AFM revealed a rough top and bottom surface likely composed of a mixture of P3HT and HPI-BT (Figure 6-5a,b). The top surface of the as-cast film shows fiber-like features consistent with other AFM studies of regioregular P3HT[55] (Figure 6-5a). Before annealing, the root- mean-square (RMS) roughness of the top surface is 6.2 nm (Table C-1) with some relatively peaked features with a height of 45.5 nm present. Even though GIWAXS results indicated that the crystalline acceptor was present in the as-cast film, there were few obvious features in the AFM images that can be unambiguously assigned to acceptor crystallites on the top surface other than the regions that are relatively tall. GIWAXS measurements at 0.07°, below the critical angle of the film, indicate that both donor and acceptor are present on the surface of the as-cast film (Figure C-8). However, the surface roughness makes it difficult to assess the penetration depth, leaving the precise composition of the near surface region unclear.

166

The bottom surface was also examined before annealing to determine if crystals had nucleated and grown off the anode interface as has been observed in other studies.[48], [56] Similar fiber-like structures covered the bottom surface, but addition- ally, larger aggregated features were also observed that were approximately 1 μm long and 0.5−0.7 μm wide (Figure 6-5b), which are likely to be the HPI-BT crystallites. In addition, the RMS roughness increased slightly to 6.8 nm due to the presence of the larger aggregates. The average height difference between the top of the aggregates and the surrounding fiber structure is 28.9 nm.

The films were reexamined after in situ annealing to determine the effect on the surface structure. The top surface of the annealed film showed features attributed to HPI-BT crystallites (Figure 6-5c). The average dimensions of the crystallites were 1 × 1 μm and were surrounded by what is likely a combination of P3HT and amorphous HPI-BT. The purity of the matrix surrounding the HPI-BT crystallites is not known. Because annealing of the films occurred without an evaporated cathode layer, the growth of the crystallites was unconstrained at the free surface. The height of the HPI-BT crystallites extended approximately 14.3 nm above the rest of the top surface film (Figure C-4c). Examination of the bottom of the annealed film similarly revealed a high density of HPI-BT crystallites (Figure 6-5d). The RMS roughness was 6.9 nm, and the height difference between the top of the HPI-BT crystallite and the surrounding film was 15.2 nm (Figure C-4d). It should be noted that the process of delaminating, flipping, and relaminating the film onto an uneven top surface contributes to the observed roughness of the bottom surface.

The effect of thermal annealing on the growth of acceptor crystallites was examined for annealing periods of 1 min up to 21 min at 100 °C. Acceptor crystallites were shown to

emerge at the top and bottom film surface after only 1 min of annealing. Shorter annealing periods were not examined, and therefore, it is possible that crystallization occurred faster than 1 min. Lateral dimensions of the crystallites remained unchanged with additional annealing (Figure C-3). Higher resolution AFM images show step-like features within the acceptor crystallites and provide information on the aggregate assembly. Within individual crystallites, thin rectangular fibers approximately 1 μm in length and 70 nm wide were observed (Figure C-5). Height profiles across individual crystallites in the topography image were examined to determine if the structures were single crystals or an assembly of smaller crystals (Figure C-6). A large variation in the step height was observed, and therefore, it was determined that acceptor crystallites assembled into fiber bundles with lateral dimensions of approximately 1 × 1 μm.

The substrate used is likely to have had a large effect on the crystallization and phase segregation behavior.[57] Hydrophilic silicon oxide substrates were found to promote crystallization of PCBM at the buried interface in P3HT:PCBM BHJs due to a PCBM rich layer forming at the high surface energy substrate.[48] P3HT segregated to the top interface as the material at the free surface is likely to be the one with the lowest surface energy.[58] Donor or acceptor accumulation at the electrodes is driven by the configuration that minimizes the difference between the surface energy of the electrode and the blend component.[56] Here, BHJs were spun on glass substrates coated with ITO and MoO_3. While the exact surface energy values of the MoO_3 and HPI acceptor are not known, the vertical phase segregation can likely be affected by wetting properties. The MoO_3 layer was not modified after casting to tune its surface energy, which is known to affect the vertical composition in BHJs with fullerenes.[59], [60]

168

6.3.4 Transmission Microscopy Imaging Through Bulk Film Proves Presence of Embedded HPI-BT Crystallites

The spatial distribution of the domains is not revealed using GIWAXS and is difficult to discern by AFM. While the AFM images could be interpreted to suggest that the HPI-BT domain size increases after thermal annealing, this hypothesis disagrees with the increase in J_{SC} of the cells. Because HPI-BT is crystalline, and P3HT is semicrystalline, transmission electron microscopy (TEM) was used to examine the morphology of BHJs. In PCBM-based BHJs, TEM is commonly used to study the degree of mixing due to the large difference in electron density between PCBM and most polymers and small molecules.[61]–[63] Here, it was expected that the more ordered HPI-BT acceptor would scatter electrons differently than P3HT due to its high degree structural order and enable observation of the domain sizes more readily.

STEM imaging proves that relatively large domains of HPI-BT are present in the BHJ before thermal annealing. Contrast between domains is generated during STEM imaging by thickness variations in the film as well as differences in the angle at which each material scatters due to its degree of order. In the as-cast P3HT:HPI-BT film, thin rectangular fibers
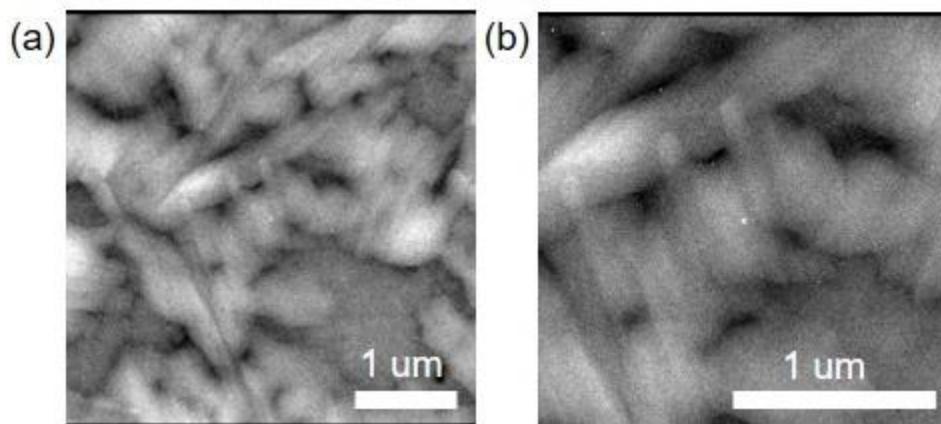
Figure 6-6. STEM images of as-cast BHJ showing embedded acceptor crystallites over (a) approximately 4x4 µm area and (b) zoomed-in to show thin rectangular fibers.

are observed and are organized into micron-sized bundles (Figure 6-6). Individual

rectangular fibers are observed within the aggregates (Figure 6-6b). Interestingly, while the

AFM of the same as-cast films showed very few micron scale acceptor crystallites at the

surface, a high density of crystallites can be seen when looking through the thickness of the

film. There is good agreement between the embedded crystals detected with STEM imaging

and the micron-sized features observed on the surface of the annealed film with AFM. This

indicates that the acceptor crystallites nucleated from the bulk and only grew to the surface

upon annealing. Similar behavior has been observed in some polymer−fullerene BHJs,

particularly where cross-sectional SEM reveals regions of fullerene encapsulated by

polymer.[64], [65] The discovery of HPI-BT crystallites within the as-cast film reinforces

the point that the assembly of each material at the surface of a film cannot be assumed to be

an accurate representation of the bulk.
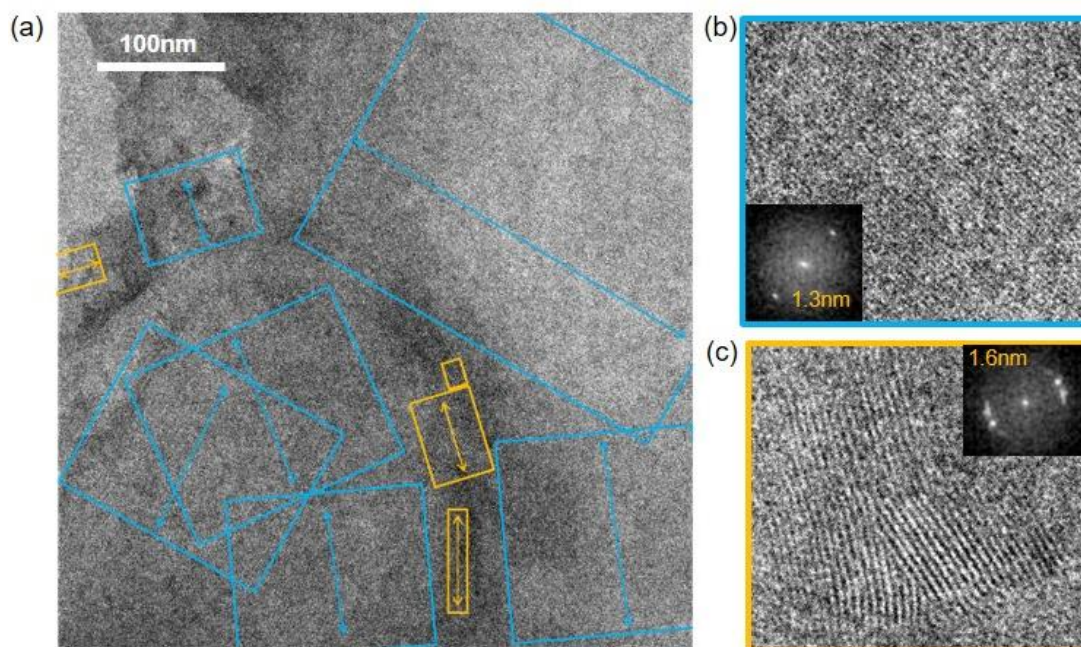
Figure 6-7. HRTEM image of as-cast P3HT:HPI-BT BHJ. a) 500 x 500 nm area showing size and location of HPI-BT crystallites (blue) and P3HT (orange). Enlarged image of b) HPI-BT crystallite, and c) P3HT where the lattice spacings are indicated in the inset.

P3HT and HPI-BT are spatially differentiated by identification of the *d*-spacings

observed within the crystallites, and additional information such as the finite crystallite size

within a region can also be extracted. In the as-cast film, P3HT crystallites were measured to

have an average width of 20−40 nm and length of 50−80 nm (Figure 6-6). However,

nanowires of P3HT were also present in the film with a width of 20 nm and length of

100−300 nm (Figure C-7). GIWAXS in situ annealing showed the formation of an HPI-BT

polymorph with an in- plane d-spacing of 1.3 nm. A HRTEM image of the as-cast blend

(Figure 6-7a) shows HPI-BT crystallites with the same lattice spacing with an average width

of 500 nm and length of approximately 1 μm. In contrast, the peak width analysis from

GIWAXS revealed a minimum crystallite coherence length of 50 nm. However, directly

imaging the size of HPI-BT domains revealed that the size of the grains was an order of

magnitude greater. This reinforces the fact that a coherence length should not be considered

as the size of a domain, and may lead to incorrect conclusions about the origin of charge

generation and efficiency.[53], [54]

6.3.5   Understanding the Role of Thermal Processing on the Performance of Solar Cells

The morphology of BHJs and their interface with the contacts have a significant effect

on the charge transport within the organic layer and subsequent charge collection at the

electrodes.[66], [67] We can now revisit the origin of the change in PCE upon annealing

considering the presence of relatively large acceptor domains in as-cast films. While there is

a change in the polymorph of HPI-BT during annealing, the current in reverse bias is nearly

identical in both cases, suggesting that charge extraction is a dominant factor in the

improvement in performance. The low J_{SC} and FF observed in the as-cast devices likely

results from a physical barrier to charge injection at the cathode interface. Before annealing, the acceptor domains are embedded within the center of the photoactive layer with a thin donor rich layer at the cathode and anode interfaces. Barriers to charge extraction at the contacts caused by either vertical phase segregation or interfacial effects tend to lead to S-shaped $J-V$ curves.[68] The current−voltage characteristics of the HPI-BT: P3HT cells do not have a severe S shape (Figure 6-1), but show a similar ultimate current in reverse bias to annealed devices. Therefore, we believe that the as-cast top surface likely contains both donor and acceptor, but the purity of the capping layer at the surface is not known. The fact that the charges are extracted efficiently at higher applied electric field is consistent with a barrier at one of the contacts. Similar behavior has been observed in structures where excess P3HT was intentionally placed at the cathode.[69] Additionally, one expects the donor− acceptor interfacial area to be similar under the two conditions, because the amount of charge extracted is the same (assuming that charge generation is relatively independent of bias).[70] The results also suggest that the as-cast polymorph of HPI-BT has similar behavior to the crystallized form.

The observation of large crystals agrees with the lack of miscibility of the P3HT and HPI-BT seen in previous studies.[46] By comparison, many PCBM-based OPVs have small and intermixed domains, enabling more effective charge separation at the D−A interface, and, therefore, can typically achieve J_{SC} values of 10−15 mA/cm^2.[28] Here, the increases in J_{SC} and FF occur after annealing due to the vertical growth of the acceptor phase, resulting in increased contact between the HPI-BT crystallites and the cathode. In previous work,[46] geminate recombination was suggested to be a limiting factor in the performance of HPI-BT acceptors. This conclusion was based on bias-dependent quantum efficiency and strong

172

photoluminescence quenching, due to the generation of charges at the interfaces without efficient extraction. Here, we find that the domains of HBI-BT are likely larger than suggested in that work. On the basis of the relatively good performance, given the large domain sizes, HPI-BT is a good candidate for alternative structures for acceptors. Further improvements in device performance can be expected with either alterations of the molecular design, or improvements to the active-layer processing method, in order to inhibit the growth of crystallites as well as to improve the donor−acceptor interfacial area.

It is an open question whether other molecular units previously considered as NFAs could be improved based on the conclusions of this study. Existing linear molecules could be modified with attached units to frustrate the packing. For example, perylene diimides (PDIs) generally show strong crystallization and large domain sizes in BHJs,[20] but attachment of multiple PDI units to a central core frustrates crystallization and improves the performance of BHJs.[26], [29], [30] Future studies may include modification of the alkyl side chains to reduce the π-stacking ability of the acceptor molecule.

6.4 Conclusions

We have examined the evolution of the morphology of BHJs of P3HT with the NFA HPI-BT and found that the changes in PCE with thermal annealing can be understood by changes in the domains of HPI-BT. Micron-sized HPI-BT domains are embedded within the BHJ in the as-cast state with a thin P3HT rich layer covering the top and bottom surfaces. Annealing for a very short time (<1 min) causes the acceptor crystallites to grow vertically through the film surface. While the performance matches previous studies,[45] the role of the donor−acceptor interfacial area on performance was not elucidated. Our results here

suggest that the change in *FF* is likely dominated by extraction at the cathode, and that J_{SC} is ultimately limited by the donor−acceptor interfacial area.

Our studies also point out the importance of using multiple methodologies to study the nanoscale morphology in BHJs. GIWAXS is commonly employed to study details of the angstrom-scale and nanoscale molecular packing and extract a crystallite coherence length of the components in BHJs. However, in systems with disorder, the domain size cannot be readily determined if only a small number of diffraction peaks are observable, but instead a lower bound on the crystallite size can be assigned.[53], [54] Our results for P3HT:HPI- BT BHJs provide a clear demonstration of a case where a phase transformation occurs without large changes in the domain size.

References

[1]   D. Kearns and M. Calvin, "Photovoltaic Effect and Photoconductivity in Organic Laminated Systems," *J. Chem. Phys.*, vol. 29, p. 950, 1958.

[2]   C. W. Tang, "Two-layer organic photovoltaic cell," *Appl. Phys. Lett.*, vol. 48, no. 2, pp. 183–185, 1986.

[3]   D. L. Morel *et al.*, "High-efficiency organic solar cells," *Appl. Phys. Lett.*, vol. 32, no. 8, pp. 495–497, 1978.

[4]   Heliatek, "Heliafilm - Technical Data." [Online]. Available: http://www.heliatek.com/en/heliafilm/technical-data. [Accessed: 23-Feb-2017].

[5]   G. Yu and A. J. Heeger, "Charge separation and photovoltaic conversion in polymer composites with internal donor/acceptor heterojunctions," *J. Appl. Phys.*, vol. 78, no. 7, pp. 4510–4515, 1995.

[6]   J. J. M. Halls *et al.*, "Efficient photodiodes from interpenetrating polymer networks," *Nature*, vol. 376, pp. 498–500, 1995.

[7]   J. Peet, A. J. Heeger, and G. C. Bazan, "'Plastic' solar cells: Self-assembly of bulk heterojunction nano-materials by spontaneous phase separation," *Acc. Chem. Res.*, vol. 42, no. 11, pp. 1700–1708, 2009.

[8]   A. J. Heeger, "25th anniversary article: Bulk heterojunction solar cells: Understanding the mechanism of operation," *Adv. Mater.*, vol. 26, no. 1, pp. 10–28, 2014.

[9]   M. C. Scharber *et al.*, "Design rules for donors in bulk-heterojunction solar cells - Towards 10 % energy-conversion efficiency," *Adv. Mater.*, vol. 18, no. 6, pp. 789–794, 2006.

[10]   C. A. Junwu and C. Yong, "Development of novel conjugated donor polymers for high-efficiency bulk-heterojunction photovoltaic devices," *Acc. Chem. Res.*, vol. 42, no. 11, pp. 1709–1718, 2009.

[11]   L. Ye, S. Zhang, W. Zhao, H. Yao, and J. Hou, "Highly efficient 2D-conjugated benzodithiophene-based photovoltaic polymer with linear alkylthio side chain," *Chem. Mater.*, vol. 26, no. 12, pp. 3603–3605, 2014.

[12]   Y. Liu *et al.*, "Aggregation and morphology control enables multiple cases of high-efficiency polymer solar cells.," *Nat. Commun.*, vol. 5, no. 9, p. 5293, Jan. 2014.

[13]   Q. Wan *et al.*, "10.8% Efficiency Polymer Solar Cells Based on PTB7-Th and PC 71 BM via Binary Solvent Additives Treatment," *Adv. Funct. Mater.*, vol. 26, no. 36, pp. 6635–6640, 2016.

[14] B. Kraabel, D. McBranch, N. S. Sariciftci, D. Moses, and A. J. Heeger, "Ultrafast spectroscopic studies of photoinduced electron transfer from semiconducting polymers to C60," *Phys. Rev. B*, vol. 50, no. 24, pp. 18543–18552, 1994.

[15] B. Kraabel *et al.*, "Subpicosecond photoinduced electron transfer from conjugated polymers to functionalized fullerenes," *J. Chem. Phys.*, vol. 104, no. 11, pp. 4267–4273, 1996.

[16] C. J. Brabec *et al.*, "Tracing photoinduced electron transfer process in conjugated polymer/fullerene bulk heterojunctions in real time," *Chem. Phys. Lett.*, vol. 340, no. 3–4, pp. 232–236, 2001.

[17] P. Sonar, J. P. F. Lim, and K. L. Chan, "Organic non-fullerene acceptors for organic photovoltaics," *Energy Environ. Sci.*, vol. 4, pp. 1558–1574, 2011.

[18] G. Ren, E. Ahmed, and S. A. Jenekhe, "Non-fullerene acceptor-based bulk heterojunction polymer solar cells: Engineering the nanomorphology via processing additives," *Adv. Energy Mater.*, vol. 1, no. 5, pp. 946–953, 2011.

[19] Y. Lin, P. Cheng, Y. Li, and X. Zhan, "A 3D star-shaped non-fullerene acceptor for solution-processed organic solar cells with a high open-circuit voltage of 1.18 V," *Chem. Commun.*, vol. 48, no. 39, pp. 4773–4775, 2012.

[20] S. Rajaram, R. Shivanna, S. K. Kandappa, and K. S. Narayan, "Nonplanar perylene diimides as potential alternatives to fullerenes in organic solar cells," *J. Phys. Chem. Lett.*, vol. 3, no. 17, pp. 2405–2408, 2012.

[21] Y. Zang *et al.*, "Integrated molecular, interfacial, and device engineering towards high-performance non-fullerene based organic solar cells," *Adv. Mater.*, vol. 26, no. 32, pp. 5708–5714, 2014.

[22] X.-F. Wu *et al.*, "Spiro linkage as an alternative strategy for promising nonfullerene acceptors in organic solar cells," *Adv. Funct. Mater.*, vol. 25, no. 37, pp. 5954–5966, 2015.

[23] Y. Lin *et al.*, "High-performance fullerene-free polymer solar cells with 6.31% efficiency," *Energy Environ. Sci.*, vol. 8, pp. 610–616, 2015.

[24] Y. Zhong *et al.*, "Molecular helices as electron acceptors in high-performance bulk heterojunction solar cells," *Nat. Commun.*, vol. 6, p. 8242, 2015.

[25] X. Zhang, C. Zhan, and J. Yao, "Non-Fullerene Organic Solar Cells with 6.1 % Efficiency through Fine-Tuning Parameters of the Film-Forming Process," *Chem. Mater.*, vol. 27, no. 1, pp. 166–173, 2015.

[26] Y. Liu *et al.*, "A tetraphenylethylene core-based 3D structure small molecular acceptor enabling efficient non-fullerene organic solar cells.," *Adv. Mater.*, vol. 27, no. 6, pp. 1015–1020, Feb. 2015.

[27]   S. Holliday *et al.*, "High-efficiency and air-stable P3HT-based polymer solar cells with a new non-fullerene acceptor," *Nat. Commun.*, vol. 7, p. 11585, Jun. 2016.

[28]   S. Li *et al.*, "A spirobifluorene and diketopyrrolopyrrole moieties based non-fullerene acceptor for efficient and thermally stable polymer solar cells with high open-circuit voltage," *Energy Environ. Sci.*, vol. 9, no. 2, pp. 604–610, 2016.

[29]   Q. Wu, D. Zhao, A. M. Schneider, W. Chen, and L. Yu, "Covalently Bound Clusters of Alpha-Substituted PDI-Rival Electron Acceptors to Fullerene for Organic Solar Cells," *J. Am. Chem. Soc.*, vol. 138, no. 23, pp. 7248–7251, 2016.

[30]   J. Lee, R. Singh, D. H. Sin, H. G. Kim, K. C. Song, and K. Cho, "A Nonfullerene Small Molecule Acceptor with 3D Interlocking Geometry Enabling Efficient Organic Solar Cells," *Adv. Mater.*, vol. 28, no. 1, pp. 69–76, 2016.

[31]   Y. Lin, Y. Li, and X. Zhan, "A Solution-Processable Electron Acceptor Based on Dibenzosilole and Diketopyrrolopyrrole for Organic Solar Cells," *Adv. Energy Mater.*, vol. 3, no. 6, pp. 724–728, Jun. 2013.

[32]   W. Zhao *et al.*, "Fullerene-Free Polymer Solar Cells with over 11% Efficiency and Excellent Thermal Stability," *Adv. Mater.*, vol. 28, pp. 4734–4739, 2016.

[33]   Y. Yang *et al.*, "Side-Chain Isomerization on an n-type Organic Semiconductor ITIC Acceptor Makes 11.77% High Efficiency Polymer Solar Cells," *J. Am. Chem. Soc.*, vol. 138, no. 45, pp. 15011–15018, 2016.

[34]   H. Bin *et al.*, "Non-Fullerene Polymer Solar Cells Based on Alkylthio and Fluorine Substituted 2D-Conjugated Polymers Reach 9.5% Efficiency," *J. Am. Chem. Soc.*, vol. 138, no. 13, pp. 4657–4664, 2016.

[35]   L. Yang *et al.*, "A New Wide Band Gap Donor for Efficient Fullerene-free All-small-molecule Organic Solar Cells," *J. Am. Chem. Soc.*, vol. 139, no. 5, pp. 1958–1966, 2017.

[36]   S. E. Shaheen, C. J. Brabec, N. S. Sariciftci, F. Padinger, T. Fromherz, and J. C. Hummelen, "2.5% Efficient Organic Plastic Solar Cells," *Appl. Phys. Lett.*, vol. 78, no. 6, pp. 841–843, 2001.

[37]   X. Yang *et al.*, "Nanoscale morphology of high-performance polymer solar cells," *Nano Lett.*, vol. 5, no. 4, pp. 579–583, 2005.

[38]   N. D. Treat and M. L. Chabinyc, "Phase separation in bulk heterojunctions of semiconducting polymers and fullerenes for photovoltaics.," *Annu. Rev. Phys. Chem.*, vol. 65, pp. 59–81, 2014.

[39]   D. R. Kozub, K. Vakhshouri, L. M. Orme, C. Wang, A. Hexemer, and E. D. Gomez, "Polymer Crystallization of Partially Miscible Polythiophene/Fullerene Mixtures Controls Morphology," *Macromolecules*, vol. 44, no. 14, pp. 5722–5726, Jul. 2011.

[40]   F. C. Jamieson, E. B. Domingo, T. McCarthy-Ward, M. Heeney, N. Stingelin, and J. R. Durrant, "Fullerene crystallisation as a key driver of charge separation in polymer/fullerene bulk heterojunction solar cells," *Chem. Sci.*, vol. 3, no. 2, pp. 485–492, 2012.

[41]   Z. Lu *et al.*, "Perylene-diimide based non-fullerene solar cells with 4.34% efficiency through engineering surface donor/acceptor compositions," *Chem. Mater.*, vol. 26, no. 9, pp. 2907–2914, 2014.

[42]   Y. Zhou, Q. Yan, Y.-Q. Zheng, J.-Y. Wang, D. Zhao, and J. Pei, "New polymer acceptors for organic solar cells: the effect of regio-regularity and device configuration," *J. Mater. Chem. A*, vol. 1, pp. 6609–6613, 2013.

[43]   V. Kamm *et al.*, "Polythiophene:Perylene Diimide Solar Cells - the Impact of Alkyl-Substitution on the Photovoltaic Performance," *Adv. Energy Mater.*, vol. 1, pp. 297–302, Mar. 2011.

[44]   P. Cheng, L. Ye, X. Zhao, J. Hou, Y. Li, and X. Zhan, "Binary additives synergistically boost the efficiency of all-polymer solar cells up to 3.45%," *Energy Environ. Sci.*, vol. 7, no. 4, pp. 1351–1356, 2014.

[45]   J. T. Bloking *et al.*, "Solution-Processed Organic Solar Cells with Power Conversion Efficiencies of 2.5% using Benzothiadiazole/Imide-Based Acceptors," *Chem. Mater.*, vol. 23, no. 24, pp. 5484–5490, 2011.

[46]   J. T. Bloking *et al.*, "Comparing the device physics and morphology of polymer solar cells employing fullerenes and non-fullerene acceptors," *Adv. Energy Mater.*, vol. 4, no. 12, p. 1301426, Aug. 2014.

[47]   E. Verploegen, R. Mondal, C. J. Bettinger, S. Sok, M. F. Toney, and Z. Bao, "Effects of thermal annealing upon the morphology of polymer-fullerene blends," *Adv. Funct. Mater.*, vol. 20, no. 20, pp. 3519–3529, 2010.

[48]   C. He *et al.*, "Influence of substrate on crystallization in polythiophene/fullerene blends," *Sol. Energy Mater. Sol. Cells*, vol. 95, no. 5, pp. 1375–1381, 2011.

[49]   N. D. Treat *et al.*, "Interdiffusion of PCBM and P3HT Reveals Miscibility in a Photovoltaically Active Blend," *Adv. Energy Mater.*, vol. 1, no. 1, pp. 82–89, Jan. 2011.

[50]   J. Rivnay *et al.*, "Drastic control of texture in a high performance n-type polymeric semiconductor and implications for charge transport," *Macromolecules*, vol. 44, no. 13, pp. 5246–5255, 2011.

[51]   A. Sharenko, M. Kuik, M. F. Toney, and T.-Q. Nguyen, "Crystallization-Induced Phase Separation in Solution-Processed Small Molecule Bulk Heterojunction Organic Solar Cells," *Adv. Funct. Mater.*, vol. 24, no. 23, pp. 3543–3550, Feb. 2014.

178

[52] E. Gann, X. Gao, C. Di, and C. R. McNeill, "Phase transitions and anisotropic thermal expansion in high mobility core-expanded naphthalene diimide thin film transistors," *Adv. Funct. Mater.*, vol. 24, no. 45, pp. 7211–7220, 2014.

[53] J. Rivnay, S. C. B. Mannsfeld, C. E. Miller, A. Salleo, and M. F. Toney, "Quantitative determination of organic semiconductor microstructure from the molecular to device scale," *Chem. Rev.*, vol. 112, no. 10, pp. 5488–5519, Oct. 2012.

[54] J. Rivnay, R. Noriega, R. J. Kline, A. Salleo, and M. F. Toney, "Quantitative analysis of lattice disorder and crystallite size in organic semiconductor thin films," *Phys. Rev. B*, vol. 84, no. 4, p. 45203, 2011.

[55] H. Yang, T. J. Shin, L. Yang, K. Cho, C. Y. Ryu, and Z. Bao, "Effect of mesoscale crystalline structure on the field-effect mobility of regioregular poly(3-hexyl thiophene) in thin-film transistors," *Adv. Funct. Mater.*, vol. 15, no. 4, pp. 671–676, 2005.

[56] D. S. Germack *et al.*, "Substrate-dependent interface composition and charge transport in films for organic photovoltaics," *Appl. Phys. Lett.*, vol. 94, p. 233303, 2009.

[57] Z. Xu *et al.*, "Vertical phase separation in poly(3-hexylthiophene): Fullerene derivative blends and its advantage for inverted structure solar cells," *Adv. Funct. Mater.*, vol. 19, no. 8, pp. 1227–1234, 2009.

[58] D. H.-K. Pan and J. Prest, W. M., "Surfaces of polymer blends: X-ray photoelectron spectroscopy studies of polystyrene/poly(vinyl methyl ether) blends," *J. Appl. Phys.*, vol. 58, no. 8, pp. 2861–2870, 1985.

[59] B. J. Tremolet de Villers, R. C. I. Mackenzie, J. J. Jasieniak, N. D. Treat, and M. L. Chabinyc, "Linking vertical bulk-heterojunction composition and transient photocurrent dynamics in organic solar cells with solution-processed MoOx contact layers," *Adv. Energy Mater.*, vol. 4, no. 5, p. 1301290, 2014.

[60] J. J. Jasieniak, N. D. Treat, C. R. McNeill, B. J. Tremolet de Villers, E. Della Gaspera, and M. L. Chabinyc, "Interfacial Characteristics of Efficient Bulk Heterojunction Solar Cells Fabricated on MoOx Anode Interlayers," *Adv. Mater.*, vol. 28, no. 20, pp. 3944–3951, 2016.

[61] J. A. Bartelt *et al.*, "The Importance of Fullerene Percolation in the Mixed Regions of Polymer-Fullerene Bulk Heterojunction Solar Cells," *Adv. Energy Mater.*, vol. 3, no. 3, pp. 364–374, Mar. 2013.

[62] J. S. Moon *et al.*, "Effect of processing additive on the nanomorphology of a bulk heterojunction material," *Nano Lett.*, vol. 10, no. 10, pp. 4005–4008, Oct. 2010.

[63] L. A. Perez *et al.*, "The Role of Solvent Additive Processing in High Performance Small Molecule Solar Cells," *Chem. Mater.*, vol. 26, no. 22, pp. 6531–6541, 2014.

[64] H. Hoppe *et al.*, "Nanoscale morphology of conjugated polymer/fullerene-based bulk-heterojunction solar cells," *Adv. Funct. Mater.*, vol. 14, no. 10, pp. 1005–1011, 2004.

[65] S. Kouijzer *et al.*, "Predicting morphologies of solution processed polymer:Fullerene blends," *J. Am. Chem. Soc.*, vol. 135, no. 32, pp. 12057–12067, 2013.

[66] H. Jin, M. Tuomikoski, J. Hiltunen, P. Kopola, A. Maaninen, and F. Pino, "Polymer−Electrode Interfacial Effect on Photovoltaic Performances in Poly(3-hexylthiophene):Phenyl-C61-butyric Acid Methyl Ester Based Solar Cells," *J. Phys. Chem. C*, vol. 113, no. 38, pp. 16807–16810, 2009.

[67] W. Tress, K. Leo, and M. Riede, "Influence of hole-transport layers and donor materials on open-circuit voltage and shape of I-V curves of organic solar cells," *Adv. Funct. Mater.*, vol. 21, no. 11, pp. 2140–2149, 2011.

[68] B. Y. Finck and B. J. Schwartz, "Understanding the origin of the S-curve in conjugated polymer/fullerene photovoltaics from drift-diffusion simulations," *Appl. Phys. Lett.*, vol. 103, p. 53306, 2013.

[69] H. Wang, M. Shah, V. Ganesan, M. L. Chabinyc, and Y.-L. Loo, "Tail state-assisted charge injection and recombination at the electron-collecting interface of P3HT: PCBM bulk-heterojunction polymer solar cells," *Adv. Energy Mater.*, vol. 2, no. 12, pp. 1447–1455, 2012.

[70] R. A. J. Janssen and J. Nelson, "Factors limiting device efficiency in organic photovoltaics," *Adv. Mater.*, vol. 25, no. 13, pp. 1847–1858, 2013.

Chapter 7

Conclusions

Efficient charge transport in the semiconducting polymer and small-molecule thin films for organic electronics relies on a highly connected morphology. The factors determining the intercrystallite packing need to be further examined. High resolution transmission electron microscopy (HRTEM) is a valuable tool for examining the nanoscale organization and molecular packing (Chapters 2-4). It is very complementary to X-ray scattering methods such as grazing incidence wide-angle X-ray scattering (GIWAXS) which can be used to determine the bulk molecular packing details. Because there can be significant variation in ordering across the film, bulk analysis methods should be combined with techniques which provide local structural information.

There are many factors to consider in order to optimize the performance of organic electronic devices. In bulk heterojunction (BHJ) solar cells, it was shown that solvent additives used in the initial processing steps must be fully removed in order to prevent degradation to the materials in the active layer (Chapter 5). When small-molecule (SM) acceptors are used in place of fullerenes, the molecular structure will be a determining factor in the acceptor morphology. When utilizing planar SMs, steps must be taken to suppress the large-scale crystallization, which will be detrimental to device performance (Chapter 6). Additionally, thermal processing details must be carefully chosen as to not degrade the polymer structure. While, degradation mechanisms can result in the loss of polymer crystallinity, this is not always the case and therefore measurements of the absorption properties after annealing are required to determine whether degradation has occurred (Chapter 5).

There are several outstanding questions in the field such as what are the factors determining the nature of grain boundaries in semiconducting polymers, as well as what are the factors which determine crystallite texture. It is generally assumed that an "edge-on" orientation minimizes the

interfacial energy at the solid−vapor interface. However, the "face-on" orientation is also observed in well-performing OPVs and OTFTs such as PSBTBT, PBDTTPD, and IDTBT. There may be novel or unexpected aspects of molecular organization in well-performing face-on materials. More investigations are required into the mesoscale morphology and an understanding of the molecular packing should not stop the angstrom-scale packing details gained with X-ray scattering methods.

7.1 Outlook

A major application of semiconducting polymers and small-molecules is the use in flexible electronics, but this will require the mechanical properties of the film to be optimized in addition to the optical and electronic. The nanoscale crystallite connectivity is likely to have a large effect on the film toughness. Preliminary observations suggested that PBDTTPD derivatives with more highly connected ordered domains also had an increased toughness. This was demonstrated during delamination and floating of PBDTTPD thin films onto TEM grids. Additionally, the donor-acceptor copolymer IDTBT is similarly mechanically robust, likely due to chain entanglements. Further studies are required to determine the effect of the nanoscale organization on the mechanical properties. It is likely that as the films become more mechanically robust through higher intracrystallite ordering, that the mechanical properties will also improve.

Finally, the knowledge of the grain boundary structure gained with HRTEM needs to be connected to the electrical properties. The mobility and conductivity of materials which form cross-chain structures need to be tested in order to definitely state whether these structures lead to an improvement in the electrical properties. Maps of the morphology generated by the analysis of large HRTEM data sets may be incorporated into transport simulations to determine the theoretical effect on the mobility. Ultimately, further development of polymers and small-molecules for organic electronics will require thinking beyond simply whether a film is crystalline or amorphous and to determine how materials interface and organize on the nanoscale.

Appendix A

Transmission Electron Microscopy (TEM) Procedure for Organic Thin Films

Disclaimers:
1. This procedure is optimized for the FEI Titan 300kV at UC Santa Barbara. On this microscope, alignments are completed through an automated menu so less details are provided in that section.
2. The software SerialEM is used for automated high resolution imaging. This might not be standard on every computer. Download if necessary (with Staff Scientist permission of course 😊)
3. Tips on sample floating and grids included at the end

Prepare microscope

1. Check vacuum levels:
    a. Gun < 30
    b. Octagon < 20
2. Fill up liquid N2 dewar (If first user cool 2 hours before)
    a. Always top off dewar (lasts about 4 hours)
    b. Use funnel and safety glasses
    c. Fill blue cylinder all the way to top (if empty from night before, make sure there is no residual condensation → dry it)
3. Retract camera
4. Home the stage and clear tracks
    a. Search (tab) > Stage (window) > Control (flap out)
    b. Make sure "Tracks" are turned on (monitors where you move on sample)
5. Change airlock pump time to 10 min (600s).
    a. It's usually at 300s
    (This is the amount of time the holder pumps down before inserting into column)

> ★ CHECK THAT <u>OBJECTIVE</u> APERTURE IS **OUT** ★

Sample holder preparation

1. Plasma clean holder before loading sample
2. Remove sample holder from desktop vacuum storage aparatus

> ★Only touch handle and silver part! Don't touch the Cu! ★

    a. Sample holder has 2 washers + 1 three-prong clamp

3. Put new kim wipe beneath holder
4. Use fine-tipped tweezers to remove washers and clamp
5. Sample loading order: washer + sample + washer + clamp
    a. Make a sketch in notebook of how sample is covering the grid (ideally if film was floated onto grid, there should be almost complete coverage)
6. Check the o-ring for dust/hair
7. Tap silver handle of holder while face down to check that clamp is secure
8. Double check one more time that sample is still on the holder (if it falls off in the microscope that is bad news)

Putting in holder

1. Take off lid
2. Take out plug like you take out holder
3. Put in holder – Don't go too slow!
    a. Align small Cu pin on holder with inner silver notch on instrument
    b. Insert holder and then once in turn rightmost until you feel a hard stop (It shouldn't be able to move/rotate during pump down)
    c. If the turbo turns off during this, need to wait for countdown to finish, then take out holder, and insert the plug. This will initiate turbo to come back on.
4. Wait for countdown (wrap cord while waiting)
5. Put holder in, attach cord, cover with lid
6. On computer:
    a. Select specimen holder type
    b. Select "stage: connect holder cable"

★ Usuallyy Octagon pressure is ~2-4 before sample holder, will jump to ~6-8 after holder in which is okay. If it spikes to >15, then something is wrong. It should shettle in a minute but if not then take holder out.
★Wait 1 hour after putting holder in before opening column valves for good images. If you can't wait then just wait ~10min
★Top off the liquid nitrogen before the 1 hour period. Never top of nitrogen right before imaging. This will cause thermal fluctuations and lead to sample drift – need microscope to be very stable for high-resolution imaging.

Find beam and region of interest

1. Check octagon pressure < 6-8
2. FE gun and HT always on
3. Open column valves
    a. You will hear the turbo pump go off once the column valves are open
4. Load FEG Register

	STEM	HR-TEM
Gun lens	6	3
Extractor voltage	4400	3900

★ Extractor voltage takes ~48 hrs to stabilize after a change. Always keep Titan in STEM mode settings. We can do "poor man's HR" w/ these settings. It's fine for polymer samples because we don't need atomic resolution.

5. Make sure that stage is not tilted (α,β=0)
    a. Go to setup tab > set > α,β=0
    b. Or set manually with buttons on control panel on desk
6. Set spot size to 8
    a. Always work in higher spot sizes (6-10 (8 is ideal for imaging))
    b. The lower the spot number the higher the dose delivered to sample (more damage)
7. If beam not visible:
    a. Set magnification to 10,000x → go to low mag if still see nothing (be aware that in low mag mode spot size will automatically go to 2)
    b. Move sample (grid might block the beam)
    c. Load alignment file
    d. Also, can try **lightly** tapping/wiggling holder to make sure it's all the way in
8. Search for a region of interest
    a. If you don't see the beam on the phosphor screen you are likely on the grid
    b. Best to search at 10,000x at spot size 8 (being zoomed out at low spot number is pre-exposing (damaging) sample)
    c. If an option, move electronically and not with the joystick (can be glitchy and cause the stage to drift)
        i. Double click on region in grid overview cartoon in menu (where you track stage movements), or
        ii. Setup tab > Set X,Y locations (move by ~2 µm at a time)

Prepare sample and objective lens

1. Press "eucentric focus" button
2. Condense beam to a spot (INTENSITY knob)
3. Move sample up/down until DP collapses into a spot
    a. In your notebook, record the "Z" value at eucentric height (this may change slightly at different spots on grid, but it is good to have a reference point)

*After eucentric focus trick, <u>sample height (z) and defocus</u> should be close to ideal

★*Additional steps (optional)*

4. Bring in objective aperture to generate a little more contrast → go into diffraction mode

185

5. Use ☐Adjust☐ button to make sure that aperture is centered on the DP

Load alignment file

1. Open system state and make sure that image-beam shift is (0,0)
2. Select supervisor alignment file
3. Highlight all "Available" alignments
4. Push to "Selected", Apply
   a. Don't click "Save" because it will overwrite the file
5. Press "R1" to normalize all

* Now need to check the gun alignments and direct alignments manually…

Center condenser apertures

1. Press the ☐Free Ctrl☐ button
2. Turn C3 off to mimic T20 settings
   a. C1: 2000, C2: 100
   b. If changing to C2: 50 later then need to go through and redo this
3. Bring beam to a point
4. Center with track ball
5. Open beam (open INTENSITY clockwise)
6. Then click ☐Adjust☐ button and use MF knobs to center on the 2nd circle (centering C2)
7. Fix condenser astigmatism here if necessary with C3 off
8. Under ☐Free Ctrl☐ turn C3 lens back on
9. Go into ☐TEM☐ mode

Center C3 lens

★The Titan also has a C3 lens (T20 does not). The C3 allows the beam to stay parallel even when changing the beam diameter. C2 and C3 work together when turning the intensity knob (notice that this changes the C2/C3 lens current). C3 allows you to have the parallel beam condition over a range of areas (especially in diffraction mode, not just one lens currrent where the beam is a point).
★In Probe mode, the beam is always focused on the sample, but the convergence angle can be changed (affects resolution).

1. Check condenser zoom
   a. Open INTENSITY clockwise and see kink when C3 kicks in. Subtle kink hard to avoid but if its bad then either:
   (Watch the C2/C3 lens current on computer. When beam is small just C2 lens current is changing. Watch for the point when the C3 lens current starts changing too. This is where the "kink" occurs (beam does not have smooth transition from C2 to C2+C3 lens))

186

2. If kink is bad then either:
   a. Condenser aperture is in the wrong position (recenter C2: 50/100)
   b. Need to fix gun cross over focus + stigmate
      i. When the focused beam before C2/C3 isnt sitting in the single plane

   Often can assume that the condenser zoom alignment is okay so kink must be from something else

Direct Alignments

(Follow instructions on computer with modifications below)

Tips
- Always be on the right side of the beam opening. Such that when using the intensity knob, turning right opens the beam (makes the diameter larger).
- Good idea to write down starting values for condenser, objective, and diffraction astigmatism in case you accidentally make it worse

1. Gun tilt *(skip step 1 if you see beam)*
   a. Drop down small view screen and spread beam. Maximize screen intensity by maximizing the dose rate w/ multi-function (MF) knobs.
   b. Step 1: If you see a beam go to the next step. No beam? Move track ball.
   c. If gun tilt pp is really off (2 spots very far apart) then need to redo gun tilt
   d. Step 4: Ignore if only made small gun tilt pp changes
2. Gun XD focus + stigmate
   a. Do step 1, ignore step 2
   b. If astigmatism in point then toggle stigmator w/ R2 (very minor adjustments) → then R2 again to toggle back
   c. Step 3 defines the plane
3. Spot size dependent gun shift
   a. Same as in T20 (make a disc and center beam on inner ring on phosphor screen; fix astigmatism with condenser stigmator)
   b. May need to fix astigmatism at each spot size
4. Switch C2 back to 50, redo alignment in FREE CTRL with C3 off
5. Check the beam spread kink after gun alignments (by opening/closing beam with intensity knob)
6. Move to new grid square after alignments
   a. Recheck eucentric
   b. Go into diffraction mode – fix diffraction astigmatism (beam opens and closes in diffraction mode using the focus knob)
7. If beam shape still isn't perfectly circular after alignments, then fix condenser astigmatism

> ★After alignments, beam may not open fully on both sides of the focus. That's okay★

Taking Diffraction Patterns

Can scan around in diffraction mode, but scattering is coming from a very large area. Use selected area aperture to see scattering over different length scales

Using a selected area (SA) aperture
1. Spread beam across the phosphor screen (so that you can see the SA aperture is when inserted – it's not always centered)
2. Set spot size
    a. Spot size 6 is good when using a SA aperture (because the aperture lowers the intensity)
    b. Can go to 4-5 if not much intensity
    c. Use higher spot number (8-10) if not using SA aperture
3. Insert SA aperture
    a. SA 10 is good for looking at local order (has a 100 nm diameter on the UCSB Titan, may vary with other microscopes. Make sure the diameter has been calibrated)
4. Center aperture
5. Set to parallel illumination with beam size of 2 µm
    a. By turning the intensity knob
    b. See the value for the beam size in the main menu on the left
    c. If the beam is too small it will read "condensing". Above a certain size it will read "parallel"
6. Go into diffraction mode
7. Set camera length
    a. With magnification knob
    b. Will vary based on peaks you are interested in, try a few different ones
    c. D = 380mm is good for looking at the alkyl stacking peak

Fix diffraction astigmatism
8. Use the focus knob to open/close the center spot in the diffraction pattern
9. Adjust diffraction astigmatism until the center spot opens/closes concentrically
10. Use the focus knob the make the center spot in DP into a point

Focusing diffraction pattern
11. Insert objective aperture
    a. Center if necessary
12. Adjust focus knob until the edge of the objective aperture looks sharp
13. Use the intensity knob to converge the beam until the spot is smallest

a. You will see a point where beam size is decreasing and forms a point, but turning the intensity knob beyond this just decreases brightness of focused beam

b. Turn the intensity knob just until the point where spot is smallest without decreasing the brightness

Changing spot size during diffraction

Any time you change the spot size while in diffraction mode, need to make sure the beam is still centered:

14. Take out SA aperture
15. Center beam (with track ball)
16. Reinsert aperture

Imaging diffraction pattern

17. Insert and center beamstop on the small phosphor view screen
18. Make sure camera is inserted and Digital Micrograph is open
19. Make sure you know the maximum intensity allowed on camera and stay below
     a. For CCD on Titan at UCSB, stay below 64k cts/pixel
20. View settings:
     a. Exposure = 0.1 s
21. Acquire settings:
     a. Exposure = 0.4s (or less, 0.1 s could even work)
     b. Tools > Sum 10 exposures
22. In the live view mode, make sure the beam stop is centered corrected
23. Raise screen to take DP image, then immediately lower screen as soon as exposure is done
     a. When the screen is down the camera is protected
24. Do an electronic stage movement of about 2µm before every image then press 'Acquire'
     a. You want to press 'Acquire' immediately after the stage move to minimize sample exposure
     b. So type the desired stage move into the Setup tab, press enter to move, wait 1-2 seconds, then press 'Acquire' to get DP
25. Check how much intensity you are getting:
     a. Analysis > Statistics > Max and Min
26. Fix signal to noise ratio
     a. Process > Simple Max > Sqrt q

★IF CAMERA EXPOSED TO DIRECT BEAM ★

1. Lower view screen
2. Spread beam with intensity knob

3. Simultaneously drastically increase focus step and defocus

Beam stop tips
- Make sure that beam blocker is covering all of the direct beam
    - Ensure that even if the beam blocker were to get bumped it would still be covering the direct beam (protect the camera!)
    - In order to capture all of the rings in DP, adjust magnification so that the DP is in the bottom right of small view screen
    - (Move the beam position with the diffraction shift X and Y (should be MF X and Y knobs)
- After the beam blocker is in a good position, unmap MF X and Y from diff shift to prevent movement and protect camera

More Tips

1. To determine the d-spacing of a diffraction peak: $\dfrac{1}{\left(\text{diameter}/_2\right)}$
2. If you want to be absolute about assigning the peak position in the diffraction pattern, need a calibration sample in the same session. Gold nanoparticles are good for this. Can put a drop of an Au nanoparticle solution (particles in water) on grid after floating sample)
3. Need to hold the beam stop steady when acquiring the DP because the beamstop can shift → this could damage the camera!
4. Can change the area illuminated by turning the intensity knob. Check the exact area by looking at the "beam settings"
5. Using the SA aperture, there are many fewer counts, so may need to move to lower spot size (have to redot all alignments)

(Instructions for the FEI T20)

Using SA aperture in diffraction mode
- Go into bright-field mode and insert SA aperture (manually)
    - 4 = largest diameter
    - 1 = smallest diameter

**Be sure not to bump the sample stage when adjusting knobs on the SA aperture!

- All the different sized apertures may not insert into the same area so need to check
   - Check size (in real space) by centering aperture in center of view screen, raise screen, then take a picture

**Remember that the first image taken at a certain exposure time will be a dark image used by the program to subtract background counts

**In diffraction mode, best to stick with one size and then slowly insert and take out the aperture

(now back to FEI Titan)

STEM mode – *Setting up*

1. Check the Octagon pressure ($\leq$ 5 for good images)
2. Go into "Probe" mode and select "Microprobe"
    a. STEM > Free Ctrl > Microprobe
3. Check that the rotation center is about the same in microprobe STEM and TEM
4. Go into TEM mode and center 50 μm C2
5. Check the condenser astigmatism
6. Before going into STEM, zoom around in diffraction mode (to make sure you're on the sample), and fix diffraction astigmatism (CL= ~680mm)
7. Go to STEM mode but clicking STEM button
    b. This goes automatically into diffraction mode
8. Blank beam
9. Insert detectors → CL = 160 mm *(300, 380 good too)*
    c. Short CL ~ atomtic contrast (high angle)
    d. Long CL ~ diffraction contrast
10. Set contrast/brightness to 50/50
11. Set image resolution
    e. 2048x2048 with short dwell time
    f. 1024x1024 with long dwell
12. Make sure Image beam shift is (0,0) in System Status
13. Pull down small view screen
14. Change MF to diff shift X/Y
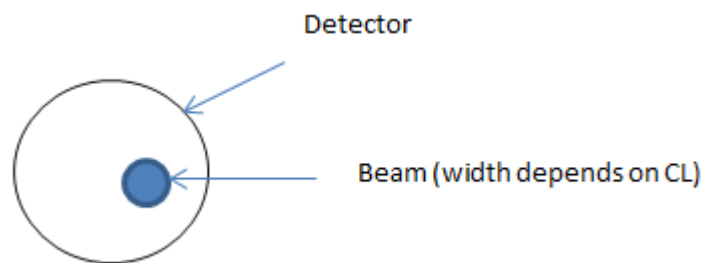
15. Click "Search" to search over sample
16. If increasing the CL then need to recenter the DP
17. Blank beam when not searching/acquiring

★Right click on picture and click "info". Check pixel size and see if its smaller than feature size (good).
- Example: feature is 1.3 nm and pixel size is 930pm. Need to increase the magnification to increase the resolution

STEM mode – *Focus beam*

1. Blank beam
2. Remove detector
3. Go out of diffraction mode
4. Increase magnification (SA 165kx)
5. Fix condenser astigmatism
6. Use focus knob to open/close beam
7. Keep as point
8. Go back into diffraction mode
9. Get sample at eucentric w/ beam in focus (eucentric focus button)
10. Click "blank" beam
11. Insert detector
12. Set image settings to 2048x2048
13. Take image
14. Blank beam 1 second before scan is finished so you know what the intensity is for "zero counts"
15. Anytime you move to a new location, put the crosshair in the corner and recheck the focus
    a. Keep focus ~ -4 μm, adjust Z to stay at ~-4 μm
16. Change the convergence angle to 4 mrad
    a. Record the C2 lens current change
    b. Need to redo alignment now
17. Redo focus beam (zoom out if you can't find the beam)

★In TEM mode, we want to illuminate a larger area → Use microprobe. A minicondenser compensates for the E-field between 2 objective lens.
★In STEM (probe mode), we don't need to minicondenser because we want a small point → Nanoprobe
★In STEM mode, if you have a thicker film, you may want a less convergent beam (<100nm = thin, >300nm=thick). To do this, turn on microprobe when in STEM (instead of the default nanoprobe)
★C2 lens is determining the convergence angle★
    In nanoprobe: 100 C2 = 18 mrad
                   50 C2 = 9 mrad

<u>High Resolution Imaging</u> - *Alignments*

1. Check that C2 is at 50
   a. Recenter if necessary
2. Typical working conditions:
   a. Magnification = 38k
   b. Spot size = 8
3. Go to twice the desired magnification to fine tune alignments
4. Check the following:
   a. Eucentric height
   b. Condenser stigmator
   c. Beam tilt pp (x and y)
   d. Rotation center
      i. Spread beam, look at image and try to minimize image movement
      ii. Try inserting the beamstop to define an absolute position to see how the image is moving (helpful to find a hole, tear, or particle in the sample to focus on)
   e. Redo beam tilt
   f. Redo condenser astigmatism

> ★If you change the mag or spot size at all after this then need to go back and redo all these alignments★

5. Set magnification to 38k (or whatever you are working at – 38k is good for seeing the akyl stacking and crystallite connectivity)
6. Move to a new area after alignments
   a. Use electronic sample shift to move to a new grid square (not joy stick – can cause stage drift)
   b. Redo eucentric
7. Spread beam beyond the 2nd circle a little on phosphor screen
   a. Check that the area of the beam is ~1.2μm
8. Lift screen (cover view screen with black cover)
9. Insert camera

<u>High Resolution Imaging</u> – *Setting up SerialEM*

★Digital Micrograph actually takes the image but need to change setting in SerialEM

1. Open SerialEM
   a. Run: C:\Programfiles\SerialEM
   b. Error → Click OK
2. If you manually set to 38k, then it will set to 43k in Serial EM (not sure why but it does)

3. Check the following boxes in the menu on the left:
    a. Low dose mode
    b. Continuous update mag & beam
    c. Blank beam when screen down
        i. Need to uncheck this before you want to go back and redo any direct alignments – if you forget to uncheck then you won't see any beam on the phosphor screen
4. Focusing
    *In this program it focuses in one place/setting and images in another
    a. Click 'Setup' button in SerialEM and check that focus is at 38k and sp8
    b. Also check 'Record' settings. They may have different settings
5. Take image
    a. Click 'Record' (It will take a reference first)
    b. Box will pop up → click NO

> ★ Shift F = fourier transform (CTRL F if you're in Digital Micrograph)
> ★ +/- = zoom in
> ★ Left click mouse and drag – to move around image
> ★ Right click mouse and drag (image shift)

6. Check "copy current area mag & beam to "R" (keeps settings for focus/record)
7. Click "Setup" button in SerialEM to change exposure time
    a. SerialEM will take a new dark reference if you change any settings
8. Open Image Settings in microscope software window and set MF X/Y to Image Shift

High Resolution Imaging – *Collecting Data*
*If you take more than >300 images, SerialEM won't let you take any more, need to File > Close and Open a new

1. File > Open New
    a. Save as "Integers"
    b. Select all extended headers
    c. Save extra info as .mdocc
    d. Create file name as .mrc (just add to end of file name)
2. Click 'Record'
3. Hover mouse over image to see how many counts per pixel
    a. Aim for ~100
4. Fourier transform image (shift F) to make check focus and astigmatism
    a. If blob in FT is assymetric then need to fix condenser astigmatism (unblank beam and go out of SerialEM to fix this on the phosphor screen)
5. File > 'Save Active'
6. Check how the sample damages

    a. Click "Record" multiple times in the same place to see how the sample is damaging

7. Use ↑↓ arrows to flip through buffers (stack of images)
8. Focus
    a. Find an edge or feature in the sample to focus on
    b. Focus > Set Target (-0.50)
9. Check the drift rate
    a. Focus > Autofocus
    b. Look in the "Log" window and look at drift rate. This lets you know when the sample is stable enough to image
    c. For some reason autofocus always says a drift of 0.00 nm/s for the first try. Click again and you will see the real drfit
    d. Drift rate $\leq$ 0.01 nm/s is good

★For about 45 min after you put the sample in, it will drift a lot. This may lead to false conclusions that things look directional bu in reality its just drifting. Best to load, then wait till drift rate is low (~ <0.02 nm/s) ★

---

10. Use MF X/Y to shift around and check things out before collecting image set
    a. Step size: 4
    b. Shift in ~0.15 incremenets
    c. Can also adust the defocus a little while scanning
11. 'Reset image shift'
12. Find a new area for imaging after alignments
    a. In TEM program, find setup tab
    b. Go to set and move X or Y by 5-10μm
13. "Record" to make sure we are still in a good area
    a. Static image means we are on the grid
    b. First image of sample after shift might look worse, 2nd image looks better
14. Click 'Hex', 'BigHex' or 'BiggerHex' for automated data collection of different numbers of images
    a. I prefer 'BiggerHex' which is usually 62 images

★If you see large fringes in the corner of the image, that is from the edge of the beam. Fix by:
    - Slightly moving trackball
    - Spreading beam a little more 1.2→ 1.6μm
★Changing the focus a lot will move the beam sometimes and need to fix

---

★Things to try if images don't look good★
1. Change the exposure time (aim for ~100 cts/pixel)
    a. Keep exposure time at a maximum of ~8-10 seconds. Instead of exposing for longer, try a lower spot # with a lower exposure time.
2. Change the spot size (7-10)
3. Try inserting the C2 100 vs. C2 50
    a. C2 100 results in higher cts/pixel so may need to lower exposure time or increase spot #
4. Always aim for ~100 cts/pixel, so whatever configuration gets you there while giving good signal. This will take some trial/error and will vary from sample to sample

High Resolution Imaging – *Fixing Astigmatism*

Check the following things when there is an astigmatism in the F.T.

1. Condenser astigmatism (need to ensure we have parallel illumination conditions and that the point source is emitting spherical waves and not elliptical)
2. Objective astigmatism
3. Beam tilts
4. Make sure beam opens symmetrically
5. Rotation center
6. Check condenser astig, beam tilt after rotation center change

★Keep dose low: ~100 cts/pix (when hovering mouse over HR image)
★Try imaging for longer or lower spot # to get more counts. However, watch out for structure that might form from damaging

Dark Field Imaging
**You found a good area, and now insert the objective aperture for set-up for dark-field
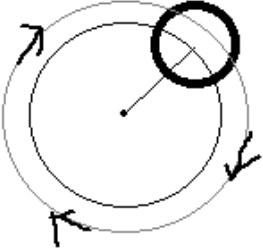
1. Go out of low dose mode
2. Reset image shift
3. Insert 10 μm objective aperture
4. Go into diffraction mode (D 400-600mm)
5. Check beam diameter
    a. Look under Setup > Beam settings > TEM > area
    b. Want ~1.2 μm
    c. Use intensity knob to change beam diameter
6. Make DP bigger
    a. Magnification to the change camera length
7. Move DP on small view screen

a. Use diffraction shift

Add   Delete   ○ None
                     ○ XY
Rot   Tilt   ✓ Conical
→ □ Dynamic
                     ↖

Dynamic has to be off!

Circle   for conical dark field
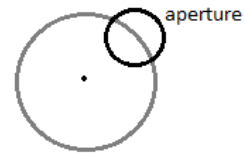   (can only use circle in
          dynamic)

- Spinning useful to center DP (direct
  beam) in center of objective aperture

- Dynamic takes Rotation (DF angle)
  and makes it the negative
  (ex. 300 deg --> -300 deg)

Back   **_to Imaging_**

1. Turn off diffraction mode
2. Turn on low dose
3. Dark field better at around 3400 (3.4k or 34k?) not
   43000
4. Find BF DF tab
   a. Use MF X/Y to move around DP

aperture

Study the Long Range Order

- Over what scale do the features in the DP go from isotropic to anisotropic?
- Check what happens when the area of the beam changes and goes from parallel to
  convergent beam
   o Example: 2 μm → 1.8 → 1.2 → 1 → 600nm

Damage and Dose

- If worried about damage during DP scanning, go up in spot size
- Use the defocus knob to change the illumination area in diffraction

Inserting Objective Aperture during Diffraction

- While in diffraction mode, can insert objective aperture (10μm)
- Use "Adjust" to center aperture, can also move manually
- We do this to cut out some diffraction contrast and then get more mass-thickness
  variations

Switching Samples

1. **Close column valves**
2. Home stage
3. Turn on turbo
4. Take out holder
5. Change sample
6. If going to wait longer than 10+ minutes before putting holder back in then put in plug
   a. Otherwise put holder back in
7. Wait for airlock pump countdown to complete (usually 5-10 minutes (check status on 'Vacuum Overview' menu)
8. Insert holder into column
9. Fill up liquid nitrogen dewar
10. Before opening column valves, wait 1 hour for vacuum to improve (10 minutes if in a rush – not ideal)
11. Previous alignments should still be set so do not need to redo all alignments (just fine tune)

Find area of interest

12. Find area of interest by electronic stage moves

Reset eucentric

13. Press 'eucentric focus'
14. Condense beam to a spot (INTENSITY knob)
15. Move sample up/down until DP collapses into a spot
    a. In your notebook, record the "Z" value at eucentric height (this may change slightly at different spots on grid, but it is good to have a reference point)
    b. If you don't see the DP, the try moving by a little to a different spot

Fine tune alignments

16. Recheck astigmatism, beam tilt pp, and rotation center
    a. Iterate between until there are no changes

Shut Down

1. Turn off any stigmator
2. Take out objective and SA aperture
3. Set magnification to 10kx
4. Spread beam to cover large screen
5. Home stage
6. Retract camera

7. Close column valves
8. Take out sample holder
9. Reset airlock pump time to 300s
10. Put plug back in

If you are the last user:

11. Remove nitrogen dewar and empty
12. Place dewar and lids face down on paper towel to dry
13. Place paper towel under cold finger
14. Start cryo cycle
15. Store holder in desktop vacuum aparatus (holder must ALWAYS be stored under vacuum – prevents contamination buildup which will worsen the microscope vacuum for the next user)

Comments on Sample Floating and Grids

Films can be prepared by methods such as spin-coating, blade-coating, drop-casting, vapor deposition, etc. The choice of substrate will depend on how the film will be processed. Because the substrate is known to affect film texturing, it is important that sample preparation conditions are consistent for morphological and electrical characterization.

Floating involves the delamination of the organic thin film from a substrate by dissolving a sacrificial layer between the substrate and the thin film being studied. A solvent must be used that dissolves the sacrificial layer but not the thin film. The most common method is to use a silicon substrate with an added thermal oxide (~1000Å or more), where the SiO_2 layer is dissolved in a weak HF solution. If BHJs are being studied then the MoO_3 or PEDOT:PSS layer below the active layer can be dissolved in water without the use of HF. In that case, any type of substrate can be used.

Before dissolving the sacrificial layer, sections of the thin film which are not ideal should be removed. Because a very small region of the film is examined in the TEM, it is important that the piece of film studied is from the very center or where the film is the most uniform. This would include thicker regions near the substrate edges. For spin-coated organic materials, the undesired sections can be easily removed by scribing with Teflon tipped tweezers.

The sample is slowly dipped in a solution of 5% HF at an angle of about 45° for 1-5 seconds. The film is then slowly removed from the HF and very slowly dipped into a bath or deionized water at an angle of 45°. The film will slowly delaminate from the substrate and rest of the surface of the water bath.

Once the film has been delaminated from the substrate, it needs to be carefully relaminated onto a copper TEM grid. I recommend Ted Pella copper grids with Ultrathin Carbon Film on

200
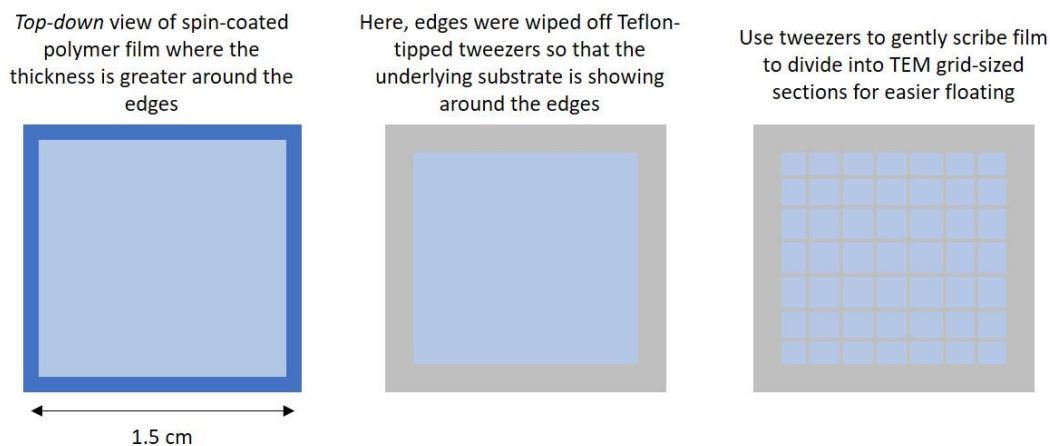
Figure A-1. Steps to prepare film before floating.

a Lacey Support Film (Prod # 01824) for high-resolution imaging. For electron diffraction, C-flat^{TM} Holey Carbon Grids on copper from EMS (https://www.emsdiasum.com/microscopy/products/grids/cflat.aspx) are ideal. I would recommend Product # CF-4/1-4C, which have 4 µm diameter holes in the carbon support and the holes are separated by 1 µm. C-flat^{TM} grids also allow one to easily calibrate the length scale they are looking at in case the microscope is not properly calibrated.

Before the film can be placed on a grid it needs to be broken into smaller pieces that are approximately the size of the grid (Figure A-1). To laminate a section of thin film onto the grid, I recommend using the Perfect Loop tool from Electron Microscopy Sciences (EMS) (https://www.emsdiasum.com/microscopy/products/preparation/ultramicrotomy.aspx).

Appendix B

Supplementary Information for Chapter 4:

The Effect of the Alkyl Side-chains on Intercrystallite Ordering in Semiconducting Polymers

B.1 Density Functional Theory Calculations (DFT)

The backbone structure was constructed in ChemDraw and imported into GaussView. Initial optimization was completed with a ground state Hartree-Fock method and 3-21G* basis set. That structure was input into a ground state DFT calculation with a B3LYP/6-31G(d,p) level of theory. Backbone repeat unit lengths and dihedral angles were measured within the GaussView program.

B.2 UV-Vis and Fluorescence Measurements

UV-Vis absorption measurements were conducted on thin films of each derivative after various anneals to test the thermal stability. This was completed in lieu of DSC and TGA because they were inconclusive over the timescales examined. Identical sample preparation methods were used, but films were deposited on transparent quartz substrates. The background signal from the quartz substrate was subtracted from each spectrum. Measurements were completed using a Shimadzu UV 3600. A sampling resolution of 1nm was used and the absorption spectra was collected from 1200 to 220nm with the "very slow" measurement setting.

Photoluminescence was measured with a Horiba FluoroMax-4 fluorimeter which is operated by the Fluoressence V 3.5.1.20 software. The fluorimeter uses a 150 W continuous Xe arc lamp and has a R928 photon counting PMT detector. The excitation and emission ranges are 200-600 nm and 265-900 nm respectively.

B.3 Polymer Molecular Weight

PBDTTPD derivatives were synthesized by Pierre M. Beaujuge's group at King Abdullah University of Science and Technology (KAUST). Values for the molecular weight were determined by gel permeation chromatography (GPC).
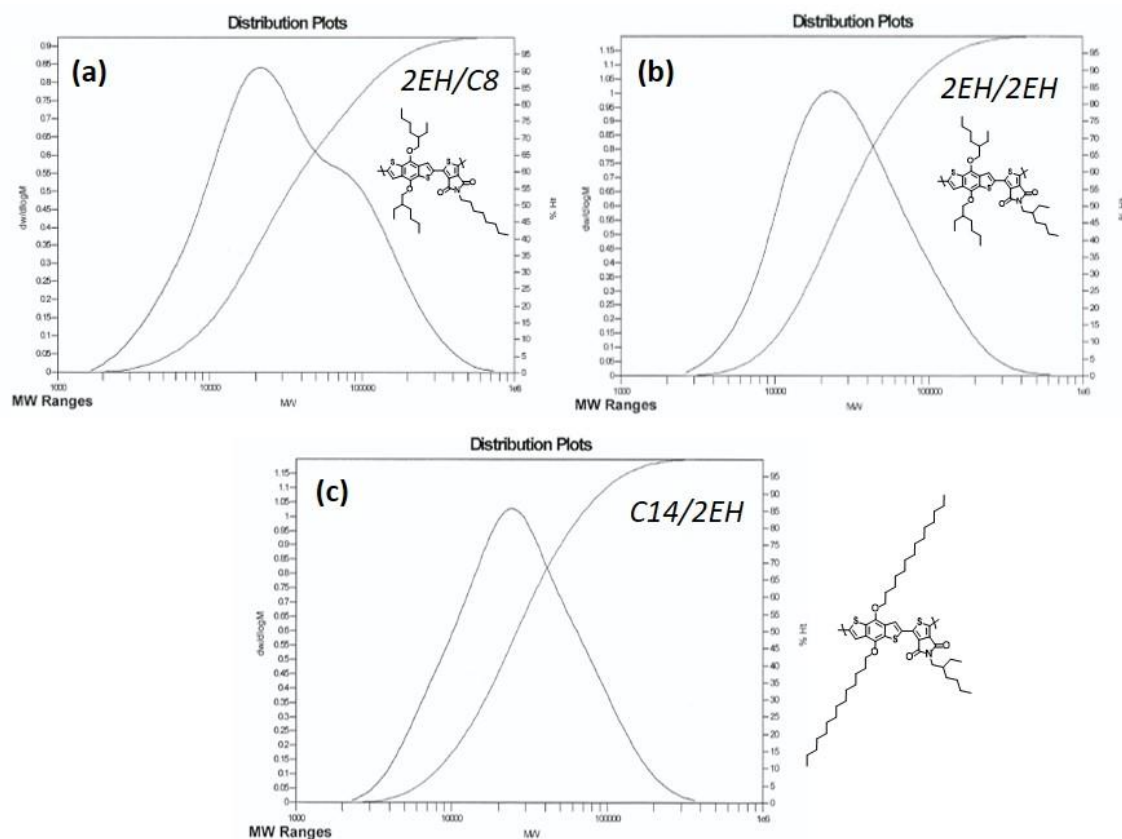
Figure B-1. GPC molecular weight results for (a) 2EH/C8, (b) 2EH/2EH, and (c) C14/2EH.

B.4 Atomic Force Microscopy

Surface topography of the as-cast thin films was investigated with atomic force microscopy (AFM). Asylum Research AFM Software (Version 14) (https://www.asylumresearch.com/) was used for image plotting. RMS roughness values were calculated with Gwyddion (http://gwyddion.net/) from the images in Figure B-2.
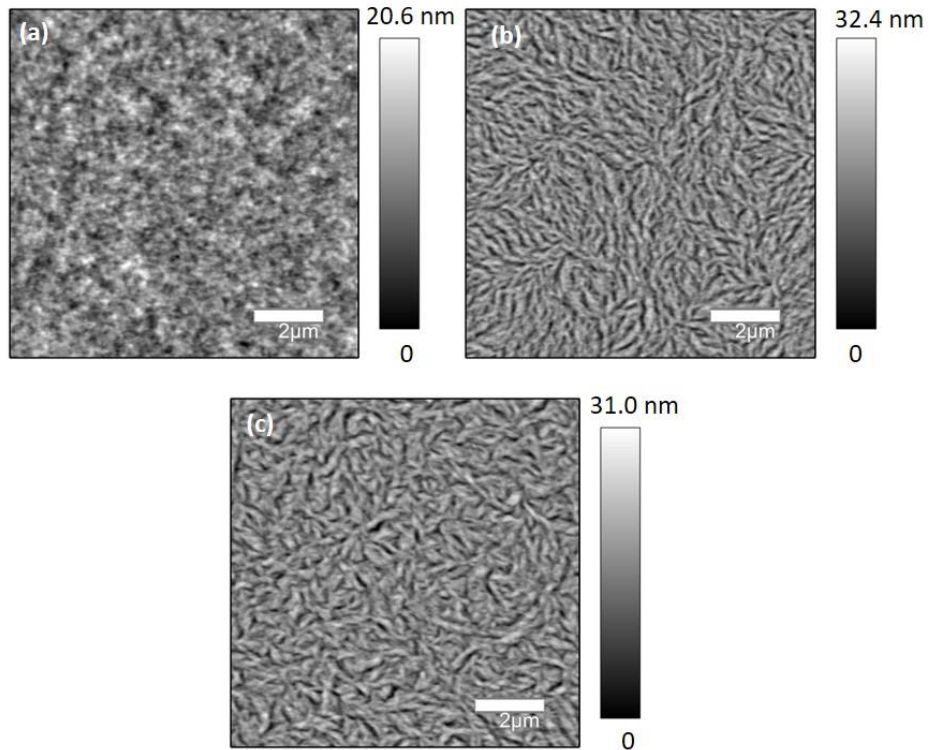
Figure B-2. AFM images of as-cast thick films (~60 nm) of (a) 2EH/C8, (b) 2EH/2EH, and (c) C14/2EH.

Table B-1. Thin film surface roughness calculated from AFM images.

	RMS Roughness (nm)
2EH/C8	2.7
2EH/2EH	4.2
C14/2EH	3.9

B.5 Grazing Incidence Wide-angle X-ray Scattering (GIWAXS)

The WAXStools software was used for GIWAXS image plotting and analysis[77]. The program was developed by Stefan Oosterhout in Michael Toney's research group at SLAC National Accelerator Laboratory.

B.6 High-resolution Transmission Electron Microscopy (HRTEM)

Electron micrographs were obtained using a FEI Titan 300 kV FEG TEM/STEM System. Spot sizes of 7-9 were used at a magnification of 43k. An average dose Spin-coated films were floated onto Ted Pella Cu grids with ultrathin carbon film on a lacey carbon support film (product # 01824) and Electron Microscopy Sciences (EMS) C-flat holey carbon grids (product # CF-4/1-4C). Film thickness ranged from 15nm for thinnest samples to 60nm for thicker films. Images were collected using the automated software SerialEM and analyzed using ImageJ.

HRTEM images were converted into simplified line drawings of the lattice fringes present from the crystalline regions. This allows for easier visualization of the ordered domains and grain boundary structure. This image decomposition was completed with MATLAB based software developed by Christopher J. Takacs.
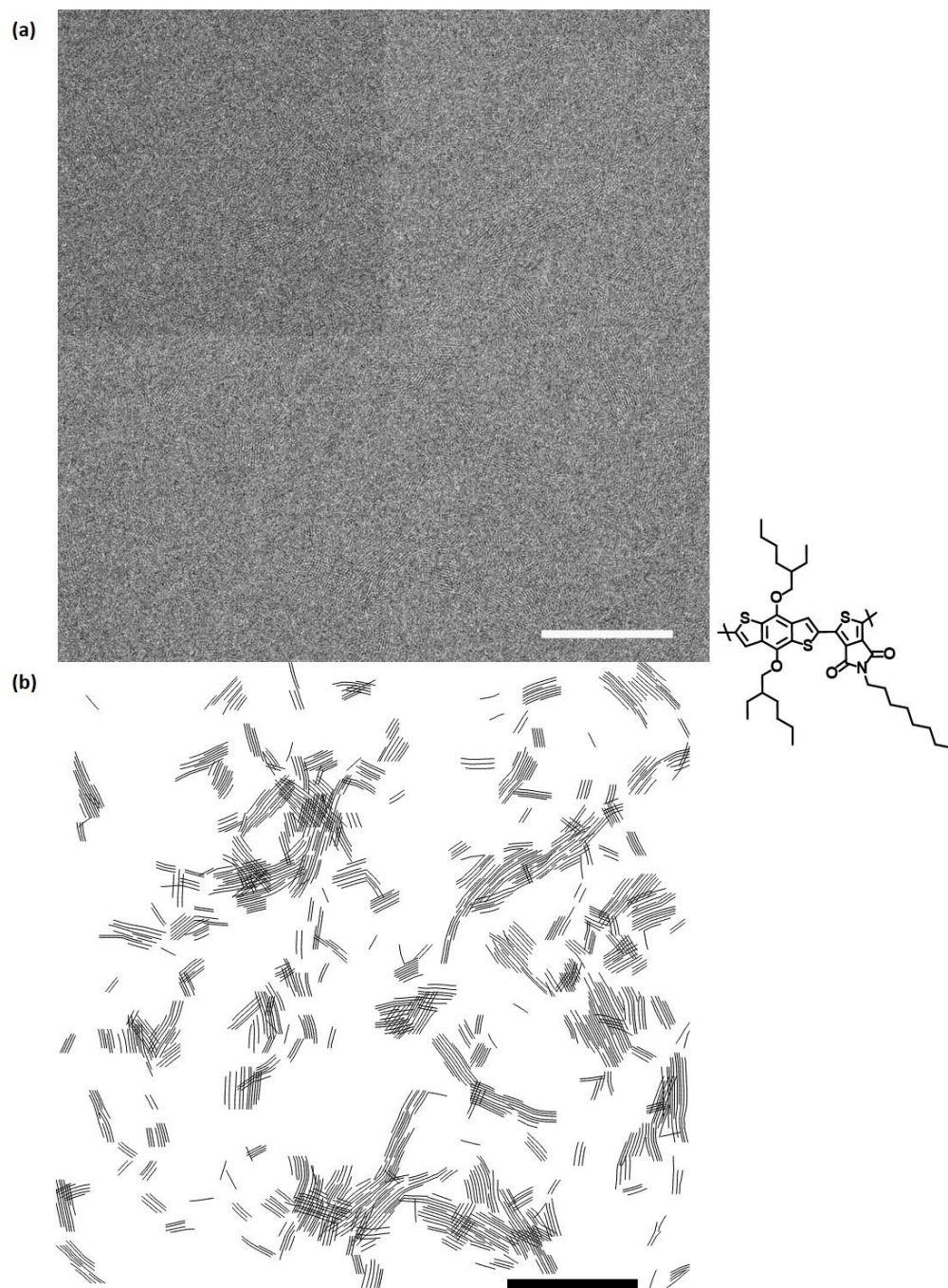
Figure B-3. As-cast thin film (15 nm) of 2EH/C8 (a) HRTEM image and (b) lattice fringe line drawing.
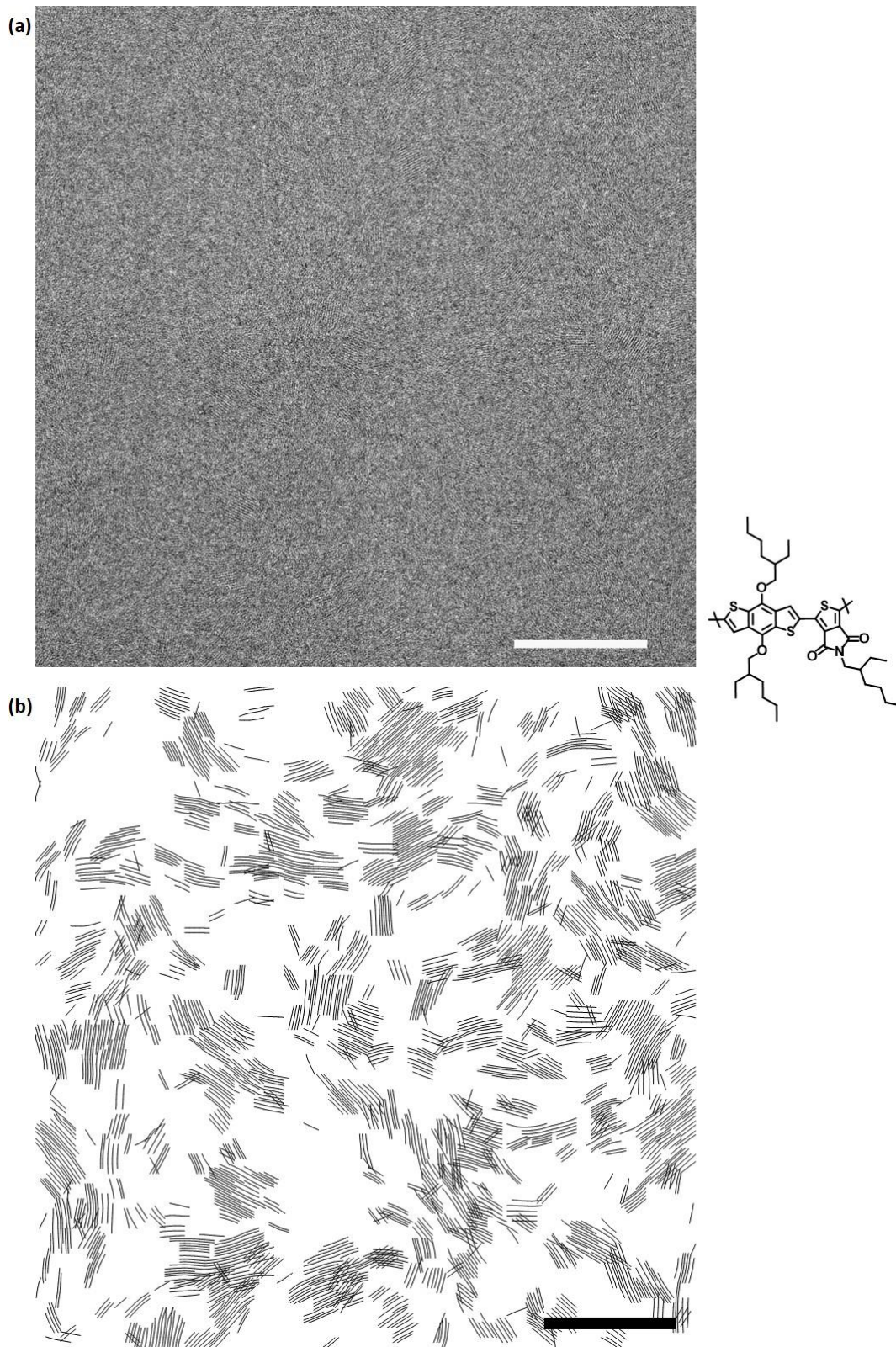
Figure B-4. As-cast 2EH/2EH thin film (15 nm) (a) HRTEM image and (b) FFT derived line-drawing of the lattice fringes in the image. Scale bars are 100 nm.
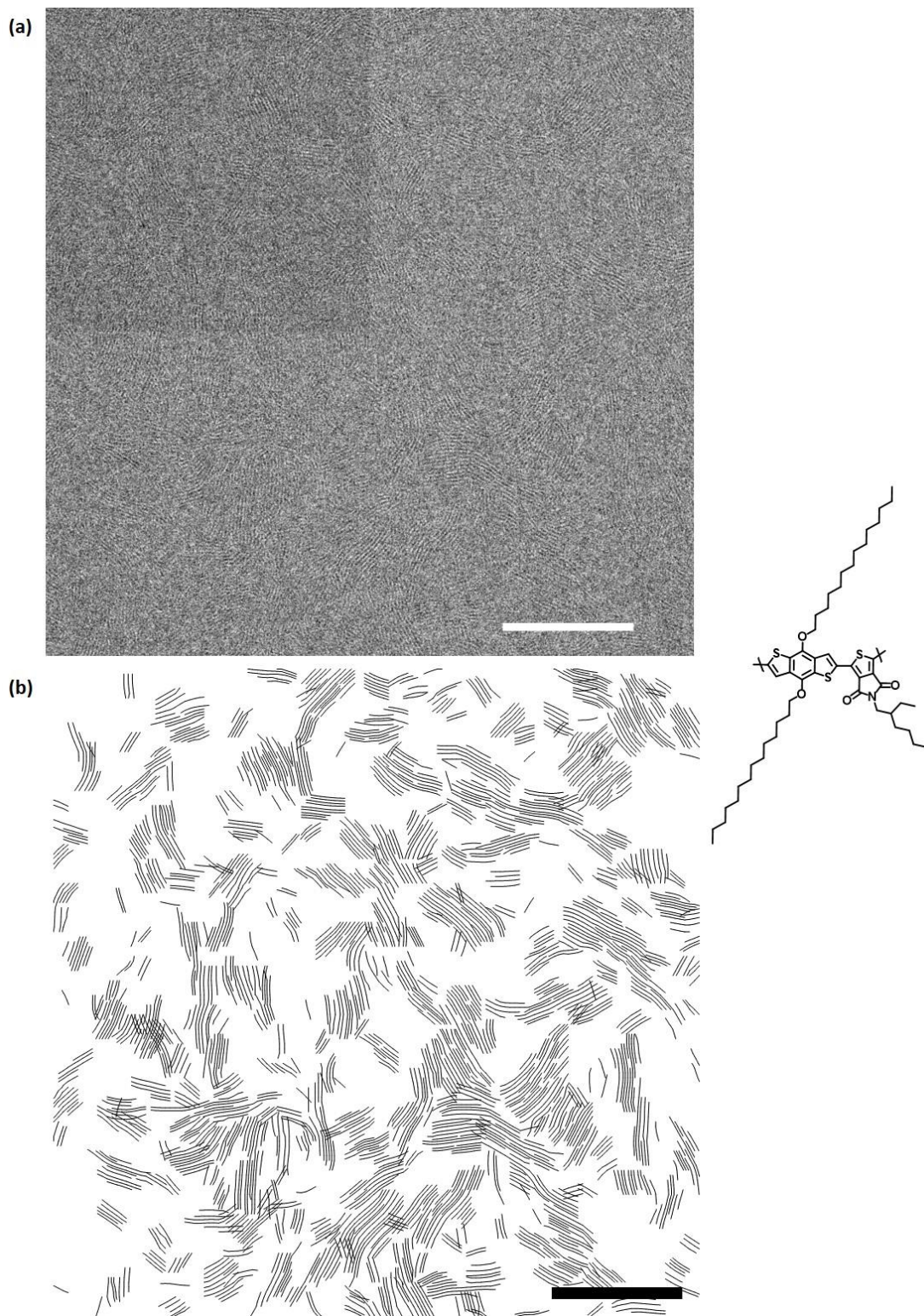
Figure B-5. As-cast C14/2EH thin film (15 nm) (a) HRTEM image and (b) FFT derived line-drawing of the lattice fringes in the image. Scale bars are 100 nm.

Appendix C

Supplementary Information for Chapter 6:

Role of Crystallization in the Morphology of Polymer:Non-Fullerene Acceptor Bulk Heterojunctions

C.1 External Quantum Efficiency (EQE) of BHJ Solar Cells

Solar cell quantum efficiency is a measure of how efficiently charge carriers are collected as a function of the incident light energy and/or wavelength. Recombination effects tend to reduce the EQE.
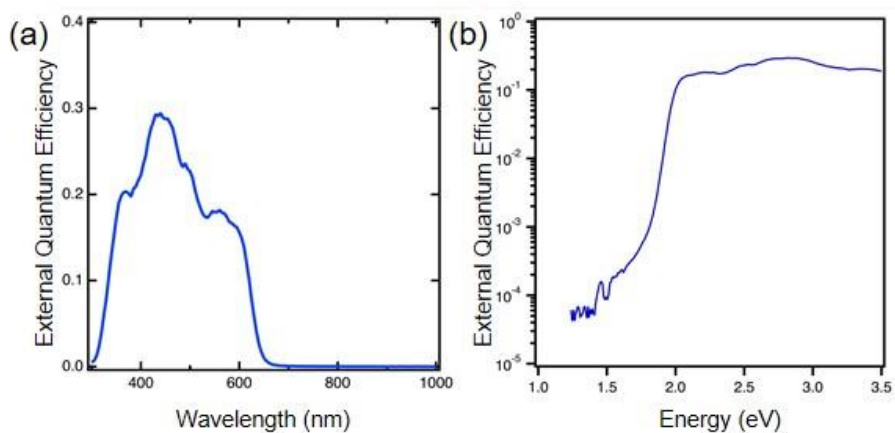
Figure C-1. External quantum efficiency of an unannealed HPI-BT:P3HT BHJ on (a) a linear and (b) log scale.

C.2   Atomic Force Microscopy

C.2.1   Surface Roughness

AFM images were plotted and analyzed using the Gwyddion software (http://gwyddion.net).
RMS roughness values were calculated by averaging RMS values from six different 10x10μm
images each for the as-cast top surface, as-cast bottom surface, annealed top surface, and annealed
bottom surface. Figure C- shows AFM images for each of these images, and roughness results are
summarized in Table C-1.
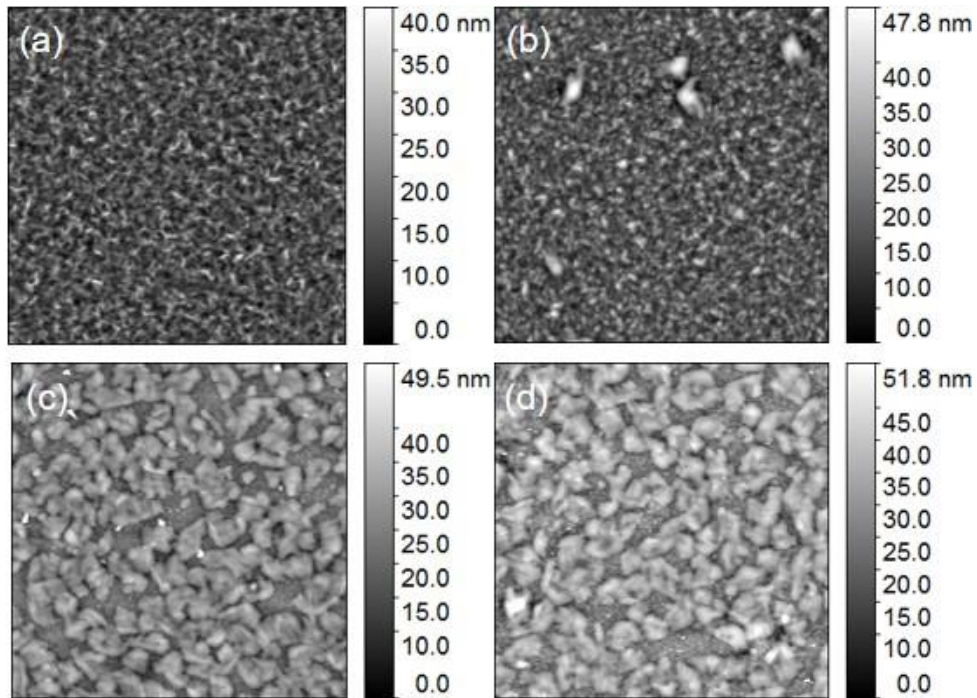
Figure C-2. 10μm x 10μm AFM images of active layer a) as-cast top surface, b) as-cast
bottom surface, c) annealed top surface, and d) annealed bottom surface.

Table C-1. Average RMS roughness values for P3HT:HPI-BT active layer.

Sample	RMS (nm)
As-cast (Top surface)	6.2 ± 1.2
As-cast (Bottom surface)	6.8 ± 1.1
Annealed (Top surface)	6.0 ± 0.4
Annealed (Bottom surface)	6.9 ± 0.4

C.2.2 Change in Surface Features with Annealing

AFM was used to examine the top surface of the BHJ after 1 and 21 minutes of annealing. Figure C- shows that the height and lateral dimensions of surface features remains approximately fixed.
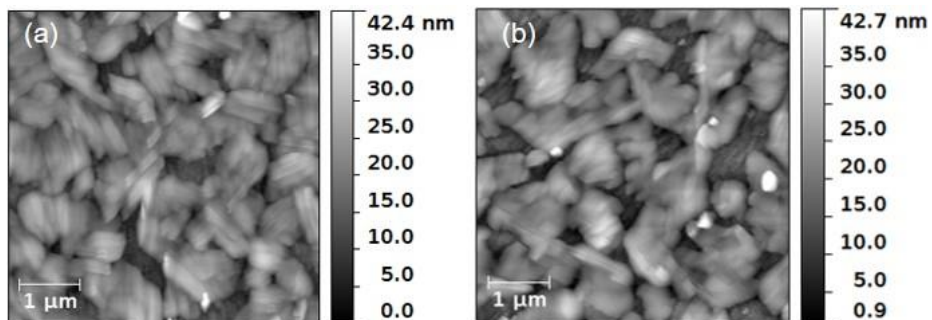
Figure C-3. AFM images of photoactive layer after thermal annealing at 100°C for (a) 1 minute, and (b) 21 minutes.

C.2.3   1-D Profile of Surface Feature Height

The coarsening of surface features was also examined through a 1-D trace of the height of surface features before and after annealing (Figure C-4).
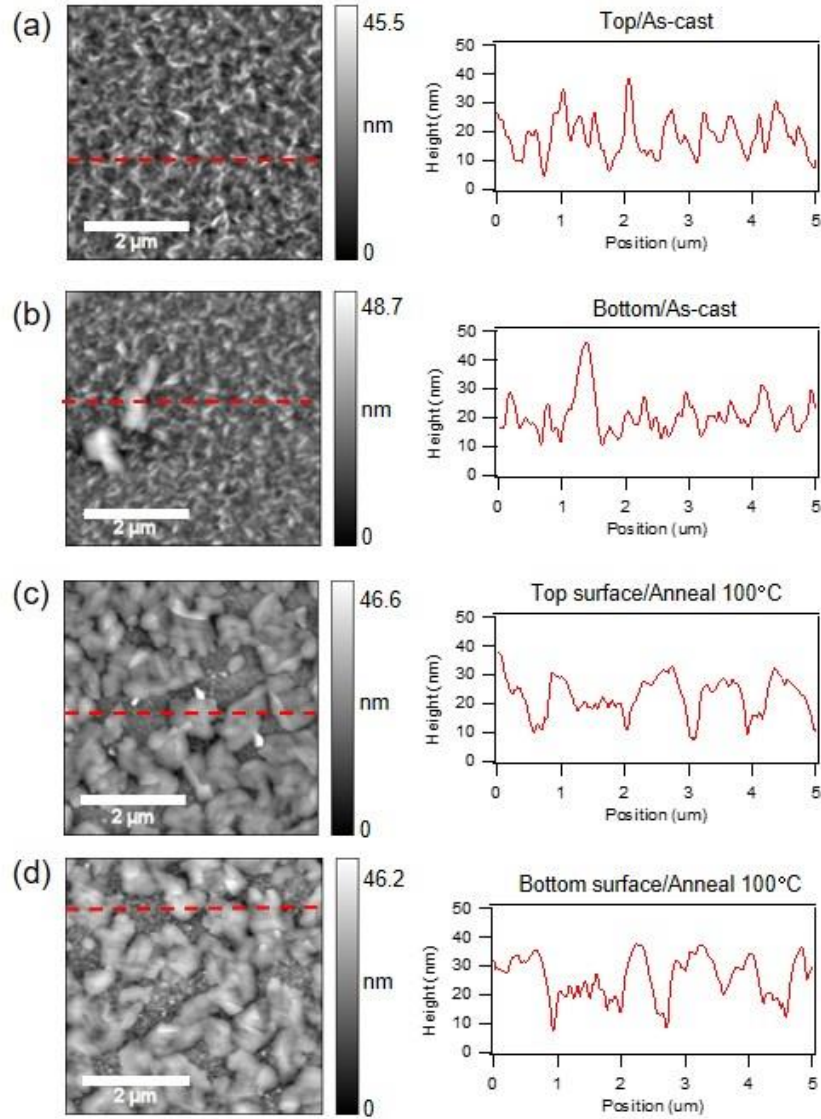

Figure C-4. AFM images of blended active layer with line-cut showing film texture for following conditions: (a) As-cast top surface, (b) As-cast bottom surface, (c) Annealed (100°C) 10 min top surface, and (d) Annealed (100°C) 10 min bottom surface.

Micron sized structures on the surface of the annealed films appear to be fibers composed into

bundles. In Figure C-5, the width of a single fiber was about 70 nm and a length of 500 nm.
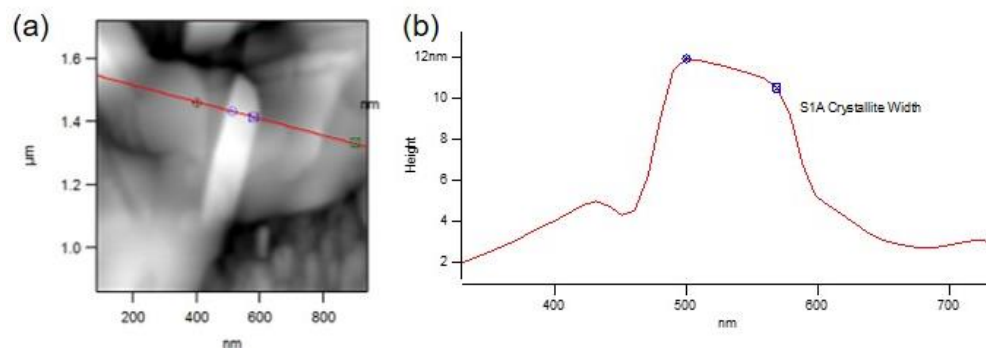
Figure C-5. Line-cut across AFM image of annealed HPI-BT:P3HT blend. Acceptor crystallites are approximately 70nm wide, 1μm long, and assemble into larger bundles.

A 1-D linecut across an assembly of fibers shows the difference in height and separation distance (Figure C-6).
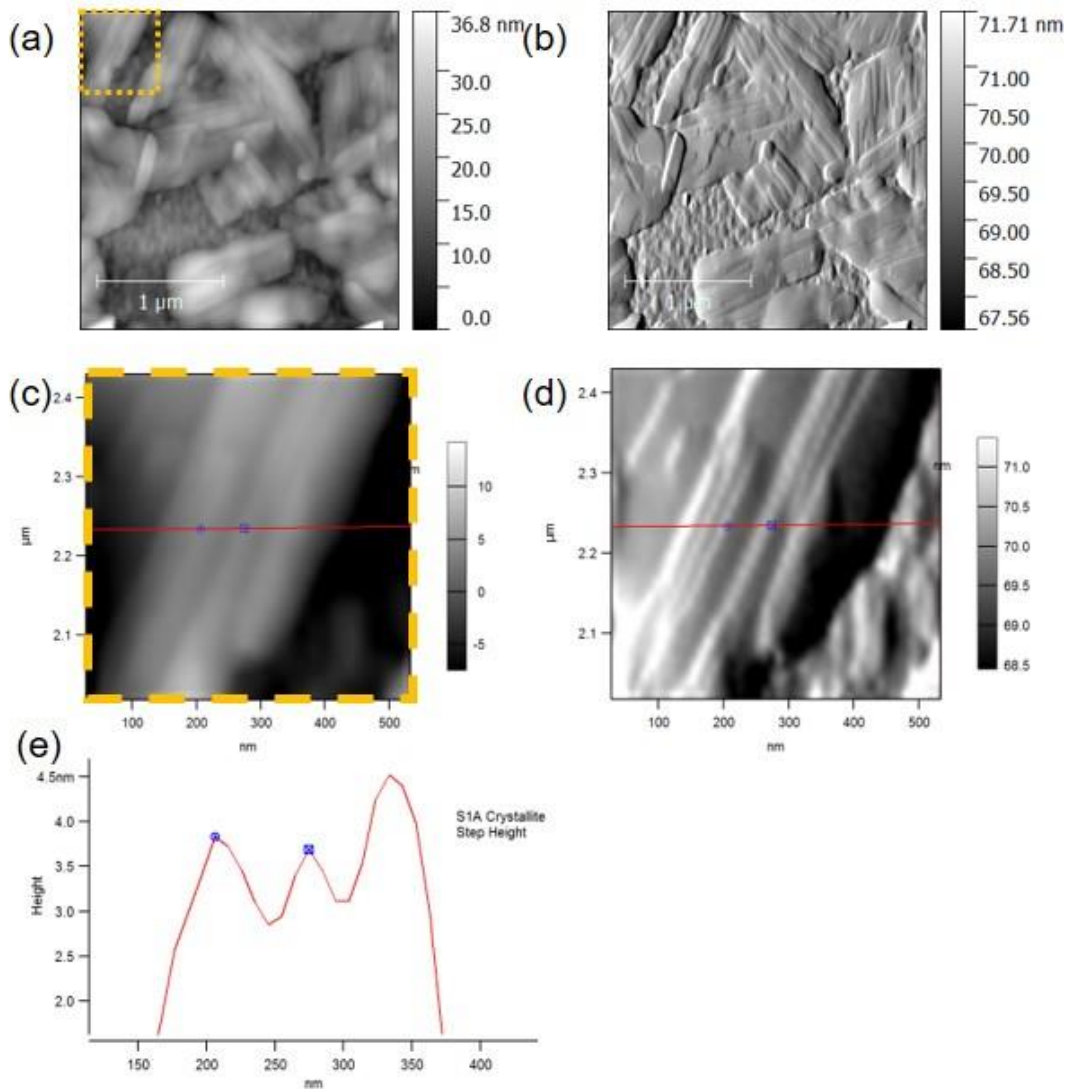
Figure C-6. AFM images of HPI-BT:P3HT film annealed for 1 minute at 100°C. a,c) Height and b,d) amplitude images show thin rectangular fibers assembled into micron size domains, (e) Height profile of crystallite features

C.3 Transmission Electron Microscopy

High resolution TEM (HRTEM) was used to examine the crystalline order of the BHJ before annealing. Nanowires of P3HT can be observed which are approximately 20 nm wide and 100-300 nm in length. These in-plane P3HT fibers had an average distribution of about one per 2-3 μm^2 area. Smaller P3HT crystallites were observed more frequently. The distribution is likely due to the polydispersity of the P3HT.
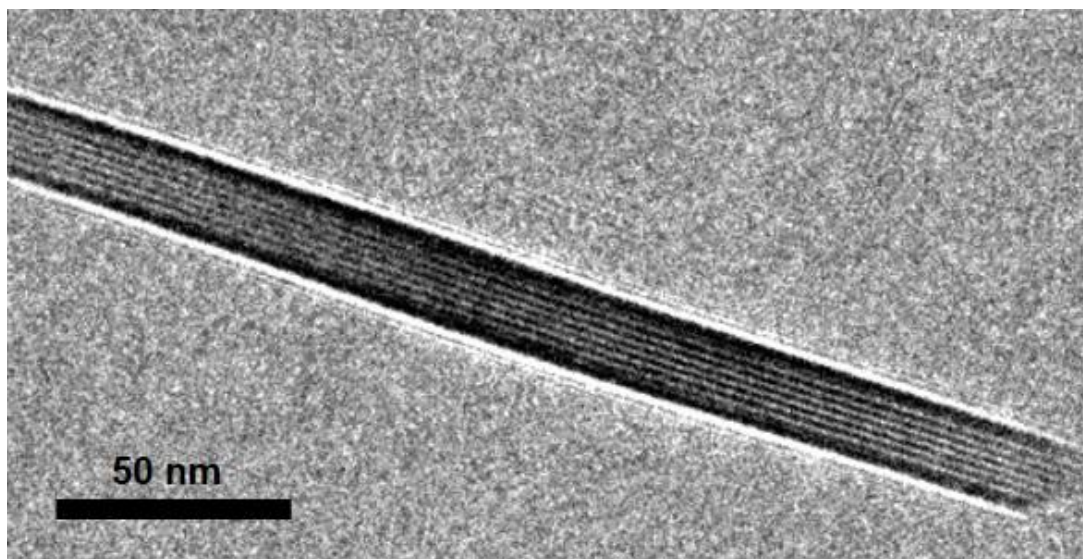
Figure C-7. High resolution TEM image of as-cast blend. P3HT nanowires visible throughout the film with thickness of about 20nm and variable length.

C.4 Grazing Incidence Wide-Angle X-ray Scattering (GIWAXS)

GIWAXS experiments were conducted at the Stanford Synchrotron Radiation Lightsource (SSRL) in Menlo Park, CA at beamtime 11-3. A heating stage was used in which the temperature of the stage holding the sample could be externally controlled while collecting scattering data with a MAR345 detector. Analysis of 2D scattering patterns was carried out using the WxDiff software developed at SSRL by Stefan C.B. Mannsfeld. Calibration of data was completed using a LaB_6 standard. Scattering images were plotted with the "missing wedge" to account for the sample geometry. The true out-of-plane scattering is not accessed in a fixed-angle grazing geometry using an area detector[1]. Polarization and $\sin(\chi)$ geometrical corrections were applied to the raw data.

C.4.1 Depth Profiling

Angle-dependent GIWAXS is a useful technique for probing structural differences at the surface of a thin film versus the bulk[2]. When the incidence angle is below the critical angle of the film, only the top few nanometers of the film are measured. The 2D scattering pattern of the bulk of the as-cast BHJ is shown in Figure C-8c where the incidence angle was equal to the critical angle of 0.10°. The surface is examined by lowering the incidence angle to 0.07° in Figure C-8d. Both donor and acceptor peaks are observed in the as-cast bulk and surface GIWAXS patterns, which can be seen more easily through the 2D line-cuts of the scattering features in the in-plane (Figure C-8e) and nominally out-of-plane direction (Figure C-8f). In the in-plane line cuts (Figure C-8e) both the P3HT alkyl stacking peak at q~0.38 Å^{-1} and HPI-BT polymorph peak at q~0.47 Å^{-1} are visible. While angle-dependent GIWAXs can measure the top few nanometers of the film, the surface of the as-cast

BHJ shows significant variation in the height of surface features (~50 nm) (Figure C-4) and therefore determining the structure of the true "surface" layer is not possible.
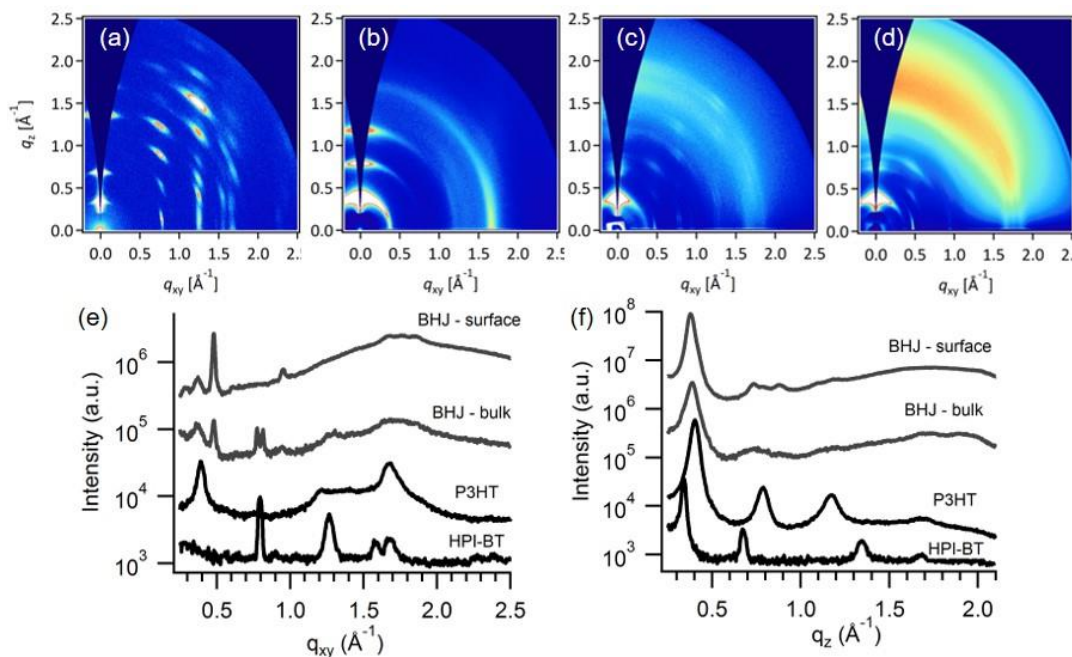
Figure C-8. 2D GIWAXS images for (a) neat HPI-BT, (b) neat P3HT, (c) BHJ bulk, and (d) BHJ surface, as well as line-cuts of the scattering data (e) in-plane and (f) nominally out-of-plane direction.

C.4.2   Comparison of BHJ GIWAXS on MoO₃ vs. PEDOT:PSS

BHJs were prepared on both MoO_3 and PEDOT:PSS and did not show any significant differences in the molecular packing details (Figure C-9). The GIWAXS of the as-cast and annealed films on PEDOT:PSS appear the same as the film on MoO_3, which was characterized in the main text. The optimized devices on MoO_3 and PEDOT:PSS also showed very similar performance characteristics (Table C-2).
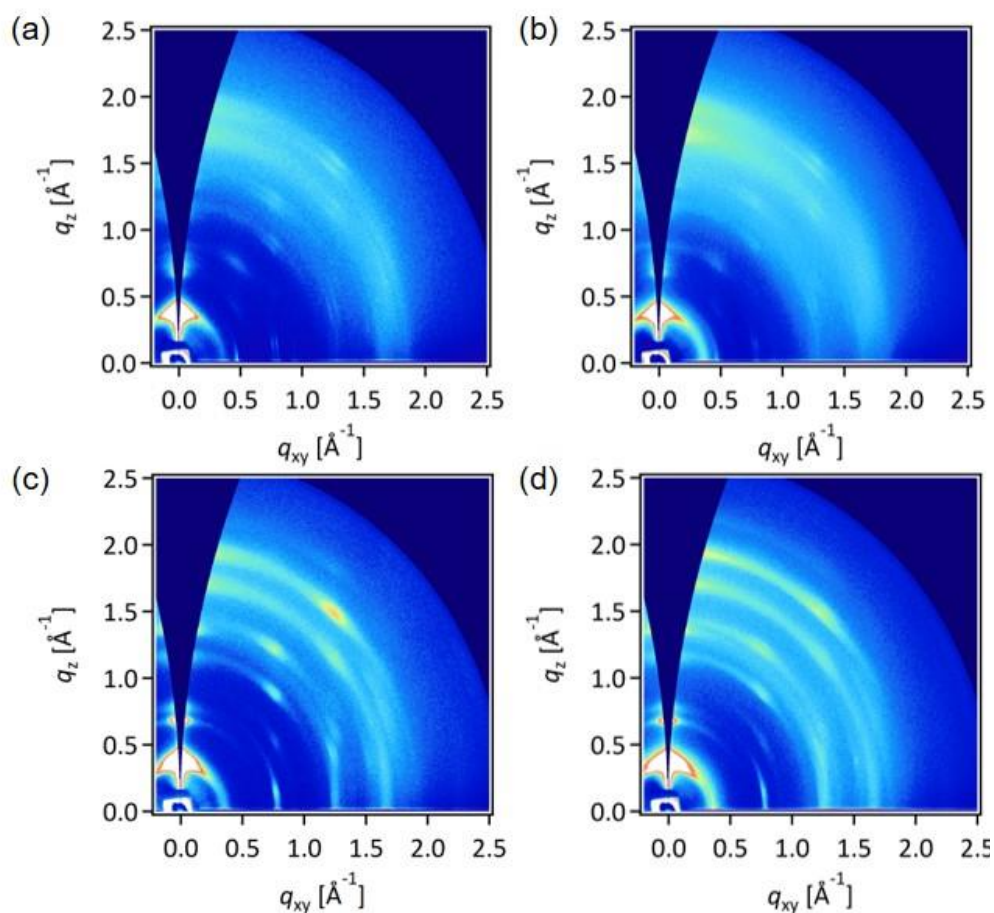
Figure C-9. 2D GIWAXS images for the as-cast BHJ on (a) as-cast BHJ on MoO$_3$, (b) as-cast BHJ on PEDOT:PSS, (a) annealed 10 minutes on MoO$_3$ and (d) annealed 10 minutes on PEDOT:PSS.

Table C-2. Device performance characteristics for MoO$_3$ vs. PEDOT:PSS as an anode interfacial layer.

Anode interfacial layer	Anneal (min)	V_{OC} (V)	J_{SC} (mA/cm^2)	FF (%)	Efficiency (%)
MoO$_3$	6	0.91	3.45	62.0	1.95
PEDOT:PSS	6	0.96	4.01	55.5	2.13

References

[1]   J. L. Baker *et al.*, "Quantification of thin film crystallographic orientation using X-ray diffraction with an area detector.," *Langmuir*, vol. 26, no. 11, pp. 9146–51, Jun. 2010.

[2]   W. Porzio, G. Scavia, L. Barba, G. Arrighetti, and S. Milita, "Depth-resolved molecular structure and orientation of polymer thin films by synchrotron X-ray diffraction," *Eur. Polym. J.*, vol. 47, no. 3, pp. 273–283, 2011.